Electrical conduction models for cochlear implant stimulation

Kai Dang

École doctorale STIC
(Sciences et Technologies de l'Information et de la Communication)
Unité de recherche : Inria

Thèse de doctorat

Présentée en vue de l'obtention du
grade de docteur en Automatique, Traitement du Signal et des Images
de
l'UNIVERSITE COTE D'AZUR

par

Kai DANG

Modèles de conduction électrique pour la stimulation de l'implant cochléaire

Dirigée par Maureen Clerc

Soutenue le 13/06/2017
Devant le jury composé de :

Andreas	Büchner	Prof. Hannover Medical School, Germany	Rapporteur
Maureen	Clerc	Prof. Inria Sophia Antipolis, France	Directeur de thèse
David	Guiraud	Prof. Inria Camin, France	Examinateur
Dan	Gnansia	Dr. Oticon Medical/Neurelec S.A.S, France	Invité
Tania	Hanekom	Prof. University of Pretoria, South Africa	Rapporteur
Valérie	Louis-Dorr	Prof. CRAN-Campus Sciences, France	Examinateur
Macherey	Olivier	Dr. CNRS Marseille, France	Examinateur

PhD THESIS

prepared at
Inria Sophia Antipolis - Méditerranée

and presented at the
Université Côte d'Azur
Graduate School of Information and Communication Sciences

A dissertation submitted in partial fulfillment
of the requirements for the degree of

DOCTOR OF SCIENCE
Specialized in Control, Signal and Image Processing

Electrical conduction models for cochlear implant stimulation

Kai DANG

Advisor	Maureen Clerc	Inria Sophia Antipolis - Méditerranée, France
Reviewers	Andreas Büchner	Hannover Medical School, Germany
	Tania Hanekom	University of Pretoria, South Africa
Examiners	David Guiraud	Inria - Camin, France
	Macherey Olivier	CNRS Marseille, France
	Valérie Louis-Dorr	CRAN-Campus Sciences, France
Invited member	Dan Gnansia	Oticon Medical/Neurelec S.A.S, France

Université Côte d'Azur

École Doctorale STIC
(Sciences et Technologies de l'Information et de la Communication)

THÈSE

pour obtenir le titre de
DOCTEUR EN SCIENCES
de l'Université Côte d'Azur
Discipline: Automatique, Traitement du Signal et des Images

présentée et soutenue par

Kai DANG

Modèles de conduction électrique pour la stimulation de l'implant cochléaire

Thèse dirigée par Maureen Clerc

Sountenue le - 13/06/2017

Composition du jury:

Advisor	Maureen Clerc	Inria Sophia Antipolis - Méditerranée, France
Reviewers	Andreas Büchner	Hannover Medical School, Germany
	Tania Hanekom	University of Pretoria, South Africa
Examiners	David Guiraud	Inria - Camin, France
	Macherey Olivier	CNRS Marseille, France
	Valérie Louis-Dorr	CRAN - Campus Sciences, France
Invited member	Dan Gnansia	Oticon Medical/Neurelec S.A.S, France

Abstract

Computational models have been widely used to improve the knowledge of the current distribution behavior in cochlear implant stimulations, optimizing electrode designs and stimulation strategies. The existing models employed no or simple electrochemical interface models and took current intensity on the electrodes as input. Therefore they have difficulties in making time domain simulations and simulating the stimulation modes that have voltage constraints, such as the Common Ground and the Multi-Mode Grounding modes.

In this PhD work, a new parametric surface mesh model of the cochlea has been developed. The shape of the model is controlled by a set of input parameters which can be tuned to fit the cochlear shape acquired from histological images, CT scans or existing cochlear mesh models. The symmetric boundary element method, which was implemented in OpenMEEG, has been applied on the model to simulate the current distribution of the cochlear implant stimulation.

Using the parametric model, comparisons on the current field has been made between the existing electrode layouts and a new transmodiolar electrodes. The new model can take either current or voltage as input for each electrode to simulate the common ground and multi-mode grounding modes. By coupling the surface model with lumped capacitor and constant phase element models, time domain simulation of the stimulation waveform has also been achieved.

To validate the simulation results and calibrate the parameters of the model, in-situ and in-vitro measurements have been carried out with custom-made devices. The in-situ measurements measured the electric potential and current intensity on the intracochlear electrodes under different stimulation modes. The in-vitro measurements took detailed potential samples near the electrode array in a 3D-printed container. The recorded data proved the effectiveness of combining lumped components with the surface model.

Keywords cochlear implant, electrical stimulation, surface mesh, boundary element method, 3D printing.

Résumé

De nombreux modèles numériques ont été proposés pour mieux comprendre comment le courant électrique est répartit lorsd'une stimulation électrique par implant cochléaire. Ceci permet à terme d'optimiser la géométrie des électrodes et les stratégies de stimulation. Les modèles précédemment proposés modélisent les modèles d'interface électrochimique de façon très basique, et ne prennent généralement compte que deque de l'intensité du courant sur les électrodes. Par conséquent, il leur est difficile de simuler la dynamique temporelle de la stimulation ou de modéliser la répartition du courant en fonction de différents modes de stimulation contrôlés en tension, tels que le mode de de retour commun (Common Ground), ou de retour multiple (Multi-Mode Grounding).

Dans cette thèse, nous avons développé un nouveau modèle surfacique de la cochlée. Le modèle géométrique dépend d'un ensemble de paramètres permettant d'ajuster la forme de la cochlée, en utilisant par exemple des données histologiques, des scans CT, ou encore des maillages de surface. Une méthode d'éléments finis surfaciques symétrique, implémentée dans OpenMEEG, a permis de simuler la distribution de courant due à la stimulation par l'implant cochléaire.

Un modèle paramétrique nous as permis decomparer les courants générés par les modèles d'électrodes actuellement disponibles et par un nouveau type d'électrode - faisceau transmodiolaire. Le modèle peut prendre en compte des courants ou des tensions en entrée à chaque électrode, ce qui permet de simuler le mode de retour commun ou multiple. En combinant le modèle surfacique avec une capacitance et des modèles d'éléments à phase constante, nous avons pu réaliser une simulation temporelle de la stimulation.

Afin de valider les résultats de simulation et calibrer les paramètres du modèle, nous avons créé un système permettant d'acquérir des mesures in-situ et in-vitro. Les mesures in-situ ont permis d'acquérir le potentiel électrique et l'intensité de courant d'électrodes intracochléaires selon différents modes de stimulation. Les mesures in-vitro ont permis d'échantillonner le potentiel électrique à proximité des électrodes de stimulation, dans un organe artificiel imprimé en 3D. Les données enregistrées ont permis de valider le modèle combinant le modèle d'interface électrochimique et le modèle tridimensionnel de cochlée.

Les implants cochléaires multi-canaux contemporains sont capables de régler la topologie de connexion interne et l'intensité du courant indépendamment sur chaque électrode. Afin d'atteindre le motif de courant désiré avec un nombre limité d'électrodes dans la cochlée, la proportion de courant sur chaque électrode dans chaque stimulation est soigneusement contrôlée, ce qui entraîne différents modes de stimulation.

Certains utilisateurs d'implants cochléaires obtiennent des scores proches de l'audition normale, en termes de reconnaissance de mots et de phrases dans un environnement calme, mais de faibles scores sont également signalés, ce qui signifie que la performance de l'implant cochléaire est variable selon les utilisateurs. Les implants ont également des performances insatisfaisantes dans certains contextes, tels que la reconnaissance vocale dans un environnement bruyant et l'appréciation de la musique. Il existe de nombreux facteurs qui pourraient expliquer ces problèmes, par exemple les limites du traitement du son, la faible résolution spatiale du courant de stimulation, le traumatisme d'insertion d'électrode et la dégénérescence du nerf auditif. Ici, les discussions porteront sur les facteurs liés à la distribution de courant à l'intérieur de la cochlée qui sont reliés à la recherche menée dans cette thèse, notamment l'étendue de l'activation qui comprend la propagation de l'excitation et le positionnement des électrodes.

Comme le réseau d'électrodes est entouré d'un tissu conducteur dans la cochlée, le courant de stimulation d'une électrode se diffuse et active une grande population de neurones, phénomène connu sous le nom de propagation de l'excitation. Par conséquent, les activations des électrodes adjacentes se chevauchent les uns les autres, conduisant à des interférences entre les électrodes et réduisant le nombre réel de canaux spatiaux indépendants.

C'est pour réduire la propagation de l'excitation que l'électrode périmodiolaire et différents modes de stimulation spatiale sont proposés. Les implants cochléaires modernes sont équipés de 12 à 20 canaux physiques (selon le fabricant), mais le nombre de canaux spatiaux indépendants observés chez les utilisateurs d'implant semble encore limité sous 10. Bien que la compréhension de la parole nécessite seulement 4 canaux indépendants, davantage de canaux sont tout de même nécessaires pour permettre la perception de la parole dans le bruit ou avec plusieurs locuteurs, ainsi que pour l'appréciation de la musique.

Il est extrêmement difficile d'obtenir des mesures électriques à l'intérieur de la

cochlée en raison de sa complexité géométrique et de sa petite taille. La simulation numérique est donc un outil précieux pour étudier les distributions de courant produite par les stimulations électriques. Les premiers modèles de la cochlée, basés sur la morphologie et la conductivité du tissu cochléaire, ont permis de simuler la distribution du potentiel et du courant et de tester l'efficacité de nouveaux modes de stimulation .

Ce paragraphe résume les principaux sujets abordés dans chaque chapitre:

Le chapitre 2 décrit le processus de construction d'un modèle cochléaire 3D paramétrique exploitant l'information morphologique de la cochlée acquise par différentes approches: extraction manuelle de la forme de la cochlée à a partir d' images histologiques, de micro-CT / CT ou bien des modèles de cochlée déjà maillés. L'outil de maillage (CGAL) et l'outil de simulation (OpenMEEG) sont également introduits dans ce chapitre.

Au chapitre 3, pour simuler les modes de stimulation de retour commun et multiple, un modèle simulant l'interface électrode-électrolyte a été construit en couplant le modèle cochléaire avec les condensateurs de blocage de l'implant et des éléments de phase constante. Les éléments de phase constante ont été approchés par des circuits R-C équivalents dont les impédances ont été ajustées dans le domaine de fréquence du courant de stimulation. Le modèle permet de simuler la distribution de courant sur les électrodes non stimulantes pendant la phase de décharge passive.

Le chapitre 4 démontre la flexibilité du modèle pour la construction rapide de différentes géométries de cochlée et dispositions d'électrodes. Des comparaisons de la distribution de potentiel et de l'activation neurale ont été réalisées pour différentes formes de cochlée et différents modes de stimulation. Deux modèles différents d'un nouveau type de matrice d'électrodes, le réseau d'électrode transmodiolaire, ont été modélisés. Les simulations de 3 nouveaux types de stimulation impliquant l'interaction entre le réseau transmodiolaire et le réseau d'électrodes normalisé ont été réalisées et comparées les unes avec les autres.

Les chapitres 5 et 6 présentent des études expérimentales de mesure du potentiel électrique dans le but de valider les résultats de la simulation. Des mesures in vitro du mode de stimulation avec retour commun ou multiple ont été faites avec le réseau d'électrodes placé dans deux conteneurs différents. La répartition spatiale du potentiel et la dstribution du courant sur les électrodes ont été enregistrées. Les résultats ont été utilisés pour adapter les paramètres du modèle d'interface

électrode-électrolyte. Des mesures in situ de plusieurs modes de stimulation ont été faites grâce un multiplexeur spécialement mis au point pour cette étude. Des mesures ont été faites in situ sur un spécimen humain (post mortem). Des données CT ont permis de réaliser un modèle paramétrique adapté à ce specimen, et les simulations ont été validées par rapport à ces mesures.

Keywords implant cochléaire, stimulation électrique, maillage de surface, méthode des éléments frontières, impression 3D.

Acknowledgements

First of all, I would like to express my sincere gratitude to my PhD advisor, Prof. Maureen Clerc, who guided my study and research in the past three and half years with her patience, knowledge and enthusiasm. Besides the professional knowledge, I also learned a lot from her attitude towards research and people, which will continue guide me in my works in the future.

I would also like to thank the Athena team, the place where I worked during my PhD thesis. Athena is a great research team with a friendly atmosphere. It is a place where the researchers can get immersed in their topics while inspiring and helping each other to progress. And this is made possible by the team leader, Rachid Deriche, and other permanent members in the team. Thank Nathanaël, Brahim, Marco, Rutger, Nathalie, Christos, Guillermo and all the other engineers, PhD students, visitors and interns in the team for the C++, Python, algorithms, making slides and presentations and many other skills I have learned from you. Thank the developers of OpenMEEG, my researches cannot be done without this well-designed tool.

As the sponsor and collaborator of my PhD, the research team of Oticon Medical / Neurelec offered me lots of help. I firstly give my special thanks to Jonathan Laudanski, who initiated the whole parametric cochlear model research project and helped me laid the foundation of my research. Although he he has left us three years ago, the contributions he made in the parametric model, bilateral implant and many other projects will continue helping both the researchers and the patients. I also give my thanks to Dan Gnansia, Pierre Stahl, Guillaume Tourrel, Manuel Segovia Martinez and many other researchers and developers at Oticon Medical, for the inspiring and constructive discussions I had with them. They also helped me designing the procedure of the in-vitro 3D measurement, provided me with all the hardwares required by the measurements and reviewed my PhD thesis. I would also like to thank the other sponsor of my PhD: the ANRT (Association Nationale de la Recherche et de la Technologie) of France.

My sincere thanks also goes to Adrien Bousseau and his research team at Inria, who provided me the 3D printer used by the in-vitro measurements, and to Nicola Guevara and Clair Vandersteen, who implanted the human specimen for the in-situ measurements. Thank Thomas Demarcy and Clair Vandersteen for providing me the user-specific cochlear meshes.

I also thank my family members: my wife, Liu Jiali and my parents, for the

encouragement and support they have provided when I worked as a PhD student.

Finally I would like to thank my thesis committee: Prof. Andreas Büchner, Prof. David Guiraud, Dr. Dan Gnansia, Prof. Tania Hanekom, Prof. and Dr.Macherey Olivier, for reviewing the thesis and attending my PhD defense.

Contents

Chapter 1

Introduction française

Contents

La cochlée joue un rôle crucial dans la construction du sens de l'ouïe. Son principe est de convertir les vibrations mécaniques des ondes sonores en impulsions électriques. Ces impulsions sont ensuite transmises au cerveau à travers le nerf auditif afin que le son acoustique puisse être compris. Des dommages causés aux cellules ciliées dans la cochlée entraînent une perte auditive. Selon la gravité de la perte auditive, différents traitements peuvent être adoptés. L'implantation d'un implant cochléaire est un traitement pour la perte auditive profonde. L'implant peut imiter la fonction des cellules ciliées en stimulant directement les fibres nerveuses auditives résiduelles dans la cochlée par des impulsions électriques modulées. Cependant, les tissus entre les électrodes et les fibres nerveuses auditives provoquent la diffusion du courant de stimulation, réduisant ainsi l'efficacité des stimuli artificiels. Afin d'améliorer la sélectivité spatiale des stimuli électriques, différents modèles de stimulation ont été développés. Cette thèse porte sur l'analyse de la distribution spatiale et temporelle du courant de stimulation dans différentes conditions, grâce à la simulation et la validation des résultats de la simulation.

Dans le premier chapitre, une brève introduction sera donnée sur l'anatomie et la physiologie de l'oreille humaine, ainsi qu'une explication des principes de fonctionnement des implants cochléaires multi-canaux actuels. Un examen des modèles existants et des algorithmes pour la simulation des implants cochléaires est également présenté dans ce chapitre. Enfin, un aperçu du contenu des chapitres suivants est donné à la fin.

1.1 L'oreille humaine

1.1.1 Anatomie & physiologie

L'oreille est l'organe sensoriel du système auditif. Il convertit le son - les vibrations mécaniques de l'air - en activités neuronales régulières. L'anatomie de l'oreille humaine est illustrée à la figure 2.1. L'oreille externe recueille le son de l'environnement et la conduit à la membrane tympanique, qui est attachée à l'extrémité du canal auditif. Dans l'oreille moyenne, les osselets (marteau, enclume et étrier) transmettent les vibrations mécaniques de la surface interne de la membrane tympanique à la membrane sur la fenêtre ovale de l'os temporal.

La cochlée se trouve derrière la fenêtre ovale. C'est l'organe qui convertit le mouvement physique de la fenêtre ovale en activité neuronale. La cochlée humaine,

située dans l'os temporal, est une spirale ovale à deux tours et demi (Palmer, 1984; Gilroy et al., 2008) remplie de liquide. Le diamètre moyen de la cochlée est de $7mm$ (Escudé et al., 2006).

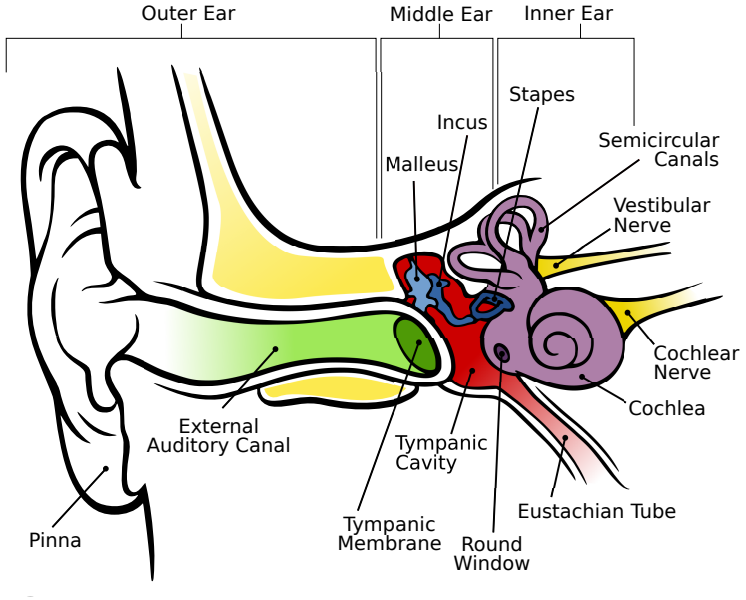

Figure 1.1: Anatomie de l'oreille humaine (Chittka L, 2009)

Figure 2.2 donne la coupe transversale du virage dans le tour basal d'une cochlée. La cochlée est séparée en 3 chambres par 2 membranes: la membrane de Reissner sépare la scala vestibuli de la scala media, la membrane basilaire sépare la scala tympani de la scala media (Dallos and Fay, 2012). Au sommet de la cochlée, la scala tympani et la scala vestibuli sont reliées par l'intermédiaire de l'hélicotrème. Les scala tympani et scala vestibuli sont remplies de périlymphe, tandis que la scala media est remplie d'endolymphe. La composition ionique du périlymphe est similaire au liquide céphalo-rachidien: faible densité d'ions potassium ($7mmol/L$) et forte densité d'ions sodium ($140mmol/L$). L'endolymphe, d'autre part, a une forte densité d'ions potassium ($150mmol/L$) et une faible densité d'ions sodium ($1mmol/L$) (Bear et al., 2007).

L'étrier est relié à la membrane au niveau de la fenêtre ovale. De l'autre côté de la membrane se trouve le périlymphe de la scala vestibuli. Le déplacement de l'étrier provoque une variation de pression dans le périlymphe, ce qui crée un déplacement vertical le long de la membrane basilaire.

La conversion des vibrations mécaniques en activité neuronale s'opère grâce aux

cellules ciliées situées dans l'organe de Corti de la membrane basilaire. Les cellules ciliées sont disposées en 4 rangées, comme le montre la figure 2.3.

Il existe 2 types de cellules ciliées: les cellules ciliées internes sont situées dans la rangée la plus proche de l'axe central de la cochlée (le modiolus); Les autres cellules ciliées sont dites cellules ciliées externes. Chaque cellule ciliée a environ 100 stéréocilia à son sommet. Le déplacement de la membrane basilaire entraîne des mouvements de la stéréocilia. Le mouvement dans une direction permet aux ions potassium de pénétrer dans l'endolymphe, provoquant une dépolarisation de la cellule ciliée, tandis que le mouvement dans le sens opposé inverse le processus et bloque le canal ionique du potassium.

Pour les cellules ciliées externes, les variations de potentiel électrique déclenchent une protéine motrice à l'intérieur de la cellule. Il en résulte une vibration rapide de la cellule dans la direction verticale. La vibration à son tour amplifie le déplacement de la membrane basilaire. Par conséquent, les cellules ciliées externes fonctionnent comme des amplificateurs dans la cochlée (Brownell et al., 1985; Ashmore, 1987; Manley and Fay, 2007). Pour les cellules ciliées internes, la dépolarisation ouvre le canal de calcium dans la cellule, provoquant la libération du neurotransmetteur et l'activation des neurones du ganglion spiral. Puisque les cellules ciliées internes couvrent 95 % des connexions aux neurones du ganglion spiral, elles sont les principales sources d'information auditive envoyée au cerveau.

Le nerf auditif des cellules du ganglion spiral se rassemble au centre de la cochlée dans le modiolus osseux. Il se confond ensuite avec le nerf vestibulaire, formant le huitième nerf crânien. Ce nerf entre dans le cerveau au niveau du pons, faisant passer l'information acoustique au système nerveux central pour son traitement.

1.1.2 Analyse de fréquence dans la cochlée

La gamme audible de fréquences sonores pour l'être humain est estimée entre $20Hz$ and $20kHz$ (Greenwood, 1990; Everest and Pohlmann, 2001). Dans la cochlée, le son d'entrée est filtré en bandes de fréquences qui sont codées séparément en impulsions sur les fibres nerveuses auditives. Deux types de codage des informations de fréquence sont utilisés par la cochlée: la tonotopie et le verrouillage de phase.

La tonotopie est basée sur les propriétés physiques de la membrane basilaire. La rigidité et l'épaisseur de la membrane basilaire changent progressivement de la base au sommet de la cochlée, de sorte que lorsque la membrane basilaire est entraînée

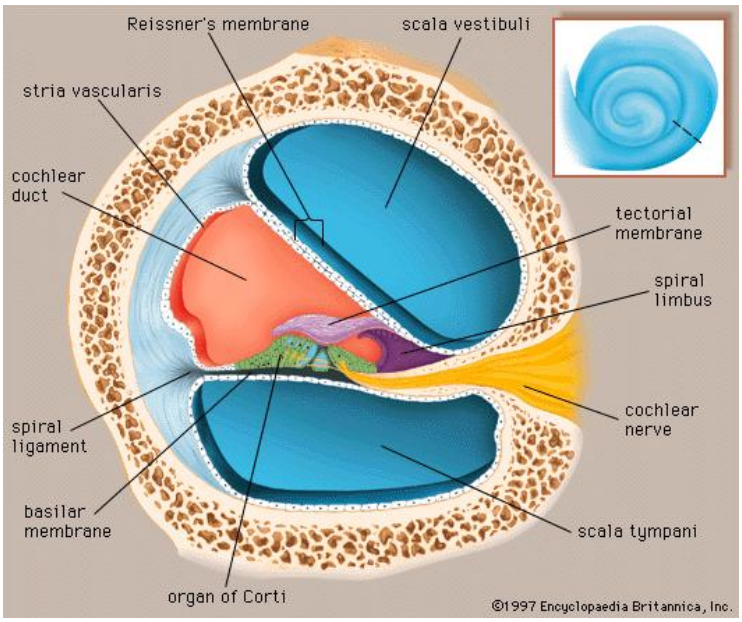

Figure 1.2: Coupe transversale de la cochlée (Online-Encyclopaedia-Britannica, 1997b)

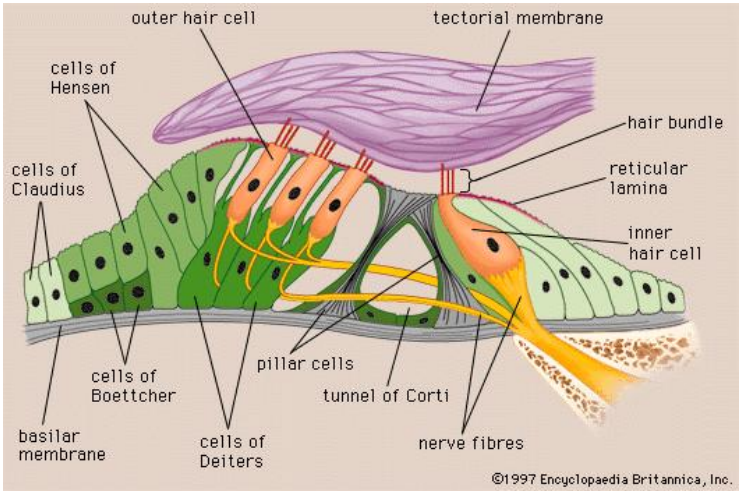

Figure 1.3: Les cellules ciliées et l'organe de corti(Online-Encyclopaedia-Britannica, 1997c)

par les vibrations mécaniques, la position du déplacement maximal diffère selon les bandes de fréquence du son d'entrée. La fréquence du son qui provoque le déplacement maximal dans une position spécifique de la membrane basilaire est la fréquence caractéristique de la position correspondante. Une carte des fréquences caractéristiques le long de la membrane basilaire est donnée en figure 2.4.

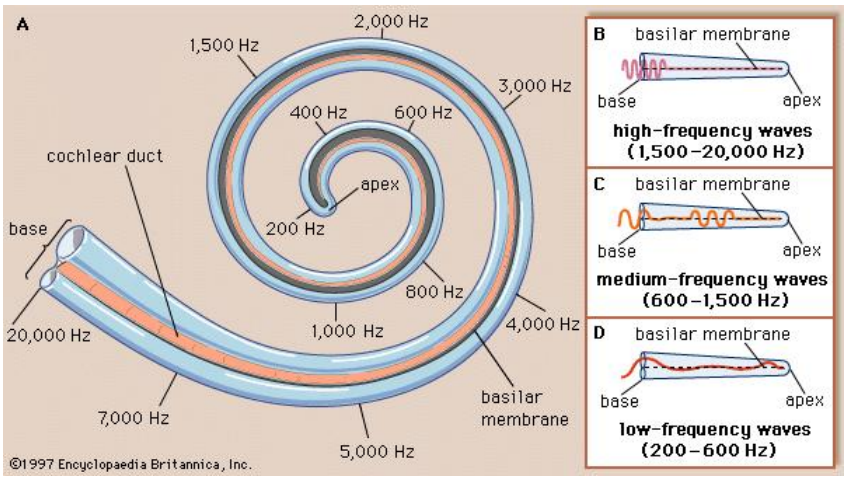

Figure 1.4: Fréquences caractéristiques à différentes parties de la membrane basilaire (Online-Encyclopaedia-Britannica, 1997a)

La fréquence caractéristique se réduit de la base au sommet de la cochlée (Greenwood, 1961, 1990; Kalkman et al., 2014). Le cerveau traite donc les sons selon la tonotopie de la cochlée. En conséquence, les bandes de fréquence du son d'entrée sont codées dans les positions des fibres nerveuses auditives activées dans la cochlée.

En plus de la tonotopie, à des fréquences inférieures à $4kHz$, le verrouillage de phase fournit des informations de fréquence supplémentaires (Bear et al., 2007). Le mouvement des stéréocilia est synchronisé avec les vibrations sinusoïdale du son, ce qui fait que les cellules ciliées ont tendance à décharger (émettre un potentiel d'action) à une phase particulière de la vibration (Johnson, 1980; Dynes and Delgutte, 1992). Par conséquent, les intervalles entre deux potentiels d'action sont toujours des multiples de la période de la tonalité d'entrée.

1.1.3 Perte auditive

En termes généraux, les pertes auditives sont classées en deux catégories: perte auditive de transmission et perte auditive neurosensorielle. Une combinaison des deux types est considérée comme une perte auditive mixte.

La perte auditive de transmission peut être causée par tout dommage au canal auditif externe ou à l'oreille moyenne. Ces dommages peuvent réduire la capacité de l'oreille moyenne à transmettre l'énergie mécanique à l'oreille interne, ce qui entraîne une perte d'intensité sonore du patient. La perte auditive de transmission est généralement réversible: avec un traitement approprié, l'audition peut être corrigée

partiellement ou complètement. En outre, les prothèses auditives peuvent également être utilisées pour compenser la perte d'audition résiduelle.

La perte auditive sensorielle est causée par des dommages à l'oreille interne, en particulier les cellules ciliées, ou par le dysfonctionnement du nerf auditif. Les dommages aux cellules ciliées peuvent être provenir d'une surexposition aux bruits forts, de défauts génétiques, du vieillissement, de maladies ou de drogues. La perte de cellules ciliées externes entraîne une augmentation du seuil sonore minimal audible et une diminution de la discrimination de fréquence. À ce stade, les prothèses auditives peuvent encore être utilisées pour récupérer partiellement la capacité auditive. Cependant, les dommages aux cellules ciliées internes provoquent une perte auditive profonde irréversible. L'absence de stimuli conduit également à la dégénérescence des cellules du ganglion spiral (Nadol et al., 1989). Dans ce cas, l'implant cochléaire est le seul moyen de récupérer un sens partiel de l'ouïe. Chez les patients atteints de perte auditive congénitale, l'implantation fournit également des stimuli essentiels qui aident à développer la perception de la parole et du langage du cerveau (Tye-Murray et al., 1995; Geers, 2002; Svirsky et al., 2004).

1.2 Implant cochléaire

L'implantation cochléaire représente à l'heure actuelle le seul traitement de la perte auditive neurosensorielle profonde causée par les dommages aux cellules ciliées (Zeng et al., 2008; Wilson and Dorman, 2008). À l'aide d'un réseau d'électrodes inséré dans la scala tympani de la cochlée, l'implant peut directement délivrer des stimuli électriques modulés aux fibres nerveuses auditives résiduelles, remplaçant ainsi la fonction des cellules ciliées endommagées.

1.2.1 Matériel et processus d'implantation

La figure 2.5 montre un système d'implant cochléaire typique, qui se compose d'un processeur de parole externe porté derrière l'oreille et un implant qui est installé sous le cuir chevelu lors de la chirurgie d'implantation.

Le processeur externe est équipé de microphones qui collectent en temps réel les signaux sonores de l'environnement et de plusieurs processeurs numériques pour traiter les signaux. Après réduction du bruit, contrôle automatique du gain et d'autres prétraitements, le signal sonore passe par un banc de filtres pour sortir

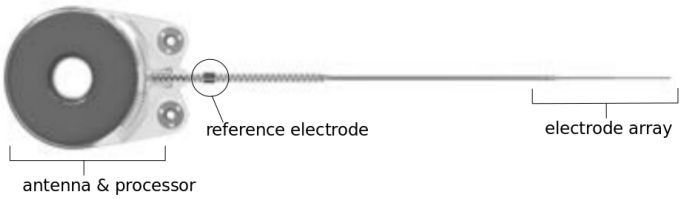

(a)

(b)

Figure 1.5: Le système d'implant cochléaire comprend une partie externe - le processeur de parole (b), un stimulateur implanté et son ensemble d'électrodes correspondantes (a). Photos adaptées de Oticon Medical, Vallauris, France.

dans une série de canaux filtrés par bande (autant que le nombre d'électrodes intracochléaires), comme le montre la figure 2.6. Les fréquences centrales du banc de filtres vont de $100Hz$ à $8kHz$, couvrant les bandes de fréquences les plus critiques pour la perception de la parole. Ce processus de décomposition imite le filtrage de fréquences effectué par la membrane basilaire.

En tant qu'indicateur de l'intensité sonore de chaque bande de fréquence, l'enveloppe de sortie de chaque filtre est extraite par filtrage passe-bas (Patrick et al., 2006) ou par transformée de Hilbert (Hochmair et al., 2006; Nie et al., 2006). Étant donné que les enveloppes extraites ont une plage dynamique relativement élevée (50dB) par rapport à la plage dynamique de la stimulation électrique des implants (3 à 15 dB), une compression logarithmique de l'amplitude est appliquée sur les enveloppes avant de les utiliser pour moduler les impulsions de stimulation des différents canaux (Zeng et al., 2002; Dorman and Wilson, 2004). Un canal de stimulation consiste en une boucle de courant indépendante dans l'implant, c'est à

dire une source de courant contrôlée, des fils et une ou plusieurs électrodes sur le réseau d'électrodes. Dans la stratégie de "continuous interleaved sampling" (CIS), qui a été mise en œuvre par tous les principaux fabricants, à chaque bande de fréquence du banc de filtres correspond son propre canal de stimulation (Wilson et al., 1991). En plus de la CIS, d'autres stratégies de stimulation ont également été développées. Par exemple, dans la stratégie "n-to-m" ($n \geq m$) m électrodes m sont encodées avec les m enveloppes énergétiques les plus élevées choisies parmi les n bandes de la banque de filtres (McDermott et al., 1992; Patrick et al., 2006).

Les paramètres des stimuli électriques calculés par le processeur externe sont transmis à l'implant à travers l'antenne, le signal radiofréquence fournissant à la fois la stratégie de codage et l'alimentation électrique de l'implant à travers le cuir chevelu. Le stimulateur décode les commandes de stimulation et génère du courant à travers ses canaux de stimulation selon la tonotopie de la cochlée, c'est-à-dire que des stimuli électriques provenant des basses fréquences sont envoyés aux canaux apicaux, tandis que des stimuli électriques provenant des hautes fréquences sont envoyés au canaux plus proches de la base.

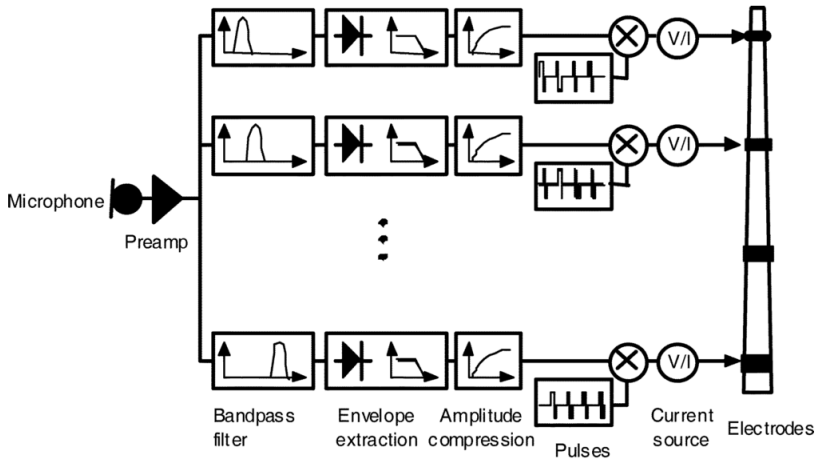

Figure 1.6: Diagrammes séquentiels du traitement du signal à l'intérieur d'un implant cochléaire, en utilisant la stratégie d'échantillonnage intercalaire continu. Image adaptée de Zeng et al. (2008)

Une illustration d'une tête implantée est donnée dans la figure 2.7. La majeure partie de l'implant est sous le cuir chevelu, et fixé au crâne par des vis. Il se compose d'une antenne, d'un processeur pour décoder les commandes de stimulation et une puce de stimulation dédiée pour générer des impulsions de courant. Un câble relie

la puce de stimulation au réseau d'électrodes intracochléaires. Une grande électrode de surface est placée hors de la cochlée pour fournir un chemin de retour pour le courant de stimulation.

Le réseau d'électrodes est équipé de contacts en platine pour conduire le courant de stimulation à différentes parties de la cochlée. La figure 2.8 donne une vue schématique de la coupe transversale de la cochlée implantée. Les matrices d'électrodes diffèrent l'une de l'autre en termes de longueur, de rigidité, de nombre et de forme des électrodes et de l'emplacement à l'intérieur de la scala tympani (Balkany et al., 2002; Wright et al., 2005). Les porte-électrodes périmodiolaires sont pré-courbés pour épouser le modiolus, ciblant le faisceau central du nerf auditif. Les porte-électrodes droits, par contre, suivent un chemin proche de la paroi latérale du scala tympani et sont plus susceptibles de stimuler le processus périphérique du nerf auditif.

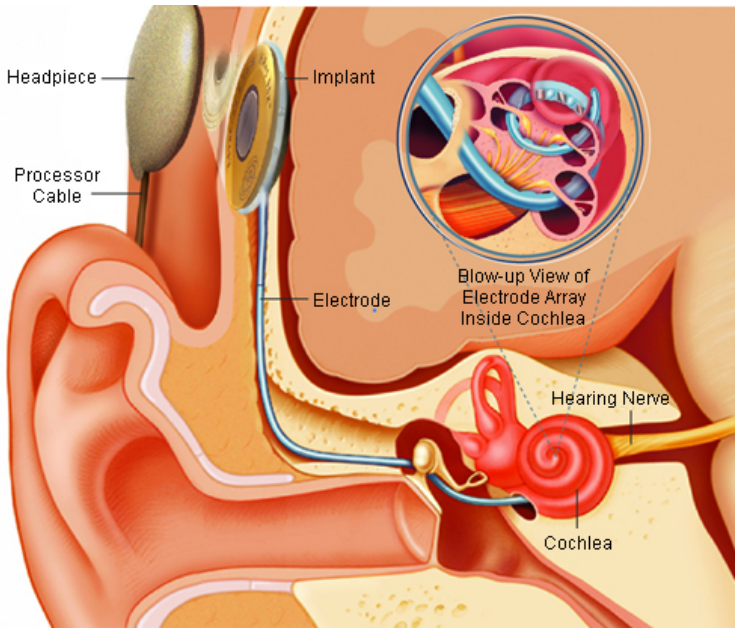

Figure 1.7: Un implant cochléaire implanté (University-California-San-Francisco, 2012)

Il existe deux méthodes d'insertion du réseau d'électrodes: la cochléostomie et l'approche par la fenêtre ronde. Au cours de la chirurgie, un trou est foré sur le crâne pour atteindre l'oreille moyenne, puis le rocher est perforé à proximité (dans l'approche de la cochléostomie) ou au niveau de la fenêtre ronde, pour insérer le réseau d'électrodes dans la scala tympani (Wilson and Dorman, 2008). L'insertion

est effectuée manuellement par le chirurgien.

L'insertion partielle, la déformation du réseau d'électrodes et même la pénétration de la membrane basilaire peuvent se produire pendant l'insertion, ce qui peut affecter la perception sonore après l'implantation (O'Leary et al., 1991; Wardrop et al., 2005a,b; Rebscher et al., 2008). Par conséquent, les tomodensitogrammes (CT scan) pré et post-opératoires du patient peuvent être utilisés pour identifier la position des électrodes (Finley and Skinner, 2008).

On observe chez les porteurs d'implants cochléaires une grande variabilité de performances perceptuelles, qui pourrait être causée par la chirurgie d'implantation, la dégénérescence des cellules neuronales, de processus de régénération et d'autres facteurs. Par conséquent, il est important d'étudier les cas au niveau individuel par des mesures objectives et subjectives. On mesure l'impédance entre paires d'électrodes pour s'assurer que tous les contacts fonctionnent et sont situés dans une région conductrice. Des impédances anormales peuvent signifier un dysfonctionnement mécanique, un traumatisme d'insertion (l'électrode n'est pas dans la scala tympani) ou l'encapsulation d'électrode par un tissu conjonctif. Le potentiel d'action composite évoqué électriquement (eCAP) est une autre mesure objective couramment utilisée pour évaluer la réponse neurale à la stimulation électrique. Elle est mesurée directement au niveau qui des électrodes intracochléaires juste après la stimulation (Abbas et al., 1999; Lai et al., 2002; Abbas et al., 2004; Botros et al., 2007). Des peuvent également être faites dans d'autres régions, c'est le cas par exemple du seuil de réflexe Stapedius émis (eSRT) ou de la réponse électrique auditive du tronc cérébral (eABR). Ces méthodes peuvent être utilisées comme outils de diagnostic pour vérifier l'efficacité de l'interface électrode-tissu: une réponse neurale observée indique une bonne communication entre l'électrode et le nerf auditif.

En cas de dysfonctionnement ou de comportements indésirables tels que la stimulation du nerf facial, l'électrode correspondante est désactivée. Pour toutes les électrodes activées restantes, on estime le seuil du niveau de courant le plus bas (niveau T) et le niveau le plus élevé conduisant à une intensité confortable (niveau C) et ces valeurs sont stockées dans l'implant pour ajuster le courant de stimulation (Zeng et al., 2008).

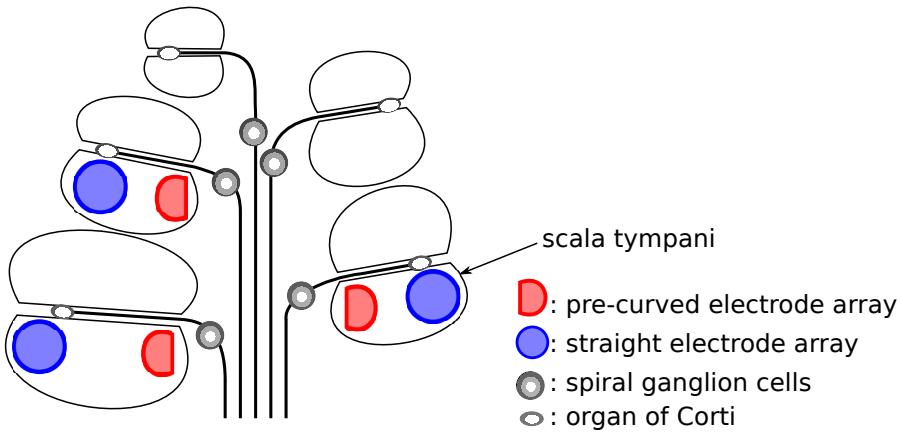

Figure 1.8: Vue schématique de la coupe transversale de la cochlée implantée

1.2.2 Modes de stimulation

Les implants cochléaires multi-canaux contemporains sont capables de régler la topologie de connexion interne et l'intensité du courant indépendamment sur chaque électrode. Afin d'atteindre le motif de courant désiré avec un nombre limité d'électrodes dans la cochlée, la proportion de courant sur chaque électrode dans chaque stimulation est soigneusement contrôlée, ce qui entraîne différents modes de stimulation. Une démonstration de différents modes de stimulation utilisés par l'implant cochléaire est donnée en figure 2.9.

La stimulation monopolaire est un mode de stimulation relativement simple, largement utilisée par les fabricants d'implants (Wilson and Dorman, 2008). En mode monopolaire, le courant de stimulation passe de l'une des électrodes intracochléaires à l'électrode de référence. Le reste des électrodes intracochléaires n'émettent ni ne reçoivent de courant. En raison de la longue distance ($50-100mm$) (Ramos-Miguel et al., 2015) entre le réseau d'électrodes et l'électrode de référence, le courant de stimulation a tendance à entrer profondément dans le tissu, ce qui donne au mode monopolaire une efficacité de stimulation élevée. Ceci signifie qu'il peut atteindre le même niveau d'activation neurale avec un niveau de courant inférieur comparé à d'autres modes de stimulation (Busby et al., 1994; Zwolan et al., 1996). Cependant, la longue distance entre les deux pôles de stimulation conduit également à une large diffusion du courant, ce qui réduit la sélectivité spatiale de ce mode de stimulation (Cohen et al., 2003; Snyder et al., 2004).

Le placement de l'électrode de retour loin de la position de stimulation réduit

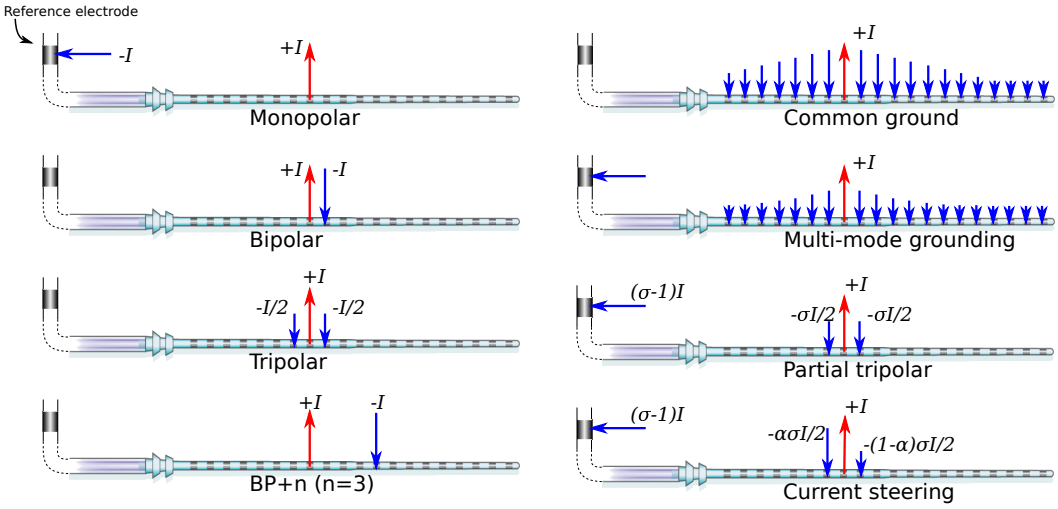

Figure 1.9: Modes de stimulation communs de l'implant cochléaire

la sélectivité spatiale de la stimulation cochléaire, mais à l'inverse, son placement dans la cochlée augmente la sélectivité spatiale, tout en réduisant l'efficacité de la stimulation. Le mode de stimulation bipolaire et le mode de retour commun sont deux exemples de modes de stimulation qui utilisent les électrodes intracochléaires non stimulantes comme électrodes de retour. Dans la stimulation bipolaire, une électrode voisine de l'électrode de stimulation est utilisée comme électrode de retour. Elle reçoit l'intégralité du courant émis par l'électrode de stimulation. La distance entre l'électrode de stimulation et celle de retour peut également être plus grande pour obtenir un compromis entre la sélectivité spatiale et l'efficacité de la stimulation. Ceci conduit à la stimulation $BP+n$, où n est le nombre d'électrodes inutilisées entre les électrodes stimulantes et de retour.

Les expériences ont montré que le nombre n est négativement lié à l'intensité de courant requise pour atteindre le même niveau d'activation neurale (Bierer and Middlebrooks, 2002). Il est à noter que la stimulation bipolaire a une répartition de courant asymétrique car l'électrode de retour ne peut être que d'un côté de l'électrode de stimulation. La stimulation tripolaire résout ce problème d'asymétrie en employant les deux électrodes voisines comme retour, chacune recevant 50 % du courant de stimulation. Ce mode de stimulation est encore plus sélectif spatialement que la stimulation bipolaire (Kral et al., 1998; Snyder et al., 2004, 2008), mais nécessite également un courant plus fort pour atteindre le même niveau d'activation

neuronale. En raison de sa sélectivité élevée, ce mode peut être utilisé pour atteindre des régions avec un mauvais contact d'électrode ou une dégénérescence neurale dans la cochlée, grâce à la mesure des seuils d'intensité de courant permettant la perception du son à différents endroits de la cochlée (Moore and Alcántara, 2001; Nelson et al., 2008). Dans la pratique, pour équilibrer la forte consommation de courant de la stimulation tripolaire, la stimulation tripolaire partielle est souvent utilisée (Kral et al., 1998; Litvak et al., 2007). En supposant que le courant de stimulation est de 1, la stimulation tripolaire partielle associe à chaque électrode voisine $\sigma/2$ de courant de retour ($0 \leq \sigma \leq 1$), tandis que le reste $(1-\sigma)$ du courant revient à travers l'électrode de référence d'origine comme dans la stimulation multipolaire. L'équilibre entre la sélectivité spatiale et la consommation d'énergie s'obtient en ajustant le facteur σ.

Le développement ultérieur de la stimulation tripolaire conduit à la stratégie de guidage du courant, qui vise à activer les fibres nerveuses auditives situées au regard des intervalles entre deux électrodes intracochléaires (Berenstein et al., 2008; Bonham and Litvak, 2008). Le guidage de courant cherche à créer des canaux de stimulation virtuels entre des électrodes voisines, ce qui entraîne une meilleure discrimination des fréquences chez les patients (Firszt et al., 2007; Koch et al., 2007). Il est mis en oeuvre par une asymétrie du retour de courant, en attribuant une proportion de courant retour $\alpha\sigma$ pour une électrode voisine de l'électrode de stimulation, alors que l'autre reçoit une proportion $(1-\alpha)\sigma$. Ici σ est le même coefficient de compensation que dans la stimulation tripolaire partielle, et α est le coefficient de guidage ($0 \leq \alpha \leq 1$). La proportion de courant qui retourne à l'électrode de référence est toujours $(1-\sigma)$.

Le mode de retour commun constitue la première tentative de focalisation du courant de stimulation. Il utilise toutes les électrodes intracochléaires non stimulantes comme électrodes de retour. Étant donné que le courant de retour est plus distribué, ceci réduit le risque d'une activation neurale inutile causée par le pic négatif du potentiel électrique sur les électrodes de retour. Contrairement aux stimulations bipolaires ou tripolaires, les électrodes de retour dans ce mode sont passives, ce qui signifie qu'elles sont directement connectées à la masse de la source de courant de stimulation, d'où le nom " common ground " en anglais (McDermott and McKay, 1994). En raison de la stratégie de retour de courant passif, la proportion du courant à travers chaque électrode de retour est inconnue. Cependant,

on peut imaginer que le chemin de courant dépend en grande partie de la position de l'électrode de stimulation: pour les électrodes situées au milieu du réseau, le courant peut retourner à travers les électrodes des deux côtés; au contraire, pour les électrodes basiques et apicales, le courant ne peut retourner que d'un côté. Cette distribution de courant sensible à la position de stimulation pourrait être la cause de la répartition non uniforme des niveaux T et C et du renversement de hauteur entre les électrodes observés par Blamey et al. (1992) et Busby et al. (1994). Le mode de retour multiple a été proposé pour éviter les inconvénients du mode stimulation avec retour commun. Ce mode permet au courant de retourner non seulement par les électrodes non stimulantes mais aussi à travers l'électrode de référence. Étant donné que la surface de l'électrode de référence est beaucoup plus grande que les électrodes intracochléaires, elle fournit un chemin d'impédance faible pour le courant, ce qui peut compenser l'impédance surélevée à la base et au sommet dans le mode de retour commun. Ce mode a été adopté par l'implant XP (Oticon Medical, Vallauris, France). Mais il n'existe pas de données qui comparent la répartition de courant selon les deux modes de stimulation (retour commun ou retour multiple).

Un autre mode de stimulation appelé "phased array" a été proposé avec l'idée de combiner à la fois la focalisation du courant et la stimulation sur plusieurs sites. Pour un réseau d'électrodes avec N sites de stimulation, une stimulation associé à un site est obtenue en distribuant le courant selon N poids, calculés de manière à annuler le potentiel sur les régions qui ne doivent pas être stimulées. La stimulation multisite s'obtient ensuite par superposition des poids correspondants des stimulations de site unique (van den Honert and Kelsall, 2007). Les mesures et les simulations ont montré que ce mode de stimulation présente des avantages potentiels par rapport à la stimulation tripolaire (Frijns et al., 2011). Mais, comme la stimulation avec retour commun, ses performances se dégradent aux extrémités du réseau d'électrodes, où le nombre d'électrodes voisines pour le retour de courant est limité (van den Honert and Kelsall, 2007).

1.2.3 Formes d'ondes de stimulation

Outre les différents modes de stimulation dans le domaine spatial, la forme d'onde de stimulation dans le domaine temporel peut également affecter l'activation neurale. Le courant injecté à travers l'interface électrode-électrolyte a deux effets dif-

férents: faradique et non faradique. Le premier se réfère au processus d'électrolyse, avec transfert de charge entre l'électrode et l'électrolyte. Selon les matériaux de l'électrode et le type d'ions dans la solution, cela peut conduire à la génération de gaz, à la dissolution de l'électrode et à la modification du pH, tous nuisibles au tissu environnant (Brummer and Turner, 1977). L'effet non faradique se réfère à l'agrégation ionique près de l'électrode, sans transfert de charge à travers l'interface électrode-électrolyte. L'agrégation d'ions est équivalente à un condensateur de charge, connu sous le nom de condensateur à double couche.

L'effet faradique peut être évité en limitant la densité de courant sur la surface de l'électrode (Shepherd et al., 1985; Robblee and Rose, 1990) et en équilibrant la charge lors des stimulations (Shepherd et al., 1991; Shepherd, 1999). Les implants peuvent être programmés pour générer des formes d'onde biphasiques équilibrées en charge (figure 2.10 (a) et (b)), mais la composante DC résiduelle n'est pas assez faible en raison de l'erreur des sources de courant fabriquées dans les puces de stimulation . Dans la plupart des produits d'implant, la stimulation équilibrée en charge est garantie en ajoutant un condensateur de blocage en série avec la source de courant, ce qui rend la composante DC négligeable ($< 1nA$) (Sit and Sarpeshkar, 2007). Une forme d'onde de stimulation biphasique avec une phase de décharge anodique active est illustrée en figure **??** (a). Pour cette forme d'onde, les stimuli doivent être espacés d'un court intervalle de temps pour permettre la décharge passive des condensateurs de blocage. La phase cathodique de la stimulation biphasique peut également être purement passive en utilisant des condensateurs de blocage, conduisant à une période de décharge passive plus longue. Un exemple de stimulation biphasique avec décharge passive est donné en figure 2.10(c).

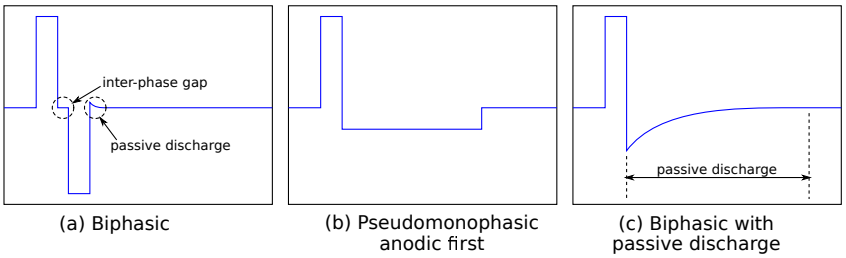

Figure 1.10: Exemples de formes d'ondes de stimulation utilisées par l'implant cochléaire.

Du point de vue de l'équilibre des charges, la forme d'onde biphasique simple semble être la meilleure façon de stimuler le nerf auditif. Cependant, des études ont

montré que la forme d'onde biphasique a un seuil de stimulation plus élevé par rapport à la forme d'onde monophasique (Javel and Shepherd, 2000; Miller et al., 2001). Une explication est que le potentiel d'action généré par la phase anodique peut être neutralisé par la phase cathodique immédiatement suivante(van den Honert and Mortimer, 1979). Le seuil peut être réduit en introduisant un écart inter-phase comme dans la figure 2.10(a) ou utilisant des impulsions asymétriques 2.10(b). Les enregistrements des réponses de neurones uniques effectuées chez le chat Javel and Shepherd (2000) ont montré que l'augmentation de l'écart inter-phase peut progressivement abaisser le seuil au niveau de la stimulation monophasique. En ce qui concerne l'onde de décharge passive monophasique, son amplitude maximale cathodique dépend de la taille du condensateur de blocage. Dans l'implant XP, il est ajusté à environ 20 % de l'amplitude maximale anodique, ce qui peut être assimilé à une forme d'onde asymétrique.

1.2.4 Limites de performance

Certains utilisateurs d'implants cochléaires obtiennent des scores proches de l'audition normale, en termes de reconnaissance de mots et de phrases dans un environnement calme, mais de faibles scores sont également signalés, ce qui signifie que la performance de l'implant cochléaire est variable selon les utilisateurs. Les implants ont également des performances insatisfaisantes dans certains contextes, tels que la reconnaissance vocale dans un environnement bruyant et l'appréciation de la musique (McDermott, 2004; Gfeller et al., 2007). Il existe de nombreux facteurs qui pourraient expliquer ces problèmes, par exemple les limites du traitement du son, la faible résolution spatiale du courant de stimulation, le traumatisme d'insertion d'électrode et la dégénérescence du nerf auditif. Ici, les discussions porteront sur les facteurs liés à la distribution de courant à l'intérieur de la cochlée qui sont reliés à la recherche menée dans cette thèse, notamment l'étendue de l'activation qui comprend la propagation de l'excitation et le positionnement des électrodes.

Comme le réseau d'électrodes est entouré d'un tissu conducteur dans la cochlée, le courant de stimulation d'une électrode se diffuse et active une grande population de neurones, phénomène connu sous le nom de propagation de l'excitation. Par conséquent, les activations des électrodes adjacentes se chevauchent les uns les autres, conduisant à des interférences entre les électrodes et réduisant le nombre réel de canaux spatiaux indépendants.

C'est pour réduire la propagation de l'excitation que l'électrode périmodiolaire et différents modes de stimulation spatiale sont proposés. Les implants cochléaires modernes sont équipés de 12 à 20 canaux physiques (selon le fabricant), mais le nombre de canaux spatiaux indépendants observés chez les utilisateurs d'implant semble encore limité sous 10 (Fishman et al., 1997; Friesen et al., 2001; Landsberger et al., 2012). Bien que la compréhension de la parole nécessite seulement 4 canaux indépendants (Shannon et al., 1995), davantage de canaux sont tout de même nécessaires pour permettre la perception de la parole dans le bruit ou avec plusieurs locuteurs, ainsi que pour l'appréciation de la musique (Fu et al., 1998; Friesen et al., 2001; Smith et al., 2002; Shannon et al., 2004).

1.3 Modélisation géométrique de la cochée

Il est extrêmement difficile d'obtenir des mesures électriques à l'intérieur de la cochlée en raison de sa complexité géométrique et de sa petite taille. La simulation numérique est donc un outil précieux pour étudier les distributions de courant produite par les stimulations électriques. Les premiers modèles de la cochlée, basés sur la morphologie et la conductivité du tissu cochléaire, ont permis de simuler la distribution du potentiel et du courant (Strelioff, 1973; Black et al., 1983; Suesserman and Spelman, 1993), et de tester l'efficacité de nouveaux modes de stimulation (Jolly et al., 1996).

Avec le développement des méthodes de simulation numérique et de la puissance de calcul, des modèles de cochlée ont été couplés à des modèles des fibres nerveuses auditives (Finley et al., 1990; Frijns et al., 1995, 1996, 2011). Ceci permet d'étudier par simulation comment les patterns d'activation varient avec le positionnement des électrodes sur les patterns d'activation (Hanekom, 2001; Choi et al., 2005), neural degeneration(Briaire and Frijns, 2006), la conductivité des tissus, la géométrie des fibres nerveuses (Kalkman et al., 2014, 2015) et celle de la cochlée (Dang et al., 2015; Malherbe et al., 2015).

De plus, en couplant le modèle de conduction électrique cochléaire avec un modèle d'interface électrode-électrolyte, il est possible de simuler le décours temporel du potentiel électrique (Choi et al., 2006; Choi and Wang, 2014) et du courant normal à la surface des électrodes (Sue et al., 2013, 2015). Des études préliminaires ont également étudié l'effet de la permittivité des tissus cochléaires (Inguva et al., 2015).

1.3.1 Modèles géométriques de la cochlée

Lumped model

Comme on le voit sur la figure 2.2, la coupe transversale de la cochlée fait apparaître une structure sophistiquée. Les premières tentatives de modélisation de la géométrie de la cochlée ont représenté la section transversale comme un réseau électrique. De tels réseaux de circuits ont été empilés pour former un modèle de cochlée déroulée, le "lumped cochlea model" (Strelioff, 1973; Suesserman and Spelman, 1993; Jolly et al., 1996; Spelman et al., 1995). Un schéma correspondant à ce type de modèle est représenté en figure 2.11 Kral et al. (1998). Dans ce modèle, le tissu cochléaire a été approximé par 19 sections transversales, chacune composée de trois couches conductrices: scala tympani, os et le reste des tissus.

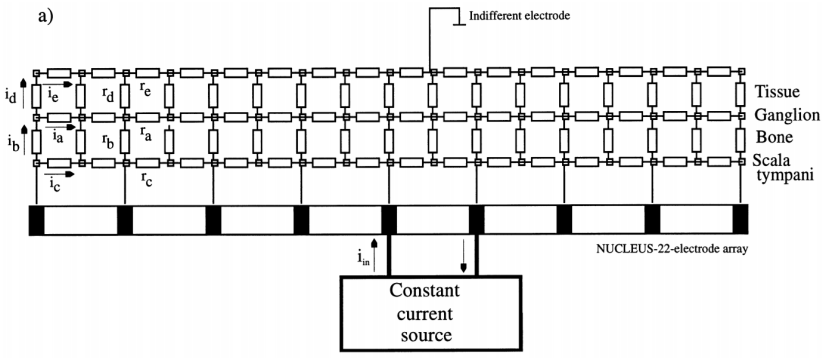

Figure 1.11: Circuit électrique représentant un modèle de cochlée (Kral et al., 1998).

Maillages tridimensionnels surfaciques ou volumiques

Par rapport à d'autres types de modèles, la puissance de calcul requise pour exécuter des simulations sur le "lumped cochlea model" est extrêmement faible. De plus, la permittivité tissulaire peut facilement être modélisée en rajoutant des condensateurs dans le circuit. Par contre, ce modèle très grossier ne permet pas une bonne résolution spatiale du potentiel électrique simulé, ni la prise en compte des interactions entre les étages de la spirale cochléaire.

Pour surmonter ces limites, les modèles de circuit électrique ont progressivement cédé la place à des maillages tridimensionnels, qui peuvent mieux prendre en compte les détails géométriques de la cochlée, tels que la membrane basilaire, la membrane

de Reissner et l'organe de Corti.

Le choix du type de maillage tridimensionnel dépend de la méthode de simulation adoptée: la méthode des éléments frontière (Boundary Element Method, BEM) nécessite un modèle de maillage surfacique, où seules les interfaces entre les domaines avec des conductivités différentes doivent être modélisées. Comme il n'y a pas de connexion entre les maillages des différentes surfaces du modèles, il est simple de modifier le modèle en déplaçant ces surfaces, tant qu'elles ne se touchent pas. Ainsi des modifications du positionnement ou de la disposition du réseau d'électrodes dans la cochlée peuvent être faites sans aucun remaillage. La BEM considère que chaque volume délimité par les surfaces du modèle a une conductivité homogène et constante. Il est donc difficile de prendre en compte un tissu anisotrope, comme celui des fibres nerveuses. Briaire and Frijns (2000) ont utilisé des triangles courbes au lieu de triangles plans pour la simulation BEM dans leur modèle maillé de cochlée de cochon d'Inde pour mieux représenter la surface incurvée de la cochlée avec un nombre limité de triangles. Leur modèle de maillage de surface à symétrie de révolution est illustré en figure 2.12.

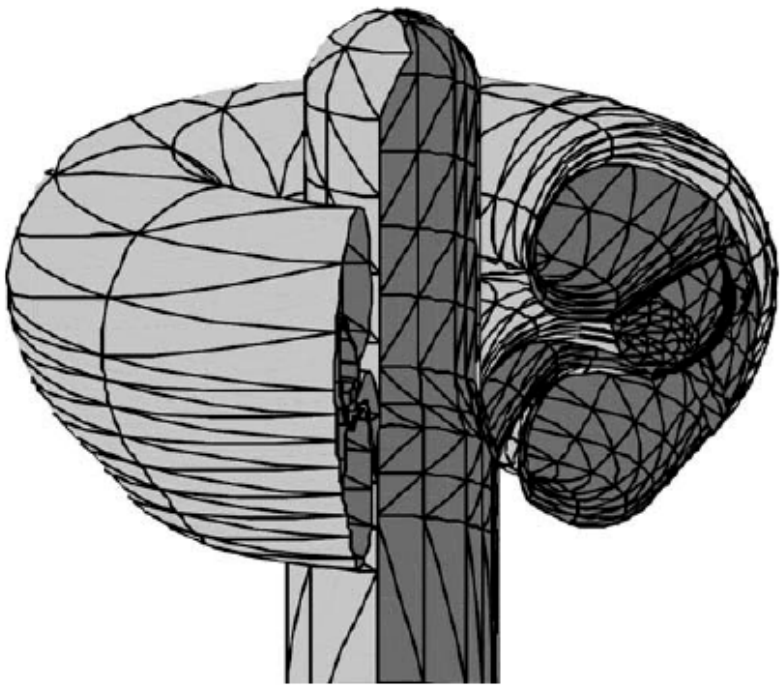

Figure 1.12: Maillage surfacique à symétrie de révolution modélisant une cochlée de cochon d'Inde (Frijns et al., 1995).

La méthode des éléments finis (Finite Element Method, FEM) repose sur un maillage volumique 3D. Dans ce type de maillage, le volume au sein du maillage est découpé en tétraèdres, ce qui, par rapport à des maillages trianfulés, augmente la complexité de la génération de maillage, mais permet la prise en compte de tissus anisotropes dans la simulation. Une image de l'extérieur d'un maillage volumique est représenté dans la figure **??**. Un ensemble d'électrodes implantées est visible au virage basal de la cochlée.

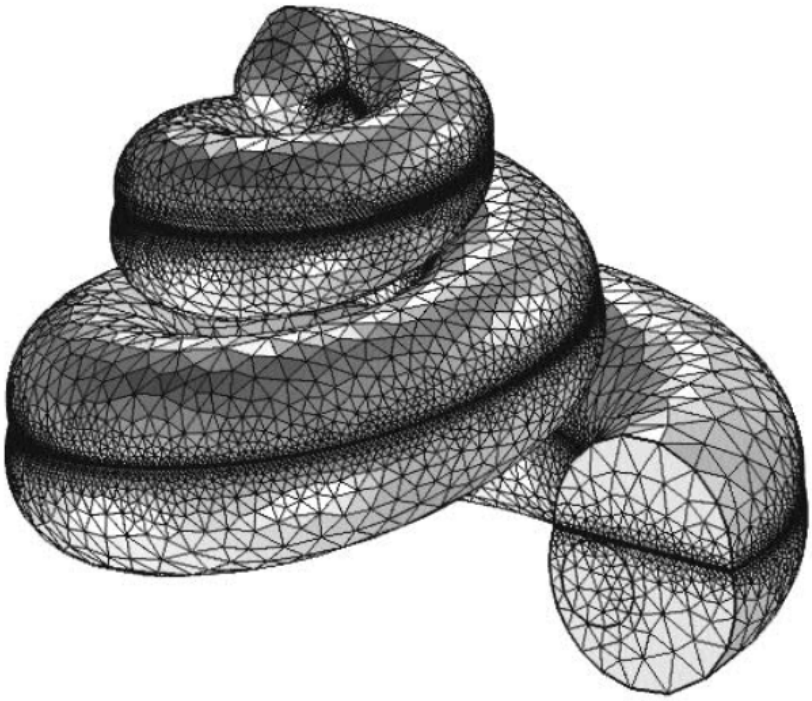

Figure 1.13: Vue extérieure d'un maillage volumique 3D de la cochlée humaine avec un réseau d'électrodes. (Saba, 2012).

Génération de maillage tridimensionnel

Des maillages 3D de la cochlée ont pu être générés à partir de modèles de coupes de la cochlée. Les maillages ont été créés à partir de ces coupes par extrusion soit longitudinale (Finley et al., 1990) soit rotationnelle (Briaire and Frijns, 2000; Choi et al., 2005, 2006; Choi and Wang, 2014; Tognola et al., 2007). Pour aboutir à une forme de cochlée plus réaliste, certains modèles utilisent des facteurs de zoom qui

modifient la taille de la section transversale lors de l'extrusion (Saba, 2012). Les facteurs de zoom diminuent progressivement de la base au sommet de la cochlée.

À mesure que des images haute résolution de la cochlée sont devenues disponibles, des modèles cochléaires plus réalistes ont été créés, reflétant les détails géométriques des individus. Kalkman et al. (2014) ont créé des modèles basés sur les images transversales histologiques de la cochlée et les ont utilisés pour étudier la distribution des fréquences perçues par rapport à l'emplacement des électrodes.

Tran et al. (2015) ont étudié la conduction volumique du courant en utilisant le modèle de reconstruction totale électroanatomique de la tête humaine, un modèle volumétrique de l'ensemble de la tête. Ils ont démontré 3 voies majeures (paroi cochléaire, modiolus et extrémité basale) du courant de stimulation monopolaire sortant de la cochlée. Leurs collègues ont créé un modèle de haute fidélité de la cochlée du cochon d'Inde selon des méthodes similaires (Wong et al., 2016).

Par rapport aux images histologiques, les images fournies par (micro-)tomodensitogrammes (CT) ont une résolution inférieure (taille de voxel d'environ 0,6 mm pour les tomodensitogrammes (Malherbe et al., 2015) et 24.8 μm pour les micro-CT (Dang et al., 2015)) et un contraste plus faible sur les tissus mous. Cependant, seules les tomodensitogrammes permettent d'avoir accès à la géométrie cochléaire et à l'emplacement de l'électrode chez les implantés cochléaires. Malherbe et al. (2015) a ajusté un modèle cochléaire à des informations spécifiques à l'utilisateur telles que la paroi extérieure de la cochlée et la position de l'électrode extraite des images CT.

1.3.2 Modèle de nerf auditif

Le couplage de la simulation de potentiel électrique avec les modèles du nerf auditif permet de prédire l'activité neurale en fonction du courant de stimulation. Colombo and Parkins (1987) ont proposé le premier modèle de nerf auditif de mammifère, qui a été progressivement raffiné en termes de caractéristiques électrophysioloques et morphologiques (Frijns et al., 1995; Rattay et al., 2001; Briaire and Frijns, 2006). Un diagramme de ce modèle est montré figure 2.14. Outre la prédiction de l'activation neurale, ce type de modèle peut également simuler la forme du potentiel d'action. Par conséquent, il est utilisé pour étudier les signaux eCAP (Briaire and Frijns, 2006, 2005; Choi and Wang, 2014).

Une façon plus simple d'estimer les réponses neuronales à la stimulation élec-

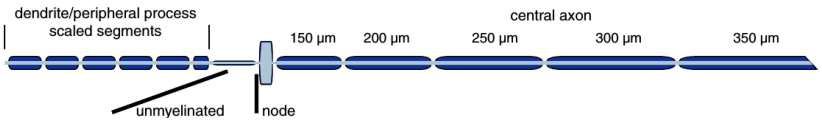

Figure 1.14: Modèle d'une seule fibre nerveuse auditive (Briaire and Frijns, 2005).

trique est de calculer la fonction d'activation (Rattay, 1986; Choi and Hsu, 2009; Wong et al., 2016). Elle prédit l'excitation d'une fibre nerveuse par la dérivée seconde du potentiel électrique le long de la fibre nerveuse. Comme la fonction d'activation est calculée à partir du potentiel électrique statique, elle ne peut pas être utilisée pour étudier l'effet de la modulation temporelle de la stimulation, comme les trains d'impulsions.

1.3.3 Interface électrode-électrolyte

Lorsqu'une électrode métallique est placée dans un électrolyte, des ions provenant de l'électrolyte se rassemblent à la surface de l'électrode et forment une couche mince appelée interface électrode-électrolyte. L'agrégation des ions sur la surface de l'électrode donne à l'interface un effet capacitif, tandis que les réactions chimiques électriques qui se déroulent à la surface de l'électrode présentent un effet résistif. Bien que l'interface soit une couche très mince, sa résistance et sa capacité ne peuvent être ignorées (Choi et al., 2006). La plupart des simulations cochléaires ne modélisent pas cette couche pour deux raisons: la première est qu'ils ont adopté l'hypothèse quasi-statique qui ignore la capacité introduite par cette couche et la seconde est celle de tous les modes de stimulation simulés par ces modèles (Kalkman et al., 2016), les intensités de courant sur toutes les électrodes sont fixées et ne sont pas affectées par la résistance de l'interface. Cependant, pour mode de retour commun et multiple, les intensités de courant sur les électrodes non stimulantes sont affectées par la résistance et la capacité de l'interface électrode-électrolyte. Par conséquent, ces deux types de stimulation n'ont pas pu être simulés par les modèles existants.

Lai and Choi (2007) ont tenté de simuler la forme d'onde de stimulation temporelle en incorporant l'interface électrode-électrolyte à un modèle cochléaire FEM. L'interface a été approchée par un maillage mince supplémentaire tout le long de l'électrode, où une permittivité complexe a été imposée. La caractéristique électrique de cette couche équivalait à un condensateur double couche $C_p = 10nF$

connecté en parallèle avec une résistance $R_p = 5k\Omega$. La simulation du domaine temporel de la forme d'onde potentielle à l'intérieur de la cochlée a été effectuée sur la base de ce modèle. Cantrell et al. (2007) a développé un modèle de couche d'interface plus sophistiqué, où C_p a été remplacé par un composant virtuel appelé élément de phase constante (constant phase element CPE) représentant l'interface entre électrolyte et électrode métallique. Ils ont également proposé un autre circuit équivalent pour simuler l'interface entre l'électrolyte et le caoutchouc de silicium non conducteur, comme le montre la figure 2.15.

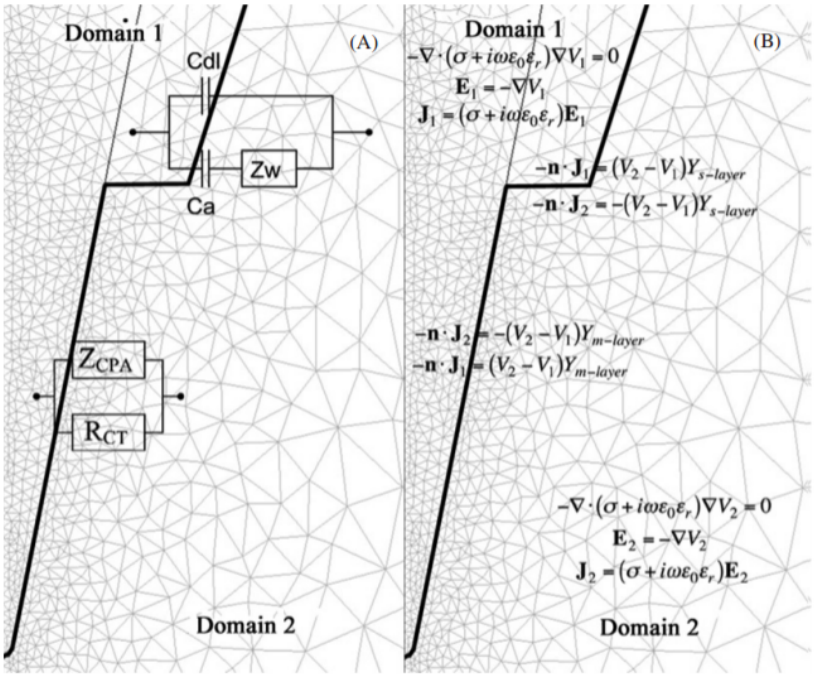

Figure 1.15: Modèle FEM incorporé à l'interface électro-électrolyte Cantrell et al. (2007). Le modèle de circuit équivalent de l'interface est montré dans (a) tandis que les équations de régulation correspondantes sont représentées sur la figure (b). La moitié supérieure des images représente l'interface entre l'électrolyte et le caoutchouc silicium, la moitié inférieure représente l'interface entre l'électrolyte et l'électrode métallique.

Sue et al. (2013) ont utilisé des modèles d'interface similaires pour estimer la distribution de courant normal sur une seule électrode pendant la stimulation électrique. Ils ont constaté que la densité de courant faradique irréversible augmente aux coins des électrodes, et pourrait être réduite en réduisant les angles la surface de l'électrode. Leurs résultats ont également montré que les réactions faradiques

réversibles contribuent à la capacité de l'interface électrode-électrolyte (Sue et al., 2015).

Dans une cochlée implantée, en plus de l'interface électrode-électrolyte habituelle, l'impédance est susceptible d'augementer à cause de phénomènes d'encapsulation (fibrose) et d'ossification autour des électrodes. Duan et al. (2004), par mesure de spectrographie d'impédance d'une cochlée d'un chat implanté, ont observé une augmentation de l'impédance intracochléaire, qui est passée de $5.4k\Omega$ au 9ème jour après implantation à $9.3k\Omega$ au 179ème jour après implantation. Hanekom (2005) ont modélisé l'ancapsulation des électrodes, et ont mis en évidence que les électrode périmodiolaires étaient plus affectées par ce phénomène que les électrodes latérales, en termes de modifications de seuils de stimulation.

1.3.4 Méthodes de validation

La méthode la plus directe de valider les modèles de cochlée est de comparer les distributions de potentiel électrique simulées avec des mesures direct du potentiel électrique, soit in vivo ou in vitro. Du fait de la taille très réduite des électrodes de l'implant, des mesures in vitro de haute résolution procurent des informations plus détaillées sur la distribution du potentiel à proximité des électrodes (Tognola et al., 2007). Par ailleurs, des mesures in situ effectuées dans la scala tympani, ont une résolution spatiale moindre (Vanpoucke et al., 2004; Wong et al., 2016; Dang et al., 2015). Ce type de mesures sont plus adaptées pour la validation de la simulation du mode de stimulation monopolaire, où le courant est moins focalisé que dans les autres modes de stimulation. Outre la validation du modèle cochléaire, Kalkman et al. (2014) ont aussi utilisé des mesures de potentiel intracochléaire pour calibrer la conductivité électrique du modèle et ainsi réduire les erreurs de simulation. Dans les cas où des mesures directes du potentiel ne peuvent pas être obtenues, les résultats de simulation peuvent être comparés à la sortie d'un circuit électrique équivalent ou d'autres modèles (Choi et al., 2006).

Concernant les modèles cochléaires couplés à des modèles de nerf auditif, il est plus difficile de valider les séquences d'activation neurale. Plusieurs groupes de recherche ont utilisé l'eCAP comme moyen indirect de valider les activités neurales simulées (Briaire and Frijns, 2005, 2006; Choi and Wang, 2014). Mais comme obsevé par Kalkman et al. (2016), les seuils de stimulation obtenus par simulation avec des fibres nerveuses isolées ne sont pas conformes aux observations cliniques, et

il faudra accumuler davantage de connaissances en neurophysiologie pour améliorer les modèles.

1.4 Structure de la thèse

Ce paragraphe résume les principaux sujets abordés dans chaque chapitre:

Le chapitre 2 décrit le processus de construction d'un modèle cochléaire 3D paramétrique exploitant l'information morphologique de la cochlée acquise par différentes approches: extraction manuelle de la forme de la cochlée à a partir d' images histologiques, de micro-CT / CT ou bien des modèles de cochlée déjà maillés. L'outil de maillage (CGAL) et l'outil de simulation (OpenMEEG) sont également introduits dans ce chapitre.

Au chapitre 3, pour simuler les modes de stimulation de retour commun et multiple, un modèle simulant l'interface électrode-électrolyte a été construit en couplant le modèle cochléaire avec les condensateurs de blocage de l'implant et des éléments de phase constante. Les éléments de phase constante ont été approchés par des circuits R-C équivalents dont les impédances ont été ajustées dans le domaine de fréquence du courant de stimulation. Le modèle permet de simuler la distribution de courant sur les électrodes non stimulantes pendant la phase de décharge passive.

Le chapitre 4 démontre la flexibilité du modèle pour la construction rapide de différentes géométries de cochlée et dispositions d'électrodes. Des comparaisons de la distribution de potentiel et de l'activation neurale ont été réalisées pour différentes formes de cochlée et différents modes de stimulation. Deux modèles différents d'un nouveau type de matrice d'électrodes, le réseau d'électrode transmodiolaire, ont été modélisés. Les simulations de 3 nouveaux types de stimulation impliquant l'interaction entre le réseau transmodiolaire et le réseau d'électrodes normalisé ont été réalisées et comparées les unes avec les autres.

Les chapitres 5 et 6 présentent des études expérimentales de mesure du potentiel électrique dans le but de valider les résultats de la simulation. Des mesures in vitro du mode de stimulation avec retour commun ou multiple ont été faites avec le réseau d'électrodes placé dans deux conteneurs différents. La répartition spatiale du potentiel et la dstribution du courant sur les électrodes ont été enregistrées. Les résultats ont été utilisés pour adapter les paramètres du modèle d'interface électrode-électrolyte. Des mesures in situ de plusieurs modes de stimulation ont été faites grâce un multiplexeur spécialement mis au point pour cette étude. Des

mesures ont été faites in situ sur un spécimen humain (post mortem). Des données CT ont permis de réaliser un modèle paramétrique adapté à ce specimen, et les simulations ont été validées par rapport à ces mesures.

Chapter 2

Introduction

Contents

The cochlea plays a crucial role in building the sense of hearing. It works by converting the mechanical vibrations of sound waves into electrical pulses. Those pulses are then conveyed to the brain through the auditory nerve so a human being can make sense of the acoustic sound. Damage to the hair cells in the cochlea leads to sensorineural hearing loss. Depending on the severity of the hearing loss, different treatments can be adopted. The implantation of a cochlear implant is a treatment for profound sensorineural hearing loss. The implant can imitate the function of hair cells by directly stimulating the residual auditory nerve fibers in the cochlea using modulated electrical pulses. However, the diffusive tissue between the electrodes and the auditory nerve fibers causes the spread of the stimulation current, reducing the efficiency of the artificial stimuli. In order to improve the spatial selectivity of the electrical stimuli, different stimulation patterns have been developed. This thesis is concerned with the spatial and temporal distribution of the stimulation current under different conditions by simulation, and the validation of the simulation results.

In the first chapter, a brief introduction will be given on the anatomy and physiology of the human ear, as well as an explanation of the working principles of the contemporary multi-channel cochlear implants. A review of the existing models and algorithms for cochlear implant simulation is also presented in this chapter. Finally, an outline of the content of the following chapters is presented at the end.

2.1 The human ear

2.1.1 Anatomy & physiology

The ear is the sensory organ of the auditory system. It converts sound — the mechanical vibrations of air — into regular neural activities. The anatomy of the human ear is shown in figure 2.1. The outer ear collects sound from the environment and conducts it to the tympanic membrane, which is attached to the end of the auditory canal. In the middle ear, ossicles (malleus, incus and stapes) connect the inner surface of the tympanic membrane to the membrane on the oval window of the temporal bone to continue the conduction of the mechanical vibrations.

The cochlea lies behind the oval window. It is the organ that converts the physical movement of the oval window into neural activity. The human cochlea is an oval spiral with two and half turns (Palmer, 1984; Gilroy et al., 2008) in the

temporal bone, filled with liquid. The average diameter of the cochlea is around $7mm$ (Escudé et al., 2006).

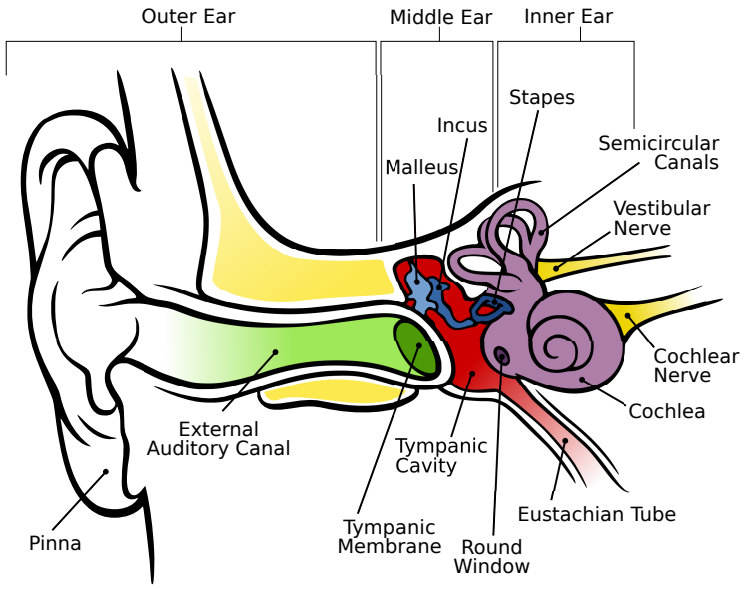

Figure 2.1: Anatomy of the human ear (Chittka L, 2009)

Figure 2.2 shows the cross-section of the basal turn of a cochlea. The cochlea is separated into 3 chambers by 2 membranes: Reissner's membrane separates the scala vestibuli from the scala media, the basilar membrane separates the scala tympani from the scala media (Dallos and Fay, 2012). At the apex of the cochlea, the scala tympani and the scala vestibuli are connected together through the helicotrema. The scala tympani and scala vestibuli are filled with perilymph, while the scala media is filled with endolymph. The ionic composition of perilymph is similar to that of cerebrospinal fluid: low potassium ion density ($7mmol/L$) and high sodium ion density ($140mmol/L$). The endolymph, on the other hand, has high potassium ion density ($150mmol/L$) and low sodium density ($1mmol/L$) (Bear et al., 2007).

The stapes is attached to the membrane on the oval window. To the other side of the membrane is the perilymph of the scala vestibuli. When the stapes moves, it causes a pressure change in the perilymph, which creates vertical displacement along the basilar membrane.

The key to converting mechanical vibrations into neural activities are the hair cells located in the organ of Corti of the basilar membrane. The hair cells are

arranged in 4 rows, as shown in figure 2.3. There are two types of hair cells: inner hair cells are located in the row closest to the central axis of the cochlea (the modiolus); the rest of the hair cells are the outer hair cells. Each hair cell has around 100 stereocilia on the top of the cell. Displacement of the basilar membrane leads to deflection of the stereocilia. The deflection in one direction allows the potassium ions from the endolymph to enter, causing depolarization of the hair cell, while deflection in the opposite direction reverses the process and shuts down the potassium ion channel.

For the outer hair cells, the changes in the electric potential triggers the motor protein inside the cell. This results in a rapid vibration of the cell in the vertical direction. The vibration in return increases the displacement of the basilar membrane. Therefore, the outer hair cells work as amplifiers in the cochlea (Brownell et al., 1985; Ashmore, 1987; Manley and Fay, 2007). For the inner hair cells, the depolarization triggers the calcium channel in the cell, causing the release of neurotransmitter and the activation of the attached spiral ganglion neurons. Since inner hair cells cover 95% of the connection to the spiral ganglion neurons, they are the major sources of the auditory information being sent to the brain.

The auditory nerve from the spiral ganglion cells gathers at the center of the cochlea in the bony modiolus. It then merges with the vestibular nerve, forming the eighth cranial nerve. The nerve enters the brain at the pons, passing the acoustic information to the central nervous system for higher level of processing.

2.1.2 Frequency analysis in the cochlea

The audible range of sound frequency for human beings is estimated to be between $20Hz$ and $20kHz$ (Greenwood, 1990; Everest and Pohlmann, 2001). In the cochlea, different frequency components of the input sound are extracted and separately encoded into the pulses on the auditory nerve fibers. Two ways of encoding the frequency information are used by the cochlea: tonotopy and phase locking.

Tonotopy is based on the physical properties of the basilar membrane. The rigidity and width of the basilar membrane gradually change from the base to the apex of the cochlea, hence when the basilar membrane is driven by the sound, the position of the maximum displacement on it differs according to the frequency components of the input sound. The frequency of sound which causes the maxim displacement at a specific position on the basilar membrane is the characteristic

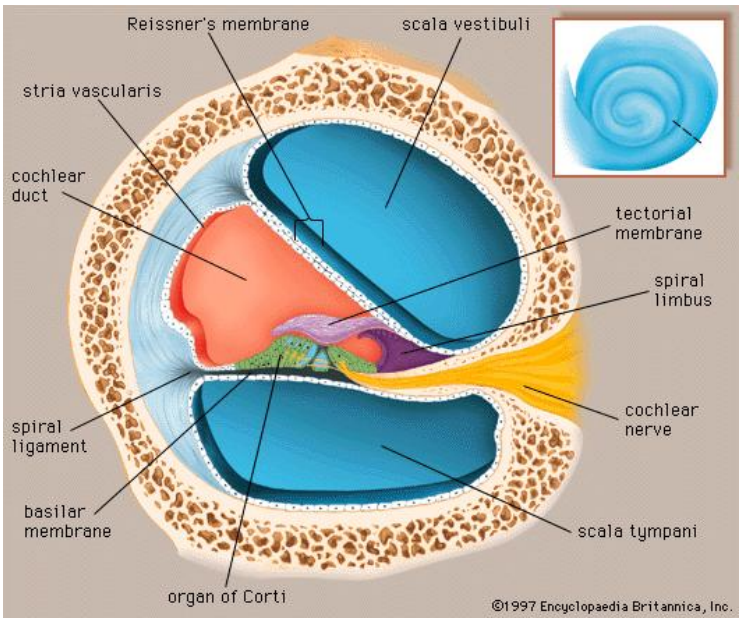

Figure 2.2: Cross-section of the cochlea (Online-Encyclopaedia-Britannica, 1997b)

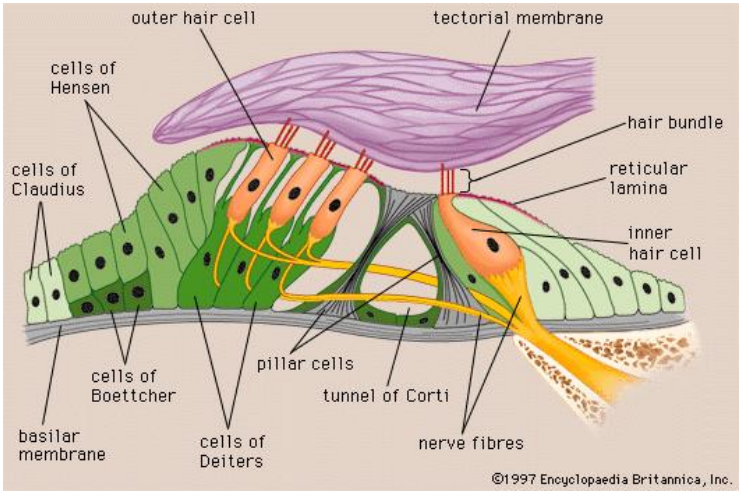

Figure 2.3: Hair cells and the organ of corti (Online-Encyclopaedia-Britannica, 1997c)

frequency of the corresponding position. A map of the characteristic frequencies on the basilar membrane is given in figure 2.4.

The characteristic frequency decreases from the base to the apex of the cochlea (Greenwood, 1961, 1990; Kalkman et al., 2014). The brain is therefore processing sounds according to the cochlea's tonotopy. As a result, the frequency components

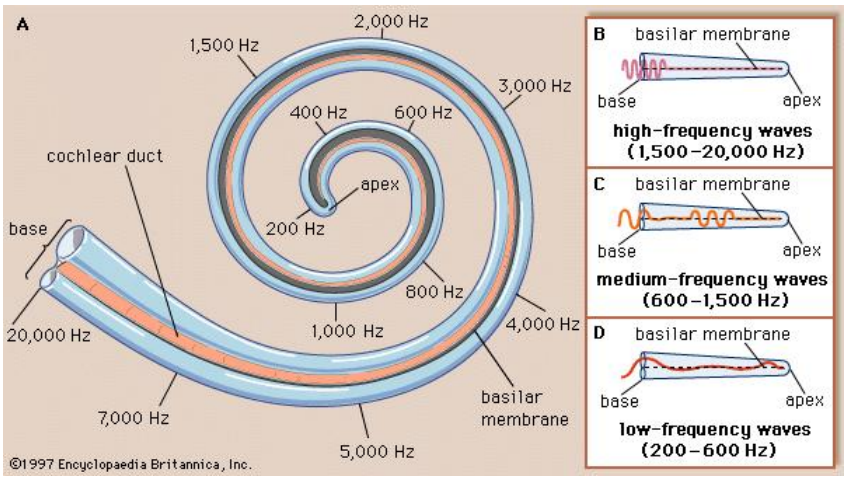

Figure 2.4: Characteristic frequencies at different parts of the basilar membrane (Online-Encyclopaedia-Britannica, 1997a)

of the input sound is encoded into the positions of the activated auditory nerve fibers in the cochlea.

At frequencies lower than $4kHz$, phase locking provides additional frequency information to the brain along with the tonotopy (Bear et al., 2007). The movement of the stereocilia is synchronized with the sinusoidal vibration of sound, which makes the hair cells tend to fire at a particular phase of the tone (Johnson, 1980; Dynes and Delgutte, 1992). Therefore, inter-spike intervals are always integer multiples of the input tone's period.

2.1.3 Hearing loss

In general terms, hearing losses are classified into two categories: conductive hearing loss and sensorineural hearing loss. A combination of both types is considered as a mixed hearing loss.

Conductive hearing loss can be caused by any damage to the external ear canal or the middle ear. These damages can lower the middle ear's ability to transmit mechanical energy to the inner ear, causing a loss of sound intensity of the patient. Conductive hearing loss is generally reversible: with proper treatment, a complete or partial improvement in hearing can be achieved. Besides, hearing aids can also be used to compensate the residual hearing loss.

Sensorineural hearing loss is caused by damages to the inner ear, especially the hair cells, or the dysfunction of the auditory nerve. Hair cells can be damaged by

over-exposure to loud noises, genetic defects, aging, diseases or drugs. The loss of outer hair cells leads to an increase in the minimal audible sound threshold of their corresponding characteristic frequencies and a decrease of frequency discrimination. At this stage, hearing aids can still be used to partially recover the hearing ability. However, damage to the inner hair cells causes irreversible profound hearing loss. The absence of stimuli also leads to the degeneration of the corresponding spiral ganglion cells (Nadol et al., 1989). In this case, the cochlear implant is the only way to recover a partial sense of hearing. To patients with congenital hearing loss, the implant also provides essential stimuli that aids the development of speech and language perception in the brain (Tye-Murray et al., 1995; Geers, 2002; Svirsky et al., 2004).

2.2 Cochlear implant

Cochlear implants are the only treatment to the profound sensorineural hearing loss caused by hair cell damage (Zeng et al., 2008; Wilson and Dorman, 2008). Using an electrode array inserted in the scala tympani of the cochlea, the implant can deliver modulated electric stimuli directly to the residual auditory nerve fibers, thus replacing the function of the damaged hair cells.

2.2.1 Hardware and implantation process

Figure 2.5 shows a typical cochlear implant system, which consists of an external speech processor (also called the behind-the-ear processor) worn behind the ear and an implant that is buried under the scalp during the implantation surgery.

The external processor is equipped with microphones that detect the real time sound signals from the environment and with several digital signal processors (DSPs) to perform signal processing. After noise reduction, automatic gain control (AGC) and other pre-processing, the sound signal goes through a filter bank and is decomposed into a series of bandpass-filtered channels (as many as the number of intracochlear electrodes), as shown in figure 2.6. The center frequencies of the filters in the filter bank range from $100Hz$ to $8kHz$, covering the most critical frequency bands for speech perception. This decomposition process is an imitation of the frequency filtering performed by the basilar membrane. As an indicator of the sound intensity of each frequency band, the envelope of the output of each filter is

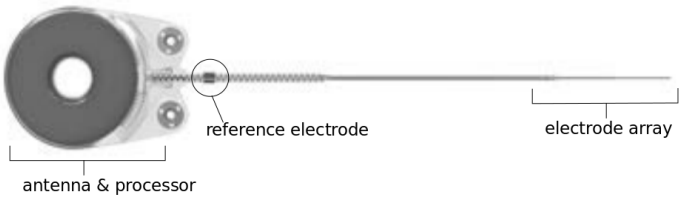

(a)

(b)

Figure 2.5: The cochlear implant system include an external part - the speech processor (b), an implanted stimulator and its corresponding electrode array (a). Pictures adapted from Oticon Medical, Vallauris, France.

extracted using either low-pass filtering (Patrick et al., 2006) or Hilbert transform (Hochmair et al., 2006; Nie et al., 2006). Since the extracted envelopes have a relatively high dynamic range (50dB) compared to the dynamic range of the electric stimulation which the implants can achieve (3 to 15dB), a logarithmic compression of the amplitude is applied on the envelopes before using them to modulate the stimulation pulses of the corresponding stimulation channel (Zeng et al., 2002; Dorman and Wilson, 2004). A stimulation channel refers to an independent current loop in the implant, which consists of a controlled current source, wires and a pair or more electrodes on the electrode array. In the continuous-interleaved-sampling (CIS) stimulation strategy, which has been implemented by all major manufactures, each frequency band of the filter bank drives different a stimulation channel (Wilson et al., 1991). Besides the CIS, other stimulation strategies have also been developed. For example, the "n-to-m" ($n \geq m$) strategy drives the m electrodes with the coding of the m highest energy envelopes selected from the n bands of the filter bank (McDermott et al., 1992; Patrick et al., 2006).

The parameters of the electrical stimuli computed by the external processor are transmitted to the implant through the antenna, the radio frequency wireless signal providing both the coding strategy and the power supply for the implant through the scalp. The implant stimulator decodes the stimulation commands and generates current through its stimulation channels according to the tonotopy of the cochlea, i.e. electrical stimuli coming from low frequency bandpass signals are sent to the apical channels while electrical stimuli coming from high frequency bandpass signals are sent to the basal channels.

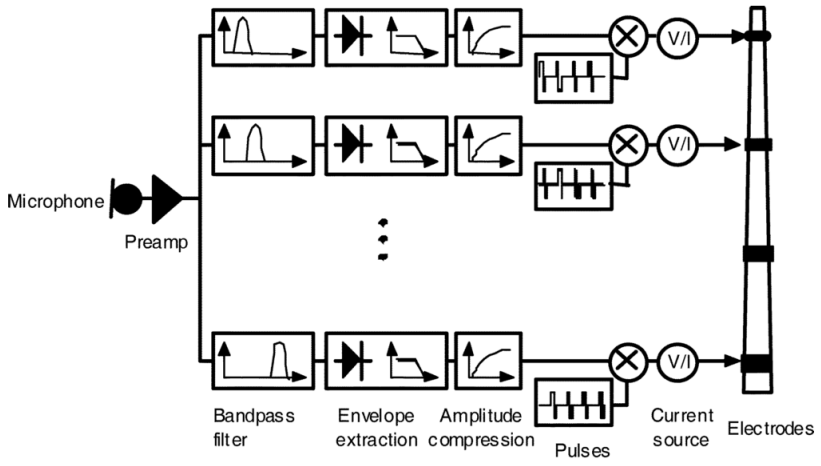

Figure 2.6: Block diagrams of the signal processing inside a cochlear implant, using the continuous-interleaved-sampling (CIS) strategy. Picture adapted from Zeng et al. (2008)

An illustration of an implanted head is given in figure 2.7. The major part of the implant is buried under the scalp, fixed by screws on the skull. It consists of an antenna, a processor to decode the stimulation commands and a dedicated stimulation chip to generate current pulses. A cable connects the stimulation chip to the intracochlear electrode array. A large surface electrode is placed out of the cochlea to provide a return path for the stimulation current.

The electrode array is equipped with platinum contacts to conduct stimulation currents to different parts of the cochlea. Figure 2.8 gives a schematic view of the cross-section of the implanted cochlea. The primary auditory neurons in the cochlea have a unique bipolar form: the organ of Corti, which is the source of neuron activity, is connected to the soma by the peripheral process of the nerve fibers; the central process of the nerve fibers gather at the axis of the cochlea (the modiolus)

and finally project to the neurons in the brainstem. The spiral ganglion is formed by the gathered cell bodies of the neurons, which rotates along the modiolus for about two turns (Stakhovskaya et al., 2007). Electrode arrays differ from each other in terms of length, stiffness, number and shape of electrodes and the location inside the scala tympani (Balkany et al., 2002; Wright et al., 2005). Perimodiolar arrays are pre-curved to hug the modiolus when inserted, targeting the central process of the auditory nerve. The straight arrays, on the other hand, follow a path close to the lateral wall of the scala tympani and are more likely to stimulate the peripheral process of the auditory nerve.

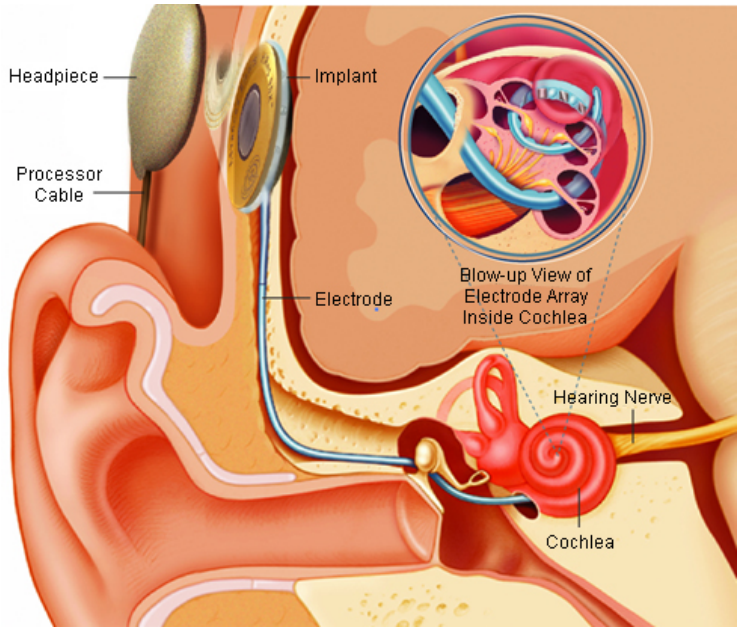

Figure 2.7: An implanted cochlear implant (University-California-San-Francisco, 2012)

Cochleostomy and the round window approach are the two methods of inserting the electrode array. During the surgery, a hole is drilled on the skull to reach the middle ear, then the temporal bone near (in the cochleostomy approach) or on (in the round window approach) the round window of the cochlea is opened to insert the electrode array into the scala tympani (Wilson and Dorman, 2008). The insertion is manually performed by the surgeon.

Partial insertion, deformation of the electrode array and even penetration of the basilar membrane can happen during the insertion which could affect the speech perception after implantation (O'Leary et al., 1991; Wardrop et al., 2005a,b; Reb-

scher et al., 2008). Therefore, pre and post-operative CT scans of the patient can be used to identify the position of the electrodes (Finley and Skinner, 2008).

CI users suffer from large performance variability, which could be caused by the implantation surgery, the neural cell degeneration, the implantation regeneration process and other factors. Therefore, it is important to study each individual case through objective and subjective measurements. Electrode impedance measurement measures the impedance between pairs of electrodes to ensure that all the electrode contacts are functioning and in a conductive region. Non typical electrode impedance can signify mechanical disfunction, insertion trauma (the electrode is not is the scala tympani) or electrode tissue encapsulation. Electrically evoked compound action potential (eCAP) is another commonly used objective measurement of the neural response to electrical stimulation, which is taken by the intracochlear electrodes right after the stimulation (Abbas et al., 1999; Lai et al., 2002; Abbas et al., 2004; Botros et al., 2007). Similar measurements can also be taken in other areas, which leads to the elicited stapedius reflex threshold (eSRT) and electrical auditory brainstem response (eABR). These methods can be used as diagnostic tools to verify the electrode-tissue interface effectiveness: an observed neural response indicates good contact between the electrode and the auditory nerve.

When malfunctioning or unwanted behaviors such as facial nerve stimulation happens, the corresponding electrode is deactivated. For all the remaining activated electrodes, the lowest current level inducing threshold (T level) and the highest level leading to comfortable loudness (C level) are estimated and stored in the implant to help fine-tune the stimulation current (Zeng et al., 2008).

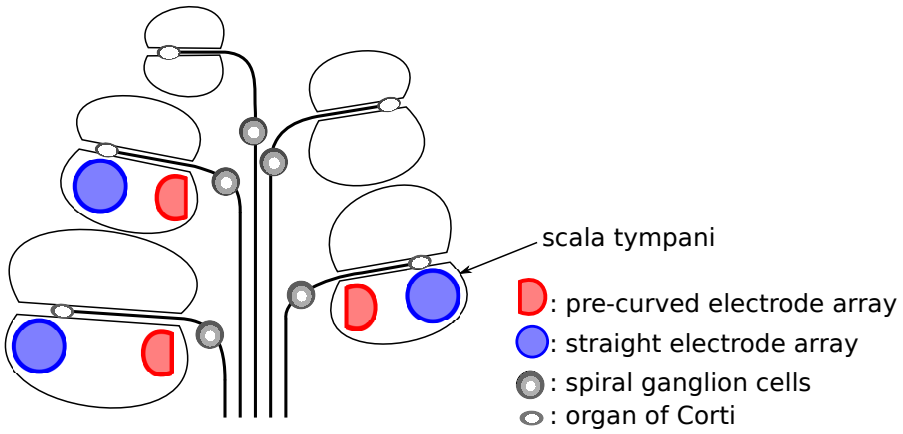

Figure 2.8: Schematic view of the cross-section of the implanted cochlea

2.2.2 Stimulation modes

Contemporary multi-channel cochlear implants are able to set the internal connection topology and the current intensity independently on each electrode. In order to achieve desired current pattern with limited number of electrodes in the cochlea, the proportion of current on each electrode in a single stimulus is carefully controlled, resulting in different stimulation modes. A demonstration of different stimulation modes used by the cochlear implant is given in figure 2.9.

Monopolar is a relatively simple stimulation mode and has been widely used by implant manufacturers (Wilson and Dorman, 2008). In monopolar mode, stimulation current flows from one of the intracochlear electrodes to the reference electrode. The rest of the intracochlear electrodes neither source nor sink current. Due to the long distance ($50 - 100mm$) (Ramos-Miguel et al., 2015) between the electrode array and the reference electrode, the stimulation current tends to penetrate deeper into the tissue, which gives monopolar mode a high stimulation efficiency, meaning that it can reach the same neural activation level with lower current level compared with other stimulation modes (Busby et al., 1994; Zwolan et al., 1996). However, the long distance between the two poles of stimulation also leads to wide current spread, which reduces the spatial selectivity of this stimulation mode (Cohen et al., 2003; Snyder et al., 2004).

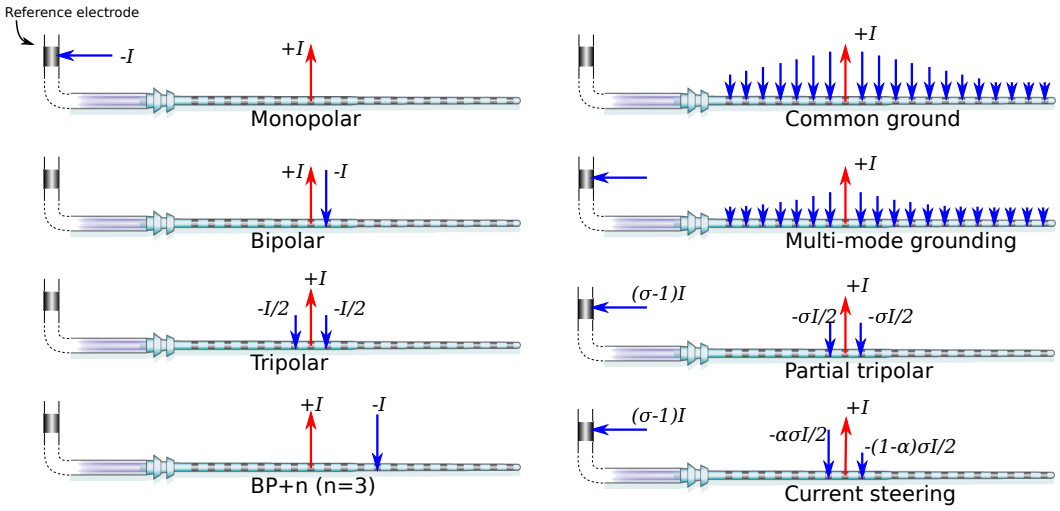

Figure 2.9: Common stimulation modes of the cochlear implant

Since a return electrode far from the stimulation position reduces the spatial

selectivity of cochlear stimulation, moving it towards the cochlea will conversely increase the spatial selectivity, at the cost of reducing stimulation efficiency. Bipolar and common ground are two examples of stimulation modes that use the non-stimulating intracochlear electrodes as return electrodes. In bipolar stimulation, one of the neighbors of the stimulating electrode is used as the return electrode, which receives the same amount of current send by the stimulating electrode. The separation between the stimulating and returning electrodes can also be increased to make a trade off between spatial selectivity and stimulation efficiency, leading to the $BP + n$ stimulation, where n is the number of unused electrodes between the stimulating and returning electrodes. Experiments have shown that the number n is negatively related to the current strength required to reach the same neural activation level (Bierer and Middlebrooks, 2002). Nevertheless, bipolar stimulation has an asymmetrical current distribution as the returning electrode can only be on one side of the stimulating electrode. Tripolar stimulation solves this problem by employing both neighbors as returning electrodes, each receiving 50% of the stimulation current. This stimulation mode is even more tonotopically restricted than bipolar stimulation (Kral et al., 1998; Snyder et al., 2004, 2008), but also requires increased current levels to reach the same neural activation level. Because of its high selectivity, this mode can be used to probe regions with poor electrode contact or neural degeneration in the cochlea, through the measurement of its current thresholds for sound perception at different places in the cochlea (Moore and Alcántara, 2001; Nelson et al., 2008). In practice, to balance the high current consumption of tripolar stimulation, partial tripolar stimulation is often used (Kral et al., 1998; Litvak et al., 2007). Assuming the stimulation current is 1, partial tripolar stimulation lets $\sigma/2$ current return from each of the neighboring electrode ($0 \leq \sigma \leq 1$), while the rest $(1 - \sigma)$ current returns through the original reference electrode i.e. the monopolar. The balance between current focus and energy consumption can be achieved by tuning the compensation coefficient σ.

Further development of the tripolar stimulation leads to the current steering strategy, which aims at activating the auditory nerve fibers that lie in the gaps between the intracochlear electrodes (Berenstein et al., 2008; Bonham and Litvak, 2008). Current steering can create virtual stimulation channels between neighboring electrodes, resulting in increased pitch perception by the recipients (Firszt et al., 2007; Koch et al., 2007). It is implemented by making an imbalanced current return

path: the ratio of the returning current taken by one neighbor of the stimulating electrode is $\alpha\sigma$, while the ratio for the other neighbor is $(1-\alpha)\sigma$, where σ is the same compensation coefficient as in the partial tripolar and α is the steering coefficient ($0 \leq \alpha \leq 1$). The proportion of current that returns to the reference electrode is still $(1 - \sigma)$.

Common ground was the first attempt of focusing the stimulation current. It uses all the non-stimulating intracochlear electrodes as return electrodes. Since the return current is more distributed, the chances of unnecessary neural activation caused by the negative peak of electric potential on the returning electrodes can be reduced. Unlike bipolar or tripolar stimulations, the returning electrodes in this mode are passive, which means they are directly connected to the ground of the stimulation current source, hence the name "common ground" (McDermott and McKay, 1994). Due to the passive current return strategy, the proportion of the current through each returning electrode is unknown. However, it can be imagined that the current path depends largely on the position of the stimulating electrode: for electrodes located in the middle of the array, current can return through the neighboring electrodes on both sides; while for the basal and apical electrodes, the current can only return to one side. This stimulation position sensitive current distribution could be the cause of the non-uniform distribution of T and C level and pitch reversal across electrodes observed by Blamey et al. (1992) and Busby et al. (1994). To avoid the drawbacks of common ground stimulation, multi-mode grounding stimulation has been proposed. Beside the non-stimulating intracochlear electrodes, this mode also allows current to return through the reference electrode. Since the surface area of the reference electrode is much larger than the intracochlear electrodes, it provides a low impedance path for the current, which may compensate for the increased impedance at the base and apex in common ground mode. This mode has been adopted by the XP implant (Oticon Medical, Vallauris, France). But there is a lack of data on actual current distribution of multi-mode grounding compared with common ground.

Another stimulation mode called phased array was developed with the idea of combining current focusing and multiple sites stimulation. For an electrode array with N stimulation sites, a single site stimulation is achieved by assigning the current weights on the electrodes according to the values in a length N current vector, which is computed for the purpose of a global voltage cancellation on the

non-stimulating sites. Then the current vector of multi-site stimulation is generated by the superposition of the corresponding vectors of single site stimulations (van den Honert and Kelsall, 2007). Measurements and simulations have shown that this stimulation mode has potential advantages over tripolar stimulation (Frijns et al., 2011). However, similar to common ground stimulation, its performance also drops at the ends of the electrode array, where the number of neighboring electrodes for current return is limited (van den Honert and Kelsall, 2007).

2.2.3 Stimulation waveforms

Besides the spatial stimulation modes in the spatial domain, the stimulation waveform in the time domain can also affect the neural activation pattern. The current injected through the electrode-electrolyte interface causes two different effects: Faradaic and non-Faradaic. The former one refers to the electrolysis process, with charge transfer between the electrode and the electrolyte. Depending on the materials of the electrode and the type of ions in the solution, it can lead to gas generation, electrode dissolution and the change of pH, which are all harmful to the surrounding tissue (Brummer and Turner, 1977). Non-Faradaic effect refers to the ion aggregation near the electrode, without charge transfer through the electrode-electrolyte interface. The aggregation of ion is equivalent to a charging capacitor, known as the double-layer capacitor.

The Faradaic effect can be avoided by limiting the current density on the electrode surface (Shepherd et al., 1985; Robblee and Rose, 1990) and delivering charge balanced stimulations (Shepherd et al., 1991; Shepherd, 1999). Implants can be programmed to generate charge balanced biphasic waveforms (figure 2.10(a) and (b)), but the residual DC component is not low enough due to the error of the manufactured current sources in the stimulation chips. In most implant products, the charge balanced stimulation is guaranteed by adding a blocking capacitor in series with the current source, which reduces the DC component to negligible ($< 1nA$) (Sit and Sarpeshkar, 2007). A biphasic stimulation waveform with active anodic discharge phase is shown in figure 2.10(a). For this waveform, a short time gap must be given between the electrical stimuli to passively discharge the blocking capacitors. The cathodic phase of the biphasic stimulation can also be purely passive using the blocking capacitors, at the cost of a longer passive discharge period. An example of the biphasic stimulation with passive discharge is given in figure 2.10(c).

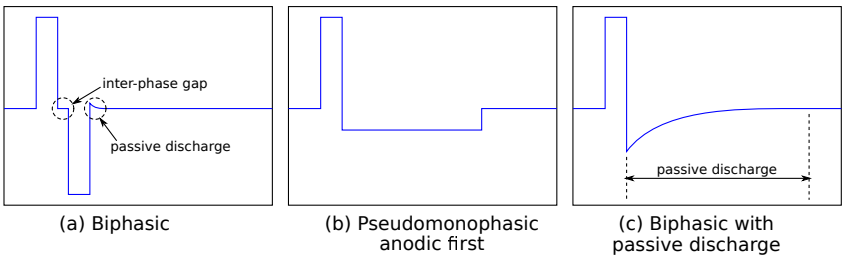

Figure 2.10: Examples of stimulation waveforms used by cochlear implant

From the charge balance point of view, the simple biphasic waveform seems to be the best way to stimulate the auditory nerve. However, studies have shown that biphasic pulse has a higher stimulation threshold compared with monophasic pulse (Javel and Shepherd, 2000; Miller et al., 2001). An explanation is that the action potential generated by the anodic phase can be neutralized by the immediately following cathodic phase (van den Honert and Mortimer, 1979). The threshold can be reduced by either introducing a inter-phase gap as in figure 2.10(a) or using asymmetric pulses 2.10(b). Recordings of single cat nerve fiber responses made by Javel and Shepherd (2000) showed that increasing the inter-phase gap can gradually lower the threshold to the level of monophasic stimulation. As for the monophasic passive discharge pulse, its maximum cathodic phase amplitude depends on the size of the blocking capacitor. In the XP implant, it is adjusted to around 20% of the anodic pulse, therefore it can be assimilated as a type of the asymmetric pulse.

2.2.4 Bottlenecks of performance

With the help of cochlear implants, some users achieved high scores in words and sentence recognition close to normal hearing in a quiet environment, meanwhile, low scores are also reported, meaning that the performance of cochlear implant varies largely from subject to subject. The implants also have unsatisfactory performances under certain scenarios, such as speech recognition in a noisy environment and music appreciation (McDermott, 2004; Gfeller et al., 2007). There are many factors that could explain the possible causes of these problems, including the limitations of sound processing, low spatial resolution of the current, electrode insertion trauma and the degeneration of auditory nerve. Here the discussions will focus on the factors related to the current distribution inside the cochlea due to the scope of research, which includes spread of excitation and electrode position.

Since the electrode array is surrounded by conductive tissue in the cochlea, the stimulation current from one electrode can diffuse and activate a large area of neurons, known as the spread of excitation. Consequently, the activation patterns of adjacent electrodes overlap with each other, leading to electrode cross-talk and reducing the actual number of independent spatial channels.

Perimodiolar electrode and different spatial stimulation patterns are developed with the idea of reducing spread of excitation. Modern cochlear implants are equipped with 12 to 20 physical channels (depending on the CI manufacturer), but the number of independent spatial channels observed on the implant users still seems to be limited under 10 (Fishman et al., 1997; Friesen et al., 2001; Landsberger et al., 2012). Although understanding speech requires only 4 independent channels (Shannon et al., 1995), increasing spatial channels is still essential for speech perception with noise or competing speakers and music appreciation (Fu et al., 1998; Friesen et al., 2001; Smith et al., 2002; Shannon et al., 2004).

2.3 Previous studies of cochlear modeling

Due to the geometrical complexity and the difficulties in taking detailed measurements inside the cochlea, numerical simulation has been used as a tool for studying the current distribution during the electrical stimuli. The first models of the cochlea were based on the morphology and conductivity of the cochlear tissue, which allowed the simulation of potential and current distribution (Strelioff, 1973; Black et al., 1983; Suesserman and Spelman, 1993), and the test of the effectiveness of new stimulation modes (Jolly et al., 1996).

As the simulation algorithm and the computing power of the computer develops, cochlear models coupled with the computational models of the auditory nerve fibers appeared (Finley et al., 1990; Frijns et al., 1995, 1996, 2011) and enabled the simulation study of neural activation pattern in terms of electrode position (Hanekom, 2001; Choi et al., 2005), neural degeneration(Briaire and Frijns, 2006), tissue conductivity, trajectory of nerve fibers (Kalkman et al., 2014, 2015) and cochlear geometry (Dang et al., 2015; Malherbe et al., 2015).

Meanwhile, coupling the conductive cochlear model with the electrode-electrolyte interface led to the simulations the time domain potential waveform (Choi et al., 2006; Choi and Wang, 2014) and the normal current distribution across the surface of the electrode (Sue et al., 2013, 2015). Preliminary studies have also been done

on the effects of permittivity of cochlear tissue (Inguva et al., 2015).

2.3.1 Cochlear geometry representation

Lumped model

As shown by figure 2.2, the cross-section of the cochlea has a sophisticated structure. In the earliest attempts of modeling the cochlea geometry, the cross-section was simplified as a circuit network. Such circuit networks were stacked to form an unrolled cochlea model, which was called lumped cochlea model (Strelioff, 1973; Suesserman and Spelman, 1993; Jolly et al., 1996; Spelman et al., 1995). The circuit diagram of a lumped cochlea model is shown in figure 2.11 Kral et al. (1998). In this model, the cochlear tissue was approximated by 19 cross sections, each contained 3 conductive layers: scala tympani, ganglion bone and the tissue beyond.

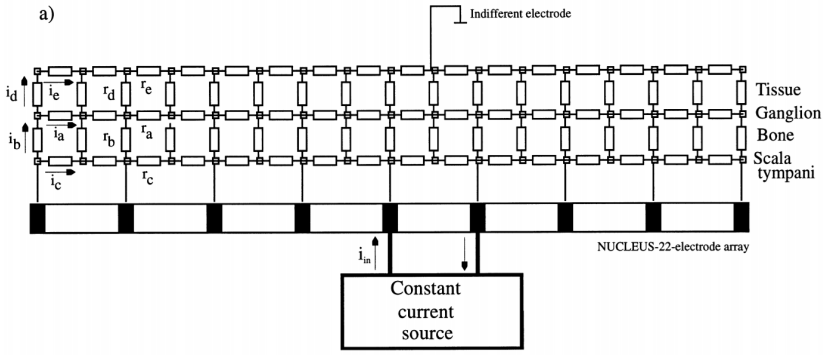

Figure 2.11: Circuit diagram of a lumped cochlea model (Kral et al., 1998).

Surface and volumetric 3D mesh models

Compared with other type of models, the computational power required to run simulations on the lumped cochlea model was extremely low. Meanwhile, incorporating tissue permittivity could be easily implemented by inserting capacitors into the circuit network. On the other hand, the spatial resolution of electric potential in this model was limited by the sketchy approximation, and implementing the cross-turn interactions caused by the spiral shape in the real cochlea was also difficult.

Due to these limitations, the lumped models were gradually replaced by 3D mesh models in simulation studies, which have much better representation of the

geometric details of the cochlea, such as the basilar membrane, Reissner's membrane and the organ of corti.

The choice of the 3D mesh type depends on the adopted simulation algorithm: boundary element method (BEM) requires a surface mesh model, where only the interfaces between domains with different conductivities need to be modeled. Since there is no connection between the surface meshes from different interfaces, different parts of the model can move freely in space as long as there is no intersection between the meshes. This feature is helpful when adjusting the position of the electrode array in the cochlea or changing the electrode array layout, as no remeshing is needed. The BEM considers the volume in between boundary meshes homogeneous and has constant conductivity, therefore it is difficult to implement anisotropic tissue, such as the nerve fibers, and complex impedance in a surface model. Briaire and Frijns (2000) used quadratically curved triangles instead of planar triangles for BEM simulation in their surface mesh model of guinea pig cochlea to better represent the curved surface of the cochlea with limited number of triangles. In this model, the edges of each triangle were curved by 3 additional points placed between the 3 vertices. A picture of his rotationally symmetric surface mesh model is shown in figure 2.12.

3D volumetric mesh corresponds to the finite element method (FEM) simulation algorithm. In a 3D volumetric mesh, the volume within the mesh is separated into tetrahedra, which increases the complexity of mesh generation and simulation, but enables the simulation of anisotropic tissue. A picture of the volumetric mesh model is shown in figure 2.13. An implanted electrode array is visible at the basal turn of the cochlea.

3D mesh generation

The 3D meshes of the cochlea could be created based on the general cross-section shape of the cochlea. These cross-sections were either longitudinally (Finley et al., 1990) or rotationally (Briaire and Frijns, 2000; Choi et al., 2005, 2006; Choi and Wang, 2014; Tognola et al., 2007) extruded to generate the mesh of the cochlea. To make the cochlear shape more realistic, some models employed zoom factors which change the size of the cross-section during extrusion(Saba, 2012). The zoom factors gradually decreased from the base to the apex of the cochlea.

As high resolution images of the cochlea became available, more realistic cochlear

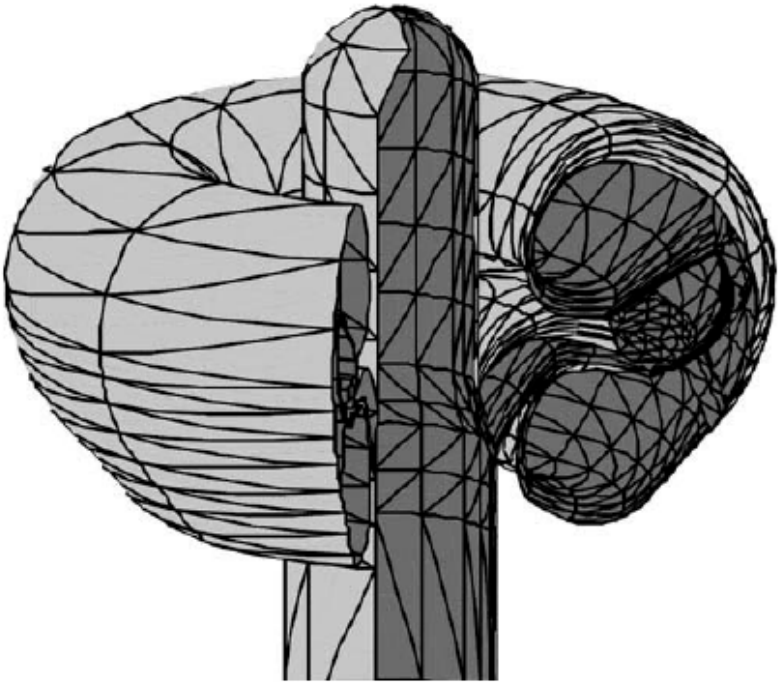

Figure 2.12: Rotationally symmetric surface mesh model of guinea pig's cochlea (Frijns et al., 1995).

models were created, which reflected the geometric details of the individuals. Kalkman et al. (2014) created models based on the histological midmodiolar cross-section images of the cochlea and used them to study the place pitch versus the electrode location. Tran et al. (2015) studied current conduction pathways using the human electroanatomical total head reconstruction model, which was a volumetric model of the whole human head. They demonstrated 3 major pathways (cochlear wall, modiolus and basal end) of monopolar stimulation current exiting the cochlea. Their colleagues created a high fidelity model of the guinea pig's cochlea based on similar methods (Wong et al., 2016).

Compared with histological images, the images provided by (micro-)CT scans have lower resolution (voxel size around 0.6mm for CT scans (Malherbe et al., 2015) and 24.8μm for micro-CT scans (Dang et al., 2015)) and lower contrast on soft tissue. However, only the CT scans can acquire the cochlear geometry and electrode location on implant users. Malherbe et al. (2015) fitted a template cochlear model with user-specific information such as the outer wall of the cochlea and the electrode position extracted from CT images.

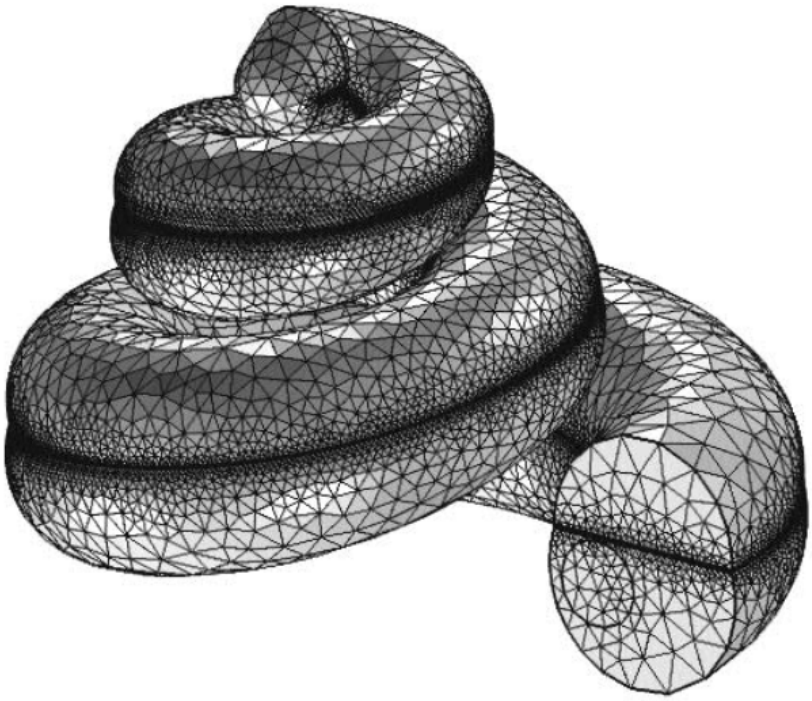

Figure 2.13: 3D volumetric mesh model of the human cochlea with the electrode array. (Saba, 2012).

2.3.2 Auditory nerve model

Coupling the electric potential simulation with the auditory nerve models allows the prediction of neural activity given the stimulation current. Colombo and Parkins (1987) proposed the first mammalian auditory nerve model, which has been continuously refined in terms of electrophysiological characteristic and morphological details (Frijns et al., 1995; Rattay et al., 2001; Briaire and Frijns, 2006). A diagram of this model is given in figure 2.14. Besides the prediction of neural activation, this type of model can also simulate the action potential waveform. Therefore it is required to make studies on the eCAP signal (Briaire and Frijns, 2006, 2005; Choi and Wang, 2014).

A simpler way of estimating the neural responses to electrical stimulation is the activation function (Rattay, 1986; Choi and Hsu, 2009; Wong et al., 2016). In the nerve models that adopt the activation function, the excitation of a nerve fiber depends on the second order derivative of the electrical potential along the nerve

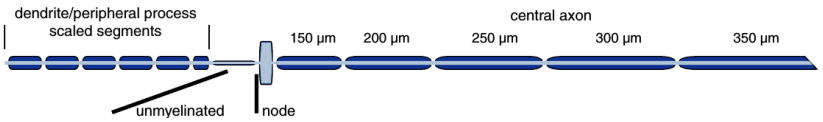

Figure 2.14: Model of a single auditory nerve fiber (Briaire and Frijns, 2005). The model is coupled with equivalent circuits at the positions of Ranvier nodes to simulate the capacitance and ionic currents.

fiber. Since the activation function is computed from static electric potential, it cannot be used to study the effect of time domain modulations of the stimulation pules, such as the pulse trains.

2.3.3 Electrode-electrolyte interface

When a metal electrode is placed in an electrolyte, the ions from the electrolyte gather at the surface of the electrode and form a thin layer, which is referred to as the electrode-electrolyte interface. The aggregation of ions on the electrode surface gives the interface a capacitive effect, while the electrical chemical reactions (faradaic process) taking place at the surface of the electrode introduces a resistive effect. Although the interface is a very thin layer, its resistance and capacitance cannot be ignored (Choi et al., 2006). Most cochlear simulations do not model this layer for two reasons: the first is that they have adopted the quasi-static assumption which ignores the capacitance introduced by this layer, and the second is that for all the stimulation modes that have been simulated by these models, including the monopolar, bipolar, tripolar, current steering and phased array (Kalkman et al., 2016), the current intensities on all the electrodes are known and fixed values which are not affected by the resistance of the interface. However, for the common ground and multi-mode grounding stimulations, the current intensities on the non-stimulating electrodes are affected by the resistance and capacitance of the electrode-electrolyte interface. Therefore these two stimulation types could not be simulated by the existing simulation framework.

Lai and Choi (2007) made an attempt of simulating the time domain stimulation waveform by incorporating the electrode-electrolyte interface to a FEM cochlear model. The interface was approximated by an additional thin layer of mesh over the electrode, where a complex permittivity was imposed. The electric characteristic of this layer was equivalent to a double layer capacitor $C_p = 10nF$

connected in parallel with a faradaic resistance $R_p = 5k\Omega$. Time domain simulation of the potential waveform inside the cochlea was performed based on this model. Cantrell et al. (2007) developed a more sophisticated interface layer model, where C_p was replaced by a virtual component called constant phase element (CPE) for the interface between electrolyte and metal electrode. They also proposed another equivalent circuit to simulate the interface between the electrolyte and the non-conductive silicon rubber, as shown in figure 2.15.

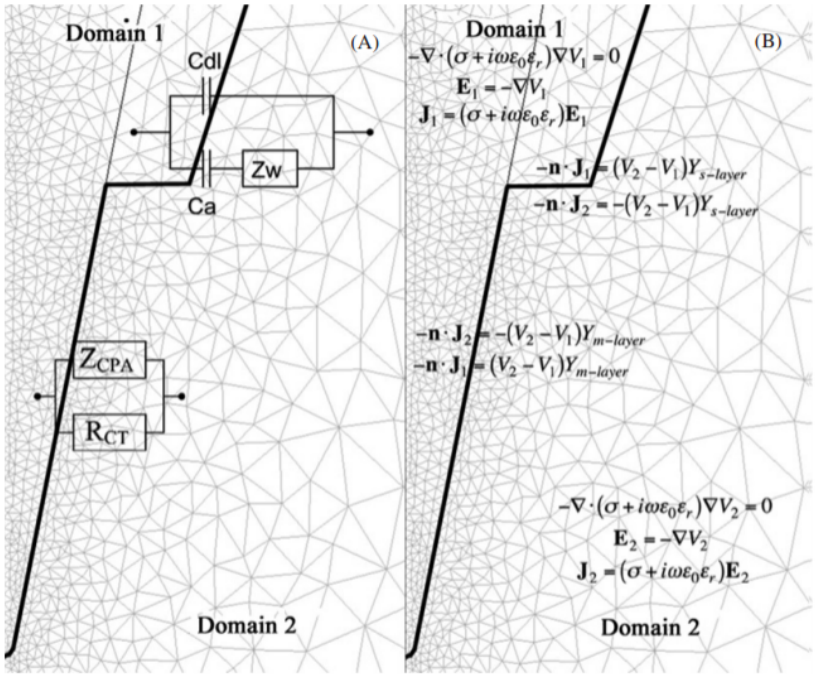

Figure 2.15: FEM model incorporated with the electro-electrolyte interface Cantrell et al. (2007). The equivalent circuit model of the interface is shown in (a) while the corresponding governing equations is shown in figure (b). The upper half of the pictures is the interface between electrolyte and silicon rubber, the lower half is the interface between electrolyte and metal electrode.

Sue et al. (2013) used similar interface models to estimate the normal current distribution on a single electrode during electrical stimulation. They found that the irreversible faradaic current density increases at the corners of electrodes, and could be reduced by increasing the recession of the electrode surface. Their results also showed that the reversible faradaic reactions contributed to the capacitance of the electrode-electrolyte interface (Sue et al., 2015).

In the cochlea of an actual implant user, besides the normal electrode-electrolyte

interface, extra impedance could be introduced by the encapsulation tissue of fibrous scar and ossification around the electrode array. Duan et al. (2004) measured the electro impedance spectrography in an implanted cat's cochlea, and observed that the intracochlear impedance grew from $5.4k\Omega$ at the 9th day after implantation to $9.3k\Omega$ at the 179th day after implantation. Hanekom (2005) modeled the encapsulation of the electrode array and found that the perimodiolar electrodes were more affected by this phenomenon than the lateral electrodes in terms of the stimulation threshold changes.

2.3.4 Validation methods

Comparing the simulated electric potential distributions with direct potential measurements either in vivo or in vitro is the most straightforward way of validating the cochlear model. Considering the small size of the intracochlear electrode array, high spatial resolution in vitro measurements can give more detailed information on the local potential distributions around the electrodes (Tognola et al., 2007). On the other hand, in situ measurements were usually carried out in the scala tympani of the cochlea and have lower spatial resolution (Vanpoucke et al., 2004; Wong et al., 2016; Dang et al., 2015). Therefore they are more suitable for validating the monopolar simulation results, where the current flow is less focused than other stimulation modes. Besides the validation of the cochlea model, Kalkman et al. (2014) also used the intracochlear potential measurements to calibrate the conductivity in the cochlea model and reduce the simulation error. In cases where the direct potential measurement data is not available, the simulation results can be compared with the output of an equivalent circuit model or other type of models (Choi et al., 2006).

For the cochlear models that have incorporated auditory nerve models, it is more difficult to validate the neural activation patterns. The eCAPs provides an indirect way of validating the simulated neural activities, which have been adopted by several research groups (Briaire and Frijns, 2005, 2006; Choi and Wang, 2014). But as observed by Kalkman et al. (2016), the neural threshold levels simulated by nerve models based on single nerve fibers still do not match the clinical observations, and more neurophysiology knowledge is required to resolve this issue.

2.4 Structure of the thesis

The following paragraphs provide the major topics discussed by each chapter:

Chapter 2 describes the process of building a parametric 3D cochlear model which exploits the morphological information of the cochlea acquired by different approaches, including manually measured average shape of the cochlea, histological images, micro-CT/CT scans and previously meshed cochlea models. The meshing tool (CGAL) and simulation tool (OpenMEEG) are also introduced by this chapter.

In chapter 3, to make simulations of the common ground and multi-mode grounding stimulation modes, the parametric cochlear model was coupled with the blocking capacitors in the implant and the constant phase elements to simulate the electrode-electrolyte interface. To run the circuit simulation algorithm on the coupled model, the constant phase elements were approximated by capacitor and resistor networks which have the same impedance characteristics within the frequency range of the stimulation pulse. The simulation result gave the current distribution on the non-stimulating electrodes during the passive discharge phase.

Chapter 4 demonstrates the flexibility of the model for rapidly constructing different cochlea geometries and electrode layouts. Comparisons of potential distribution and neural activation patterns were made between different cochlea shapes and stimulation modes. Two different layouts of a new electrode array type, the transmodiolar electrode array, were modeled. The simulations of 3 new stimulation types involving the interaction between the transmodiolar array and the normal electrode array were made and compared with each other.

Chapter 5 and 6 present the potential measurement experimental studies for the purpose of validating the simulation results. In vitro measurements of the multi-mode grounding and common ground stimulations were taken with the electrode array placed in two different containers. The spatial potential distribution and current intensities on the electrodes were recorded. The results were used to fit the parameters of the electrode-electrolyte interface model. In situ measurements of a variety of stimulation modes were taken with a self-made multiplexer. 3D scans of the human specimen used by the in situ measurements were acquired. Comparisons were made between the measurements and the simulations of the parametric model adapted to the scan data.

Chapter 3

Parametric cochlear model

Contents

3.1 Morphology information sources used by cochlear models

The morphology information sources refers to either numbers or images related to the dimensions and structures of the cochlea, from which the shape of the cochlea model can be inferred.

Cochlear models have different information sources in terms of the cochlea morphology, as shown by figure 3.1.

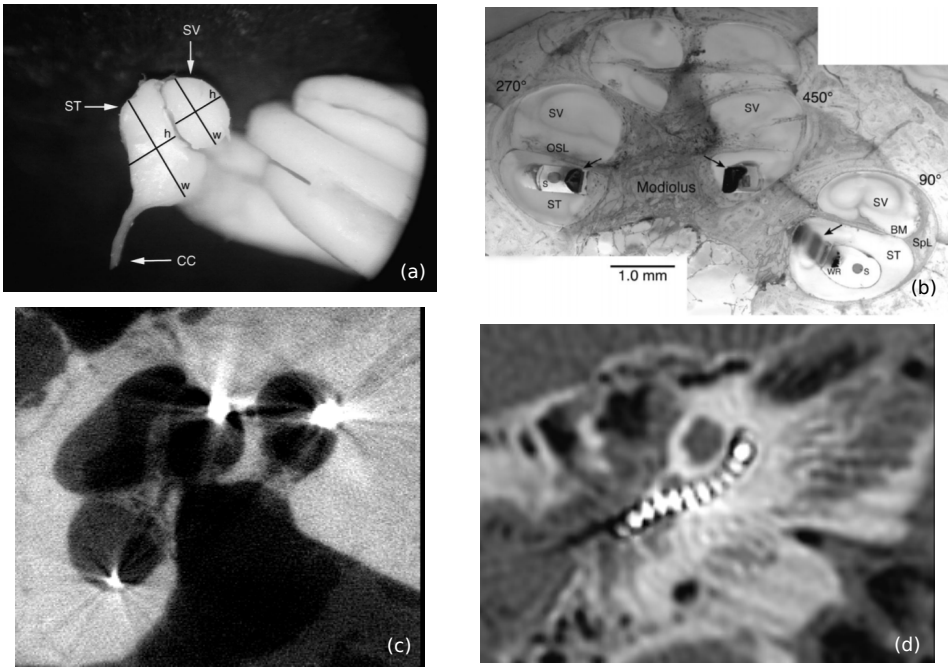

Figure 3.1: Morphological information sources of 3D cochlea models: (a) manually measured cochlear dimensions (Wysocki, 1999); (b) histological microscopic image (Rebscher et al., 2008); (c) micro-CT scan; (d) CT scan.

Each source has its advantages and disadvantages. General cochlear shape data gives the manually measured and averaged cochlear size information, which is the easiest to implement in the cochlear models. Due to the amount of work of manual measurements, researches in this direction were limited to a certain aspect of the cochlear morphology at each time and presented the mean values of results, sometimes with standard variations. Cohen et al. (1996) gave the averaged spiral trajectory of the cochlea based on the raidographs of 30 implant users. The trajectory was described as a function of the angle of cochlear rotation θ, from the round

window to the apex. Wysocki (1999) measured the average dimensions of the human vestibular and tympanic scalae of 25 human temporal bones from human cadavers (figure 3.1(a)). Stakhovskaya et al. (2007) microdissected 9 cadaver cochleae and measured the length of spiral ganglion and organ of Corti, and examined the nerve fiber trajectories between the two parts. They found that despite the variations in the length of spiral ganglion and organ of Corti across subjects, the trajectory of peripheral nerve fiber connections between them is fairly constant.

Histological microscopic images have the highest resolution of the cochlear tissue, including the Reissner's membrane, the basilar membrane and even the auditory nerve fibers (figure 3.1(b)). But in many cases only one midmodiolar cross-section is available (Rebscher et al., 2008; Saba, 2012; Kalkman et al., 2014). Micro-CT scans also have a high resolution of the cochlea, but a limitation of the X-ray computed tomography is that bone tissue has higher contrast in the images while the soft tissue is less visible. When an implanted cochlea is scanned, the metallic intracochlear electrodes generate artifacted images (figure 3.1(c)) which makes the modeling work more challenging.

CT scans have the lowest resolution of the cochlea, where the structures inside the cochlea are mostly invisible (figure 3.1(d)), but it is the only method that can be applied on cochlear implant users (micro-CT cannot be applied on living humans due to the high level of X-ray radiation it produces, but it can at least preserve the original sample compared with other more invasive measurements). CT scans are usually used in combination with other data sources when modeling the cochlea, where it plays the role of determining the cochlea size and the position of the electrode array (Kalkman et al., 2014; Malherbe et al., 2015).

To sum up, a comparison between these information sources listed in table 3.1.

The parametric cochlear model aims to give a fast way of generating user-specific model of the cochlea while being able to easily benefit from different cochlear morphological information sources. The modeling process must be compatible with the data sources mentioned above so that the simulation results given by the models of different data sources are comparable. To achieve this target, the morphological information of the cochlear is organized into a set of parameters which are independent of each other, hence the modeling process can be simplified as extracting and tuning the parameters. Moreover, parameters from a variety of sources can be shared between models to maximize the advantages of each data source.

Table 3.1: Comparison of the morphological information sources of 3D cochlea models

Information sources	Averaged cochlear shape	Microscopic images	Micro-CT	CT
Spatial resolution	Low	Highest	High	Low
3D data	No	Some cases	Yes	Yes
Case specific	No	Yes	Yes	Yes
Electrode array	Some cases	Some cases	Yes	Yes
Invasivity	High	High	Medium	Low
Modeling difficulty	Low	Moderate	Moderate	High

3.2 Simulation and meshing tools

3.2.1 The simulation algorithm

The parametric cochlear model uses 3D surface mesh as the representation of cochlear geometry in order to achieve a faster meshing speed and the ability to make adjustments on the placement of the electrode array or even insert a new one without remeshing. Therefore it adopts BEM as the simulation algorithm. Figure 3.2 (b) gives an approximated geometry representation of the original geometry (a), where σ stands for the conductivity. In the original geometry, the conductivity is a function of the 3D coordinates (x, y, z). While for BEM, the conductivity inside the geometry is considered as piecewise constant (σ_1 and σ_2), and domains with different conductivities are separated by the surface mesh called interfaces. The domains themselves do not need to be meshed.

Compared with FEM and finite difference method (FDM), the major drawback of BEM is not to be able to deal with anisotropy of conductivity shown mostly by the nerve fibers. The method adopted by the presented model is the symmetric BEM , which achieves lower simulation error than the FEM for a given computation time (Olivi, 2011). The software used to perform the symmetric BEM simulation is OpenMEEG (`https://openmeeg.github.io/`), which is a C++ implementation for solving the forward problems in the field of electroencephalography (EEG) and magnetoencephalography (MEG) (Kybic et al., 2005; Gramfort et al., 2010).

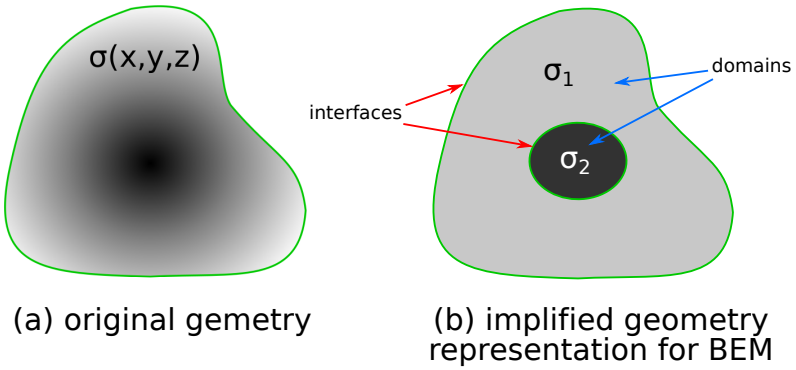

Figure 3.2: An example of the original geometry (a) and the corresponding geometry representation in BEM (b). The conductivity is indicated by the grayscale colors.

3.2.2 Adapting OpenMEEG for cochlea simulation

When computing electric potential at low frequencies, the quasistatic approximation can be applied to Maxwell's equations. With such approximation, the electric potential V is governed by the following equation:

$$\nabla \cdot (\sigma \nabla V) = \nabla \cdot \mathbf{J^p} \tag{3.1}$$

where σ stands for the conductivity and $\mathbf{J^p}$ is the distribution of the electrical sources. In EEG forward problem, the sources are the post-synaptic activities of pyramidal neurons in the cortex, which are approximated as current dipoles. The output is the potentials at the electrodes on the scalp.

In the case of cochlear simulation, the sources are the stimulation current from the intracochlear electrodes. This scheme is similar to electrical impedance tomography (EIT). In the EIT model, the source term $\mathbf{J^p}$ of equation 3.1 is zero. Instead, a boundary condition describes the normal current distribution on the interfaces that touch the zero-conductivity domains:

$$\sigma \nabla V \cdot \mathbf{n} = I \quad \text{on} \quad \Gamma \tag{3.2}$$

where Γ is the set of interfaces between the conductive and non-conductive regions, and $\mathbf{n}$ is the normal vector of the interfaces in Γ. The normal current distribution noted as I.

For the cochlear stimulation simulation, the whole domain inside the electrode array is set as non-conductive. However, on the positions which correspond to

the metal electrode array, several triangles were selected as the input positions of the boundary current. Hence the current stimulation through the intracochlear electrodes is represented, as shown in figure 3.3.

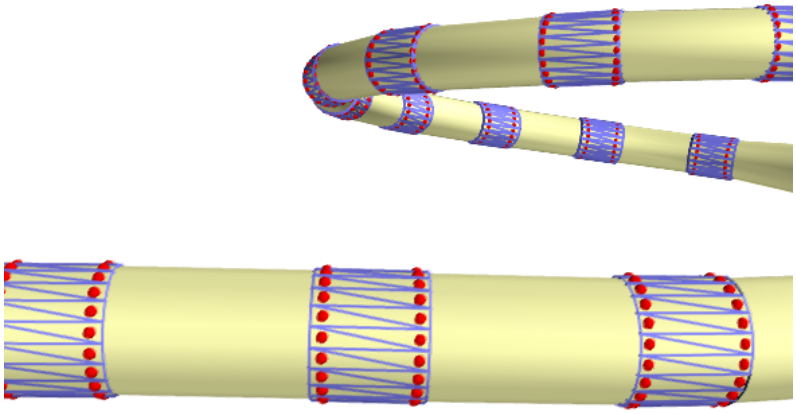

Figure 3.3: Triangles (blue) selected as boundary current injection positions from an interface to the non-conductive domain (yellow), in order to simulate the metal electrodes on an electrode array made of silicon rubber. In OpenMEEG, the selection process is completed by finding the closest triangle of a point marker (red dot).

In the original version of OpenMEEG, only the outermost domain could be set as non-conductive, which corresponds to the air in EEG and MEG simulations. To simulate the electrode arrays, the function of handling multiple non-conductive domains has been implemented and integrated into OpenMEEG.

The output of cochlear simulation exploits two output modes of OpenMEEG: the EIT leadfield matrix gives the electric potential of a chosen point on the interfaces that touches the non-conductive domains, which is used to simulate the electric potential on the electrode array; the IP (internal potential) leadfield matrix, on the other hand, gives the potential estimations of the chosen coordinates inside a conductive domain, which is used to compute the potential along the trajectory of the auditory nerve fibers.

A flowchart of the operations supported by OpenMEEG is plotted in figure 3.4. The `-EITIP` option of `om_gain` was another new feature added to OpenMEEG in order to perform cochlea related simulations, which computes the electrical potential

at the specified points inside the conductive domain based on the boundary current inputs. The contributed source codes have been merged into the master branch of OpenMEEG on github (`https://github.com/openmeeg`).

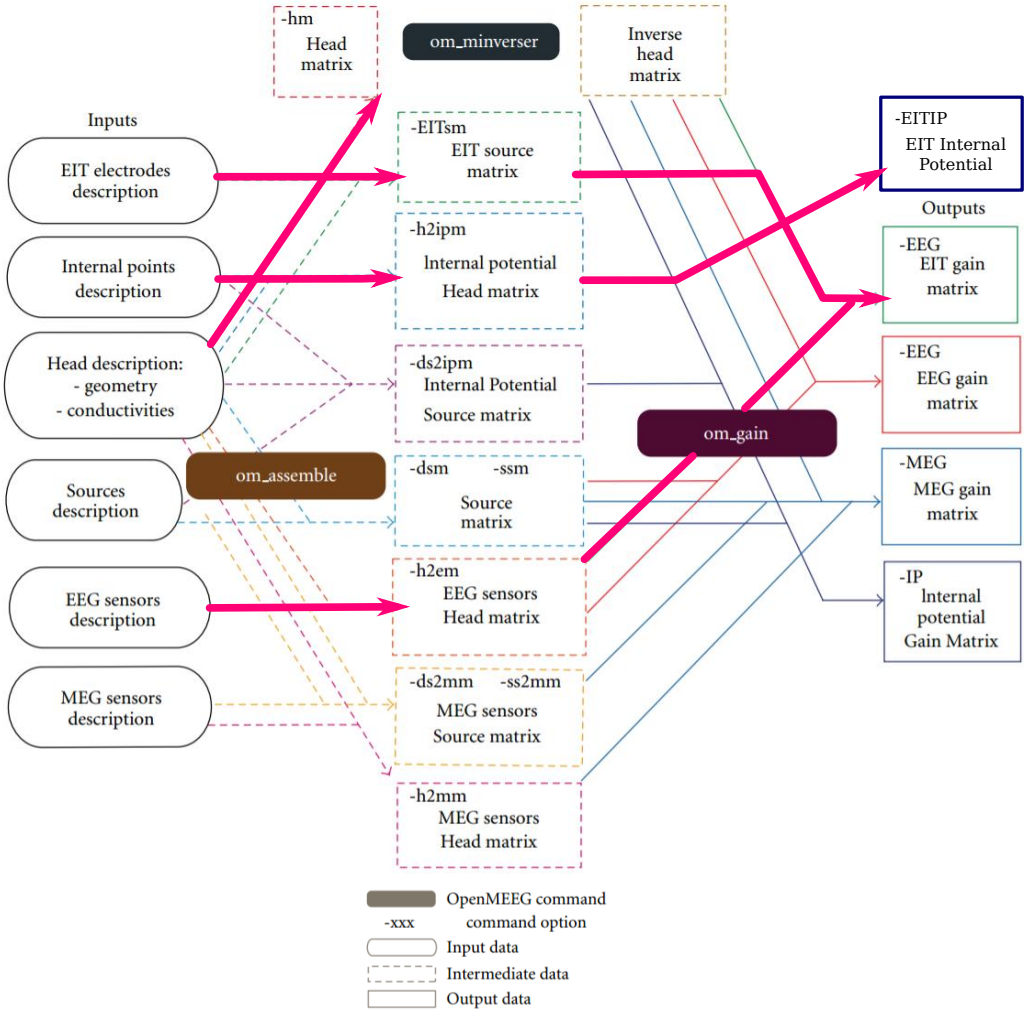

Figure 3.4: A flowchart of the operations supported by OpenMEEG. The operations used by cochlear implant simulation are marked by thick red arrows. Picture adapted from Gramfort et al. (2011)

3.2.3 3D surface meshing using CGAL

The meshing tool chosen to build the parametric cochlear model is the Computational Geometry Algorithms Library (CGAL) (Fabri and Pion, 2009). CGAL

implemented a variety of geometric algorithms including generation of 3D volumetric or surface meshes based on Delaunay triangulation and mesh simplification.

The original meshes generated by the parametric cochlear model were created through the concatenation of cross-sections (called structured meshes). An example of the original scala tympani mesh is given in figure 3.5(a).

The structured mesh has two drawbacks if used directly for BEM simulation: Firstly, to have a correct representation of the geometry, a large number of vertices must be used, which slows down the computing speed of the simulation and increases the memory footprint. For OpenMEEG, the memory required to a model with more than 40000 total vertices will exceed the memory size of normal PCs. Secondly, structured mesh has no control on the angle size of the its triangles. A thin and long triangle with acute angles is usually considered to increase the simulation error.

CGAL can generate meshes from implicit functions (often called oracles). A implicit function is a user defined function to tell CGAL whether a given test point is inside the geometry to be modeled or not (Alliez et al., 2016). To compute this function in the parametric model, each cross-section of the cochlea is slightly extruded to form a short pillar in 3D and calculate the intersection with the given point, the whole cochlear shape is then formed by the concatenation of these short pillars. CGAL provides 3 parameters for meshing control:

- **angular bound** sets the lower limit in degrees of the angle that can appear in the output mesh. It was set to 30 in the parametric cochlear model to avoid thin triangles.
- **radius bound** sets the radius of the Delaunay ball, which is related to the edge length of the output mesh. For the mesh in figure 3.5(b), the value was set to $0.1mm$.
- **distance bound** controls the distance error between the vertices and the implicit surface. A large distance bound leads to a coarse mesh with shorter computation time, and vice versa. The distance bound is usually set to $10\% - 25\%$ of the radius bound so that the vertex density of the output mesh is adaptive to the local curvature of the surface. The value adopted by the mesh in figure 3.5(b) was $0.01mm$.

Different conductive domains in the cochlear model can be generated together using the domain label function of CGAL, where different implicit functions can be

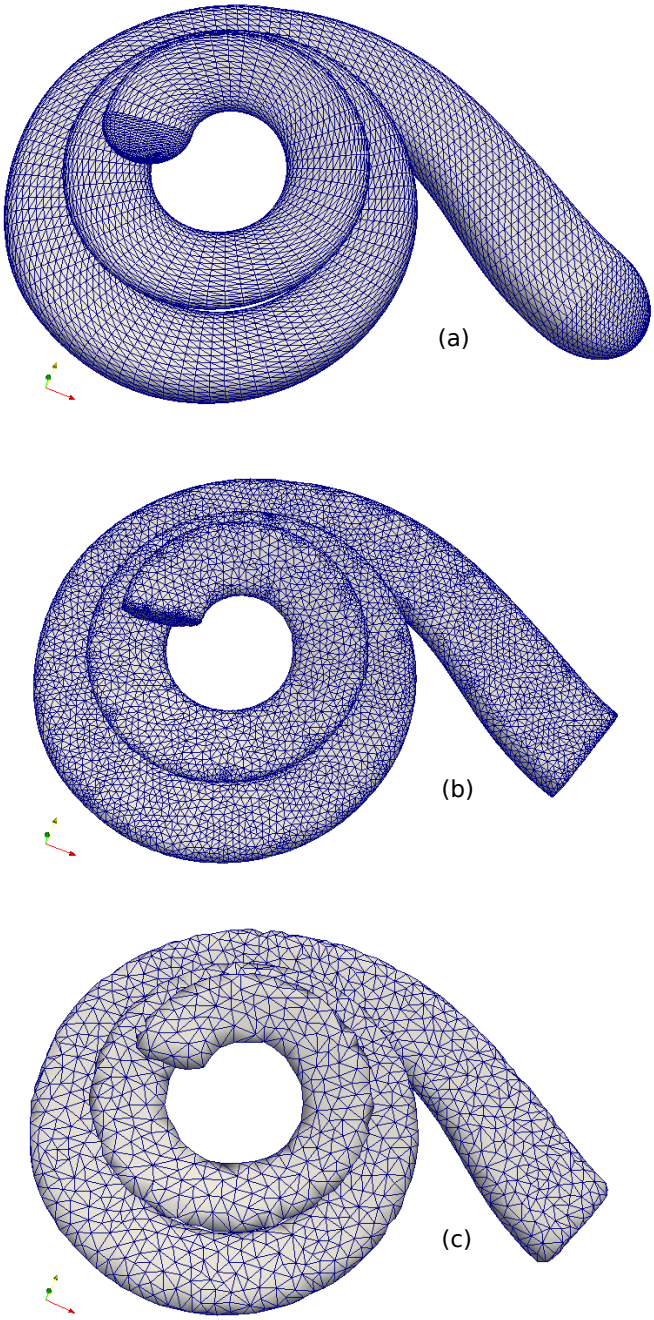

Figure 3.5: Comparison of surface meshes of the scala tympani: (a) structured mesh created through the concatenation of cross-sections; (b) mesh created using the implicit function of CGAL; (c) simplified mesh used for BEM simulation.

assigned to each domain. The output of this function was a labeled 3D volumetric mesh. The surface meshes of the interfaces between the domains can be extracted and stored separately following the labels.

To accelerate the computation speed, the surface meshes were simplified with the edge collapse function of CGAL, which reduces the number of edges and vertices under the thresholds set by the user (Cacciola, 2016). Figure 3.5(c) (2668 vertices, 5332 triangles) is the simplified mesh of figure 3.5(b) (12554 vertices, 25104 triangles).

3.3 Parameterization of the cochlear model

To demonstrate the parameterization process of the cochlear model, a cochlear average shape based model was built step by step in the following sections. As for the geometric details that were not covered by the average shape studies, the corresponding parameters were measured from a microscopic cochlear image of Rattay et al. (2001) shown in figure 3.6.

3.3.1 The central line

The parametric model was generated by extruding a variable cross-section along the central line which represented the spiral shape of the cochlea. The central line was stored as the x, y and z coordinates of the geometric center of each cross-section. The number of key cross-sections can be modified according to the spatial resolution of the morphological information source. For a 3D micro-CT scan, more cross-sections can be measured form the midmodiolar images with different rotation angles. For other types of data with less measurable cross-sections, parameters between two cross-sections were estimated using spline interpolation.

To start with, the number of cross sections was set at 800. The central line of the cross sections in 3D was computed from the equations given by Cohen et al. (1996), which were summarized from the radiographic images of 30 cochlear implant users. The equation was originally used for the scala tympani (Clark et al., 2011), but since the diameter of the scala tympani generally equals to the diameter of the cochlear cross-section, there was not much difference between the spiral radius of

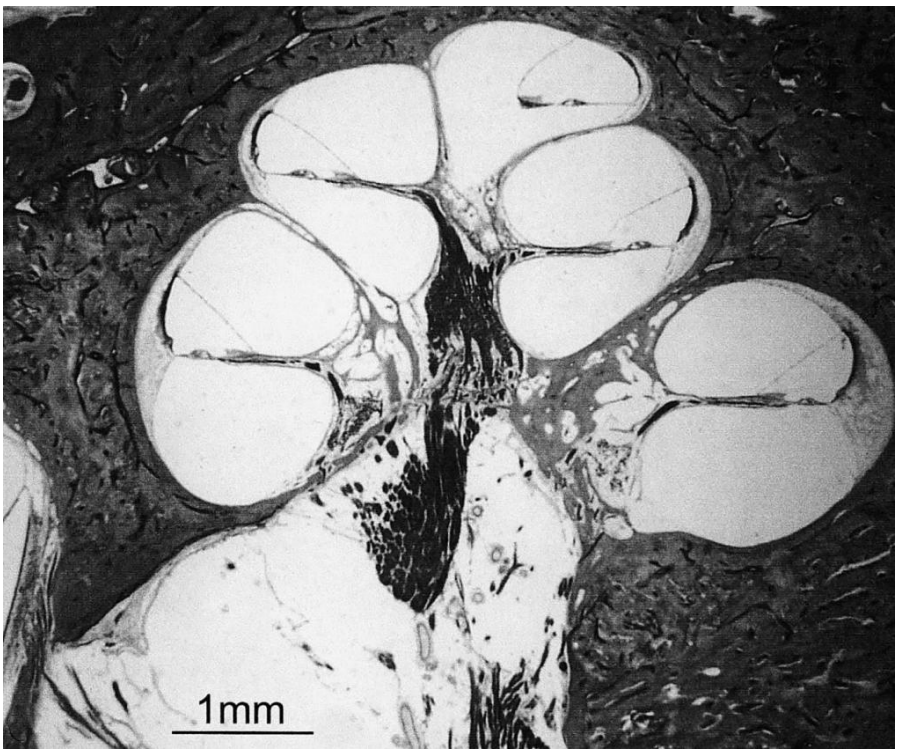

Figure 3.6: A cochlear midmodiolar cross-section image to measure the parameters not provided by the average cochlear shape studies. Picture adapted from Rattay et al. (2001).

the two parts.

$$R = \begin{cases} C(1 - Dln(\theta - \theta_0)), & (0° \leq \theta \leq 100°) \\ Ae^{-B\theta}, & (100° < \theta \leq 910.3°) \end{cases} \tag{3.3}$$

where R is the spiral radius and θ is the rotation angle of the cochlea in degrees.

The first derivative of the spiral radius computed from equation 3.3 was discontinuous at the segmentation point ($\theta = 100°$), which caused the intersection of cross-sections. This is because when placing the cross-section along the central line, the direction vector of the cross-section was the tangent of the central line at the placement point. Hence this part of radius was replaced by the spline interpolation of the neighboring points, as shown in figure 3.7.

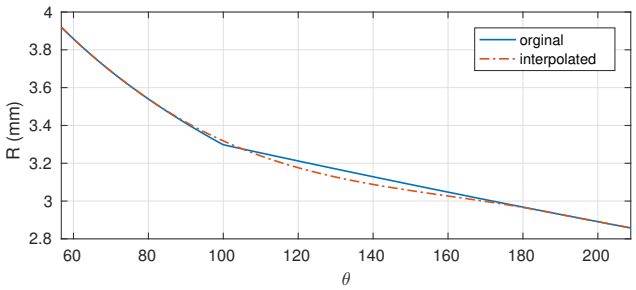

Figure 3.7: Interpolation of the spiral radius R. The blue line is original R with discontinuous first order derivative at $\theta = 100°$. The red dotted line is the fixed spiral radius.

The x and y coordinates of the central line were acquired by:

$$\begin{aligned} x &= Rsin(\theta) \\ y &= Rcos(\theta) \end{aligned} \tag{3.4}$$

In addition, Yoo et al. (2000) added the z coordinates to the spiral:

$$z = E(\theta - \theta_1) \tag{3.5}$$

The values of the constants A, B, C, D, E and θ_1 in equation 3.3 and 3.5 are given in table 3.2. The computed coordinate values are in mm.

Table 3.2: Values of the constants in the 3D cochlear spiral equations

A	B	C	D	E	θ_1
3.762	0.001317	7.967	0.1287	0.003056	10.3

The computed 3D spiral is shown in figure 3.8.

3.3.2 The cross-section

An illustration of the cochlear cross-section implemented by the parametric model is shown in figure 3.9. The cross section consists of 10 conductive domains, including the temporal bone that surrounds the cochlea.

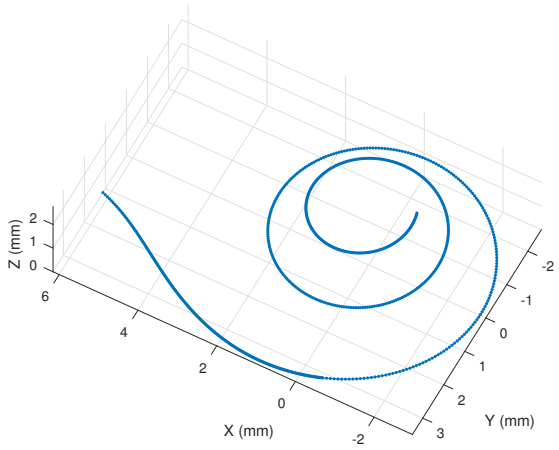

Figure 3.8: 3D view of the spiral cochlear central line.

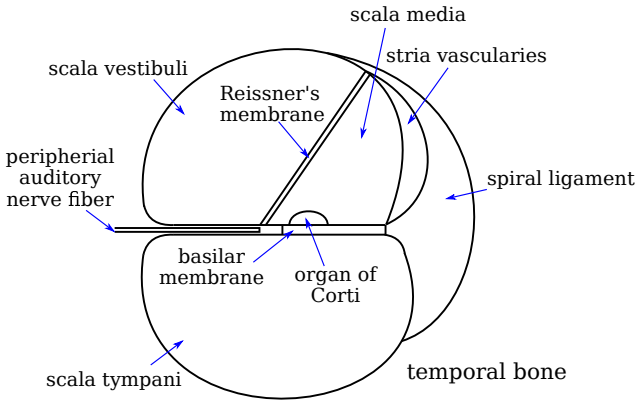

Figure 3.9: Cross-section shape of the parametric cochlear model.

Scala tympani and scala vestibuli

The cross-sections of scala tympani and scala vestibuli were two semicircles with smoothed corners. The scala vestibuli cross-section discussed in this section is actually the contour of the upper half of the cochlear cross-section, which includes the scala vestibuli, the scala media and the Reissner's membrane.

The parameters to describe their shapes consist of the height of the scala vestibuli and scala tympani: h_{sv} and h_{st}, width w and tilt angle in relation to the horizontal plane ψ. These parameters were measured by Wysocki (1999) from 25 cadaver temporal bones. While the cross-section shape of both the scala tympani

and scala vestibuli were considered as ellipses, he also measured the width of the scala vestibuli, which in most cases has less that 10% difference with the scala tympani width except at the very basal and apical parts. Since the parametric model has adopted the semicircular cross-section, the scala vestibuli here shares the same width as the scala vestibuli. The semicircular cross-section with rounded edges is also more similar to the average cross-section shapes measured by Rebscher et al. (2008) from 79 implanted cadavers.

Table 3.3 listed the averaged cross-section size data used by the cochlear model, which was presented by Wysocki (1999); Clark et al. (2011). The original positioning parameter of the cross-sections was the distance to the round window, here it has been converted to the rotation angle of the cochlea ϕ through the mapping on the spiral central line computed in the previous section, in order to be consistent with other parameters.

Microscopic images and averaged cross-section shapes showed that at the apex of the cochlea, the cross-section of the scala tympani became vertically asymmetric due to the extrusion of the neighboring turns. To describe this phenomenon in the parametric model, a shift parameter k was introduced, which is the x coordinate of the scala tympani semicircle's top, normalized by the width w of the current cross section. The values of k was measured from the averaged cross-section shapes presented by Rebscher et al. (2008), as listed in table 3.4. The deformation of the scala tympani was not as obvious as the the scala tympani in the microscopic images, therefore it was not shifted in this set of parameters based on the average cochlea size. However, its corresponding shift parameter was preserved to cope with the possible shift in the user-specified data.

In table 3.4, the values of k at $\theta = 10.3°$ and $910°$ was taken from their nearest neighbors as their corresponding cross-section shapes were not provided in Rebscher et al. (2008).

The relationship between the cross-section shape and the control parameters of the scala tympani is illustrated in figure 3.10. The same relationship is shared by the scala vestibuli as well.

Reissner's membrane and scala media

The upper half of the cochlear cross-section is divided into scala vestibuli and scala media by the Reissner's membrane. The scala vestibuli is filled with perilymph

Table 3.3: Averaged dimensions of the scala tympani and scala vestibuli (Wysocki, 1999; Clark et al., 2011)

ϕ (deg)	h_{st} (mm)	h_{sv} (mm)	w (mm)	ψ (deg)	ϕ (deg)	h_{st} (mm)	h_{sv} (mm)	w (mm)	ψ (deg)
10.30	1.30	1.21	2.10	0.00	331.99	0.75	0.90	1.33	10.31
20.51	1.18	1.04	2.10	0.57	355.95	0.73	0.88	1.32	10.89
32.36	1.14	0.95	1.95	1.15	380.69	0.72	0.86	1.31	11.46
45.50	1.13	0.84	1.85	1.72	406.26	0.67	0.82	1.30	12.03
59.79	1.08	0.79	1.80	2.29	432.72	0.66	0.79	1.30	12.61
75.15	1.03	0.77	1.74	2.86	460.14	0.63	0.77	1.30	13.18
91.53	0.98	0.75	1.70	3.44	488.58	0.59	0.76	1.30	13.75
108.84	0.94	0.76	1.68	4.01	518.13	0.54	0.75	1.30	14.32
126.62	0.90	0.77	1.63	4.58	548.88	0.47	0.70	1.30	14.90
144.83	0.86	0.78	1.60	5.16	580.93	0.43	0.66	1.30	15.47
163.49	0.84	0.80	1.59	5.73	614.38	0.39	0.59	1.31	16.04
182.62	0.83	0.81	1.51	6.30	649.39	0.38	0.57	1.31	16.62
202.24	0.82	0.85	1.50	6.88	686.08	0.39	0.54	1.26	17.19
222.39	0.82	0.87	1.54	7.45	724.64	0.37	0.52	1.25	14.32
243.08	0.81	0.88	1.46	8.02	765.25	0.36	0.48	1.23	11.46
264.35	0.81	0.93	1.45	8.59	808.17	0.38	0.47	1.25	8.59
286.23	0.79	0.93	1.43	9.17	910.40	0.38	0.47	1.25	5.73
308.77	0.77	0.92	1.38	9.74					

Table 3.4: Values of the shift parameter of the scala tympani

ϕ (deg)	10.3	90	180	270	360	450	540	910
k	-0.27	-0.27	0	-0.13	-0.11	-0.18	-0.22	-0.22

while the scala vestibuli is filled with endolymph. Reissner's membrane is thin ($12\mu m$ (De Fraissinette et al., 1993; Lareida et al., 2009; Shibata et al., 2009)) piece of tissue with a very low conductivity. To properly model it, an approach similar to Briaire and Frijns (2000) has been adopted which enlarged the thickness of Reissner's membrane by a factor of 5, in order to have a mesh with reasonable thickness.

The morphology of Reissner's membrane was controlled by parameter ψ_{rei} and

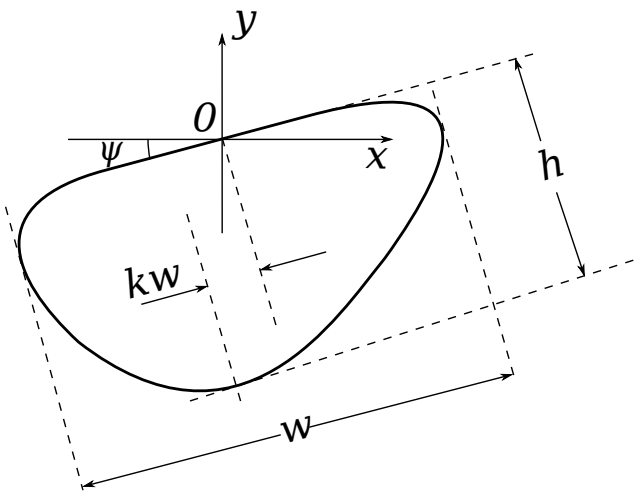

Figure 3.10: The cross-section of the scala tympani generated from the shape control parameters

x_{rei}. Each described the angle and the x coordinate of the intersection point between the Reissner's membrane and the x-axis. Both parameters were applied to generate the Reissner's cross-section before the global cross-section tilt angle ψ was applied. The cross-section of the scala media was automatically separated from the scala vestibuli once the position of Reissner's membrane has been determined.

The values of ψ_{rei} and x_{rei} in relation to the rotation angle ϕ were manually measured from figure 3.6 and listed in table 3.5 below. Although Rattay et al. (2001) did not mention the rotation angle where the microphotograph has been taken, it can be estimated from their final model that the angle was around 90°, which was also one of the angles used by the images which have been taken to study the average scala tympani cross-section shapes in Rebscher et al. (2008).

Table 3.5: The parameter values to determine the morphology of Reissner's membrane

ϕ (deg)	10.3	90	270	450	630	810	910
x_{rei} (mm)	0.11	0.11	0.06	0.075	-0.02	-0.08	-0.08
ψ_{rei} (deg)	36.2	36.2	44.5	39.2	38.4	35.7	35.7

The values of x_{rei} and ψ_{rei} at $\theta = 10.3°$ and 910° were also taken from their neighbors for the same reason as in the previous section.

An illustration of the parameters of Reissner's membrane is shown in figure 3.11.

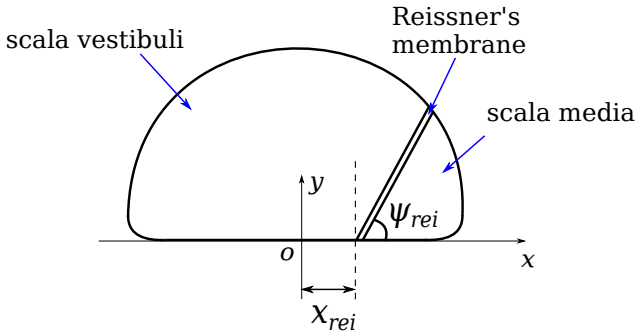

Figure 3.11: Shape control parameters of Reissner's membrane

Stria vascularis and spiral ligament

The stria vascularis is a layer of tissue attached to the lateral wall of the scala media, which produces the endolymph that fills in the scala media. The length of the stria vascularis in the cochlear cross-section can be determined given the size of the scala media from the previous section. So there was only one parameter h_{stv}, to adjust the thickness of the stria vascularis in the parametric model. Although measurements have been done on the average stria vascularis thickness of animals (Engle et al., 2013; Thomopoulos et al., 1997; Hequembourg and Liberman, 2001), there was a lack of data on the same measurement of human beings. Therefore, this parameter was still manually measured from figure 3.6, which was set to $0.08mm$ for all the cross-sections.

The spiral ligament is the most lateral tissue surrounding the cochlear spiral. It was described by 3 parameters in the parametric model: the maximum thickness h_{sl}, and the two angles created by the upper and lower endpoints of the spiral ligament in relation to the plane of basilar membrane, ψ_{sl1} and ψ_{sl2}. The values of these parameters measured from figure 3.6 are listed in table 3.6. According to the midmodiolar cross-section image, the position where the scala ligament reaches maximum thickness is always found near the interface between scala tympani and scala media, regardless of the values of ψ_{sl1} and ψ_{sl2}.

An illustration of the parameters of the stria vascularis and the spiral ligament is shown in figure 3.12.

Table 3.6: The parameter values of the spiral ligament

ϕ (deg)	10.3	90	270	450	630	810	910
h_{sl} (mm)	0.432	0.432	0.270	0.189	0.135	0.108	0.108
ψ_{sl1} (deg)	82.7	82.7	73.2	54.5	53.3	28.5	28.5
ψ_{sl2} (deg)	-44.5	-44.5	-41.8	-38.5	-21.2	-17.2	-17.2

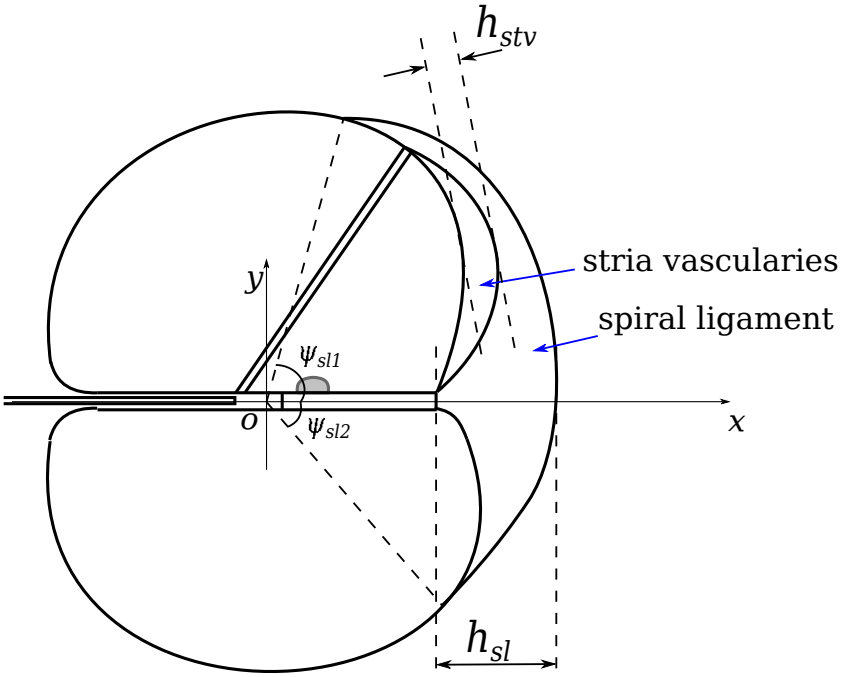

Figure 3.12: Shape control parameters of the stria vascularis and the spiral ligament

Basilar membrane and organ of Corti

Due to the important role the basilar membrane has played in the sound processing, its dimensions have been measured in the early researches of the cochlea. Wever (1938) measured the widths of the basilar membrane in 25 human cochleae and plotted them against the cochlear length from base to apex. The results showed that despite the variations in the cochlear length across subjects, a consistency was found in their basilar membrane width, which increased linearly from $0.15mm$ to $0.45mm$ from base to apex. The large variations in basilar membrane width were only found at the last $10mm$ of the apical cochlea. The thickness of the basilar membrane was also enlarged by a factor of 5 in the model for the same reason as the Reissner's membrane. The organ of Corti was modeled as a semi-ellipse and

attached to the top left of the basilar membrane. Due to its small size, the organ of Corti failed to be generated using the CGAL implicit function. Hence a simplified structured mesh model was used instead.

Figure 3.13 gives a global view of the meshes generated by the steps above. The meshes were visualized by ParaView (Kitware Inc., New York, USA).

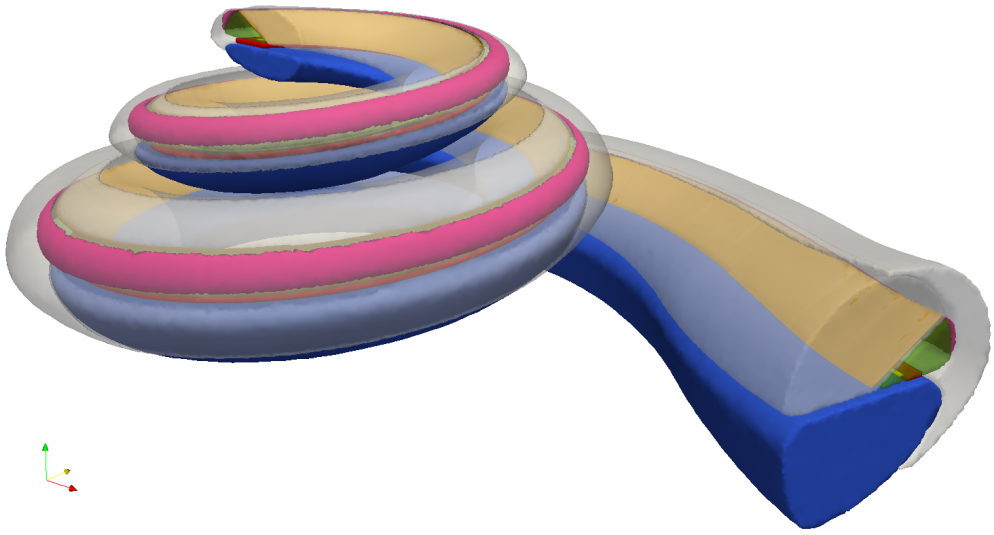

Figure 3.13: A 3D view of the meshes generated from the parametric cochlear cross-section. The shown meshes are: scala tympani (blue), scala vestibuli (white), scala media (green), stria vascularis (magenta), spiral ligament (white), Reissner's membrane (orange), basilar membrane (red) and organ of Corti (yellow). The transparency of the scala vestibuli, spiral ligament and scala media was set to 0.4 to view the meshes underneath.

Since the implicit function of CGAL only have 2 return values (inside and outside), the mesh created in this way naturally became a closed surface suitable for OpenMEEG simulation. But more details need to be considered when simplifying the mesh. Figure 3.14 gives the error in the surface meshes caused by simplification, which was proportional to the curvature of the mesh. The scala tympani has a smooth surface hence the distortion caused by simplification was small. Therefore more vertices can be removed from it when simplifying in order to increase the final computation speed. On the other hand, the spiral ligament has sharp turns at both ends in the cross-sections, hence more distortion caused by simplification was observed. To avoid this, more vertices were preserved in the simplified mesh.

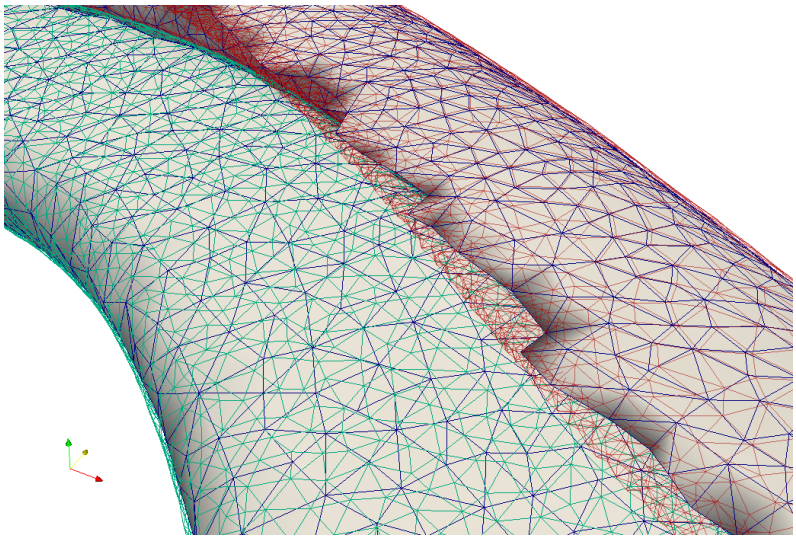

Figure 3.14: The mesh simplification process. Green and red edges come from the original mesh of the scala tympani and spiral ligament respectively. Blue edges are from the simplified meshes. Distortions caused by simplification are mostly found at the left boundary of the spiral ligament because the surface has a large curvature here.

A comparison of the vertex number of each mesh before and after simplification is given in the table below:

Table 3.7: Numbers of vertices of the cochlear meshes

Mesh name	Number of vertices	
	Original	Simplified
Scala tympani	12797	2232
Scala vestibuli	14308	2232
Scala media	18032	1850
Spiral ligament	32602	8000
Stria vascularis	16922	1636
Reissner's membrane	16000	1400
Basilar membrane	16000	1180
Organ of Corti	3200	830
Auditory nerve	51200	6500
Total	181131	25860

3.3.3 Modeling the auditory nerve

Planar auditory nerve fibers

The nerve tissue was first modeled by a 2D contour within each cross-section plane of the cochlear model. An example of the contour at the basal turn of the cochlea is given in figure 3.15(a). Its shape was controlled by 4 key points: k_1 and k_2 mark the beginning and ending positions of the lamina spiralis ossea respectively. k_3 is the position of the center of spiral ganglion. k_4 is the end of the central axon been simulated.

As shown in figure 3.15(b), the points for internal potential computation were arranged along the trajectory of the nerve fiber within the contour. There was a constant number of points within each segment of the auditory nerve regardless of the cross-section shape: 22 points for peripheral process, 10 for the spiral ganglion and 18 for the central axon. From the lateral side to the center of modiolus, the points were indexed from 1 to 50. According to the dimensions of the human auditory nerve fiber model by Briaire and Frijns (2005, 2006), points 1, 5, 9, 13, 17, 21 in the peripheral process segment and points 35, 39, 44, 50 in the central axon segment were chosen as the position of Ranvier nodes to compute the activating function. As for the spiral ganglion segment, the average potential of the 4 middle points was used as the potential of the spiral ganglion.

Oblique nerve fiber trajectory

The auditory nerve fibers generated using the method discussed in the previous section were bounded to the cross-section planes. However, the actual nerve fiber trajectory in the human cochlea has a more sophisticated shape. Stakhovskaya et al. (2007) measured the morphology of the auditory nerve fibers inside the cochlea from 9 cadaver cochleae and found an oblique fiber trajectory from the spiral ganglion to the organ of Corti. The organ of Corti rotated 990° from the round window whereas the spiral ganglion only rotated 720°. Therefore, the peripheral nerve fibers connecting the two parts is not always perpendicular to the tangent of the cochlear spiral.

According to Stakhovskaya et al. (2007), the organ of Corti length of the 9 studied cases varied from $30.5mm$ to $37mm$ while the spiral ganglion length varied from $12.5mm$ to $14.6mm$. On the other hand, a consistent relationship was found

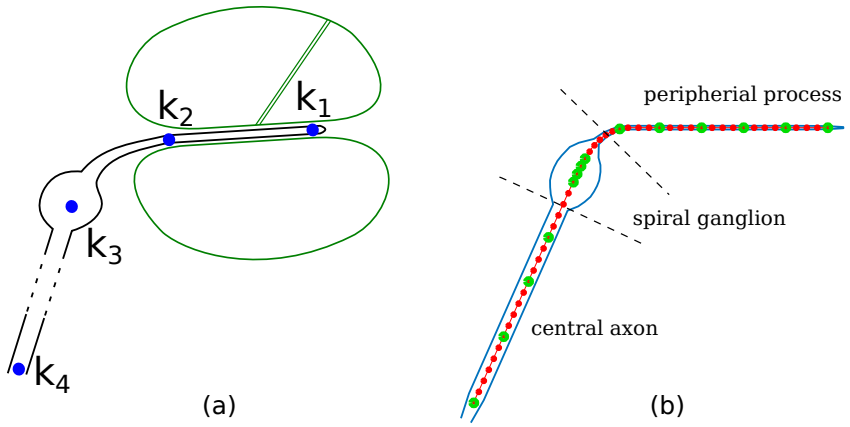

Figure 3.15: The planar contour of the auditory nerve in the parametric model. Figure (a) gives the position in relation to the other parts of the cochlea, k_1 to k_4 are the key points which control the contour shape. Figure (b) plots the electric potential computation points (red dots) that follow the trajectory of the nerve fiber within the contour. Dots with green edges represent the Ranvier nodes the positions where the electric potential were taken to compute the activating function.

between the nerve fiber connections (frequency-matched positions) and the length of the two counted in percentage, which is given in figure 3.16. Since the measurements of Stakhovskaya did not include a part of the most basal turn of the cochlea (2.6mm to 2.8mm long measured from round window), Kalkman et al. (2014) filled the fiber trajectory data of this part based on the assumption that the nerve fibers were roughly radial to the cochlear turn. The same assumption has also been adapted by this cochlear model.

For the rest part of the cochlea, the oblique nerve fiber trajectories were approximated by a piecewise linear function (equation 3.6) in the parametric cochlear model, which is plotted as the red line in figure 3.16.

$$l_{SG} = \begin{cases} 1.34 \times l_{OC}, & (0 \leq l_{OC} \leq 50) \\ 1.1 \times l_{OC} + 12.0, & (50 < l_{OC} \leq 70) \\ 0.48 \times l_{OC} + 33.48 & (70 < l_{OC} \leq 94) \end{cases} \tag{3.6}$$

In equation 3.6, l_{SG} and l_{OC} stand for the percentage length of the spiral ganglion and organ of Corti respectively from the starting position of Stakhovskaya's measurement to the apex.

The oblique nerve fiber trajectories used in the model were generated from the

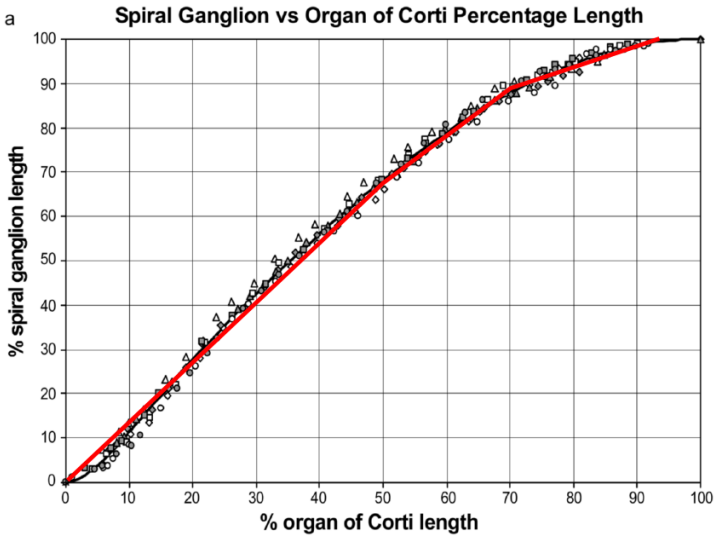

Figure 3.16: Nerve fiber mapping between spiral ganglion and organ of Corti measured by percentage length. Data from different cases are indicated by the markers (Stakhovskaya et al., 2007). The piecewise linear function used to approximate the measurements is plotted as the red line.

planar nerve fiber demonstrated in the previous section. Figure 3.17 (a) gives the nerve fiber trajectories in an unrolled modiolus while the 3D views of the corresponding modiolus are given in figure 3.17 (b) and (c). The original nerve fibers were mapped as straight lines (blue dotted) in figure 3.17 (a) because they were perpendicular to the cochlear spiral. Then the oblique nerve fibers were plotted (as red lines) in the same figure according to the distribution given in figure 3.16. Finally, the intersections between the blue lines and the red lines were recorded and mapped back to the 3D space to generate the 3D oblique fibers across multiple cross-sections. The mesh interface of the nerve tissue inside the cochlea was also generated from the nerve contours in each cross-section, as shown in figure 3.18.

3.4 Conductivities of the cochlear tissue

Due to the way in which OpenMEEG was implemented, the conductivities of the electrode array silicon rubber was set to 0, (i. e. , completely non-conductive). For some cochlear models that have assigned the conductivity of the silicon rubber, a very low value was adopted ($1 \times 10^{-12} S/m$ by Saba (2012)). For the same reason, since the stimulation current was directly interpreted as the normal current of the

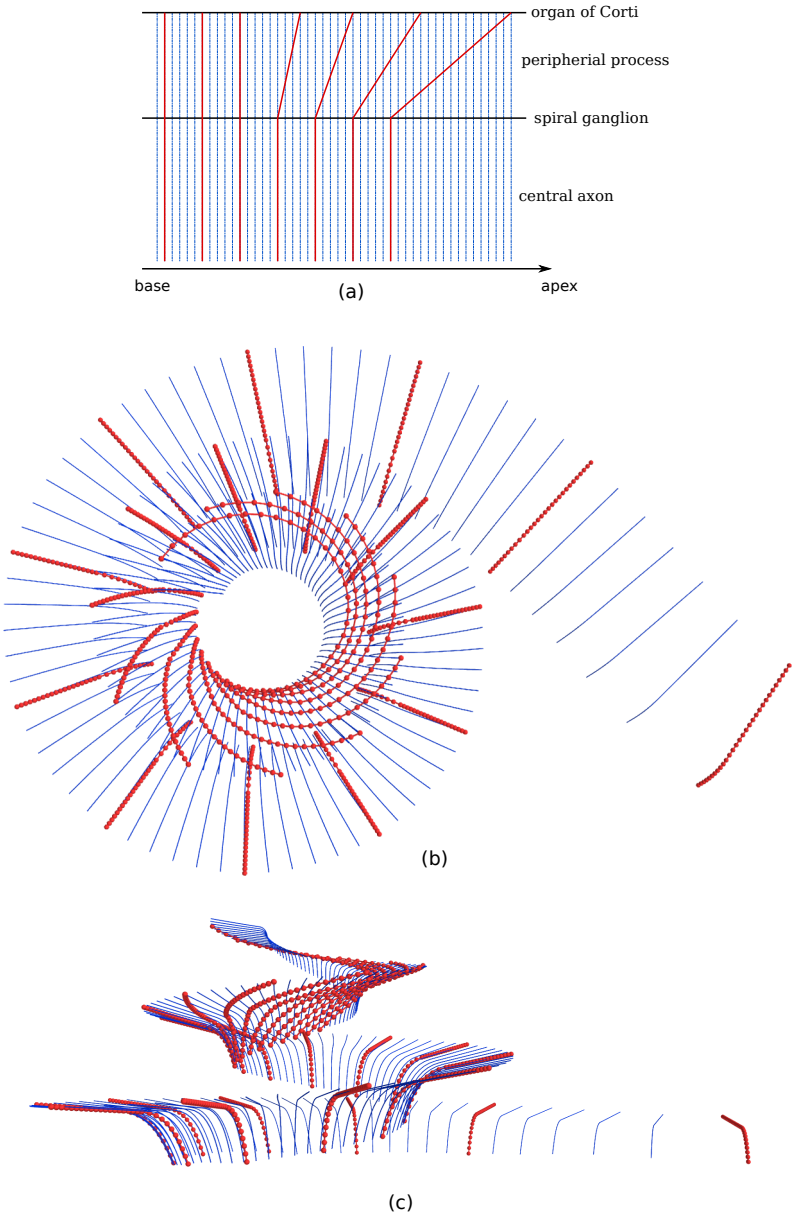

Figure 3.17: Implementing the oblique nerve fibers in the parametric cochlear model. Figure (a) is a 2D plot of an unrolled modiolus. Figure (b) and (c) are the top and side views of the nerve fiber trajectories in 3D. In all the figures, blue lines indicate the original straight nerve fibers while red lines indicate the oblique ones. Dots on the red lines are the internal potential measure points. Only the peripheral and spiral ganglion segments of the nerve are plotted in the 3D views for the sake of simplicity. For the same reason, only 1 of every 5 straight and 1 of every 30 oblique nerve fiber, are plotted.

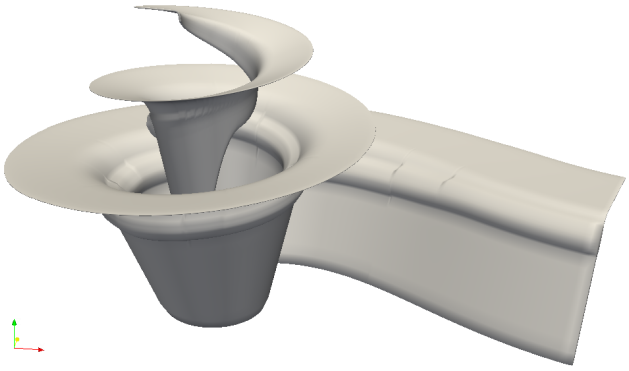

Figure 3.18: Surface mesh of the nerve tissue inside cochlea, which is the 3D contour of the auditory nerve fibers.

interface triangles, the conductivity of the metal part was not required either.

As for the conductivities of the cochlear tissue, Saba (2012) carried out a comprehensive review on the values that have been adopted by different cochlear models (Finley et al., 1990; Briaire and Frijns, 2000; Hanekom, 2001; Rattay et al., 2001). Without considering the individual conductivity adaptation, the values summarized by Saba (2012) was used as the conductivities of the average shape based parametric cochlear model except for the temporal bone and the nerve tissue, as listed in table 3.4. The values were also in consistent with the summarization made by Inguva et al. (2015) of cochlear tissue conductivities at low frequencies.

Kalkman et al. (2014) calibrated the conductivities of the temporal bone and the nerve based on measurements from 16 patient models. The results were significantly different from the conductivity values used before. Hence the calibrated values were used adopted by the parametric model.

3.5 Parameterization of the electrodes

3.5.1 Electrode array layout

From a geometrical point of view, the surface of the electrode array can be simplified as longitudinally stacked conductive regions (metal) and non-conductive regions (silicon rubber). The parameters modeled the electrode array were the total length of the electrode array and diameter changes along the array, plus the starting and ending positions of the electrodes on the array. In some electrode arrays, the metal

Table 3.8: Tissue conductivities of the average shape based parametric cochlear model

Tissue	**Conductivity** (S/m)
endolymph	1.67
perilymph	1.43
temporal bone	0.014
Reissner's membrane	$9.8\times10^{-3*}$
organ of Corti	0.012
basilar membrane	0.025*
auditory nerve	0.2
spiral ligament	1.67
stria vascularis	5.3×10^{-3}

*: The conductivities actually used in the model were the values given in this table timed by 5, since the thickness of Reissner's membrane and basilar membrane was enlarged 5 times when meshed.

electrodes formed a whole metal ring around the silicon rubber, while others have a partial coverage of the metal electrode. Hence the angles of electrode coverage was added into the parameters.

Using the EVO electrode array of Oticon Medical as an example, we acquired its corresponding mesh model, which is plotted in figure 3.19 (a). All the electrodes on the EVO array are cylindrical with $0.5mm$ height. The basal 10 electrodes have $0.6mm$ diameter while the apical 10 electrodes have $0.5mm$ diameter. Figure 3.19 (b) gives the method of modeling the electrode coverage, which was achieved by manipulating the number of chosen current injection triangles. Since the triangles of the mesh generated by CGAL were randomly arranged, it is very difficult to have a smooth edge of the metal electrodes on the mesh. Therefore, the electrode array was modeled with structured mesh.

3.5.2 Electrode placement in the cochlea

The placement of the electrode array inside cochlea in each cross-section was controlled by a pair of parameters: x_{EL} and y_{EL}. The former one was the distance from the geometric center of the electrode array to the tangent of the lateral wall of the scala tympani. The tangent was chosen in the condition that it was perpen-

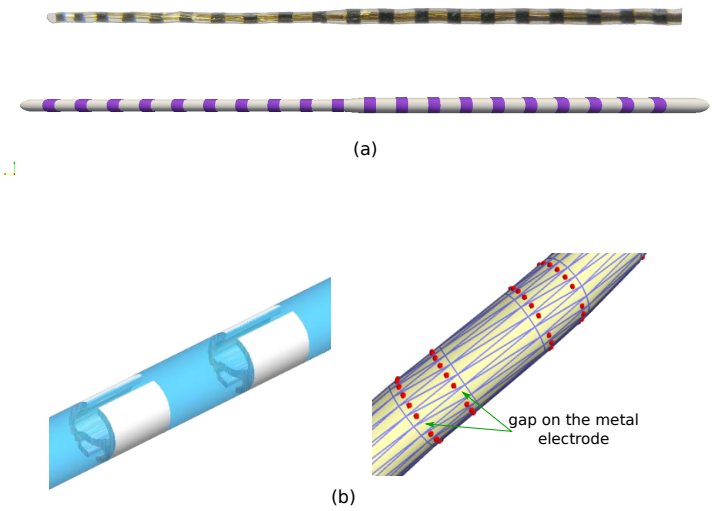

Figure 3.19: Meshing the electrode array. Figure (a) gives the layout of the EVO electrode array in the upper half. The lower half is the corresponding mesh generated by the parametric cochlear model. Figure (b) tested the ability of modeling electrode details, in which a gap on the metal electrode ring is modeled following the illustration of the electrode.

dicular to the extension line of the basilar membrane. y_{EL} was measured as the distance between the electrode geometric center to the extension line of the basilar membrane. The definition and effects of the two parameters are also shown in figure 3.20.

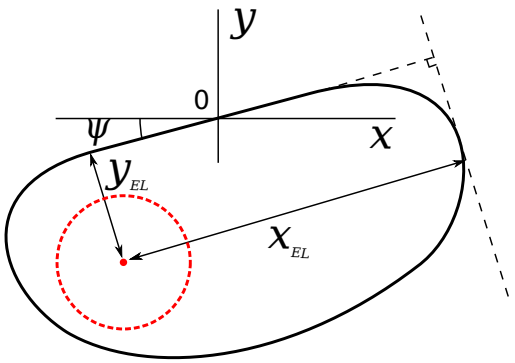

Figure 3.20: The two parameters which control the electrode position in the cochlear cross-section: x_{EL} and y_{EL}.

In the general shape based model, the electrode array was located along the geometric center of the scala tympani.

3.5.3 Reference electrode

The reference electrode is an electrode placed between the skull and scalp of the implant user. It has a much larger surface area than the intracochlear electrodes. The reference electrode provides pathways for the return current in several stimulation modes such as the monopolar, partial tripolar and multi-mode grounding. In the parametric cochlear model, the whole cochlear was placed in the center of a bounding sphere that simulated the temporal bone. The reference electrode was located at the surface of the bounding sphere, on the basal side of the cochlear mesh. The radius of the bounding sphere was $50mm$.

Usually the shape of the reference electrode is a sphere or a cylinder, depending on the implant model. Since the reference electrode is far from the cochlear compared with other electrodes, its shape has less effect on the intracochlear current distribution than its surface area. Here the reference was approximated by a round electrode array which has the same surface area as the actual reference electrode. For example, the reference electrode that works with the EVO electrode array has a surface area of $14mm^2$, therefore a round electrode with $2.1mm$ radius was created on the bounding sphere. The creation of electrode with varying sizes exploited the feature of setting electrode radius inside OpenMEEG.

3.6 Simulation results

The final model consists of 33241 vertices, each simulation performed by OpenMEEG took around 80 minutes on a PC with a quad-core processor. But once the leadfield matrix, which is the output of OpenMEEG, has been acquired, simulating different stimulation patterns was simplified as a matrix multiplication operation without recomputing the geometry matrix.

The parametric model takes current intensities on the electrodes as input and gave the following output as the simulation results:

Intracochlear potential distribution

Figure 3.21 gives the electric potential distributions measured along the organ of Corti when a monopolar stimulation scan is preformed on the electrode array. The general level of electric potential was in consistent with the results from other

cochlear models (Saba, 2012) and the intracochlear impedance measurements (Vanpoucke et al., 2004).

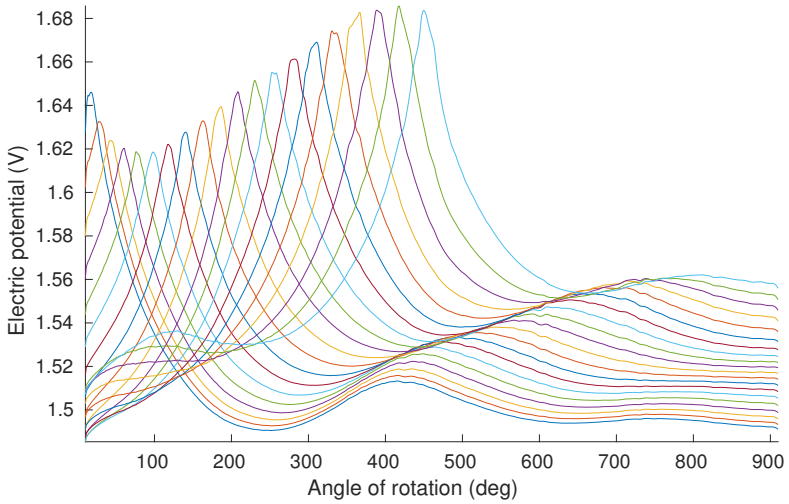

Figure 3.21: Electric potential distributions measured along the organ of Corti during a monopolar stimulation scan.

A 3D view of the intracochlear potential distribution on the simulated nerve fibers is given in 3.22. The stimulation mode was monopolar. The stimulating electrode was the 4th electrode on the array counted from base to apex.

The normalized values of activating function computed for simulated nerve fibers are plotted in 3.23. The x-axis is the index of the stimulating electrode counted from base to apex. The y-axis are the frequencies of the corresponding nerve fibers computed from greenwood function (Greenwood, 1990). The values of the activating function are indicated by the colors.

3.7 Conclusions

In this chapter, a parameterized way of generating the cochlear surface mesh model suitable for BEM simulation has been proposed through the process of building an average shape based cochlear model. The parameterization provides an easy way of controlling the geometric details in the cochlear model. The morphological information from different sources, either averaged or user-specific, can be integrated together into one model, which avoided the shortcomings of each single information source. By tuning the parameters, users can easily create a model with the specified

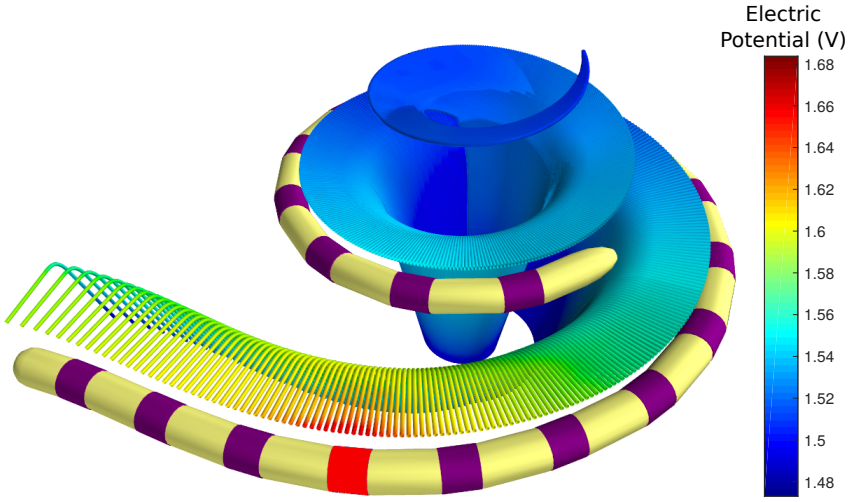

Figure 3.22: 3D view of the intracochlear potential distribution on the simulated nerve fibers during monopolar stimulation. The stimulating electrode is marked as red.

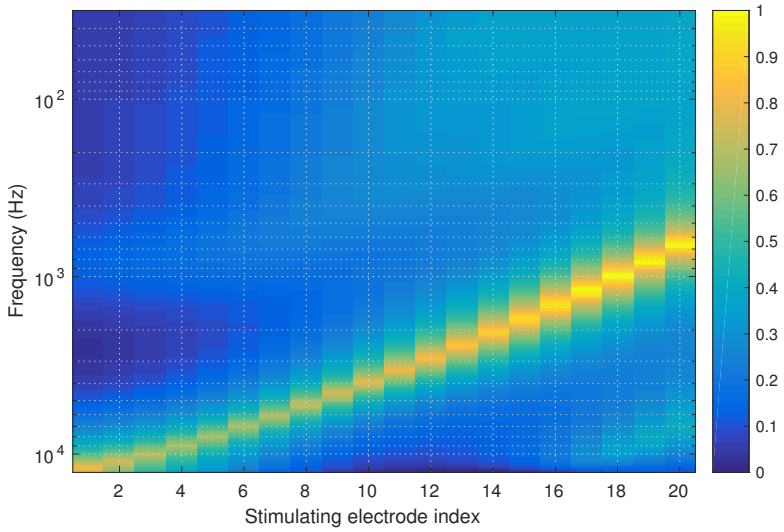

Figure 3.23: Simulated neural activation patterns of monopolar stimulations. The color indicates the value of activating function with the given stimulating electrode and characteristic frequency.

geometric characteristics need to be studied. The model gives intracochlear electric potential distribution and an estimation of the neural activation pattern as output.

However, due to a lack of the electrode-electrolyte interface, the model was unable to predict the impedance matrix of the intracochlear electrodes. Further discussions on the topic will be carried out in the next chapter.

Chapter 4

Simulation of the spatial potential distribution and the neural activation under several conditions

Contents

In this chapter, the parametric cochlear model has been used to simulate the spatial potential distribution and neural activation patterns under several different conditions. The optimal number of vertices of the model was firstly studied through a mesh convergence test.

Other cochlea related researches also build surface meshes of the cochlea, being able to reuse these meshes for BEM simulation can effectively reduce the workload of building mesh models from scratch. Therefore we presented a way of adapting the parametric model to other cochlear meshes which were originally made to study the electrode insertion in this chapter.

Finally, implanting a transmodiolar electrode array through the modiolus may reduce the energy consumption of the monopolar stimulation, and provide a way of stimulating the auditory nerve fibers in the apex of the cochlea. Using the parametric model, we can build different types of the transmodiolar electrodes and make comparisons between them in terms of electric potential distribution and neural activation pattern.

4.1 Mesh convergence test

A mesh convergence test was performed on the average shape based cochlear model to avoid over simplifying the meshes. 5 sets of meshes were generated using the mesh simplification program with different total vertex number constrains. The coarsest set of meshes contain 10332 vertices while the finest set of meshes contain 31034 vertices. Reducing the total number of vertices in the model to less than 10000 can lead to intersections between the simplified meshes and was therefore excluded from the test. The simulations were run on a mobile workstation with Intel Core i7 3840QM cpu and 32GB memory. The peak memory usage when simulating the finest meshes was around 30GB.

A monopolar stimulation on the 5th intracochlear electrode was simulated using the 5 sets of meshes. The simulation error was estimated by $\|V - V_0\|/\|V_0\|$ where V_0 was the vector of electric potential on all the intracochlear electrodes simulated by the finest meshes, while V was the same electric potential simulated by other meshes. The result is plotted in figure 4.1. According to the figure, keeping the total number of vertices in a model around 25000 has 0.1% simulation error compared with the finest mesh. On the other hand, the computation time was reduced from about 90 minutes to about 45 minutes. Therefore this value was used as the vertex

number limit in the mesh simplification step.

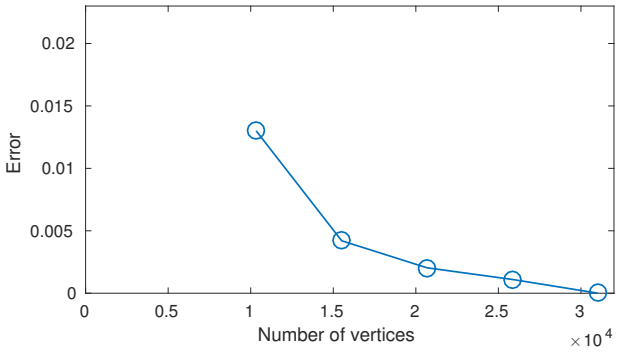

Figure 4.1: Mesh convergence test

4.2 Creating user-specific model from other cochlear meshes

Creating a highly detailed cochlear model requires a lot of manual labor since the segmentation of the cochlear images can not be done automatically yet. On the other hand, besides the electric potential simulation, the cochlear mesh models were also created in other context, such as studies of the electrode array insertion (Demarcy et al., 2016). Being able to reuse the meshes in the electric potential simulation would accelerate the modeling speed and avoid duplication of effort.

4.2.1 Modeling steps

Figure 4.2 shows the model created by Demarcy et al. (2016) from micro-CT scans of the cochlea. The model was placed in a cylindrical coordinate system similar to the parametric cochlear model: the z-axis was located in the center of the modiolus and pointing from the base to the apex. The model consists of two meshes: the scala tympani and the scala vestibuli. Other structures in the cochlea were not modeled since they were not clearly visible due to the resolution of the scans. Both meshes were made from concatenated cross-sections (structured meshes). The total number of vertices was 115200.

To uses these meshes for BEM simulation, there are several problems to be solved. First, the number of vertices in the meshes must be reduced. Second, both

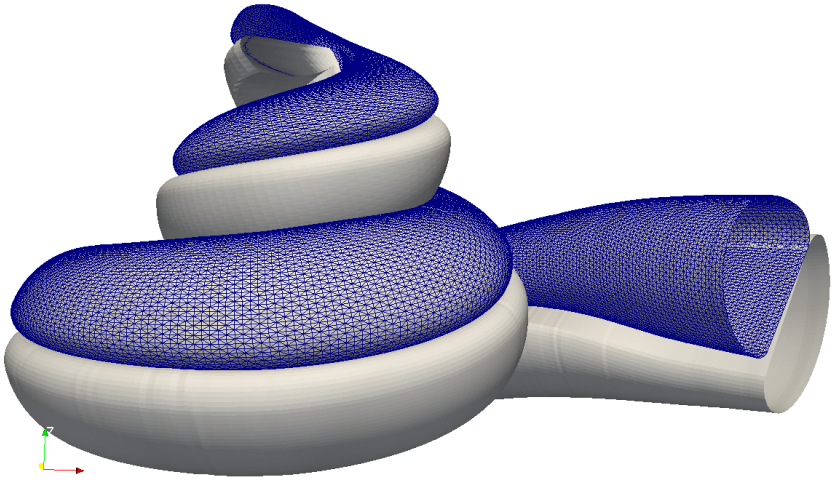

Figure 4.2: Surface mesh model of the cochlea for studying the electrode array insertion (Demarcy et al., 2016). The edges of the scala vestibuli mesh are shown in blue to demonstrate its structure.

meshes have open ends at the base and apex whereas BEM simulation requires closed surface meshes. These two issues can be easily fixed by the remeshing and simplification process of CGAL introduced in chapter 3. Figure 4.3 shows other two issues influencing the BEM simulation: there are a few intersections between the two meshes, and the scala tympani mesh has an artifact near the apex. These issues need to be fixed manually according to the following methods.

Each mesh of the original model consists of 480 cross sections. Each cross-section consists of 120 vertices. The first 120 vertices in the mesh file corresponds to the first cross-section (counted from the base to the apex), etc. Therefore the vertices of each cross-section were easily separated. The geometry centers of the cochlear cross-sections, which include both the scala tympani mesh and the scala vestibuli mesh, were computed and used as the central line of the cochlear spiral.

The normal vector of a cross-section was acquired by computing the cross product of two vectors in this cross section. Once it was computed, the cross section was translated to the origin point and rotated to the x-y plane using the normal vector for further processing and measurements. The position of the artifact in the apical cross-sections can be located by the indices of the vertices. It was then removed from the cross-section, and the gap was filled by the spline interpolation of the

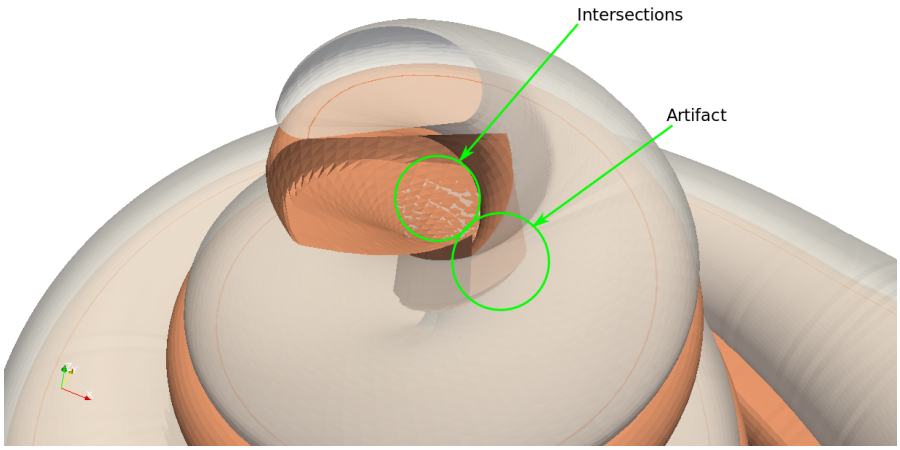

Figure 4.3: Intersections between the two meshes and the artifact at the apex of the scala tympani mesh.

neighboring points. The same cross-section before and after fix are shown in figure 4.4. The line of basilar membrane can be detected by the straight line detection algorithm using Hough transformation (Duda and Hart, 1972). The tilt angle was computed as the angle between the x-axis and the line of basilar membrane. To remove the intersection between the meshes, the cross-sections were zoomed to 95% of their original size.

One of the advantages of the parametric cochlear model is that the parameters are independent of each other. Hence the parameters can be shared between models without compatibility issues. As for this model, the missing parameters in the original mesh were about the fine structures in the cochlea, such as the widths of the stria vascularis and spiral ligament. The values of these parameters were directly taken from the average shape based model. Figure 4.5 is a picture of the adapted model. The model is already simplified and ready for simulation.

4.2.2 Number of cross-sections required by geometry adaptation

The previous section presented a way of turning other cochlear meshes into a BEM model that fully exploited the morphology information of all the 480 cross-sections in the original mesh. But in other cases, when the input is the original scan data or non-structured meshes, the parameters need to be measured manually. Therefore it is necessary to study the minimal number of cross-section samples required for a valid geometry adaptation in order to accelerate the speed of modeling.

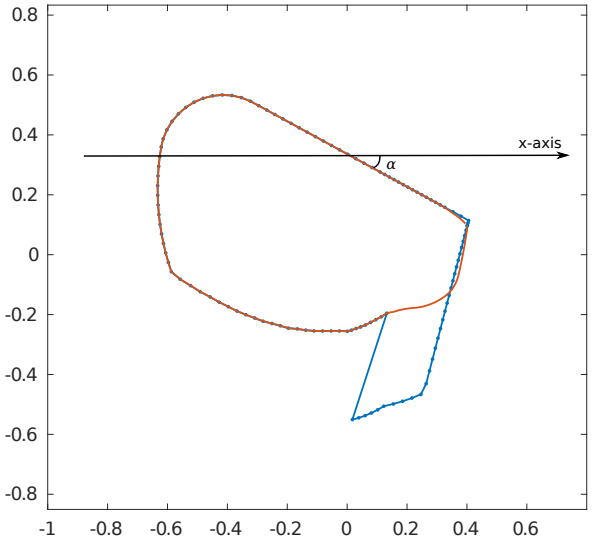

Figure 4.4: Fixing the artifact and detecting the tilt angle of the cross-section. Blue and red plots represent the original and fixed cross-sections respectively.

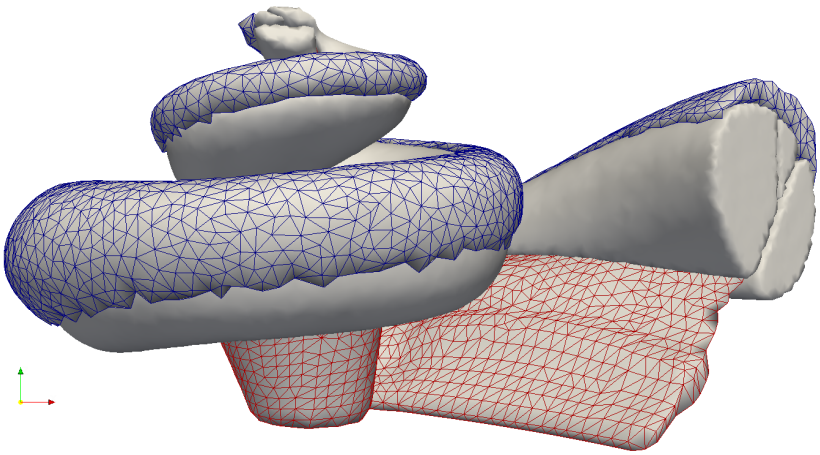

Figure 4.5: Parametric cochlear model adapted to the shape given by other cochlear meshes. The edges of the spiral ligament (blue) and nerve tissue (red) are shown in the picture.

As shown in figure 4.6, the cross-sections of the original meshes were sampled at the positions indicated by the red lines. The numbers beside the red lines represent the angle of cochlear rotation. Since the cochlear spiral starts at 10.3° (Cohen et al.,

2003), the position of the first sample was corrected from 0° to 10.3°.

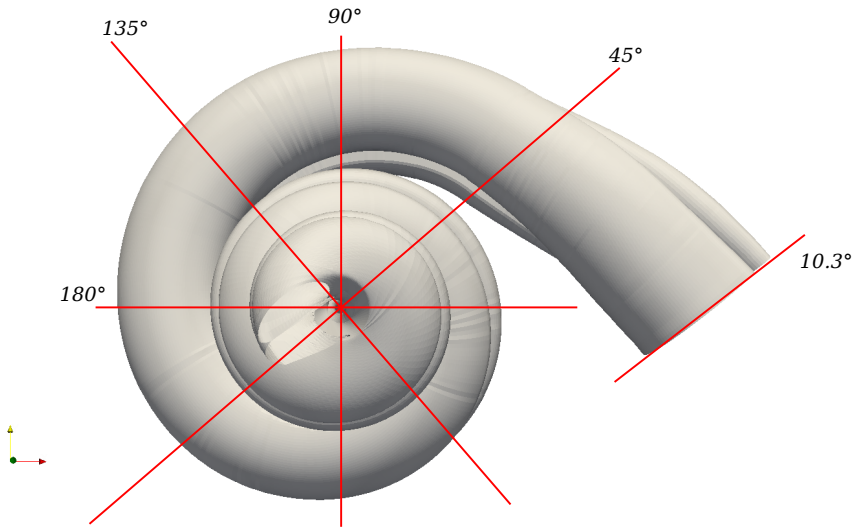

Figure 4.6: Positions where cross-section samples were taken from the original model to study the minimal number of samples for geometry adaptation.

Let ϕ denote the increment of the rotation angle between two consecutively sampled cross-sections, 3 groups of samples were taken with $\phi = 45°, 90°$ and $180°$ respectively. When $\phi = 45°$, cross-section samples were taken from all of the 4 planes indicated by the red lines plus one extra cross-section at $\phi = 10.3°$. In contrast, when $\phi = 180°$, only the cross-sections from the $180°$ and $10.3°$ planes were taken, which was similar to the cochlear geometry reconstruction from a single midmodiolar cross-section image.

6 parameters were extracted from the sampled cross-sections for the geometry reconstruction: the cross-section width w, heights of the scala tympani and scala vestibuli h_{st} and h_{sv}, tilt angle ψ, the radius and z-coordinate of the cochlear spiral R and z. Values between the cross-section samples were estimated using spline interpolation. Figure 4.7 compared the original values of w and h_{st} with the values interpolated from the sampled cross-sections. The plot shows that the error between the original and interpolated values increased as ϕ increases, and the error was mainly concentrated at the base and the apex of the cochlea.

3 models based on the 3 sets of sampled values were generated in order to compare their differences with the original model in terms of electric potential distribution. The models are noted as 45° sampled, 90° sampled and 180° sampled in the following sections.

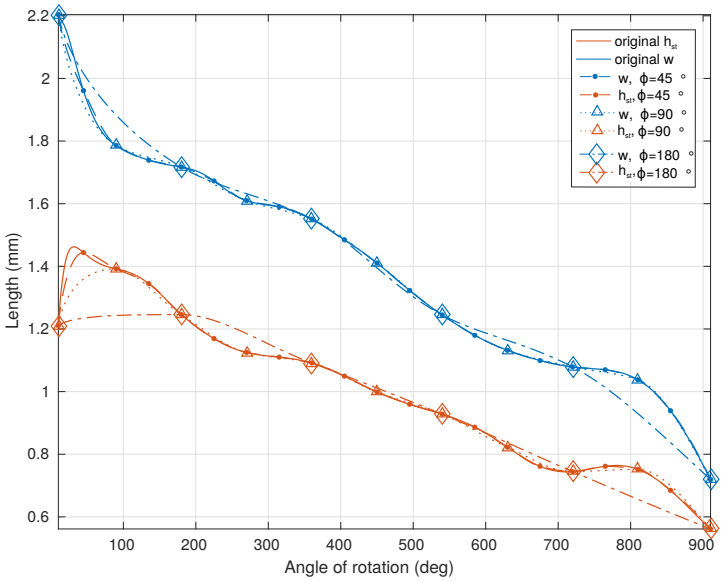

Figure 4.7: The original and interpolated values of w and h_{st}.

4.2.3 Simulation results

This section compares the simulation results of 5 models: the average shape based model built in chapter 3, the user-specific model built from the cochlear meshes of Demarcy et al. (2016) and 3 models built from sampled cross-sections of the same cochlear meshes. The electrode array was located along the center of the scala tympani in all these 5 models.

Figure 4.8 is a comparison of the electric potential measured along the organ of Corti on the 5 models during a monopolar stimulation from the 3rd electrode. The reason of choosing this stimulation site for demonstration was that a relatively large difference between the values of the original parameters and the interpolated parameters was found near this place, as shown in figure 4.7.

The result in figure 4.8 shows that compared with the average shape based model, all the models that have adapted to the user-specific cross-sections have more accurate estimations of the peak position of the electric potential along the cochlear spiral. Besides, the accuracy in predicting the amplitude of the electric potential increases as more cross-section samples were used by the model. For the model with 21 adapted cross-sections interval of 45°, the simulation result was almost identical to the original user-specific model which was built on 480 user-

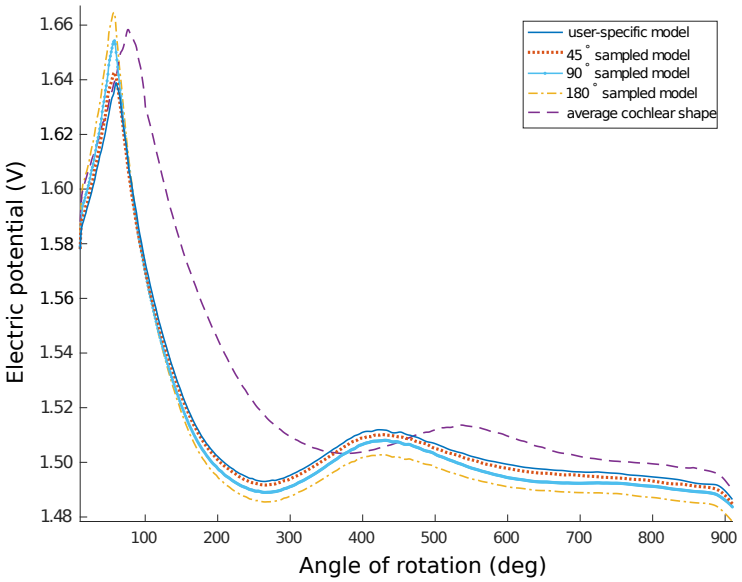

Figure 4.8: Electric potential distribution along the organ of Corti simulated by different models. The stimulation type was monopolar. The 3rd intracochlear electrode was used for stimulation.

specific cross-sections. On the other hand, the effects of the more subtle structures in the cochlea, such as the positions of the Reissner's membrane, remains to be studied.

4.3 Simulations of the transmodiolar electrode array

Transmodiolar electrode array refers to a type of electrode array which is vertically inserted into the modiolus from the apex of the cochlea. Figure 4.9 demonstrates the position of an implanted transmodiolar electrode array in relation to the cochlea. Unlike the bendable electrode array in the scala tympani, the transmodiolar electrode array must have a certain level of stiffness to insert through the modiolus (Tourrel, 2016). During the implantation, a small hole was first drilled through the modiolus, then the transmodiolar array was placed through the hole.

Despite the probability of damaging the cochlea structure and the auditory nerve in the modiolus, the transmodiolar electrode array has several advantages over the usual way of stimulating the auditory nerve fibers. The transmodiolar electrode array can be used either for stimulation or as the ground of the monopolar

stimulation from normal electrode arrays. In the first case, its current can stimulate the apical turns of the cochlea where the normal electrode arrays failed to reach. In the second case, due to its short distance to the electrode array in the scala tympani, the power consumption of monopolar stimulation can be reduced.

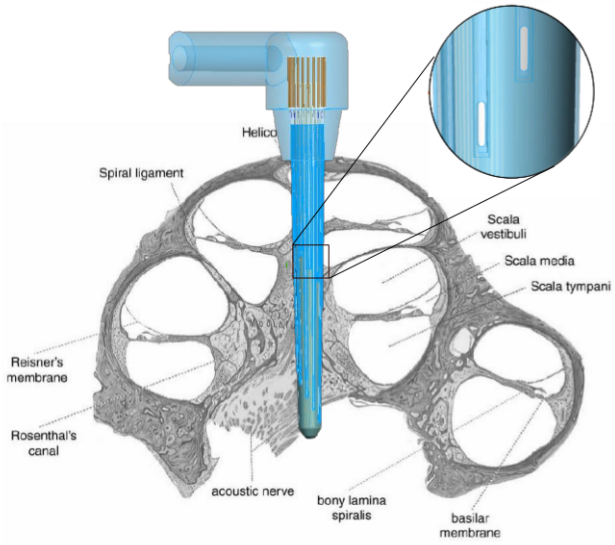

Figure 4.9: The ideal position of a transmodiolar electrode inside cochlea. The background is a midmodiolar cross-section image of the cochlea (Tourrel, 2016).

4.3.1 Modeling the transmodiolar electrode array

Two types of transmodiolar electrode arrays with different layouts have been modeled. The first one has cylindrical electrodes surrounding the array, as shown in figure 4.10.

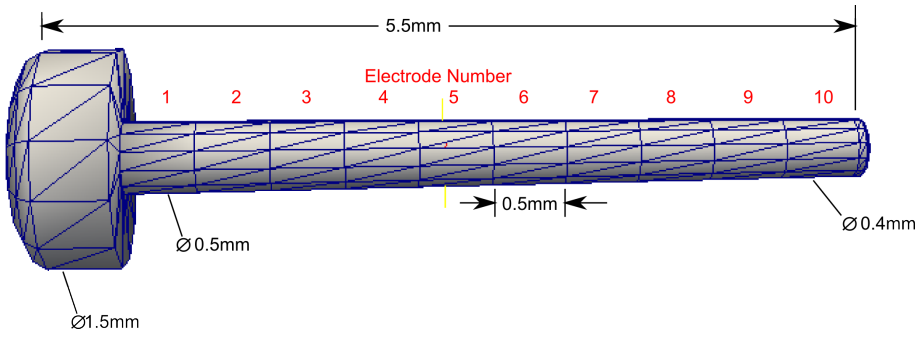

Figure 4.10: Transmodiolar electrode array type 1: with cylindrical electrodes.

The shape of electrode array in figure 4.10 is close to a nail. In order to simulate as many stimulation positions as possible on this layout, 10 cylindrical electrodes were placed continuously along the array without gaps between the electrodes. After implantation, electrode 10 will reach the basal turn of the cochlea while electrode 1 lies at the apex.

The second type of transmodiolar electrode array is shown in figure 4.11.

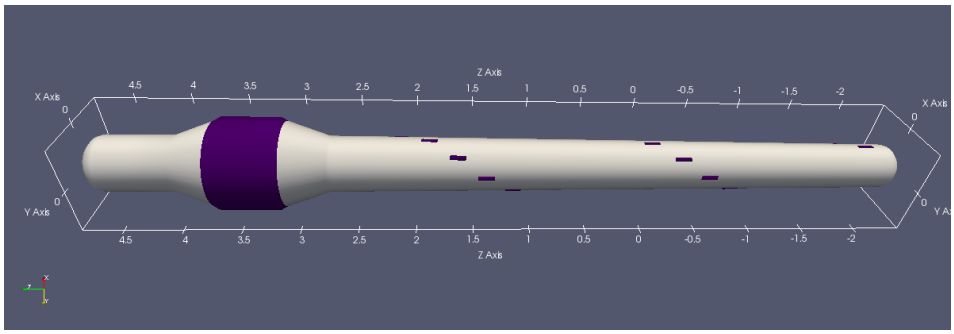

Figure 4.11: Transmodiolar electrode array type 2: with rotationally arranged electrodes. The dark parts on the array represent the metal electrodes.

A big cylindrical electrode was located at the end of the array and was used only as the reference electrode. A series of 20 $0.12mm \times 0.03mm$ rectangular stimulation electrodes were rotationally arranged along the electrode array for 2.5 turns.

Only the average shape based model was selected for transmodiolar electrode insertion because it has enough space at the center of the modiolus to avoid mesh intersection. The models inserted with either the normal and transmodiolar electrode arrays are shown in figure 4.12.

4.3.2 Work modes of the transmodiolar electrode array

The transmodiolar electrode array type 1 has the following work modes:

- **Ground** The electrode array in the scala tympani works in the standard monopolar mode while one or more electrodes on the transmodiolar array are used as the ground of the monopolar stimulation.
- **Transmodiolar bipolar** The stimulation current flows from one of the electrode on the transmodiolar array to another.

The transmodiolar electrode array type 2 can work in the following stimulation modes:

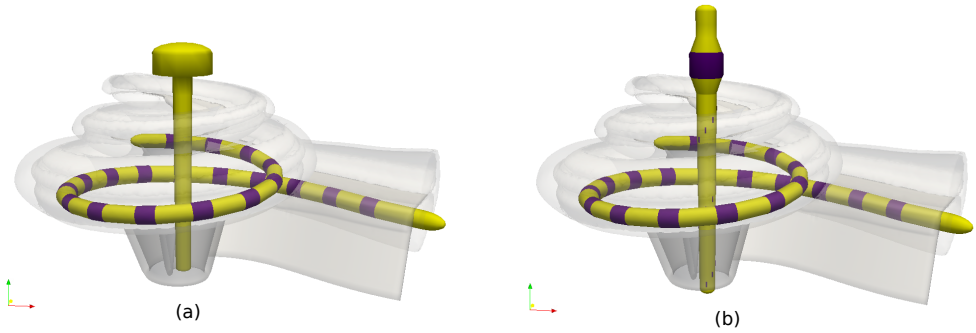

Figure 4.12: The cochlear model inserted with transmodiolar electrode array type 1 (a) and type 2 (b).

- **Ground** The cylindrical electrode is used as ground for standard monopolar stimulations of the electrode array in the scala tympani.

- **Transmodiolar monopolar** The stimulation current flows from one of the small rectangular electrode to the big cylindrical electrode at the apex of the cochlea.

4.3.3 Results and discussions

When modeling the inserted transmodiolar electrode array in the parametric cochlear model, we assumed that the array went through the center of the modiolus without damaging the auditory nerve fibers around it. Therefore the array was surrounded mostly by the nerve fibers from the apical turns of the cochlea. An EVO electrode array was placed in the scala tympani of the same model. Based on these conditions, the electric potential distribution on the auditory nerve fibers has been simulated. An example of the 3D potential distribution is shown in figure 4.13. In the figure, the type 2 transmodiolar electrode array was working at the monopolar stimulation mode. The stimulating electrode array was in the middle part of the modiolus. A high electric potential, shown by the red and orange colors, is observed on the nerve fibers in the modiolus.

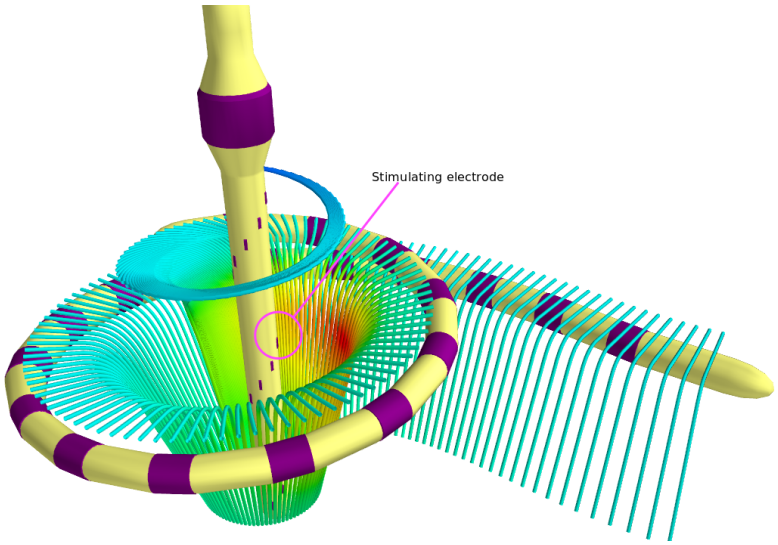

Figure 4.13: An example of the intracochlear electric potential distribution generate by a monopolar stimulation from the transmodiolar electrode.

Using transmodiolar electrodes for grounding

To make a more quantitative comparison between the stimulation modes, the values of activation function were computed from the potential distributions. In order to estimate the spread of excitation, we set the neural excitation threshold to 70% (-3dB) of the maximum value of the activation function. In the following figures, the x-axis represent the positions of the stimulating electrode, while the y-axis gives the positions of the corresponding firing neurons. The positions are noted as the cochlea turns from base to apex.

Figure 4.14 gives the simulated neural activation patterns of the monopolar stimulation using different grounding methods.

In the standard monopolar scheme, the grounding electrode is placed between the skull and scalp of the user. In the model, it was simulated by a round flat electrode placed on the bounding sphere of the model. Figure 4.14 (a) is the activation pattern of the standard monopolar stimulation. The positions of the activated neurons grew from the base to 1.25 turns of the cochlea as the stimulation position changes.

Figure 4.14 (b) and (c) give the simulated neural activation patterns when using a single electrode on the transmodiolar array type 1 for grounding. The transmodiolar electrode 1 (most apical) and 10 (most basal) were used for (b) and (c)

respectively. The surface areas of electrodes on transmodiolar array type 1 and EVO electrode array are close to each other, hence they have similar current density distributions near the electrodes. Therefore the spread of excitation depends mostly on the distance between the nerve fibers and the electrode: a closer distance to the electrode array leads to higher activation function values and larger spread of excitation. Since the transmodiolar electrodes are closer to the nerve fibers than the EVO electrodes, a larger spread of excitation is expected near their locations as indicated in the figures. Compared with transmodiolar electrode 1, electrode 10 was even closer to the nerve fibers in the modiolus. Neural activities near the stimulating EVO electrodes were completely suppressed in figure 4.14 (c) by the high level of neural activation near electrode 10.

Using multiple electrodes simultaneously as the ground can enlarge the grounding surface area and reduce the current density near the electrodes, hence eliminating the unwanted neural excitations. As shown by figure 4.14 (d), using electrode 1-5 together as the ground significantly reduced the firing of the apical neurons in the monopolar stimulation. When all the 10 electrodes are used for ground, as shown in figure 4.14 (e), the apical excitations were eliminated. Figure 4.14 (f) is the simulation result when using the cylindrical electrode of transmodiolar array type 2 as ground, which already have a large surface area ($1mm^2$). The extra neural firings were only found at the very apical part of the cochlea.

Among the 5 new grounding methods with the transmodiolar electrode array plotted in figure 4.14, the first 3 were not applicable due to the large area of unwanted neural firings near the apex of the cochlea. For the last 2 methods, the neural activation patterns at the lower turns of the cochlea were similar to the standard grounding method. However, the electric potential on the stimulating electrode was on average reduced by 67% and 61% respectively with the same stimulation current intensity in the simulated cochlear geometry. Therefore, we can confirm the advantage of reducing energy consumption using the transmodiolar electrodes for grounding.

4.3.4 Using transmodiolar electrodes for stimulation

Due to the lack of a dedicated grounding electrode on the array, transmodiolar array type 1 can only perform the bipolar stimulation. Figure 4.15 (a) is the simulated neural activation pattern of a bipolar scan across the array. When the electrode

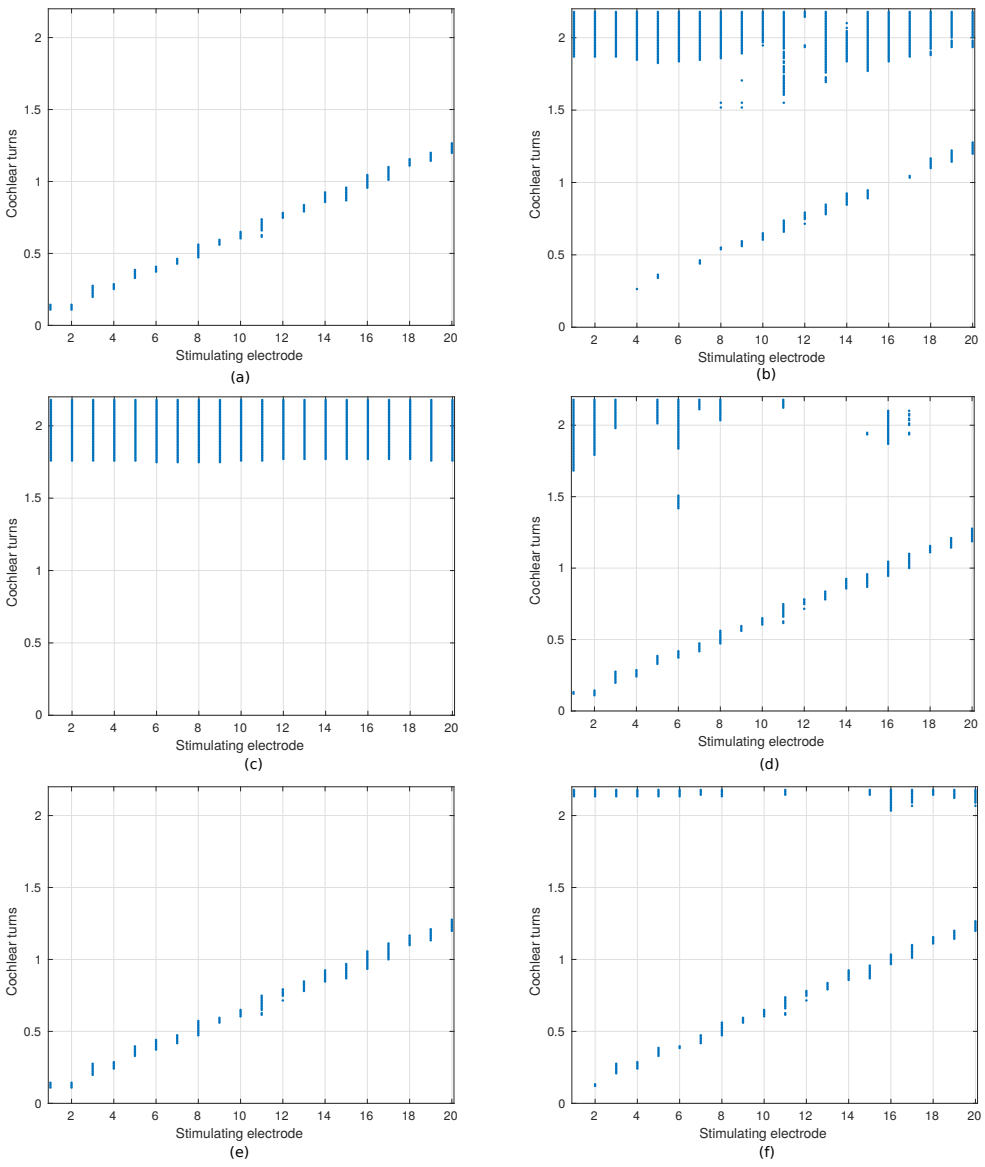

Figure 4.14: Neural activation patterns of monopolar stimulation with different grounding methods: (a) standard grounding electrode, (b) grounding with electrode 1 of transmodiolar array type 1, (c) electrode 10 of array type 1, (d) electrode 1-5 of array type 1, (e) all electrodes on array type 1, (f) grounding with the cylindrical electrode of transmodiolar array type 2.

pair N and $N-1$, $2 \leq N \leq 10$ were used for stimulation, the stimulating electrode in the plot was simply noted as N.

As the stimulating electrode went from 2 to 10, the actual stimulation site in

the cochlea moved from the apex to the base in the modiolus. The results shown in figure 4.15 (a) indicate that this vertical displacement can not effectively change the position of neural activation in the cochlea. The only parameter that changed by the stimulation position was the size of excitation spread. Actually, since the trajectory of the auditory nerve fibers are mostly parallel to the electrode array in the modiolus, moving the stimulation position vertically can only change the activated position on the same nerve fibers.

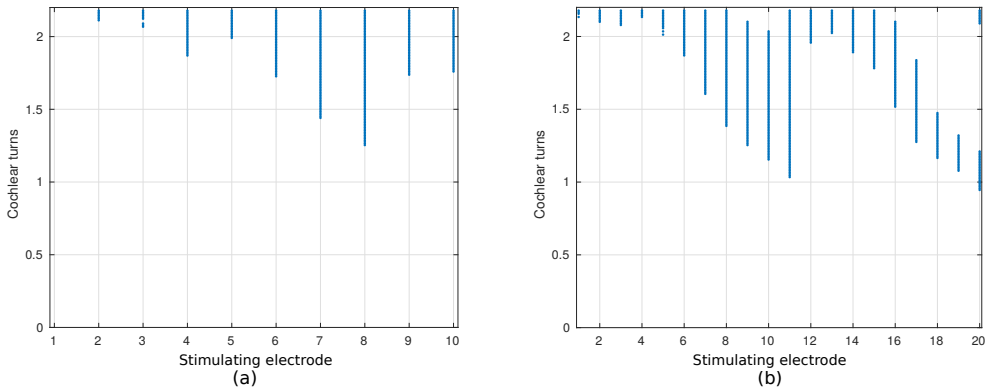

Figure 4.15: Neural activation patterns of: (a) a bipolar stimulation scan on transmodiolar array type 1; (b) a monopolar stimulation scan on array type 2.

Figure 4.15 (b) give the neural activation pattern of a monopolar stimulation scan using the transmodiolar electrode array type 2. The numbering of the electrodes on array type 2 was in the same direction as type 1: the index increases as the electrode goes from the apex to the base in the cochlea.

The electrodes rotated for two turns along the type 2 array. Therefore a periodicity was found in the activation patterns: the position of neural activation moved from the 2nd turn to the 1st turn of the cochlea as the stimulating electrode moved from 1 to 11, and the same pattern was repeated from electrode 12 to 20 but with less spread of excitation. The results showed that rotationally arranged electrodes on the transmodiolar array was able to control the neural activation site in the cochlea, and they can effectively reach the apical part of neurons.

The first turn and second turn on the type 2 array have different sizes of excitation spread, which can be explained by the images given in figure 4.16. Because of the oblique nerve fiber trajectory near the apex, stimulating from the apex (figure

4.16 (a)) activated more neurons than stimulating from the base (figure 4.16 (b)).

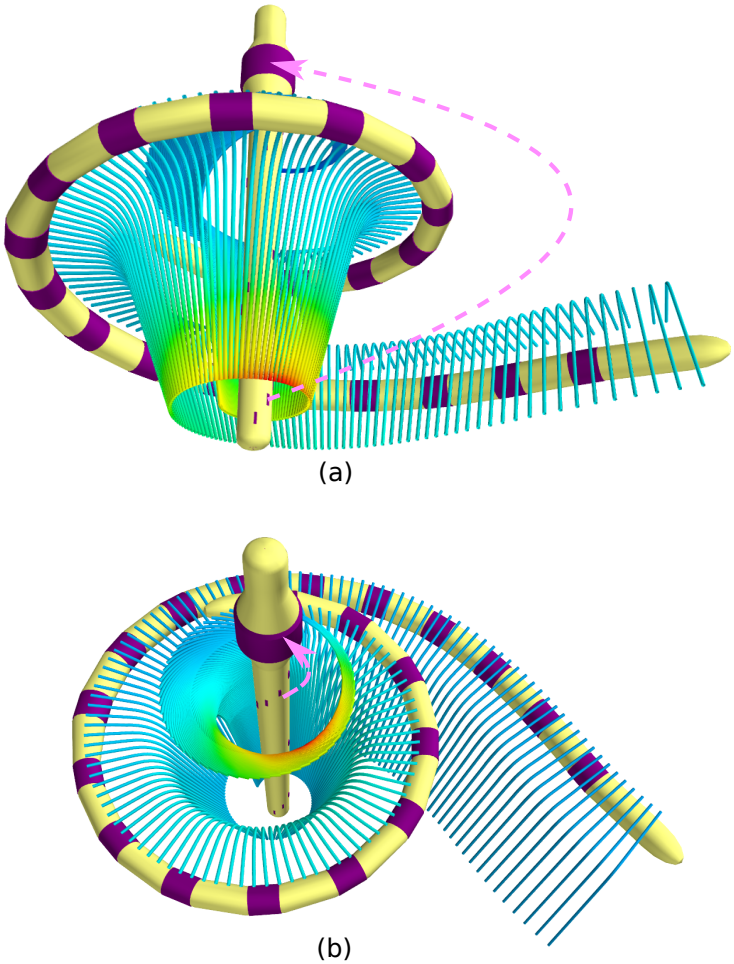

Figure 4.16: Electric potential distribution on the auditory nerve fibers generated by a monopolar stimulation using transmodiolar electrode array type 2. The stimulating electrodes were: (a) at base of the cochlea; (b) at the apex of the cochlea. The general directions of current flow are indicated by the pink arrows.

4.3.5 Conclusion

In this chapter, a convergence test was performed on the cochlear meshes to determine the optimal number of vertices in the mesh. The result showed keeping the number of vertices around 25000 can reach a balance between the accuracy and the computation speed.

This chapter also demonstrated a way of turning other cochlear meshes into a

BEM model. To estimate the number of cross-sections required by the geometry adaptation, 3 models adapted to the same geometry were generated using cross-sections with different sampling angle intervals. The simulation result indicated that a 45° of sampling angle interval can provide enough morphology information for a satisfying cochlear geometry reconstruction.

Finally, the function of transmodiolar electrode array was investigated using the simulation approach. Two types of transmodiolar electrode arrays have been modeled. The simulation results suggested that using the transmodiolar electrode array as the ground of the monopolar stimulation can effectively reduce the stimulation energy consumption, but larger surface area of the grounding electrode is required in order to avoid unwanted neural excitation. When using the transmodiolar array for stimulation, rotationally arranged electrodes were preferred and a deeper insertion into the modiolus was recommended to avoid the oblique nerve fibers at the apex of the cochlea.

Chapter 5

Coupling the BEM model with a circuit model of the electrode-electrolyte interface

Contents

5.1 Introduction

3D model based simulations have been used to study the current distribution and spread of excitation of the stimulation modes which have fixed current intensities on the electrodes, including the monopolar, bipolar, tripolar, current steering and phased array stimulations. In these modes, the current intensity I for each electrode is known. Therefore the current distribution in the model is solved with the Neumann boundary condition:

$$\sigma \nabla V \cdot \mathbf{n} = I \quad \text{on} \quad \Gamma \tag{5.1}$$

where σ is the conductivity, V is the electric potential field, $\mathbf{n}$ is the normal vector of the boundary Γ of the conductive domain and I is the normal current distribution on the boundary Γ.

However, there is a lack of work on the simulation of common ground and multi-mode grounding stimulations which have adopted the passive current return strategy, as described in section 2.2.2. For these stimulation modes, equation 5.1 still holds for the stimulating electrode, where I is controlled by the current source inside the stimulation chip. On the other hand, for the electrodes that have been used as passive ground, the boundary condition becomes equation 5.2:

$$V = V_i \quad \text{on} \quad \Gamma_i \tag{5.2}$$

where V_i and Γ_i stand for the voltage and boundary of the ith grounding electrode. Equation 5.1 and 5.2 together turn the Neumann boundary condition into a mixed boundary condition.

It is noteworthy that, due to the existence of the blocking capacitor and the electrode-electrolyte interface, the V_i of the grounding electrodes are not equal. As shown in figure 5.1, the parametric BEM model presented in chapter 3 only considers the resistive cochlear tissue. The electric potentials on the surface of the electrodes computed by the model are V_2, V_1 and V_0. On the other hand, the actual potential on the surface of the metal electrodes are V_2', V_1' and V_0'. The difference between V and V' are the voltages on the electrode-electrolyte interfaces. Assuming all the electrodes are in good contact with the electrolyte, the impedances of all the intracochlear electrodes should share the same value, which is noted as Z_b. The

reference electrode has another impedance value, noted as Z_{ref}.

For the reference electrode, the electric potential on its surface, V_0', directly equals to the potential of the stimulation ground V_{GND}. Whereas for the intracochlear grounding electrodes, the difference between V_1' or V_2' and V_{GND} is the voltage that falls on the blocking capacitor C_b. The value of V_{GND} depends on the choice of the potential reference. In the simulation, V_{GND} was a non-zero constant since the reference was assigned as the mean potential of the outermost interface of the model by OpenMEEG.

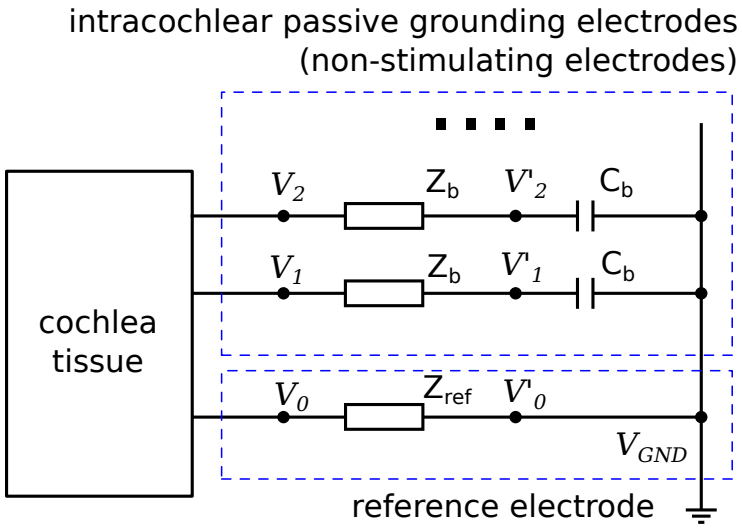

Figure 5.1: The equivalent circuit of the grounding electrodes for the multi-mode grounding mode. 2 intracochlear grounding electrodes and the reference electrode are plotted. C_b stands for the blocking capacitor. Z_D and Z_ref are the impedances of the electrode-electrolyte interfaces on the intracochlear and reference electrode respectively.

The blocking capacitors are continuously getting charged or discharged during the stimulation pulse, which affects the global current distribution by changing the boundary condition V_i in equation 5.2.

In the rest of this chapter, a new method will be presented under the framework of the parametric cochlear model and BEM simulation in order to solve the mixed boundary condition problem. It involves the computation of a new matrix from the leadfield matrix, which can give the current intensity on the non-stimulating electrodes based on the tissue resistance between the electrode pairs. To further compute charging and discharging of the blocking capacitors during the stimulation pulse, circuit simulation algorithms are integrated into the simulation process. The

simulation result gives the normal current intensities and the electric potentials on all the intracochlear electrodes.

5.2 The electrode-electrolyte interface

A schematic representation of the electrode-electrolyte interface is given in figure 5.2, which includes the faradaic and capacitive (non-faradaic) reactions.

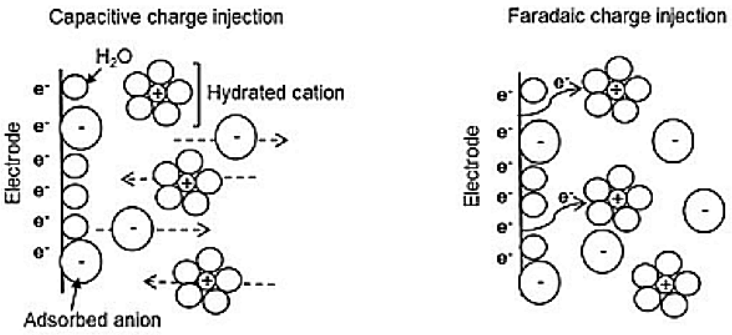

Figure 5.2: Mechanisms of the capacitive and faradaic reactions on the electrode-electrolyte interface (Bareket-Keren and Hanein, 2013).

The faradaic reaction refers to the net charge transfer between the electrode and the electrolyte. It causes chemical reactions that are generally irreversible. The chemical reactions can involve the oxidization or dissolution of the electrode surface, the generation of gas and the change of pH in the electrolyte, all causing damage to the tissue nearby. Therefore, the faradaic reaction is avoided in cochlear stimulations by delivering charge balanced pulses.

The capacitive reaction refers to the charging and discharging of the electrode-electrolyte double layer, which is formed by the adsorption of ions on the surface of the electrode when a voltage is applied over the electrode-electrolyte interface.

The electrode-electrolyte interface is usually characterized by its complex impedances measured at different frequencies. The result is plotted as an electrochemical impedance spectrum. Figure 5.3 gives an example of electrochemical impedance spectra based on in-vivo measurements taken inside a cat's cochlea Duan et al. (2004). In the spectra, the imaginary part of the measured impedance is plotted against the real part. It can be observed from the spectra that the impedances at different frequencies measured immediately after implantation formed a straight line in the plot, which from a frequency response point of view, indicated a con-

stant phase shift at different frequencies, hence the electrical characteristics of the electrode-electrolyte interface can be modeled by an equivalent circuit model which consists of a virtual component called constant phase element (Brug et al., 1984; Duan et al., 2004).

The impedance spectra measured following the days of implantation still showed the constant phase characteristic, but the lines were shifted to the right. This phenomenon indicated an increase of the real impedance in the cochlear environment, which was caused by the ossification and the growth of the fibrous tissue.

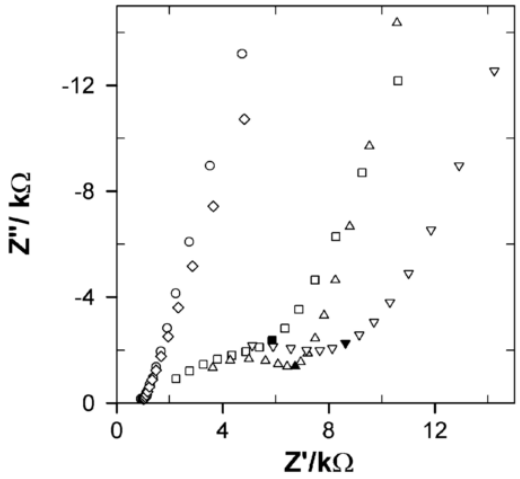

Figure 5.3: electrochemical impedance spectra measured between a pair of electrodes implanted in a cat's cochlea (Bareket-Keren and Hanein, 2013). The symbols indicate the time between the operation and the measurements: (○) immediately after the surgery, (□) 9 days, (△) 23 days, (▽) 179 days, and (◊) explanted and measured in saline after 179 days.

5.3 Models of the electrode-electrolyte interface

To model the electrode-electrolyte interface inside the cochlea, a variety of equivalent circuit models have been proposed (Johnson, 1980; Duan et al., 2004; Vanpoucke et al., 2004; Lai and Choi, 2007; Sue et al., 2013, 2015). Figure 5.4 (a) is a general circuit representation of a single intracochlear electrode, in which Z_b is the impedance of the electrode-electrolyte interface and Z_s represents the impedances of the tissue and electrolyte. The contact deposits and internal circuits of the cochlear implant could be the other factors contributing to Z_s (Vanpoucke et al., 2004).

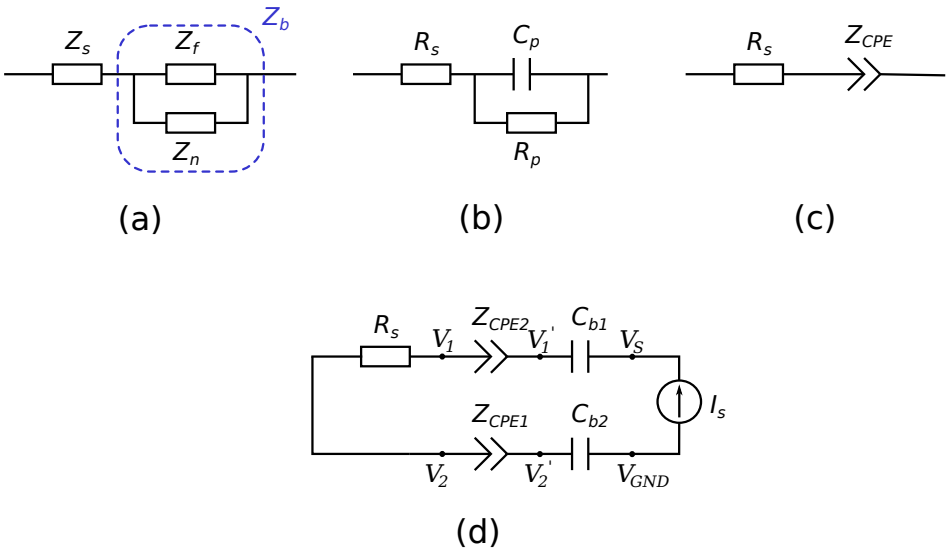

Figure 5.4: Equivalent circuit models of the electrode in the electrolyte

When fitting the impedance measurements taken in saline or acute implantation experiments, the electrolyte impedance Z_s can be simplified as a resistance R_s as in figure 5.4 (b) and (c) (Duan et al., 2004). In other cases, Z_s should be modeled by the transmission line circuit model (Bisquert, 2000; Bisquert et al., 2000).

Z_b can be further divided into two complex impedances connected in parallel: the impedance of the faradaic reaction Z_f and the impedance of the non-faradaic reaction Z_n. As discussed in section 5.2, the irreversible faradaic reaction causes neural damage and is hence avoided by delivering charge balanced pules in cochlear stimulations. The impedance of the residual reversible faradaic reaction is pseudo-capacitive in nature and can be counted into the double layer impedance according to the studies of Richardot and McAdams (2002); Brunton et al. (2012); Sue et al. (2015).

The double layer capacitance Z_n created by the non-faradaic reaction could be simply modeled by a capacitor C_p and a resistor R_p connected in parallel, as suggested by figure 5.4 (b) (Lim et al., 1990; Sit and Sarpeshkar, 2007). Lai and Choi (2007) incorporated this circuit into a 3D cochlear model to make predictions of the voltage waveform between electrode pairs during the biphasic current pulse. But the electrical impedance spectrum of such a circuit is plotted as a semicircle on the complex plane, which is significantly different from the actual electrical impedance spectra given in figure 5.3.

Compared with the parallel circuit model, the constant phase element (CPE) can better represent the impedance of the electrode-electrolyte interface (McAdams et al., 1995). The impedance of a CPE is given by the empirical relation:

$$Z_{CPE}(\omega) = \frac{1}{Q}(j\omega)^{-\beta} \tag{5.3}$$

where ω is the angular frequency ($\omega = 2\pi f$, f is the frequency in Hz), $j = \sqrt{-1}$, Q and $\beta, (0 \leq \beta \leq 1)$ are the magnitude and angular coefficients. When $\beta = 1$, the CPE acts as a perfect capacitor. Figure 5.4 (c) is the equivalent model where the electrode-electrolyte impedance is represented by a CPE.

Using the Laplace transform, the time-domain response of the CPE to a current step (equation 5.4) can be calculated as follows (Sadkowski, 1993):

$$I(s) = \frac{I_0}{s} \tag{5.4}$$

let $s = j\omega$ in equation 5.3 and applying Ohm's law in the complex frequency domain,

$$V_{CPE}(s) = I(s) \cdot Z_{CPE}(s) = \frac{I_0}{Qs^{1+\beta}} \tag{5.5}$$

the time domain voltage response can be computed using inverse Laplace transform:

$$V_{CPE}(t) = \frac{I_0}{Q\Gamma(1+\beta)}t^{\beta} \tag{5.6}$$

where V_{CPE} is the voltage on CPE, t is the time in seconds and Γ is the Gamma function.

As for the parametric cochlear model, the equivalent circuit in figure 5.4 (c) has been adopted to incorporate the electrode-electrolyte interface. Figure 5.4 (d) gives the equivalent circuit between a pair of stimulating and grounding intra-cochlear electrodes in the parametric cochlear model after the incorporation with the electrode-electrolyte interface. The impedance between the electrode pairs consists of the tissue and electrolyte R_s, the two electrode-electrolyte interfaces Z_{CPE1} and Z_{CPE2} and the two blocking capacitors C_{b1} and C_{b2}, which were inserted in series with the electrodes to guarantee charge balanced stimulation pulses. I_s indicates the source of the stimulation current. The value of the resistive component R_s was simulated by the original model in chapter 3. The rest of the components were simulated using the circuit simulation algorithms introduced in this chapter.

5.4 Solving the mixed boundary condition problem

To simulate the stimulation modes described by mixed boundary conditions, the original leadfield matrix must be modified in order to take potential description as part of the inputs.

5.4.1 Applying electric potential constraints to the leadfield matrix

The original EIT leadfield matrix computed by OpenMEEG gives the relationship between the boundary current and the electric potential at specific positions on the mesh:

$$\mathbf{V} = \mathbf{M}_{lf} \times \mathbf{I} \tag{5.7}$$

in which $\mathbf{V}$ is the vector of the electric potentials, $\mathbf{M}_{lf}$ is the leadfield matrix, $\mathbf{I}$ is the vector of current intensities.

The leadfield matrix is designed to solve problems with Neumann boundary conditions, where $\mathbf{V}$ can be easily computed with the given $\mathbf{I}$.

Equation 5.7 is expanded as follows:

$$\begin{bmatrix} v_1 \\ v_2 \\ \vdots \\ v_n \end{bmatrix} = \begin{bmatrix} l_{11} & l_{12} & l_{13} & \dots & l_{1n} \\ l_{21} & l_{22} & l_{23} & \dots & l_{2n} \\ \vdots & \vdots & \vdots & \ddots & \vdots \\ l_{m1} & l_{m2} & l_{m3} & \dots & l_{mn} \end{bmatrix} \times \begin{bmatrix} i_1 \\ i_2 \\ \vdots \\ i_n \end{bmatrix} \tag{5.8}$$

In equation 5.8, v_k and i_k, $(1 \leq k \leq n)$ each represents the average electric potential and normal current intensity of the corresponding triangle on the boundary mesh of the electrodes. Assuming an electrode consists of the triangles with subscript from 1 to p, these triangle share the same electric potential (the resistivity of the metal electrode is negligible compared the resistivity of the cochlear tissue):

$$v_1 = v_2 = v_3 = \cdots = v_p = V_i \tag{5.9}$$

where V_i is the electric potential measured from the electrolyte side of the electrode-electrolyte interface, such as V_1 and V_2 in figure 5.4 (d).

From equation 5.9 we have $p-1$ new equations:

$$\begin{aligned} v_1 - v_2 &= 0 \\ v_2 - v_3 &= 0 \\ &\cdots \\ v_{p-1} - v_p &= 0 \end{aligned} \tag{5.10}$$

which can be expanded as:

$$\begin{bmatrix} l_{11}-l_{21} & l_{12}-l_{22} & l_{13}-l_{23} & \dots & l_{1n}-l_{2n} \\ l_{21}-l_{31} & l_{22}-l_{32} & l_{23}-l_{33} & \dots & l_{2n}-l_{3n} \\ \vdots & \vdots & \vdots & \ddots & \vdots \\ l_{(p-1)1}-l_{p1} & l_{(p-1)2}-l_{p2} & l_{(p-1)3}-l_{p3} & \dots & l_{(p-1)n}-l_{pn} \end{bmatrix} \times \begin{bmatrix} i_1 \\ i_2 \\ \vdots \\ i_n \end{bmatrix} = \begin{bmatrix} 0 \\ 0 \\ \vdots \\ 0 \end{bmatrix} \tag{5.11}$$

If this electrode is an stimulating electrode, the sum of the normal current of all its triangles equals to the intensity of the stimulation current I:

$$\sum_{k=1}^{p} i_k = I \tag{5.12}$$

Otherwise, if this electrode is one of the non-stimulating electrodes, according to equation 5.6, $V_{CPE}(t=0) = 0$, meaning that the voltage over the CPEs is 0 when the stimulation pulse occurs. Similarly, it can be computed that the voltage over the blocking capacitors V_C also equals to 0 when $t = 0$. Hence in figure 5.4 (d), $V_1 = V_1' = V_S$ and $V_2 = V_2' = V_{GND}$ at time $t = 0$. Since V_{GND} is the voltage of the reference and is shared by all the non-stimulating electrodes, these electrodes can be considered together as a single virtual electrode for current distribution computation at $t = 0$.

Because in the 3D model, the normal current intensity on all the electrodes sums up to 0, we have:

$$\sum_{k=1}^{p} i_k = -I \tag{5.13}$$

here p is the number of triangles of the bit virtual electrode, which consists of all the non-stimulating electrodes in the model.

In the actual cochlear implant, the reference electrode is used as the reference

point of the electric potential, whereas in the parametric cochlear model, Open MEEG considers the average potential of the outermost interface to be zero through the deflation process of the geometry matrix.

Finally, the initial current distribution when $t = 0$ was solved from the electric potential constraints (equation set 5.11 for the stimulating and non-stimulating electrodes) and the current intensity constraints (equation 5.12 or 5.13).

5.4.2 Solving ill-posed problem using Tikhonov regularization

The new equation set for solving the initial current distribution was acquired by combining equation 5.11, 5.12 and 5.13. It was noted as:

$$\mathbf{Mx} = \mathbf{b} \tag{5.14}$$

where $\mathbf{x}$ is the vector of current intensities to be solved while $\mathbf{M}$ and $\mathbf{b}$ contain the information of the mixed boundary condition .

Based on equation 5.14, the current distribution of common ground or multi-mode grounding stimulation in the parametric cochlear model has been computed. The result is plotted in figure 5.5.

The the strong ripple of current distribution in figure 5.5 suggests the equation 5.14 is an ill-posed problem, which means the solution of the equation changes greatly by small perturbations (usually the truncations during during the calculation) on the coefficients.

To obtain the correct solution, the Tikhonov regularization method was applied to the problem 5.14. It replaces the original problem by another minimization problem:

$$\hat{\mathbf{x}} = \arg\min\{||\mathbf{M}\hat{\mathbf{x}} - \mathbf{b}||_2^2 + \lambda||\mathbf{L}\hat{\mathbf{x}}||_2^2\} \tag{5.15}$$

where the matrix $\mathbf{L} \in \mathbb{R}^{k\times n}$, $k \leq n$ is the regularization matrix. λ is the regularization coefficient. $\hat{\mathbf{x}} \in \mathbb{R}^n$ is the estimation of the solution $\mathbf{X}$ of the original problem in 5.14.

Two different regularization matrices have been tested in the following experiment. The first one was the identity matrix $\mathbf{I}$, which minimized the l^2-norm of $\hat{\mathbf{x}}$. The other one was the discretized first order derivative operator matrix, which minimized the differences between adjacent elements in $\hat{\mathbf{x}}$. The regularization coefficient λ controls the balance between the error to the original solution $||\mathbf{M}\hat{\mathbf{x}} - \mathbf{b}||_2^2$

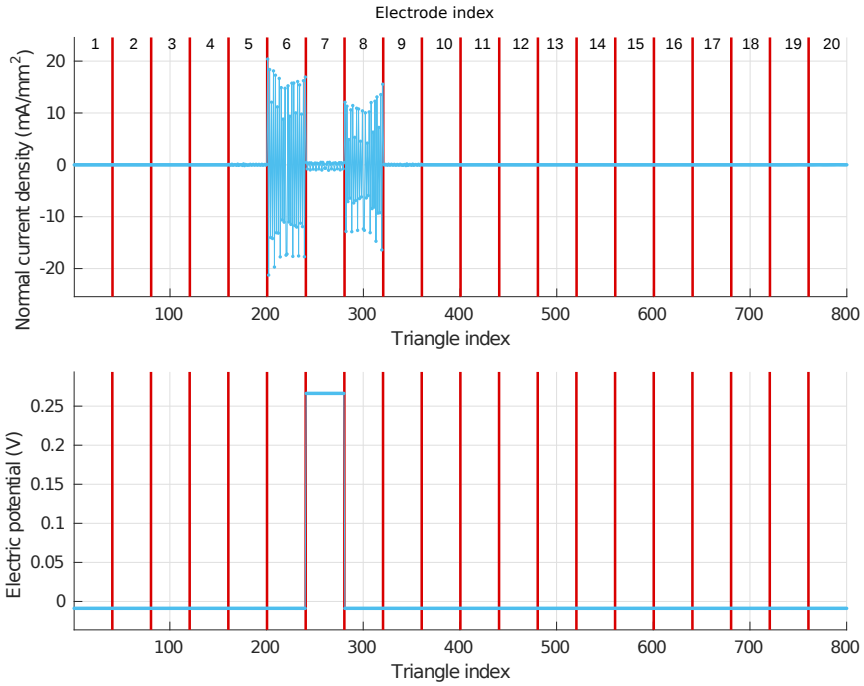

Figure 5.5: Initial solution of the normal current and electric potential distribution of the common ground stimulation. X-axis gives the indices of the mesh triangles of the electrodes. Each electrode consists of 40 triangles. The triangles which belong to different electrodes are separated by the vertical line. The 7th electrode (from base to apex) was the stimulating electrode.

and the regularization term $||\mathbf{L}\hat{\mathbf{x}}||_2^2$.

The values of λ for each regularization matrix were chosen from the L-curves plotted in figure 5.6. The L-curve plotted $||\mathbf{M}\hat{\mathbf{x}} - \mathbf{b}||_2^2$ against $||\mathbf{L}\hat{\mathbf{x}}||_2^2$ under a logarithmic coordinate system. The curve itself is generated by increasing or decreasing the value of λ (Hansen, 1999; Calvetti et al., 2000). Usually, the λ value at the left bottom corner of the curve is considered to reach the balance between the two terms. Here another constraint was added to the choice of λ based on the electrical characteristic of the stimulation, which was that all the triangles from a single physical electrode shared the same polarity of the normal current, since it was obvious that the same electrode cannot be stimulating and grounding at the same time. The final λ values were 1.5 for the identity matrix and 0.5 for the derivative operator matrix.

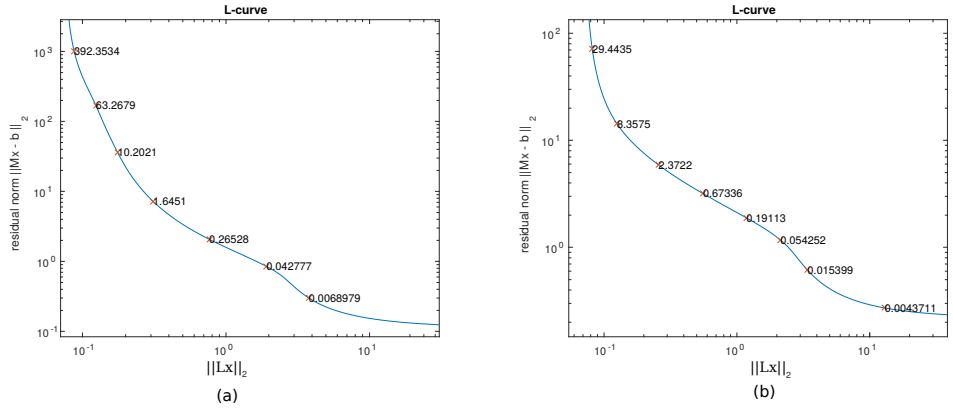

Figure 5.6: The L-curves of tikhonov regularization using different regularization matrices: (a) identity matrix; (b) discretized first order derivative operator matrix.

The initial current distributions of common ground stimulation using the 7th electrode were solved by Tikhonov regularization and plotted in figure 5.7 (identity matrix) and 5.8 (derivative operator matrix). In the two figures, the upper plots are the computed normal current density on the triangles representing the metal electrodes in the model. The lower plots are the corresponding electric potential on the same triangles, which was computed by multiplying the original leadfield matrix with the normal current density plotted above. The electric potential is an intuitive indication of the error introduced by Tikhonov regularization. In the ideal situation, it should be a constant on the triangles from the same electrode, as shown in figure 5.5.

Both results in figure 5.7 and 5.8 give reasonable normal current distributions at the cost of errors in the electric potential on the surface of the electrodes. The cross talk between electrodes caused by the rotational shape of the cochlea was observed in both results on electrode 20.

When setting the Neumann boundary condition for the parametric model in chapter 3, an assumption was made that the normal current density was a constant on each single electrode. Here in the results, a non-uniform normal current distribution on the triangles from the same electrode is observed, indicating that the normal current density on the electrode was affected by the cochlear geometry.

Compared with using the identity matrix as the regularization matrix, the major drawback of using the derivative operator matrix was the current intensities between adjacent triangles were averaged, even when these triangles belonged to

different electrodes and have several millimeters' physical distance. Therefore the identity matrix was chosen for the following simulations. However, the derivative operator matrix could be replaced by a gradient operator matrix generated based on the actual triangle tessellation of the electrode array, in order to minimize the normal current density difference between physically connected triangles, which may provide better results than the identity matrix.

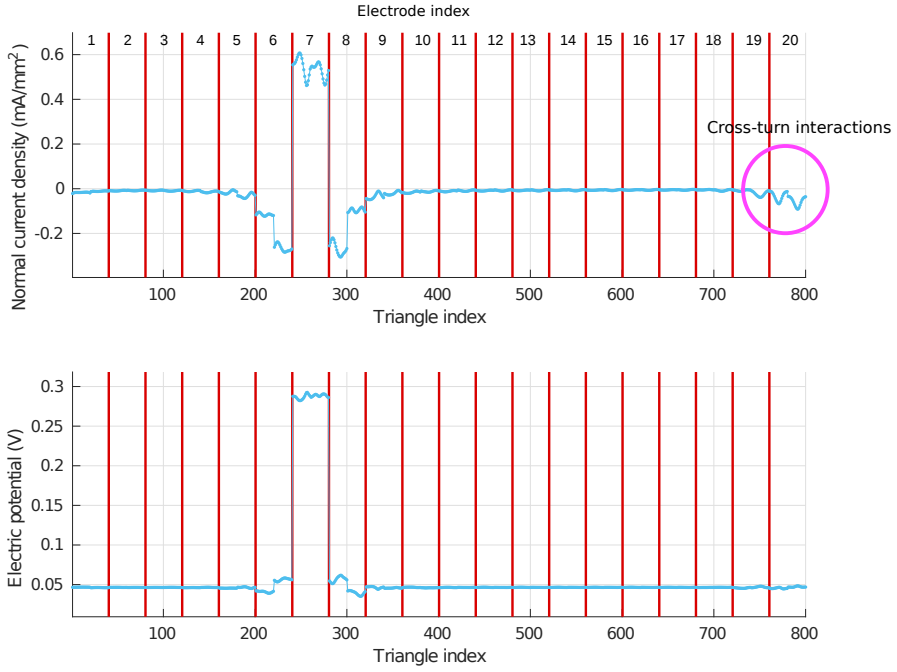

Figure 5.7: Initial solution of the normal current and electric potential distribution of the common ground stimulation, solved by Tikhonov regularization with identity matrix as the regularization matrix.

5.5 Equivalent circuit model of the CPE

The previous sections acquired the initial solution of the common ground stimulation by exploiting the fact that the voltage over the blocking capacitors and constant phase elements are zero at $t = 0$. In the following chapters, the current distributions at time $t > 0$ will be computed using the circuit simulation algorithms.

Although the voltage response of a CPE to a current step can be computed through the inverse Laplace transform, it is still necessary to acquire the voltage

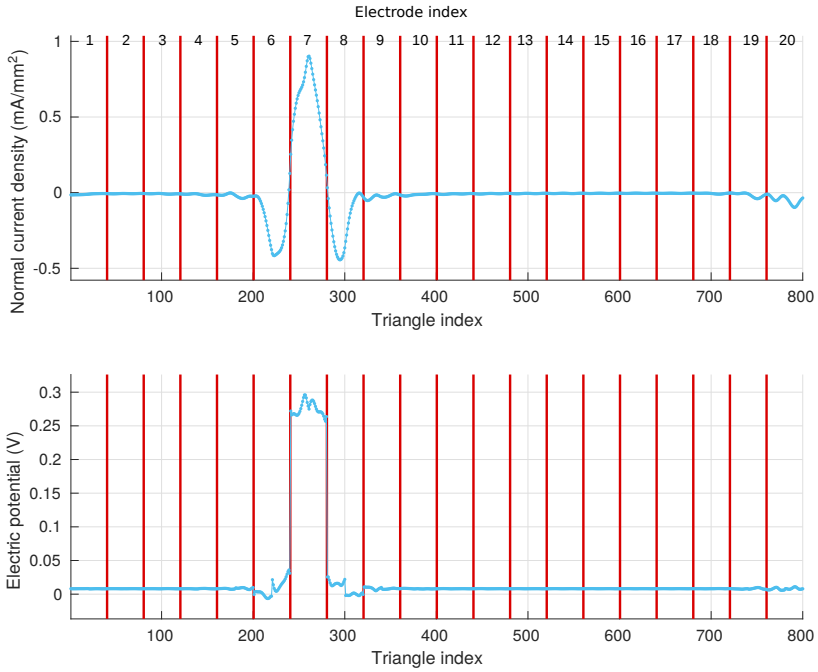

Figure 5.8: Initial solution of the normal current and electric potential distribution of the common ground stimulation, solved by Tikhonov regularization with discretized first order derivative operator matrix as the regularization matrix.

output of CPE with arbitrary current input in order to integrate such components into the simulation. Here a method of creating equivalent circuit model of the CPE developed by Valsa et al. (2011) has been adopted. This method replaced the original CPE with a circuit network consists only capacitors and resistors. Hence the common circuit simulation algorithms can be applied on it.

Valsa et al. (2011) proposed two basic schemes of the circuit network, the first one was a parallel model while the second was a series model. Here the series model was chosen since it was easier to simulate using current intensity as the input. Figure 5.9 gives the electrical scheme of the equivalent circuit model. It consists of m stages of resistors and capacitors connected in parallel and simulate the response CPE within a given frequency range. This model was a simplification of the original model proposed by Machado et al. (2001). The R_s and C_s were added as correction factors to replace part of the stages in the original model, since they have little contribution to the total impedance in the frequency range specified by the user.

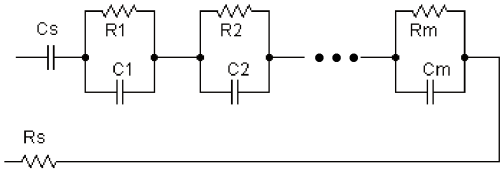

Figure 5.9: The electrical scheme of the equivalent circuit model of CPE (Valsa et al., 2011).

The values of the resistors and capacitors in the circuit was determined by:

$$R_k = R_1 a^{(k-1)}, \quad C_k = C_1 b^{k-1}, \quad k = 1, 2, ...m \tag{5.16}$$

and

$$R_s = R_1 \frac{a^m}{1-a}, \quad C_s = C_1 \frac{1-b}{b}. \tag{5.17}$$

where a and b depended on the phase shift β and the minimal ripple in the approximated phase response, while R_1 and C_1 were computed from the amplitude term Q in equation 5.3. The detailed computation process can be found in Valsa et al. (2011).

For the EVO electrode array, the coefficients of the CPE attached to its electrodes were: $Q = 4.68 \times 10^{-6}$ and $\beta = 0.74$ according to the in-vitro measurements taken in saline (presented in chapter 6). The duration of the stimulation pulses ranged from $30\mu s$ to $100\mu s$. Hence the valid frequency range of the equivalent circuit was set from $50Hz$ to $3MHz$ in order to cover at least the first 100 harmonics of the stimulation pulse. The ripple of the constant phase response of the circuit was set to $1°$.

Based on the information above, a sixth order equivalent circuit model has been designed with $a = 0.187$ and $b = 0.639$. Other parameters of the model are listed in table 5.1.

Table 5.1: Parameters of the equivalent circuit model of CPE

R_s	R_1	R_2	R_3	R_4	R_5	R_6
0.1175Ω	1140.1Ω	237.4Ω	49.44Ω	10.29Ω	2.144Ω	0.4465Ω
C_s	C_1	C_2	C_3	C_4	C_5	C_6
$1.29\mu F$	$1.75\mu F$	$1.01\mu F$	$592.4nF$	$335.6nF$	$193.4nF$	$111.4nF$

The frequency response of the equivalent circuit compared with the ideal constant phase element is plotted in figure 5.10. The plot shows that between $30Hz$ and $3MHz$, the equivalent circuit has the same amplitude response and nearly the same phase response compared with the ideal CPE.

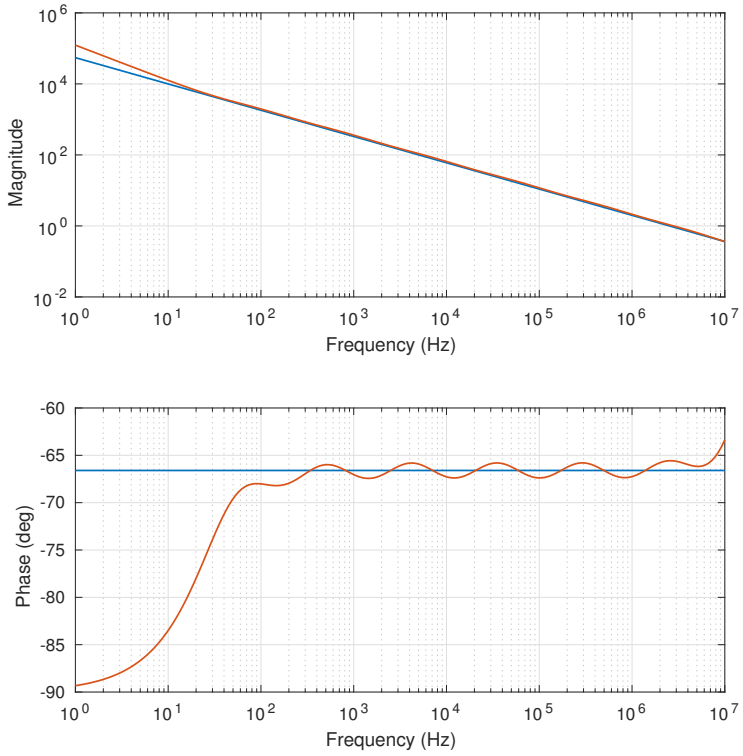

Figure 5.10: Frequency response of the equivalent circuit (red line) compared with the ideal CPE (blue line).

For the reference electrode, the parameter β of its CPE was the same as the intracochlear electrodes, while the parameter Q was decided by:

$$Q_r = Q_s \frac{S_r}{S_s} \tag{5.18}$$

where S_r and S_s are the surface areas, Q_r and Q_s are the parameter Qs of the reference and intracochlear electrodes respectively.

5.6 Time domain circuit simulation algorithms

The Euler backward integration and trapezoidal integration algorithms have been implemented to simulate the time domain electric potential waveforms, which were also used by the circuit simulation software SPICE (Nichols et al., 1994; McCalla, 2012). In the simulation algorithms, each capacitor in the model was replaced by a current source and a resistor connected in parallel. Figure 5.11 gives an example of the stage k ($1 \leq k \leq m$) in the CPE model, in which (a) is the original circuit while (b) is the simulated circuit with C_k replaced by R_{ck} and I_{ck}. The values of resistor R_{ck} and current source I_{ck} were decided by:

$$R_{ck} = \frac{\Delta t}{C_k}, \quad I_{ck} = \frac{V_0 C_k}{\Delta t} \tag{5.19}$$

in the Euler backward integration algorithm and

$$R_{ck} = \frac{\Delta t}{2C_k}, \quad I_{ck} = \frac{2V_0 C_k}{\Delta t} + I_0 \tag{5.20}$$

in the trapezoidal integration algorithm.

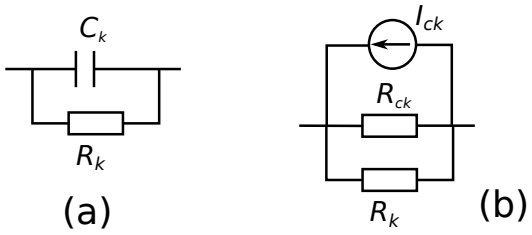

Figure 5.11: The equivalent circuit of a capacitor in the circuit simulation algorithms: (a) a stage of the original CPE model; (b) equivalent circuit of (a) during simulation.

In equation 5.19 and 5.20, Δt stands for the minimal time step of the simulation. V_0 and I_0 represent the voltage and current on the capacitor at the end of the previous time step respectively. Generally, the Euler backward integration was used to simulate the first time step from $t = 0$ to $t = \Delta t$, since I_0 was unknown at first. $V_0 = 0$ at $t = 0$ according to the discussion in section 5.4.1. The trapezoidal integration was used to simulate the following time steps.

To validate the circuit simulation results, the simulated voltage response on CEP to a current step signal starting at $t = 0$ is plotted in figure 5.12. Δt was set at $1ns$ and the amplitude of the current step was $1mA$. The parameters of the

equivalent circuit was taken from table 5.1. The voltage waveform from 0 to 100μs was simulated.

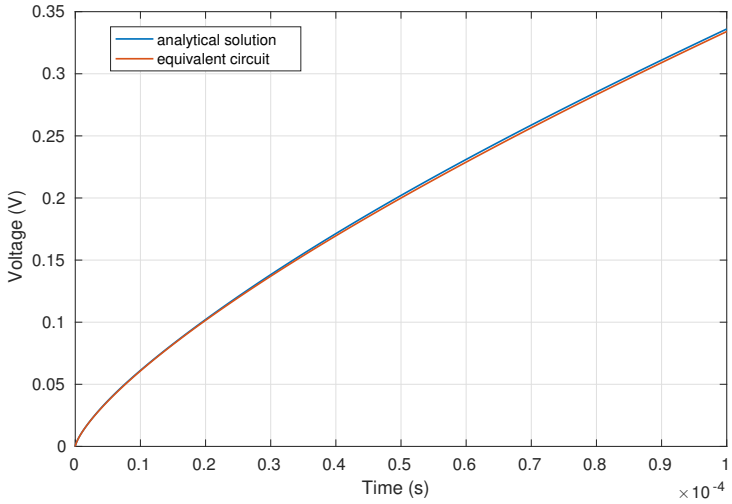

Figure 5.12: Voltage response on CPE to a current step starting at $t = 0$.

In the plot, the blue line is the analytical solution while the red line is the simulation result of the equivalent circuit. The simulation result had 0.6% error compared to the analytical solution at the end of simulation, which was due to the approximation error of the equivalent circuit. In the following simulations, the maximum duration of the stimulation pulses was 60μs. Therefore, the accuracy of circuit simulation can be considered to meet the requirements of simulating the cochlear implant stimulations. Simulation results of the blocking capacitor showed higher accuracy than the CPE simulation since the capacitors can be simulated directly without approximations.

5.7 The iteration process of electric potential simulation

The output of OpenMEEG, leadfield matrix, is equivalent to a resistor network connecting specified current sources and measure points within the geometry. Therefore the circuit simulation algorithms can be applied on it as well. The time domain potential simulation was carried out iteratively, a time length of Δt was simulated in each iteration.

The time domain simulation was further divided into 2 types according to the types of the stimulation pulse. For an active stimulation phase, where one of the intracochlear electrode is sending out a constant stimulation current while the others are passively discharging, the steps of incorporating CPE and blocking capacitors with the leadfield matrix are given below:

1. **Initialization**

   Solve the current distribution $\mathbf{I}_0$ at $t = 0$ according to the steps in section 5.4.1.

2. **Simulate CPEs and blocking capacitors**

   Compute the voltages (noted as a vector $\mathbf{V}$) on all the CPEs and blocking capacitors, based on $\mathbf{V}$ and $\mathbf{I}$ of the previous iteration.

3. **Update current distribution**

   A new matrix is generated from the original leadfield matrix. The rows corresponding to the grounding electrodes were directly copied from the leadfield matrix to the new matrix. For the rows corresponding to the stimulating electrode, equation 5.11 and 5.12 were used in the new matrix to make the sum of the normal current on these rows equals to the stimulation current. The new matrix is then inverted and multiplied by the $\mathbf{V}$ computed in the previous step to get the updated current distribution $\mathbf{I}$. The actual inversion operation here is replaced by the tikhonov regularization again as the matrix is ill-posed in most cases.

4. **Finish iteration**

   Record $\mathbf{V}$ and $\mathbf{I}$, go back to step 2 for the next iteration.

For a passive discharging phase, where all the intracochlear electrodes are internally connected to the ground to passively discharge the blocking capacitors, the steps above are changed as follows:

1. **Initialization**

   The final voltage distribution $\mathbf{V}$ of the preceding active phase is used as the initial voltage distribution $\mathbf{V}_0$. The initial $\mathbf{I_0}$ is unknown.

2. **Simulate CPEs and blocking capacitors**

   Compute the voltages (noted as a vector $\mathbf{V}$) on all the CPEs and blocking capacitors, based on $\mathbf{V}$ and $\mathbf{I}$ of the previous iteration. For the first iteration, only the Euler integration method can be applied since $\mathbf{I}_0$ is unknown.

3. **Update current distribution**

   Directly compute the current distribution $\mathbf{I}$ from the voltage distribution $\mathbf{V}$ by inverting the leadfield matrix using tikhonov regularization.

4. **Finish iteration**

   Same as the step 4 above.

Figure 5.13 illustrates the coupling between the BEM model and the circuit model. The notations of the voltages and components are the same as in figure 5.1.

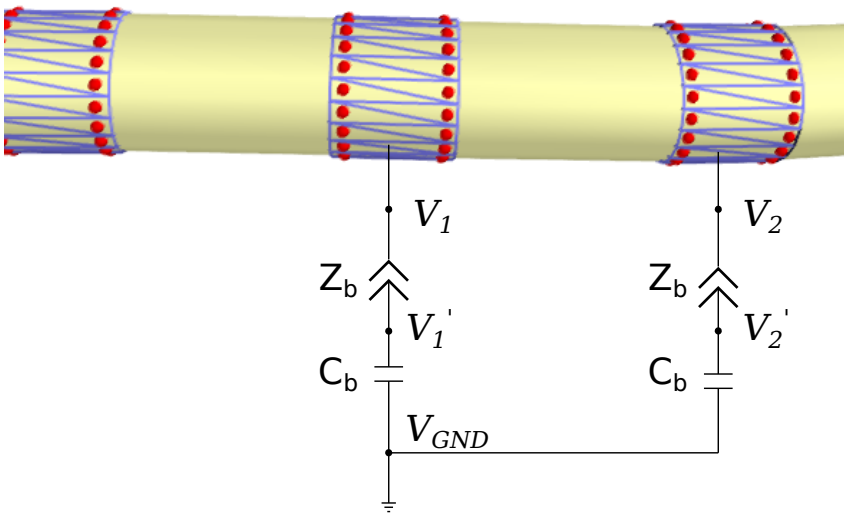

Figure 5.13: Coupling the BEM model with the circuit model.

In the BEM model, an electrode consists of multiple triangles and potential measure points, the normal current density and electric potential is computed for each triangle and potential measure point respectively. Whereas in the circuit model, one electrode only has one electric potential and current intensity. Hence the same potential and normal current density values were applied on all the triangles from the same electrode when transferring data from the circuit model to the BEM model, and the average potential and the sum of normal current were transferred

back. Despite the simplicity in terms of implementation, this method reduced the resolution of electric and normal current density on a single electrode.

5.8 Results

5.8.1 Spatial current distribution

The surface mesh model was the same average shape based cochlear model as in chapter 3. The common ground and muti-mode grounding stimulation modes were simulated. The simulated current distribution on the non-stimulating electrodes at $t = 0$ are plotted in figure 5.14.

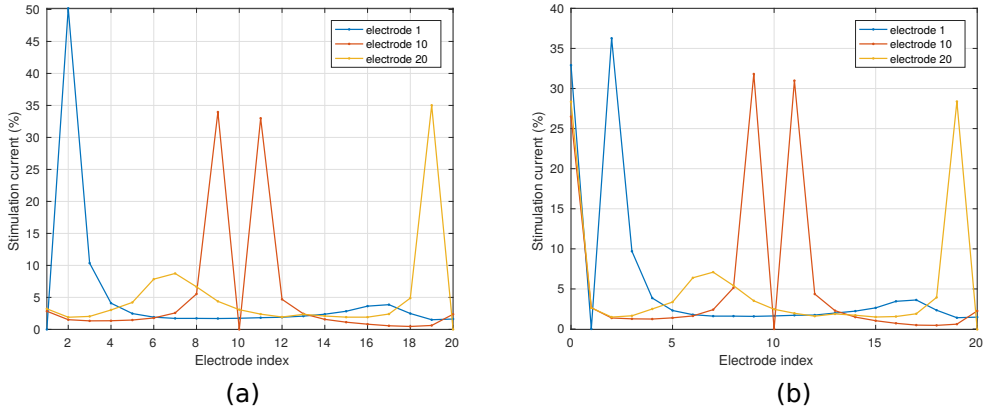

Figure 5.14: Current distribution on the non-stimulating electrodes of: (a) common ground stimulation, (b) multi-mode grounding stimulation. Each plot contains 3 stimulation positions. Electrode 0 represents the reference electrode in figure (b). The current values on the stimulating electrodes should be -100% but are set to 0 to enlarge the rest parts of the plot.

5.8.2 Stimulation waveforms

The stimulation waveform been simulated was biphasic with a passive discharging phase. The duration of the stimulation phase was $60\mu s$. The length of simulated passive discharging phase was $300\mu s$. The simulation time step Δt was $1ns$.

Figure 5.15 gives the simulated electric potential waveform on the surface of the stimulating electrode (blue) and the electrode next to the stimulating one (red). The electric potential on the stimulating electrode is the sum of voltages on the

blocking capacitor and the current source, while the potential on a non-stimulating electrode directly equals to the voltage on its corresponding blocking capacitor.

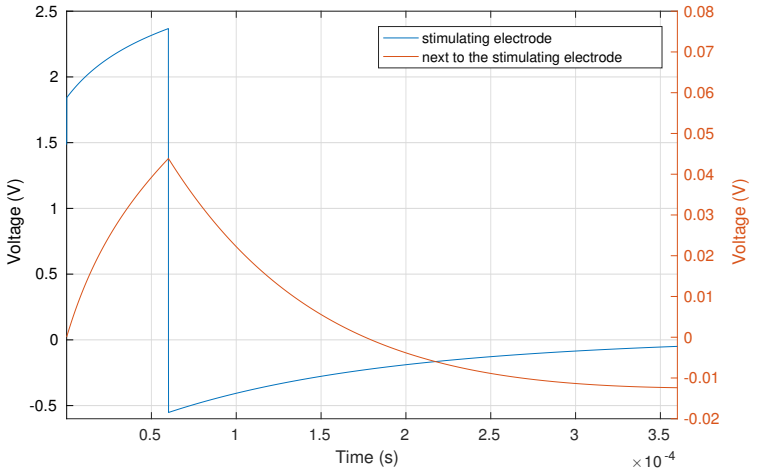

Figure 5.15: Simulated potential waveform on the stimulating electrode (blue) and the electrode next to the stimulating one (red). The first $60\mu s$ of the simulation is the stimulation phase of the pulse. The following $300\mu s$ is the passive discharging phase.

5.9 Conclusions

This chapter proposed a method of incorporating the resistive cochlear model with the electrode-electrolyte interface model and the blocking capacitors of the cochlear implant. The electrode-electrolyte interface model was represented by constant phase elements, and was further approximated by the equivalent circuit model of capacitors and resistors. The electric potential changes in time, which were caused by the capacitive components in the model, were simulated by the circuit simulation algorithms. After the incorporation, the model was able to simulate multi-mode grounding and common ground stimulation modes and give more realistic predictions of the time domain waveforms.

Chapter 6

In vitro measurements of the spatial potential and current distribution of cochlear stimulations

Contents

In order to characterize the spatial potential distribution of the multi-mode grounding stimulation, and validate the simulation results of the new BEM model, in vitro current distribution and electric potential measurements have been taken on the EVO electrode array with the XP implant. 3 different stimulation modes: monopolar, common ground (CG) and multi-mode grounding (MMG) were tested. 2 different container shapes were used: a water tank and a narrow tube shaped container made with 3D printing. Results showed that the potential distributions of the common ground and the multi-mode grounding stimulation are highly dependent on the container size. The measured waveforms were used to calibrate the parameters of the electrode tissue interface model, improving the precision of the time domain simulation.

The measurements were carried out in two consecutive steps: 1) measurement of the current distribution on the grounding electrodes (for CG and MMG only); 2) measurement of the spatial potential distribution near the electrode array.

6.1 Current distribution measurement

6.1.1 Method

Finding out the current distribution on the grounding electrodes is the first step of characterizing the CG and MMG modes. Figure 6.1 gives the internal circuit of the implant and the equivalent circuit of the electrode-electrolyte interface. The implant is configured as the MMG mode. Only 3 stimulation channels: a, b and c are drawn for simplicity's sake, in which channel b is stimulating, while a and c are the grounding channels. The stimulation current is generated by the internal current source I_s. The difference between a grounding intracochler electrode and the reference electrode in MMG mode in terms of electrical circuit is that the intracochlear electrode is in series with a blocking capacitor C_b. As discussed in chapter 5, the electrode-electrolyte interface is simplified as constant phase elements (CPE). After CPE, electrodes are interconnected through the electrolyte.

The simplest way to measure the current intensity on each electrode is inserting a sampling resistor R_s between the blocking capacitor and the electrode. The resistance of the sampling resistor should be relatively low (several Ohms) in order not to introduce significant change to the global current distribution. When the voltage across the resistor V_s is recorded, the current intensity I can be computed

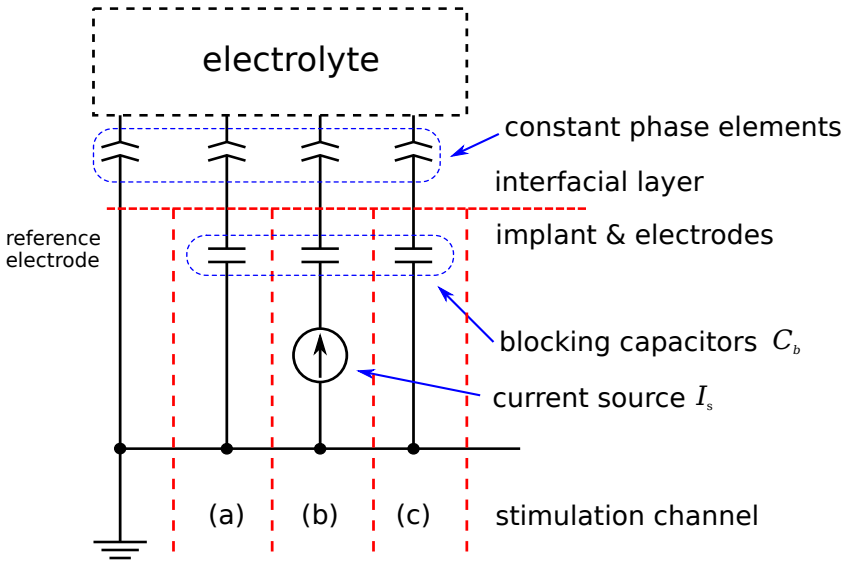

Figure 6.1: Internal circuit of the implant and the equivalent circuit of the electrode array in the electrolyte.

using Ohm's law: $I = \frac{V_s}{R_s}$. For this measurement, the problem of adopting sampling resistors is that the current intensity on each electrode is already quite low ($1mA$ for the stimulating electrode, several hundred micro ampere or less for the grounding electrodes), therefore the voltage across the sampling resistors would be difficult to measure.

As an alternative, the measurements can be taken directly by exploiting the blocking capacitors, without introducing any extra components into the circuit. Voltage V_c across a blocking capacitor is linearly related to the total charge Q in it: $V_c = \frac{Q}{C_b}$, where C_b is the size of the capacitor. The current intensity can be computed by:

$$I = C_b \frac{dV_c}{dt}$$

Because the capacitance of C_b is small ($220nF$), a small current can cause significant change in V_c. For example, a $10nC$ charge corresponds to $45mV$ change in the voltage over the blocking capacitor, which can be easily captured and recorded by standard oscilloscopes.

The reference electrode has no blocking capacitor. But the current through it can be computed indirectly when the measurements have been taken on all the

intracochlear electrodes:

$$I_{ref} = I_s - \sum_{k \in \mathbf{K}} I_k$$

where I_s is the stimulation current intensity, $\mathbf{K}$ is the set of grounding intracochlear electrodes and I_{ref} is the current through the reference electrode.

6.1.2 Hardware implementation

Analog multiplexer

The measurements were taken on a XP implant with EVO electrode array (Oticon Medical, Vallauris, France), which has 20 stimulation channels. When using either one for stimulation, measurements must be taken on all the 20 electrodes in order to have a complete map of current distribution. Due to the number of measurements needed, it cannot be done manually. So an in-house analog multiplexer has been designed to automatically switch the measure point between electrodes.

The schematic of the analog multiplexer is shown in figure 6.2. It consists of three 74HC4067 multiplexer chips (Texas Instruments, Dallas, Texas, USA). Each 74HC4067 can create a electrical connection between one of its 16 input channels and the common output to conduct analog signal, while blocking the signals from the rest of the input channels. Three chips can provide 48 input channels to the common output, enough to cover the positions of measurements needed to be taken on the EVO electrode. The resistance between the selected input and the output R_{on} is 60Ω, which is negligible compared with the input resistance of the measuring devices (several MΩ) at the output side. Each input channel has $5pF$ input capacitance, which is also negligible compared with the size of the blocking capacitor ($220nF$).

The index of the channel selected is indicated by the 4-bit *channel address* signal. Another *chip selection* signal can globally enable/disable the chip to avoid multiple selection when several chips are working in parallel. The channel address and chip selection signals are given by a microcontroller (Arduino UNO, Italy), which receives commands from PC through USB connection.

The inputs of the multiplexer are connected between the electrode and the blocking capacitor of each stimulation channel, as shown in figure 6.6. For non-stimulating channels, the voltage over the blocking capacitor is measured, while for the stimulating channel, the measured voltage is the voltage over the blocking capacitor plus the current source.

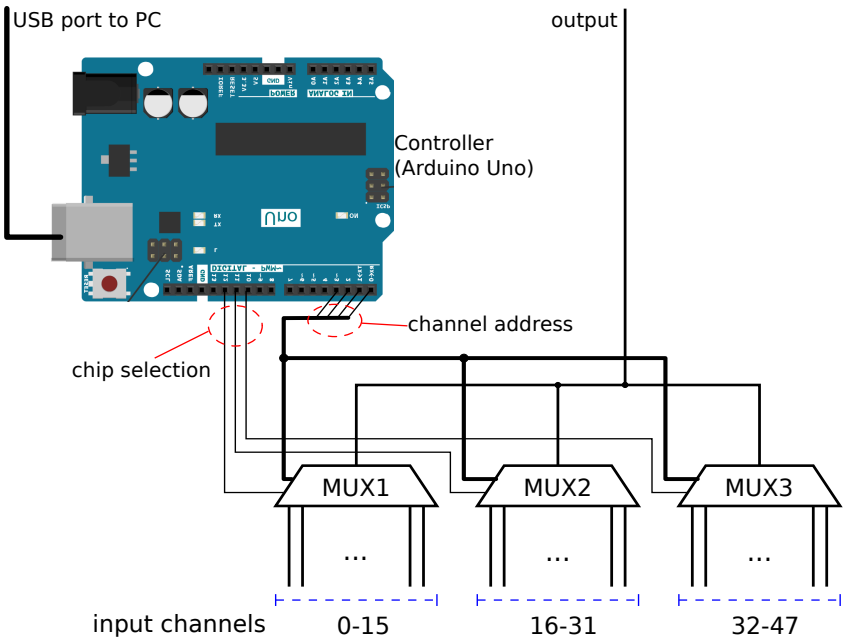

Figure 6.2: Schematic of the analog multiplexer

Low-pass filter, amplifier and recording devices

Preliminary recordings of the voltage on the blocking capacitor revealed that although the signal is detectable, it is heavily contaminated by the noise from the wireless communications between the implant and the speech processor. As shown by figure 6.3(a), the amplitude of the noise is much higher than the stimulus. Frequency analysis (figure 6.3(b)) showed that the noise is a modulated 7MHz signal. Knowing that the duration of the stimulation pulse is more that 10μs, a low-pass filter can effectively separate the noise and the target signal. Although applying digital filtering after recording the signal has better performance and is easier to implement than building an analog filter, a basic analog filter is still required because when the stimulation pulse is buried under noise, it cannot properly trigger the oscilloscope for recording. Besides, a higher gain in the oscilloscope can be chosen while recording a less noisy signal, hence the amplitude resolution of the recordings is improved.

In order to reduce the distortion of the recorded stimulation pulse, the -3dB cut-off frequency of the analog filter was set at 1MHz. The filter was a 4-order Butterworth type. Its frequency response is given in figure 6.4(b). According to the graph, the attenuation it provides at 7MHz is 60dB. The circuit of the analog

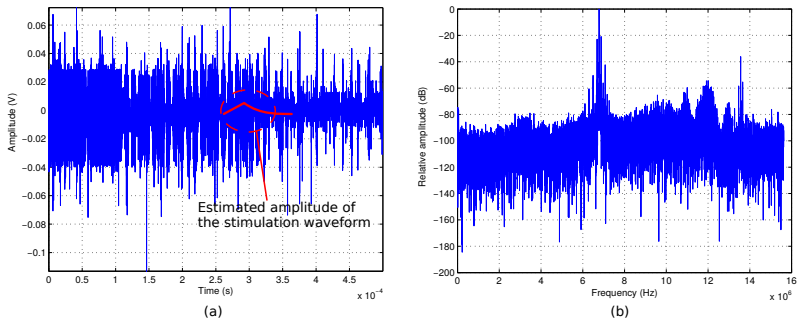

Figure 6.3: Waveform (a) and spectrum (b) of the original recordings of the voltage over the blocking capacitor

filter was designed using the WEBENCH Designer tool (Texas Instruments, Dallas, Texas, USA) and implemented using two operational amplifiers, as shown by the schematic in 6.4(a). A buffer amplifier was inserted between the output of the multiplexer and the input of the filter isolate the two parts of circuit. Finally, another amplifier with $\times 10$ gain was added to the output of the filter to provide isolation towards the oscilloscope and enlarge the signal amplitude. In order to keep the electrical isolation from the stimulation part, the whole circuit is powered separately by battery groups. A picture of the whole in-house circuit board is given in figure 6.5.

The output of the analog circuits recorded by a PicoScope 2205A digital oscilloscope through a TA045 differential probe (Pico Technology Ltd., Cambridgeshire, United Kingdom). The differential probe has 500kΩ input resistance and 7pF input capacitance. It also has a fixed 1/10 attenuation, which was compensated by the amplifier above. The oscilloscope discretized the signal with 12 bits amplitude resolution. The recorded signal was sent to PC through USB and stored as .mat file.

Figure 6.6 gives a global view on the connections between different parts in the current distribution measurement system. The synchronization between the stimulation part and the recording part is controlled by the PC. For each stimulus sent by the implant, the microcontroller generates another pulse that serves as an external trigger for the oscilloscope to mark the position of the stimulus, which is recorded as the red waveform in figure 6.4(c).

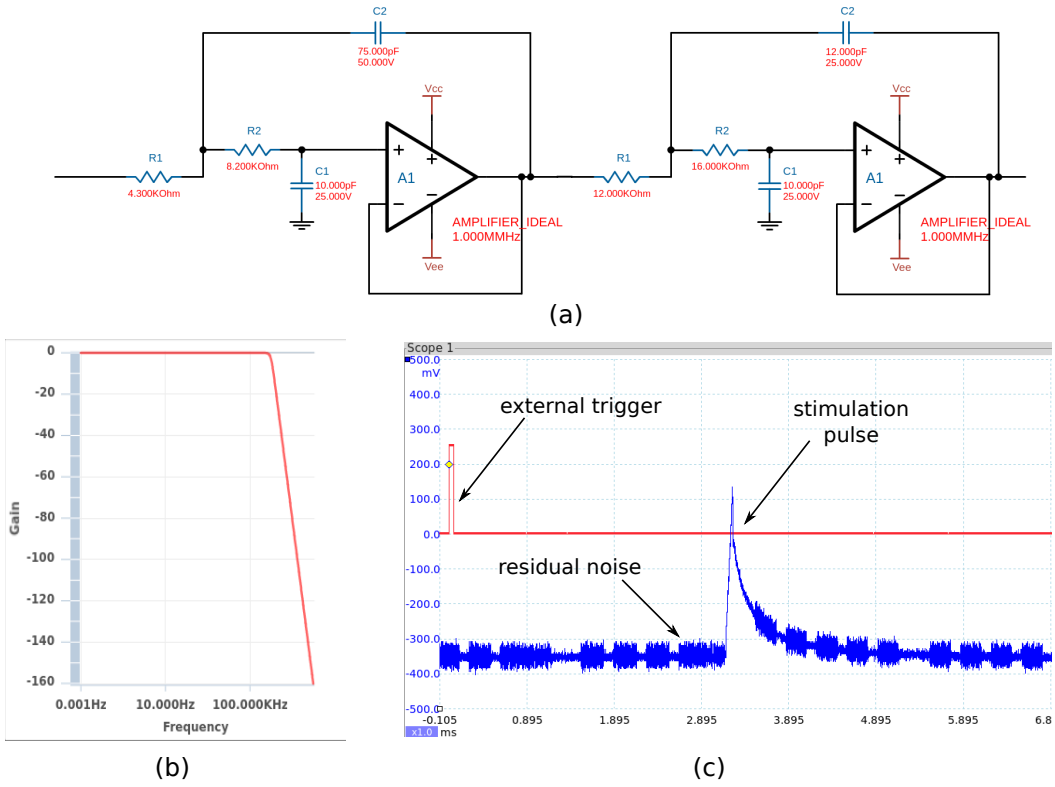

Figure 6.4: Schematic (a) and frequency response of the low-pass analog filter. The signal processed by the filter is shown in (c).

6.2 Computing current distribution

Figure 6.7 shows the raw voltage waveforms recorded by the measurement system. The pulse used by the experiment was biphasic with passive discharging pulse showed in figure 2.10(c). It can be divided into two parts in time: the stimulation part and the passive discharging part. Figure 6.7(a) is the waveform recorded on the stimulating electrode, hence in the stimulation part, it represents the voltage over the current source plus the blocking capacitor, while in the passive discharging part, it equals to the voltage over the blocking capacitor. Figure 6.7(b) is the waveform recorded on one of the grounding electrodes, which equals to the voltage on the blocking capacitor of the corresponding stimulation channel.

According to the calculations in section 6.1.1, the total charge through each electrode during the stimulation phase of the biphasic pulse can be estimated by measuring the maximum voltage of at the beginning of the passive discharging part

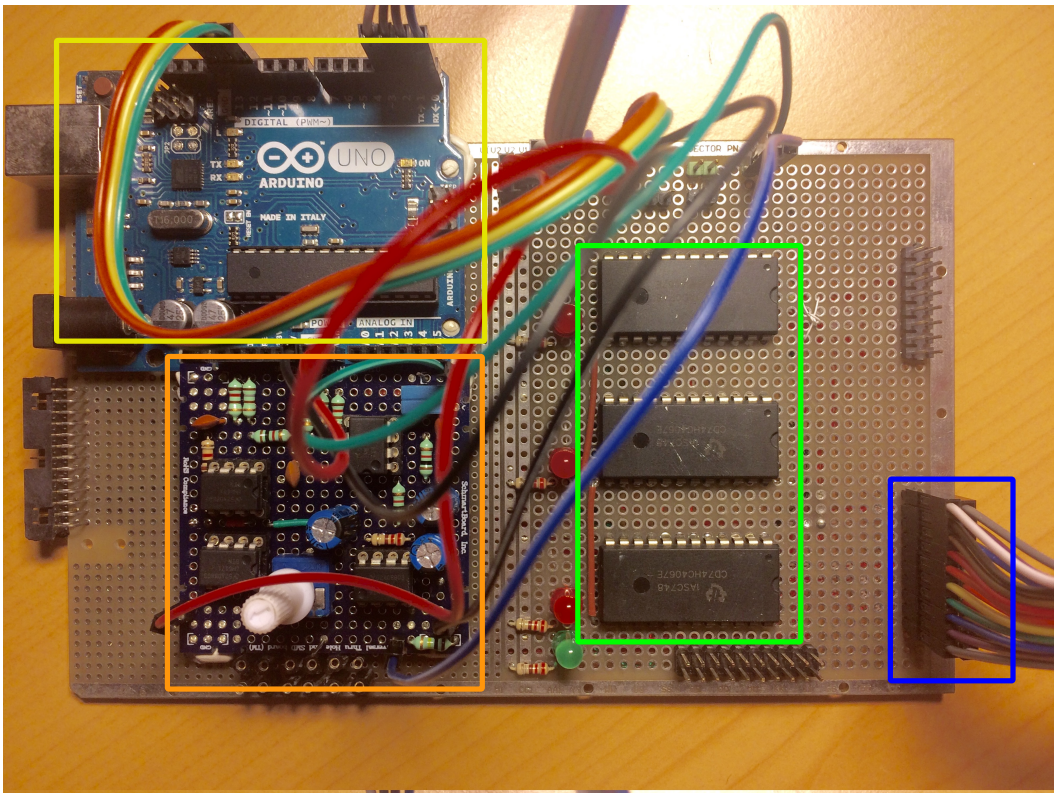

Figure 6.5: Picture of the in-house circuits. Including the connector to the blocking capacitors (blue box), multiplexer chips (green box), microcontroller (yellow box) and the analog filter/amplifier (orange box).

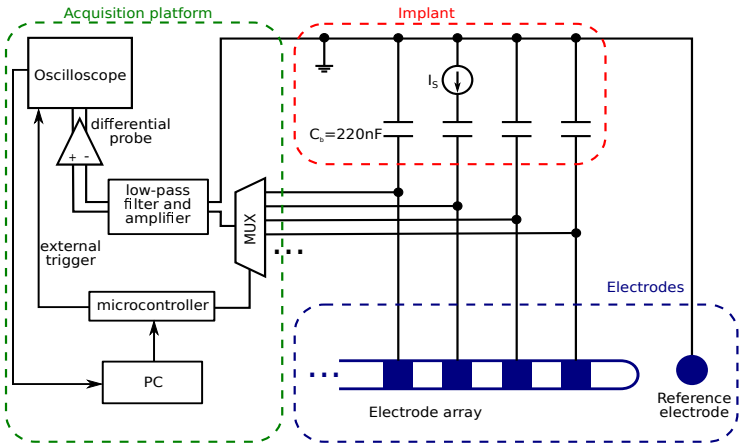

Figure 6.6: Experimental setup for the current distribution measurements

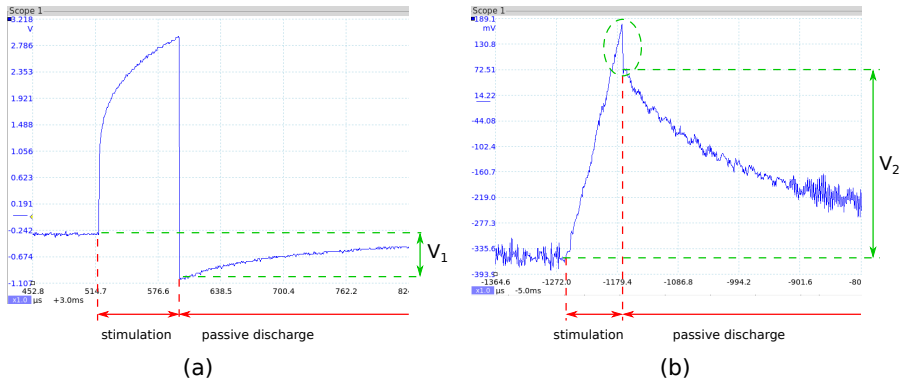

Figure 6.7: Raw voltage waveforms recorded by the system. (a) is recorded from the stimulating electrode while (b) is recorded from one of the grounding electrodes.

in both waveforms, represented as V_1 and V_2 in figure 6.7. The charge Q is computed by $Q = C_b V$ where $C_b = 220nF$ is the size of the blocking capacitor.

The stimulation part of figure 6.7(b) show the voltage over the blocking capacitor grows linearly during the stimulation pulse, indicating that the current through the grounding electrode is a constant value. Since the stimulation current also has a constant intensity, it means the current distribution was generally time-invariant and is not affected by the rising voltage on the blocking capacitor and double layer capacitor.

Ideally, when the stimulation pulse switched from active stimulation phase to passive discharging phase, the electric potential on the blocking capacitor should be continuous. However, a gap between the electric potential of the two parts was found in figure 6.7(b). This gap could be caused by the internal circuits of the cochlear implant when switching between phases. The height of the gap was around 15% of the total recording's amplitude. Since the loss of charge was most likely to happen inside the implant, the voltage V_2 measured from the beginning of the passive discharge phase was still used to estimate the amount of charge on the corresponding electrode.

6.3 Preliminary results on the water tank measurements

Tognola et al. (2007) measured the electric potential field of monopolar and bipolar stimulation in a $5.0 \times 7.5 \times 3.5cm^3$ water tank. In order to compare with these

results, the preliminary measurements of the current distribution of CG and MMG were taken under similar experimental conditions. As shown in figure 6.8(a), the electrode is placed horizontally at the center of the water tank. The size of the water tank is $7.5 \times 7.5 \times 5.5 cm^3$. The water tank is filled with saline. One measurement of the CG mode and two of the MMG mode have been taken. The distance between the electrode array and the reference electrode was $1cm$ in the first MMG measurement and increased to $5cm$ in the second measurement. The measurements were taken at room temperature. The intensity of the stimulation current was 60 current units ($1.33mA$). The pulse duration was $80\mu s$. Hence the total charge delivered in one pulse was $106.6nC$.

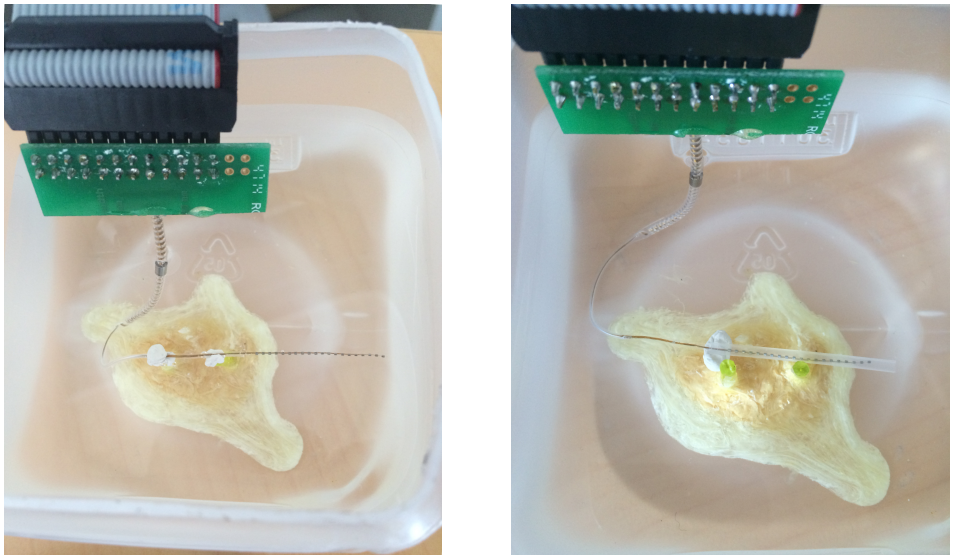

(a) (b)

Figure 6.8: Electrode placement in the water tank for current distribution measurements. Two electrode configurations were tested: (a) directly placed in the saline; (b) inside a non-conductive narrow tube with $1.5mm$ inner diameter.

Results of the water tank measurements are given in figure 6.9 and 6.10. Figure 6.9 plots the charge distribution on the intracochlear electrodes. For the 3 stimulation positions given in the figure, the current distributions of both MMG and CG modes are almost identical: the charge returned through each non-stimulating electrodes are similar to each other, except for the most apical and basal electrodes, where a 10% higher charge is observed.

This stimulation-position-independent current distribution is obviously different from the current distribution inside the cochlea during CG and MMG stimulations.

In the cochlea, the electrode array is surrounded by the perilymph in the scala tympani, which is surrounded by the temporal bone. Since the conductivity of the perilymph is higher than the temporal bone, the stimulation current has a trend to flow close to the electrode array, which increases the amount of charge that returns through the neighbors of the stimulating electrode. Whereas in the water tank, its large volume allows current to diffuse more isotropically, so a more even current distribution is observed.

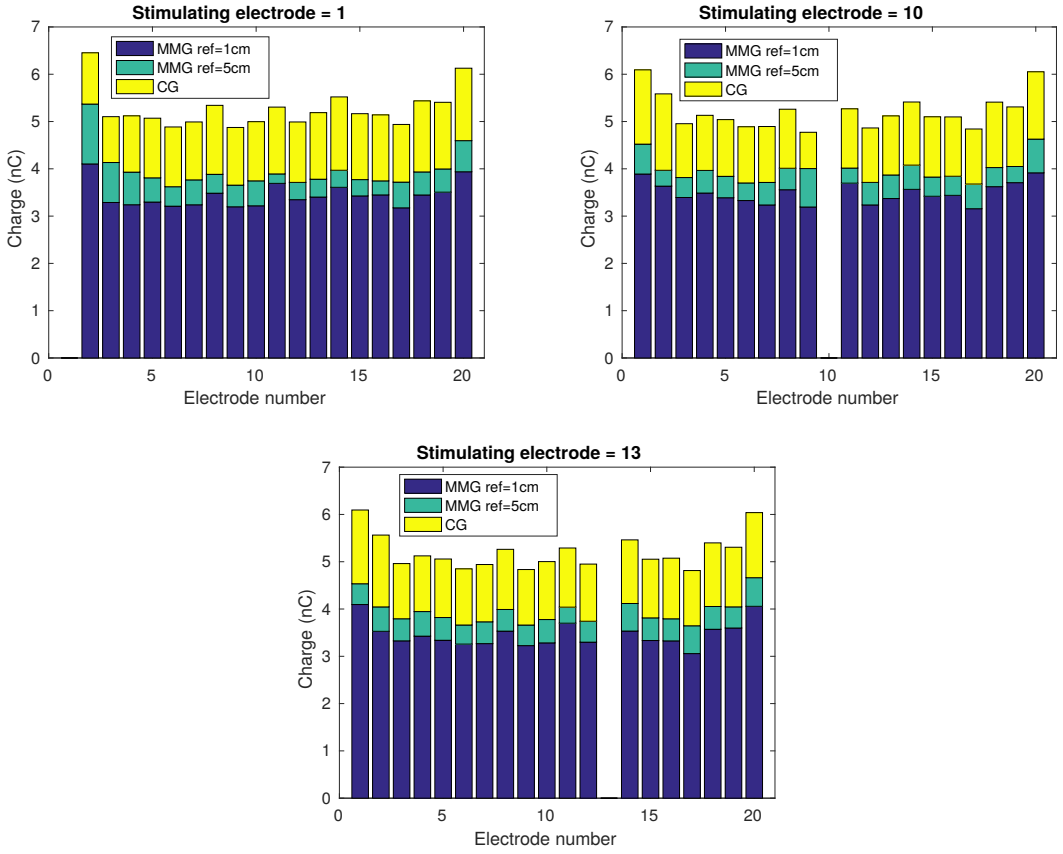

Figure 6.9: Current distribution on the intracochlear electrodes. The stimulating electrode from left to right are: 1 (most basal), 10 (middle) and 13 (apical). The stimulation mode is represented by the color of the bar. In the MMG mode, the ref value corresponds to the distance between the electrode array and the reference electrode.

Figure 6.10 plots average amount of charge returned through the reference electrode in MMG mode against the distance between the electrode array and the reference electrode. It shows that 31.8% of the current returned through the refer-

ence electrode when it is placed 1cm away from the electrode array in saline. This value was reduced to 23.5% when the distance increased to 5cm. The surface area of the reference electrode is around 25 times larger than the intracochlear electrodes. Therefore it is expected to take more charge than the other electrodes.

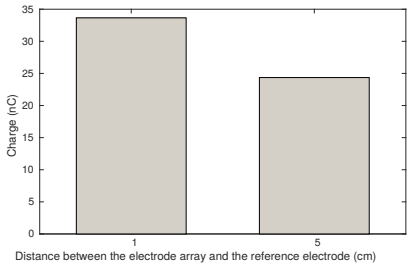

Figure 6.10: The amount of charge returned through the reference electrode in MMG mode, in relation to the distance between the distance between the electrode array and the reference electrode.

In order to verify the current distribution's sensitivity to the geometry, the water tank experiment was repeated. This time the electrode array was inserted into a plastic tube that blocks the current diffusion. The tube has 1.5mm inner diameter and 3.5cm length. The insertion was completed in the saline to avoid air bubble between the electrode array and the tube, as shown by figure 6.8(b).

The current distribution of CG stimulation measured with the electrode array in the plastic tube is shown in figure 6.11. Electrode 10 was the stimulating electrode. From electrode 9 to 1 and 11 to 20, a decrease of charge is observed as the distance to the stimulating electrode increases, which is significantly different from the current distribution measured without the plastic tube. The current distribution in MMG mode was also measured under the same condition. The result was the same as the CG mode, with less than 5% of the current returned through the reference electrode.

6.4 3D electric potential measurements

Results of water tank measurements showed the current distributions in both CG and MMG modes are sensitive to the shape of the container. Since the tube-shaped container is geometrically more similar to the actual container of the electrode array in the cochlea (the scala tympani), it is better to take potential measurements using

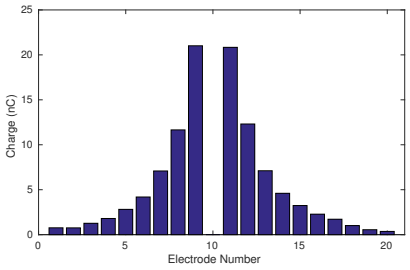

Figure 6.11: Current distribution in the CG mode when the electrode array was placed in the plastic tube. Electrode 10 was used for stimulation.

this container instead of the water tank.

In order to take samples of the electric potential under the similar current distribution, an electrode container made with 3D printing technology has been used. The 3D printer which makes the container has also been used for high precision positioning of the probe that samples the electric potential in the container. The results of the 3D measurements gives a detailed map of the potential distribution of CG and MMG stimulation modes. The measured data helped characterizing these stimulation modes and was used to validate the simulation results of the cochlea model. The results also showed that although the tube shaped container is suitable for the study of CG and MMG modes, it has difficulties in reproducing the potential distribution of the monopolar stimulation, where a larger volume of tissue is involved in current conduction.

6.4.1 Container of the electrode array

Figure 6.12 gives the 3D model and cross-sections of the electrode container used during the in vitro potential measurements. The 3D model of the container was created using OpenSCAD. The container is made of two U-shaped indents with different diameters. The part that contains the electrode array is designed to simulate the dimensions of the scala tympani. It has a diameter of 2mm. The other part contains the reference electrode has 4mm diameter. The size of the cross-section changes linearly at the junction to have a smooth transition between the two parts.

In the previous water tank measurement (figure 6.8(b)), only a small proportion (5%) of the charge returned through the the return current. This can be explained by the small diameter of the tube ($1.5mm$) and the fact that one side of the tube was blocked by the thicker base of the electrode array. By adopting a smooth transition

in the container with an increasing diameter, the current between the intracochlear electrodes and the reference electrode will no longer be blocked.

The electrode array is fixed on two small pillars at the end of the array to keep it at the center of the indention with out touching the borders. Since the array cannot be perfectly straight, further steps have been taken to track its trajectory in the saline to make sure the sample points do not drift away from the electrodes. This part of work is explained later in section 6.4.3.

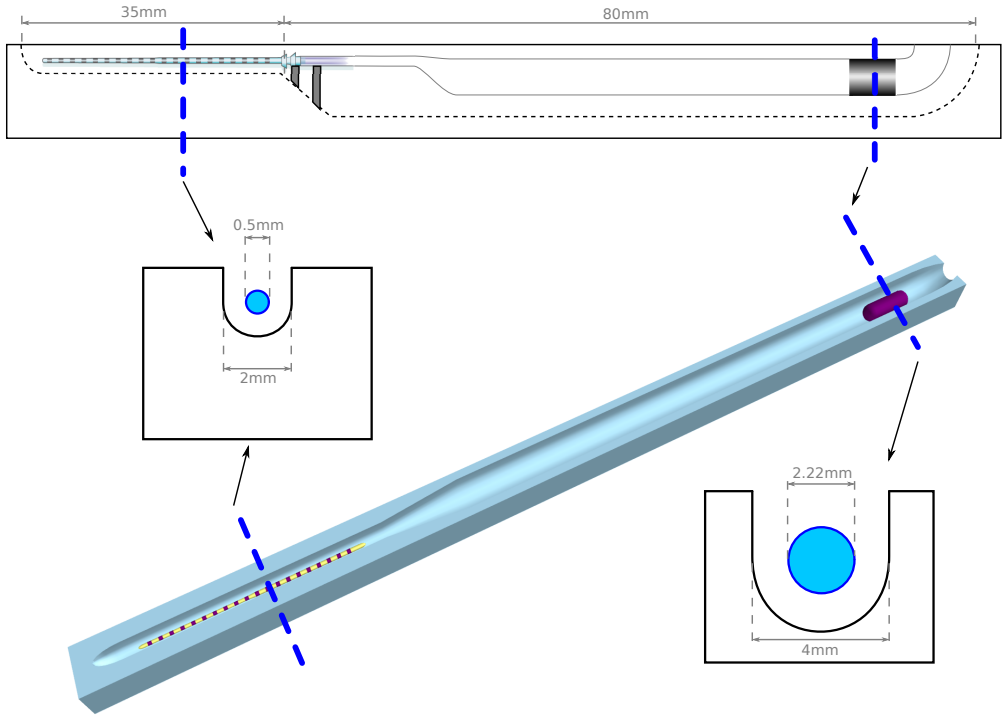

Figure 6.12: 3D model and cross-sections of the electrode container used by in vitro potential measurements

The whole container was printed by the Ultimaker2 3D printer (Ultimaker B.V.4191 PN Geldermalsen, The Netherlands) using polylactic acid (PLA) plastic. The vertical resolution of 3D printing is 0.05mm while the horizontal resolution is 0.1mm.

6.4.2 Probe movement control and measure points

Electric potential measurements in the saline were taken by a probe made of insulated wire. The insulation at the tip of the wire was removed. The diameter of the

wire is 0.1mm.

The probe was attached to the printing nozzle of the Ultimaker2 3D printer. The printing nozzle controlled by 2 step motors can be programmed to move in the horizontal plane. The container was attached to the printing platform, which moves vertically. The minimal step of movement of the printing nozzle and platform are $12.5\mu m$ and $5\mu m$ respectively. Movements of the printing head and platform were controlled by a G-code program. To complete one measurement, the 3D printer first directs the probe to the right position in the container, then sends a ready signal to PC through the USB cable. The PC starts the stimulation and measurement in the same way as the current distribution measurements. The following lines give the G-code required to complete a single potential measurement:

1. `G1 X81.700 Y114.299 Z100.000`
   Move printing nozzle to coordinate (81.70, 114.30, 100.00).

2. `M114`
   Report current nozzle position to PC through USB, which is used as the start signal of stimulation.

3. `G4 P1000`
   Wait 1000ms for the stimulation and measurement to complete.

The complete G-code program was generated using a python program with the coordinates of all the measure points. By adopting the 3D printer as the positioning device, the speed of measurement was significantly increased with each measurement took only 1.2 second. 1134 measure points were required to cover the whole electrode array, which took about 22 minutes. Then the container was emptied and refilled with new saline before the next series of measurements. Therefore, despite the small volume of the container, the conductivity change caused by the vaporization of saline can be ignored.

The sample points of electric potential were arranged from the base to the apex in the saline near the electrode array. Their positions are plotted in figure 6.13.

The measure points were organized as 9 straight line segments in the same direction as the electrode array. Each line is 25.2mm long with 126 equally spaced measure points. The distance between neighboring points in the grid was 0.2mm. The projection of the 9 line segments on the yOz plane formed a 3×3 grid to cover the space near the electrode array. The spacing between lines is also 0.2mm.

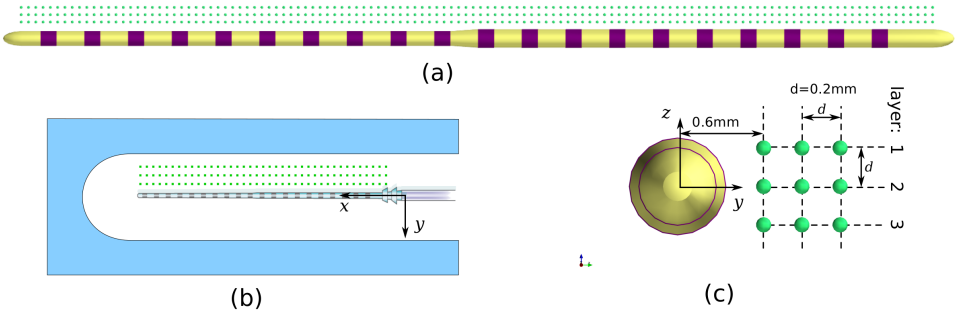

Figure 6.13: Positions of electric potential measure points, marked by green dots in the figure. Top and side views of the measure points in relation to the electrode array are given in (a) and (c). (b) gives the positions in relation to the container.

A picture of the experimental setup for the potential field measurements is shown in figure 6.14.

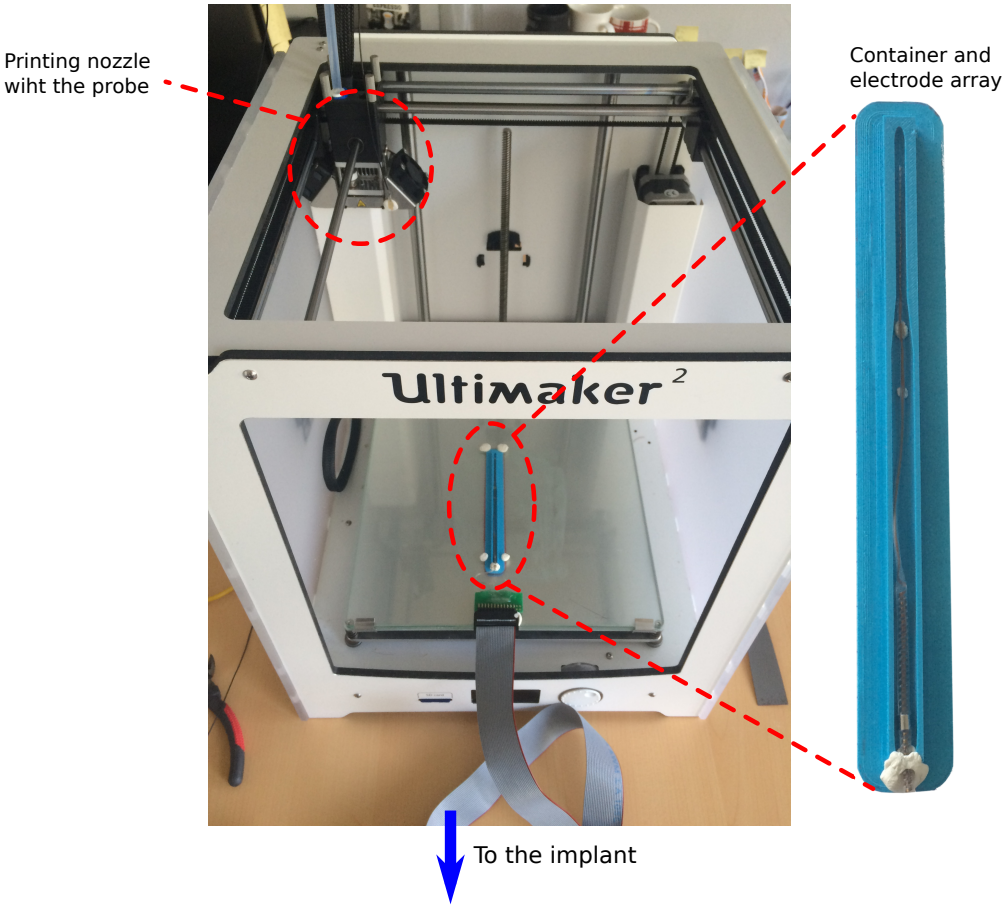

Figure 6.14: Experimental setup for the electric potential measurements

6.4.3 Tracking the curved electrode array in saline

As shown in figure 6.13(c), the 9 lines of measure points were organized as 3 horizontal layers, based on their z coordinates. Ideally, the potential field around the electrode array should be rotationally symmetric, therefore taking samples only from layer 2 would be enough to measure the potential distribution. But the actual electrode array could not be perfectly straight. The electrode array used in the measurements has been carefully chosen, yet it still slightly bended towards one direction from the middle of the array. Considering the high density of the measure points, a small displacement caused by the bending electrode could have a significant implant on the potential field measured.

In order to take potential samples at a constant distance from the electrode array from the base to the apex, two extra layers of measure points, layer 1 and 3, have been added. Before the electrode array was fixed in the container, it was first rotated so that the bending direction is vertical. For a measure point in layer 2 with coordinate $(x, y, 0)$, its corresponding points in layer 1 and 3 have coordinates $(x, y, +d)$ and $(x, y, -d)$ respectively $(d = 0.2mm)$. Since the point closest to the electrode array records the highest electric potential, the maximum potential recorded among 3 points was selected as the potential recorded at position (x, y).

An illustration of tracking the vertical bending of the electrode array using the 3 layers of measure points is given in figure 6.15. The chosen points are always the closest to the electrode array in terms of the z coordinate.

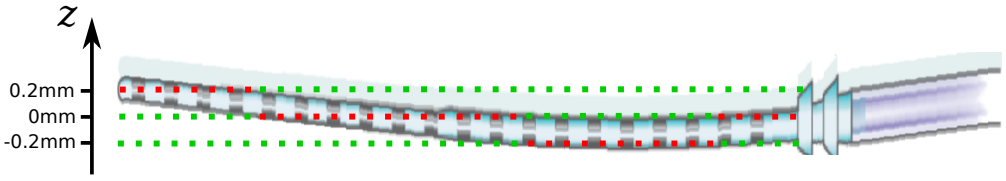

Figure 6.15: Tracking the vertically bended electrode array using 3 layers of measure points with different z coordinates. Red dots indicate the chosen measure points, green dots indicate the discarded measure points.

6.5 Results and discussions

6.5.1 Electric potential distribution

Electric potential distributions of MMG and monopolar modes were measured with the printed container. Since the XP implant hardware only supports the MMG stimulation mode, the monopolar stimulations were simulated by connecting only the stimulating electrode and the reference electrode to the implant to force the current flow only from the intracochlear electrode to the reference.

The type of the stimulation pulse was biphasic with passive discharging. The intensity of the stimulation current was $1mA$. Duration of the active stimulation phase of the pulse was $60\mu s$. The passive discharging phase began right after the active phase and lasted until the end of recording. The total length of recording was $400\mu s$.

Figure 6.16 gives the original waveforms of the electric potential recorded in the 3D printed water tank.

The 10th electrode (in the middle of the array) was used for stimulation. The stimulation mode was MMG.

As for the recording side, the same device setup was used as in the previous water tank recordings. The internal moving average filter (length = 5 sample points) of the oscilloscope scope was used to remove the residual noise caused by the antenna of the implant.

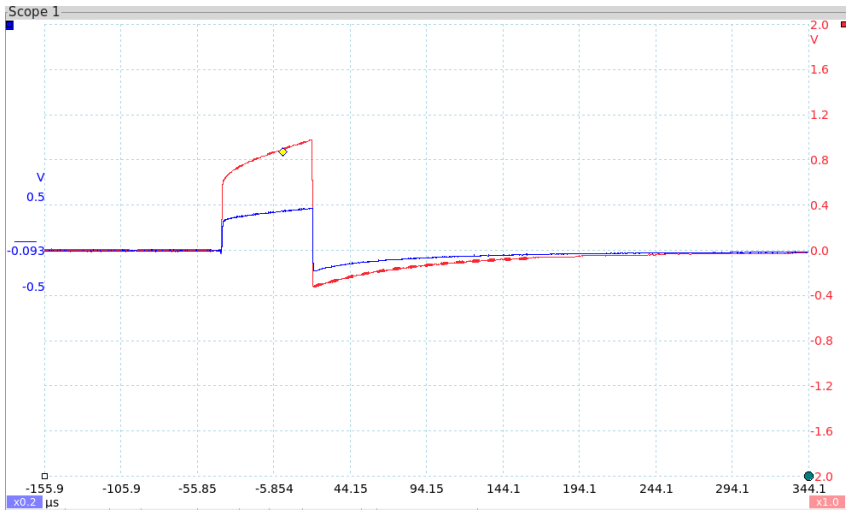

Figure 6.16: The original recorded potential waveforms from the stimulating electrode (red) and the measure point closest to the stimulating electrode (blue).

By comparing the two waveforms in figure 6.16, it can be found that the anodic phase and cathodic phase of the stimulation pulse have different attenuation rates from the surface of the electrode array to the saline. The maximum amplitude of the anodic phase reduced by 51% from $984mV$ to $483mV$, while the cathodic phase only reduced by 30% from $310mV$ to $217mV$. This difference can be explained by the residual charge on the double layer capacitor of the electrode-electrolyte interface after the active stimulation phase. When the passive discharge phase started, the polarity of normal current on each electrode were also inverted. Hence part of the voltage drop caused by the saline between the electrode and the measure point was compensated by the voltage on the electrical double layer. This result showed the necessity of considering the electrode-electrolyte interface when studying the asymmetric stimulation pulses, since the ratio between the phases' amplitudes are not the same after crossing the interface.

Figure 6.17 is a 3D view of the electric potential changes in time recorded from the row of measure points closest to the electrode array. The stimulation mode was MMG.

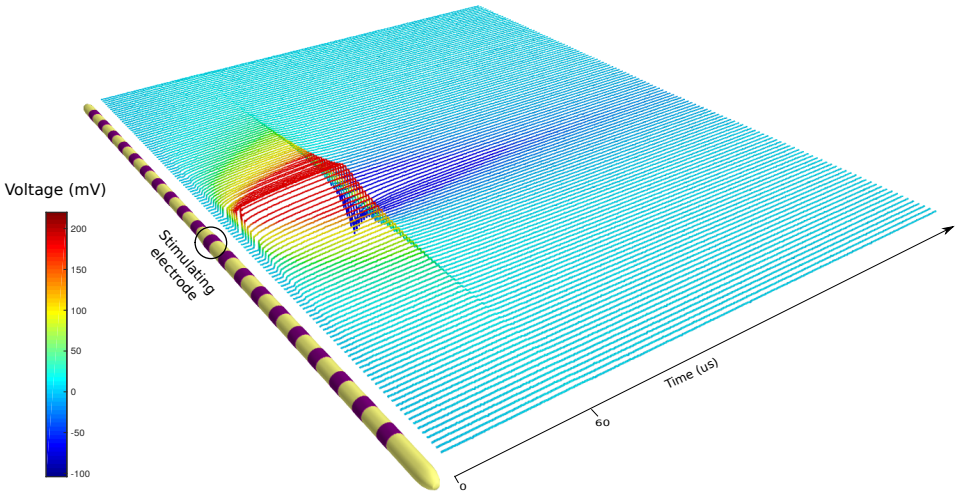

Figure 6.17: 3D view of the electric potential waveforms along the electrode array in the printed container during MMG stimulation.

The data in figure 6.17 corresponds to the solid red line in figure 6.18, which is a comparison of the electric potential distributions along the electrode array. The lines in the upper half of figure 6.18 were plotted from the maximum elec-

tric potentials recorded during the stimulation phase, while the lines in the lower half were from the maximum absolute values of the potential waveform of the passive discharging phase. The color of the lines indicates the distances between the measure points and the electrode array. The solid and dashed lines were recorded while stimulating from the 1st and 10th electrode respectively. The location of the reference electrode was at the left side with a x-coordinate of $-80mm$ using the coordinate system in the plot.

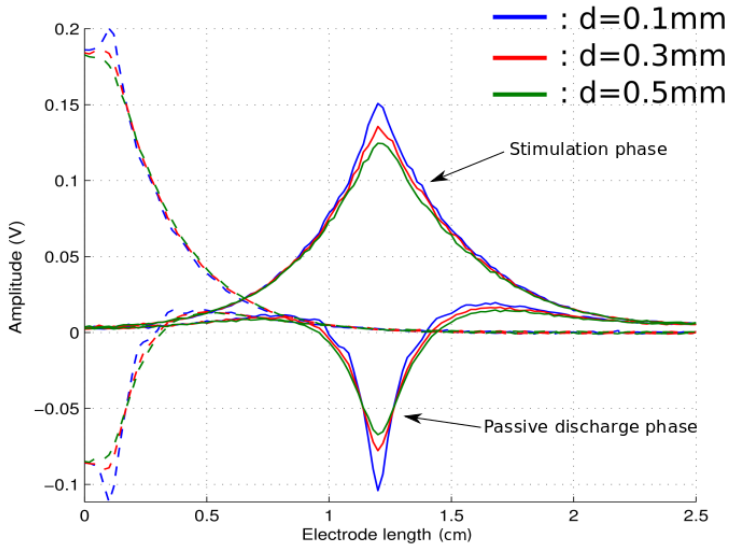

Figure 6.18: Electric potential distribution of the MMG stimulation mode along the array. The dashed and solid lines corresponds to the potential distributions when stimulating from the base and middle of the electrode array respectively.

Figure 6.18 showed that spatial potential distributions of the passive discharging phase and the active stimulation phase are not symmetric. The former one is more focused than the latter one.

To explain this fact, we can firstly consider the the active stimulation phase of the pulse. At this stage, the blocking and double layer capacitors were loaded with the charge opposite to the direction of the stimulation current. Hence a resistance to current injection was found on the intracochlear grounding electrodes. Grounding electrodes close to the stimulating electrode have stronger resistance to the current than the further electrodes since they have higher current intensities and hence higher voltage on the capacitors. Therefore the spread area of current got larger in this stimulation phase. In the passive discharge phase, the direction of current was

reversed. The polarity of the charge on these capacitors was the same as the current direction. So the passive discharging process was accelerated and the spread of current was reduced. As a comparison, the current spread of the active stimulation phase of CG and MMG mode was between the monopolar mode and the CG mode without considering the blocking capacitors and electrode-electrolyte interfaces; the current spread of the passive discharge phase was between the tripolar mode and the the CG mode without capacitors.

The maximum electric potential in saline reached $0.2V$ when stimulating from the most basal electrode while it only reached $0.15V$ when stimulating from the middle of the electrode array, which means that despite the existence of the reference electrode in the MMG mode, the current distribution was still strongly affected by the number of close grounding electrodes linked to the stimulation position.

Considering that the container has only $2mm$ diameter, when stimulating from the middle of the electrode array, current at the right side of the stimulation position cannot access to the reference electrode, hence it can be seen as the CG stimulation at this side, while the left side was still in MMG mode.

It can be found in figure 6.18 that at the right side of the electrode array, the maximum electric potential near the stimulation position (x coordinate from $1.4mm$ to $1.8mm$) was higher than zero in the passive discharging phase due to the residual charge on the blocking capacitors, while the potential at the corresponding position at left side was close to zero. The asymmetry in the potential distribution of the passive discharging phase showed the contribution of the reference electrode in a faster discharging of the blocking capacitors at the discharging phase.

Compared with active discharging, one of the drawbacks of the passive discharging was its slow speed. Here an interesting phenomenon related to this problem was found from the comparison of the raw voltage recordings on two electrodes with different distance to the stimulation site.

Figure 6.19 gives the voltage waveforms on the blocking capacitor of electrode 9 and 5 during stimulation. The voltage on electrode 9 first decreased to 0 (red line in the plot) and then went below 0, whereas the voltage on electrode 5 gradually decreased to 0 at a slower speed.

This phenomenon indicated that the blocking capacitors on the grounding electrodes near the stimulating electrode were first fully discharged and then reversely charged by the current from the stimulating electrode again in the passive discharg-

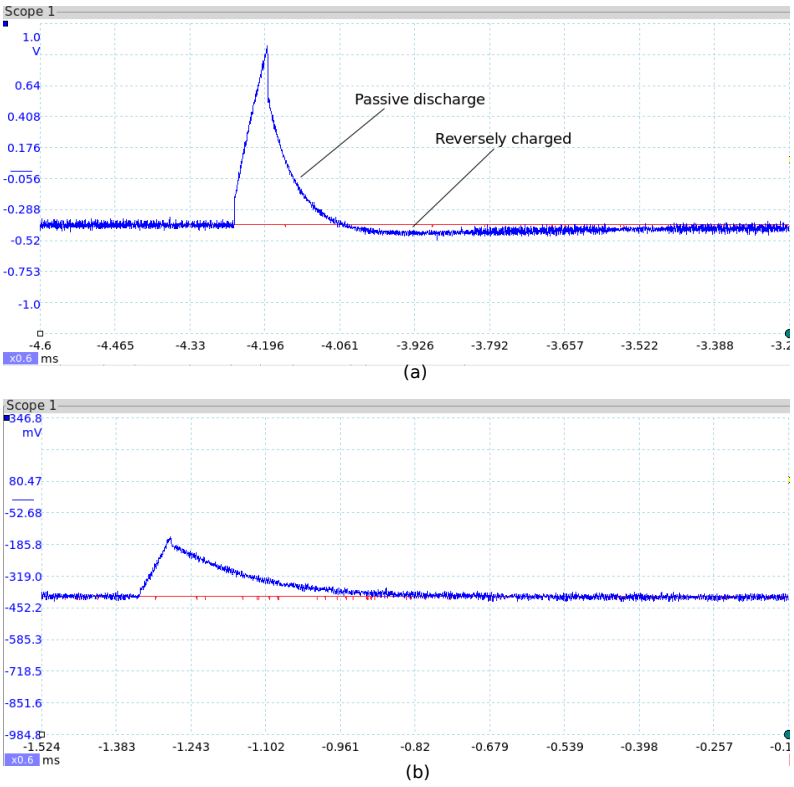

Figure 6.19: Raw voltage recording on the blocking capacitor of electrode 9 and 5 in (a) and (b) respectively. The stimulating electrode was the 10th.

ing phase. Furthermore, it means the passive discharging process of the CG and MMG modes was not a reverse in time of the active charging phase. The speed of discharging gets slower as the grounding electrode gets further from the stimulation site. Whether the same phenomenon can also be found from in vivo stimulations remains to be studied.

6.5.2 Considerations on the container shape

By comparing the current distributions recorded in the tube-shaped container and the water tank, it can be concluded that the tube-shaped container is a better approximation of the intracochlear geometry than the water tank in terms of CG and MMG stimulations.

However, the electric potential recordings of the the monopolar stimulation were different. Figure 6.20 is plotted in the similar way as figure 6.17, except that here the stimulation mode was changed to monopolar and only the maximum potentials

of the active stimulation phase were plotted.

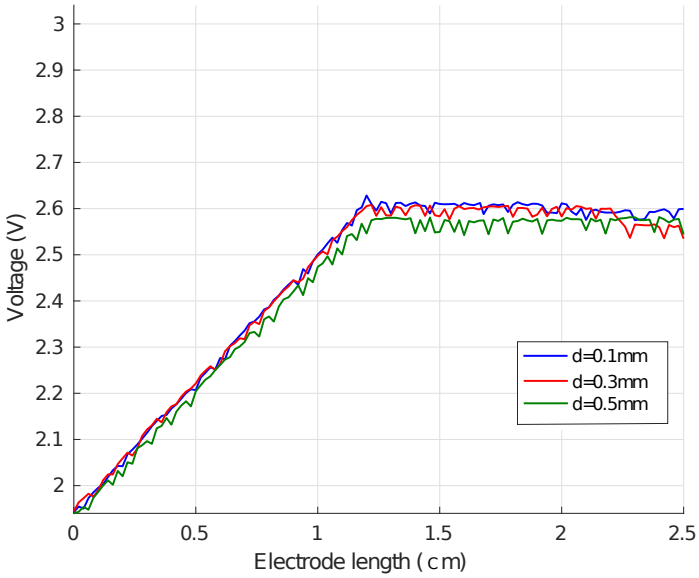

Figure 6.20: Electric potential distribution of the monopolar stimulation mode along the array.

In figure 6.20, the position of the reference electrode was also placed at $x = -80mm$. Electrode 10 was still the stimulating electrode at $x = 12mm$. The recorded electric potential decreases linearly from the stimulating position towards the reference electrode, while it remained almost a constant on the other side. The result suggests that for the CG and MMG stimulations, the current distribution is more affected by the conductivity of the tissue near the stimulation site. This conclusion may also be extended to the bipolar and tripolar stimulations where the stimulating and grounding electrodes are close to each other. For the monopolar stimulation, a larger volume of tissue is involved in the current conduction, therefore a water tank container may have better performance than the tube shaped container in terms of predicting the current distribution. From the simulation point of view, it indicates CG and MMG are more sensitive to the conductivity of the intracochlear tissue, while a good model of the temporal bone is required to make accurate estimations of monopolar's current distribution.

With the help of 3D printing, more sophisticated and realistic cochlear shapes can be printed and inserted with the electrode array for measurements. But in terms of current distribution, a rotationally shaped container will provide the same

result as a straight one because the plastics used for printing are non-conductive. Considering this fact and the difficulties of arranging measure points in a spiral container, the straight container was finally chosen for the experiment.

6.5.3 CPE parameter fitting

The studies of Duan et al. (2004) on cat showed that the intracochlear electrochemical impedance spectra measured right after implantation was similar to the spectra measured from the same electrode in saline. Therefore here the voltage recordings taking in saline were used to calibrate the parameters of the CPE used in chapter 4.

The voltage response of a CPE to the current step is:

$$V_{CPE}(t) = \frac{I_0}{Q\Gamma(1+\beta)} t^{\beta} \tag{6.1}$$

in which I_0 is the intensity of the stimulation current, Q and β are the parameters to be determined.

The actual voltage response of CPE was acquired by subtracting the electric potential measured from the simulating electrode by the one measured near the electrode in saline, i.e., subtracting channel B by channel A of the recordings plotted in figure 6.16. The result was the voltage on CPE and the saline between the two. Since the active stimulating phase of the pulse was a current step, its corresponding potential waveform was extracted. Also because $V_{CPE}(t=0) = 0$, the first sample of the extracted waveform was shifted to 0 to remove the voltage on the saline. Finally, the shifted waveform was compared to the analytical solution generated by different β values, as shown in figure 6.21. The coefficient Q was computed from the ratio between the amplitude of the measured voltage and the analytical solution with a given β value.

The fitted values were: $\beta = 0.74$ and $Q = 4.683 \times 10^{-6}$.

6.5.4 Validation of the simulation results

The saline conductivity was set to $1544 S/mm$ in the following simulations.

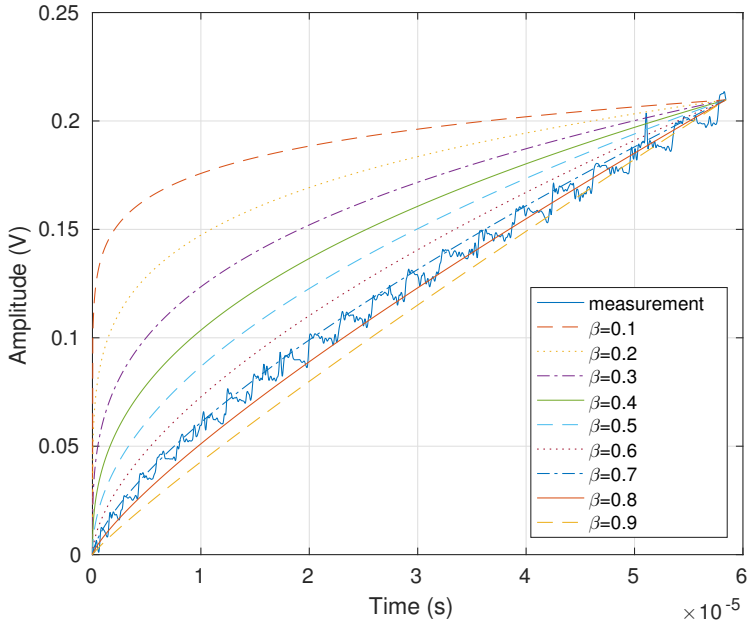

Figure 6.21: Fitting the parameters of the CPE model to the measured voltage waveform.

Water tank

The geometry of a simulated water tank is shown in figure 6.22. The electrode array was straight and located in the center of the tank as in the experiment. The size of the water tank was the same as the one used in the measurements.

The initial current distributions of the CG stimulation simulated with the model above are plotted in figure 6.23.

In the results, the maximum current intensity on the grounding electrodes was $-57\mu A$ while the minimum was $-46\mu A$. The error between them was $8\mu A$ which is 19.30% of the maximum current intensity. Whereas the same value for the measured data was 23.54%. The result showed the simulation was able to predict the equally distributed current on the grounding electrodes of CG stimulation in a water tank.

Printed container

Figure 6.24 is the simulated geometry of the printed container.

The stimulation pulse used for simulation was the same as used in the measurements above. The simulated electric potential on the surface of the electrode 10

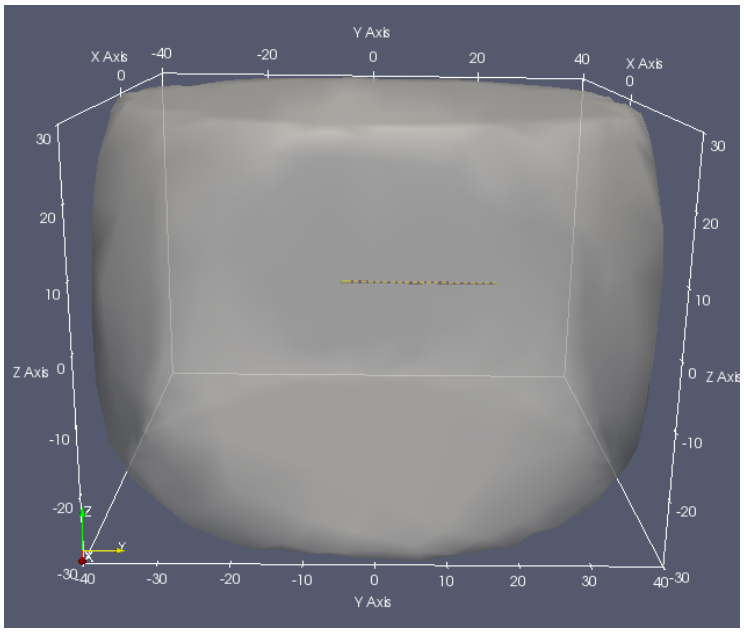

Figure 6.22: Geometry of the simulated water tank.

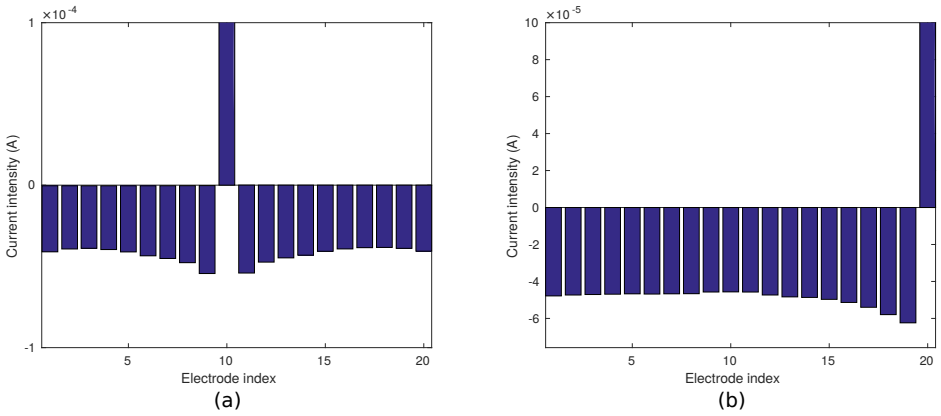

Figure 6.23: Simulated current distribution of the CG stimulation in a water tank. The stimulating electrode was located at: (a) one side of the array; (b) middle of the array. The bar representing the stimulating electrode was truncated to enlarge the view on the grounding electrodes.

(stimulating) and 9 are plotted in figure 6.25.

The general shapes and amplitudes of the simulated potential waveforms matched the measured potential waveforms. The reversed charging was also found in the simulated potential waveform of electrode 9.

The simulated spatial potential distribution is plotted in the similar way as

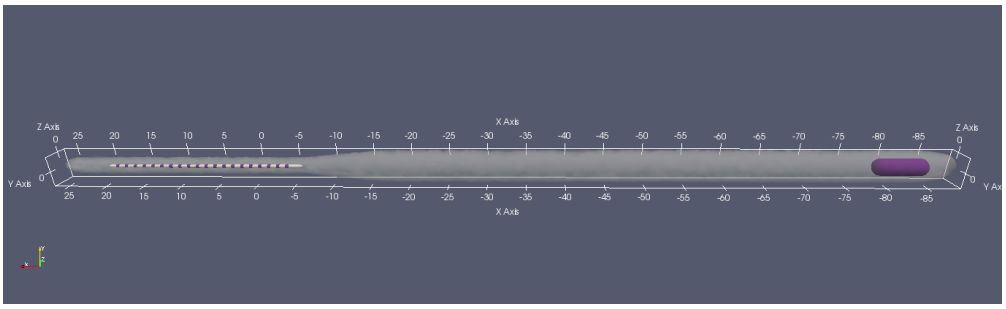

Figure 6.24: Geometry of the simulated tube-shaped container.

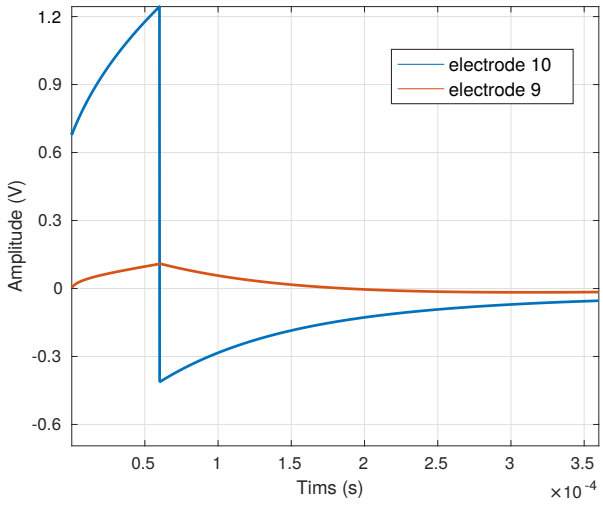

Figure 6.25: Simulated electric potential on the surface of the electrode 10 and 9. Electrode 10 was used for stimulation.

figure 6.18 in figure 6.26. The maximum amplitude and shape of the simulated potential distribution matched with the measurements.

6.6 Conclusions

This chapter presented the process of taking current intensity and electric potential measurements on the cochlear implant using homemade devices. Two different container shapes, a water tank and a 3D printed tube were used as containers of the electrode array during the measurements. The results of measurements from the two containers show that the current distributions of the CG and MMG modes were largely affected by the shape of the container, and that the tube shaped container

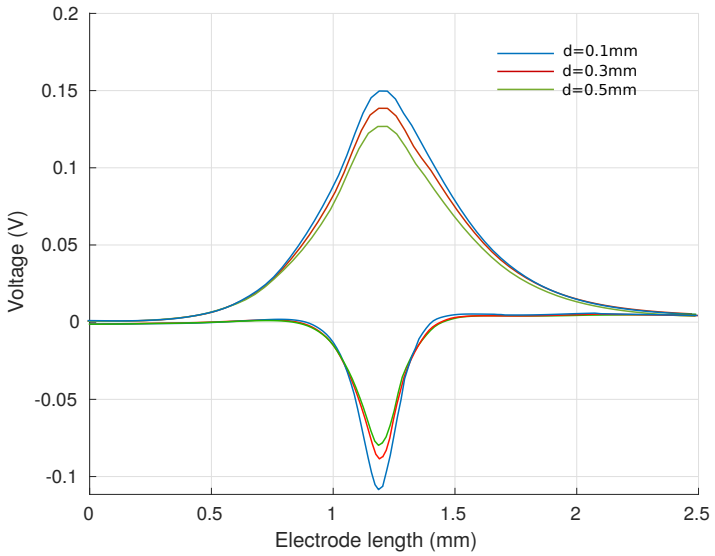

Figure 6.26: Simulated electric potential distribution in the saline during MMG stimulation on electrode 10.

could better approximate the current distribution in the actual cochlea.

To make spatial potential distribution measurements, the electrode array was placed in a 3D printed tube shaped container. Measurements were taken along the electrode array with different distances to the array.

The validation of the parametric model coupled with the electrode-electrolyte interface was carried out by comparing the simulated and measured current and electric potential distributions plus the time domain potential waveforms. The results show a good match between the two in all the three compared aspects.

Chapter 7

In situ measurements of electric potential and current intensity of cochlear stimulations

Contents

To better validate the simulation results, in situ measurements have been performed on implanted human specimens. The electric potential measurements on all the intracochlear electrodes were made on the first human specimen for monopolar, bipolar, BP+3 and tripolar stimulations. A 3D micro-CT scan (resolution 24.8μm in each direction) was conducted on the cochlea after implantation.

As for the MMG stimulation, another human specimen was used for the measurements. The current intensities on all the intracochlear electrodes were measured instead of the electric potential. A CT scan was conducted after implantation to determine the general positioning of the electrode array.

In both cases, the left cochlea of the human specimen was used for implantation, the implanted electrode array was the EVO electrode array. The reference/ground electrode that worked with the EVO electrode array was a platinum cylinder, with 2.22mm diameter and 2.5mm length. It was placed between the skull and scalp of the human specimen. The measuring process started right after implantation and lasted for about 3 hours.

7.1 Electric potential measurements

A stimulation research platform was used to generate the required stimulations during the measurement. The intensity of the stimulation current was 1mA. The stimulation waveform was biphasic with active discharging, as shown in figure 7.1.

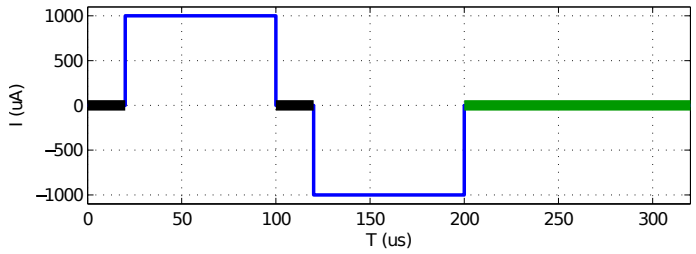

Figure 7.1: Biphasic stimulation waveform with active cathodic discharging phase. Colors indicate the work modes of the electrode: (black, high impedance); (blue, stimulate); (green, passive discharge). The final passive discharge period was added to remove the residual charge on the blocking capacitors.

The devices that handled the electric potential measurements from the intracochlear electrodes were the same as the devices used by the in vitro measurements presented in chapter 6, which included an analog multiplexer, a microcontroller and

a digital oscilloscope. The electric potential waveforms were sampled at 5MHz and 16bits amplitude resolution.

7.2 Geometry adaptation using micro-CT scans

The first step of adapting the 3D model from micro-CT images was to build the same cylindrical coordinate system used by the parametric model in the scan data. As an approximation, the plane of the basal turn of the cochlea was set to $z = 0$. According to the surgeon who has performed the implantation, the second electrode was located at the round window when the insertion process finished. Therefore the direction of the polar axis of the cylindrical coordinate was set to point to this electrode from the center of the modiolus, as shown in figure 7.2 (a).

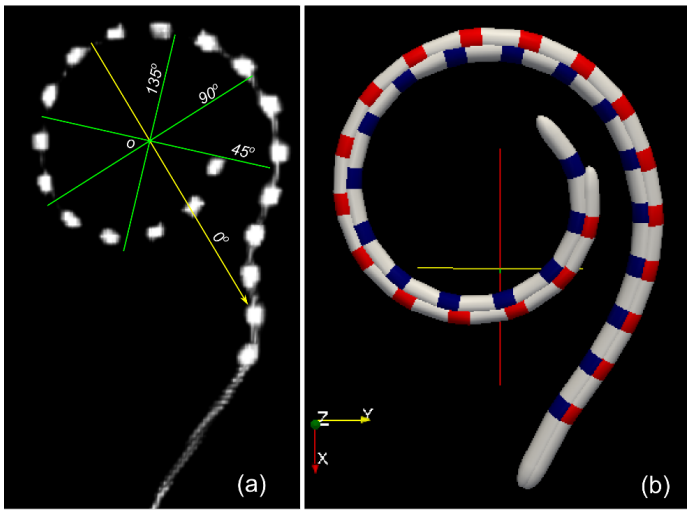

Figure 7.2: Position of the electrodes extracted from micro-CT scan (a). The yellow arrow is the polar axis of the cylindrical coordinate system, green lines are the positions where the cross-section samples were taken. The 3D electrode array models are shown in figure (b), in which the blue and the red array each represents the position of the electrode array before and after adaption.

As discussed in chapter 4, cross-section samples taken with a 45° interval along the angle of rotation can provide enough morphology information for a geometry adaptation. To perform the adaptation, vertical cross-section images were extracted from the scan data at 4 rotation angles: 0°, 45°, 90° and 135°, each image contained multiple cross-sections of the scala vestibuli and scala tympani with the electrode array. An illustration of the positions of these images in the cylindrical coordinate

system is given in both figure 7.2 (a) as green lines and figure 7.3. The actual images are shown in figure 7.4. Parts of the shape parameters of the cochlear model: the cross-section width w, heights of the scala tympani and scala vestibuli h_{st} and h_{sv}, tilt angle ψ, the radius and z-coordinate of the cochlear spiral R and z, plus the position of the electrode array inside the scala tympani, were manually measured from these images using the 3D visualization tool provided by medInria (Toussaint et al., 2007). However, even the manual segmentation failed to recognize the scala tympani and scala vestibuli at the apical turns of the cochlea, as indicated by the red circled areas in figure 7.4. Only 10 cross sections were successfully measured.

The values of these parameters between the sampled cross-sections and at the apex of the cochlea were again, acquired by spline interpolation. As for the parameters required by the parametric cochlea model but could not be measured from the micro-CT images, the values of the average shape based cochlear model were used.

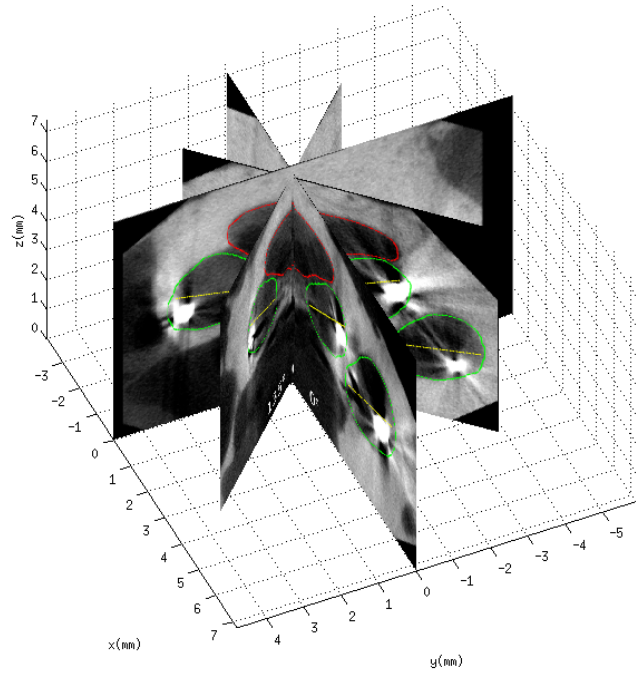

Figure 7.3: A 3D view of the positions of the cross-section images taken for geometry adaptation

The initial position of the array was at the center of the scala tympani, while the adapted array was located to the lateral side in accordance with the Micro-CT scan. As a result, the position of the electrode array's end was shifted along the

longitudinal direction in the scala tympani. Figure 7.2 (b) compares the positions of the electrode array before (blue) and after (red) adaptation.

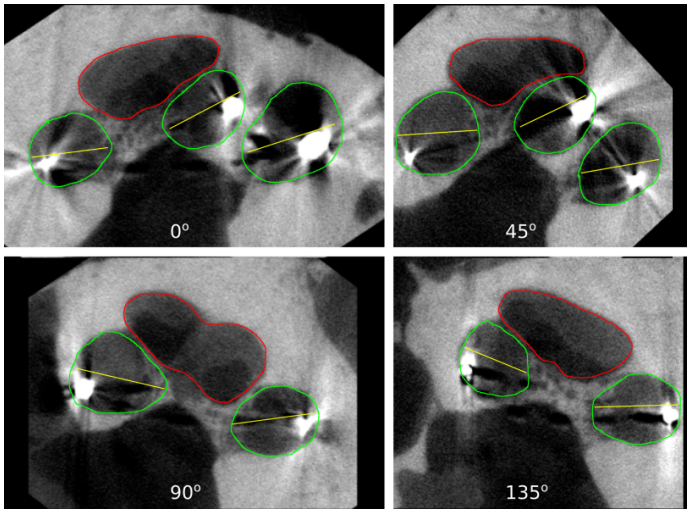

Figure 7.4: Vertical cross-sections of the cochlea taken at 4 rotation angles. Green curves are the manually segmented scala tympani and scala vestibuli, separated by the estimated line of the basilar membrane and the lamina spiralis ossea (yellow). The red curve is the apex of the cochlea where the scala tympani and scala vestibuli cannot be separated.

7.3 Validation of the simulated potential distributions

The geometrically adapted parametric model with the electrode-electrolyte interface was used to give simulations of the intracochlear electric potential to be compared with the measured values. The values of the electrode-electrolyte interface parameters were taken from the in vitro measurements in chapter 6. The simulated intracochlear electric potential on the surface of the electrodes was directly compared to the measured potential. Both the simulation and the measurement used the peak value of the biphasic stimulation pulse as the estimation of the potential value on the electrode during stimulation. The results are plotted in figure 7.5. Four stimulation modes with different stimulation positions are compared in the plots.

Among the 4 plots showed by figure 7.5, the monopolar stimulation showed the largest difference between the simulation and measurements. Concerning that the potential distribution of the monopolar stimulation was affected by the impedance

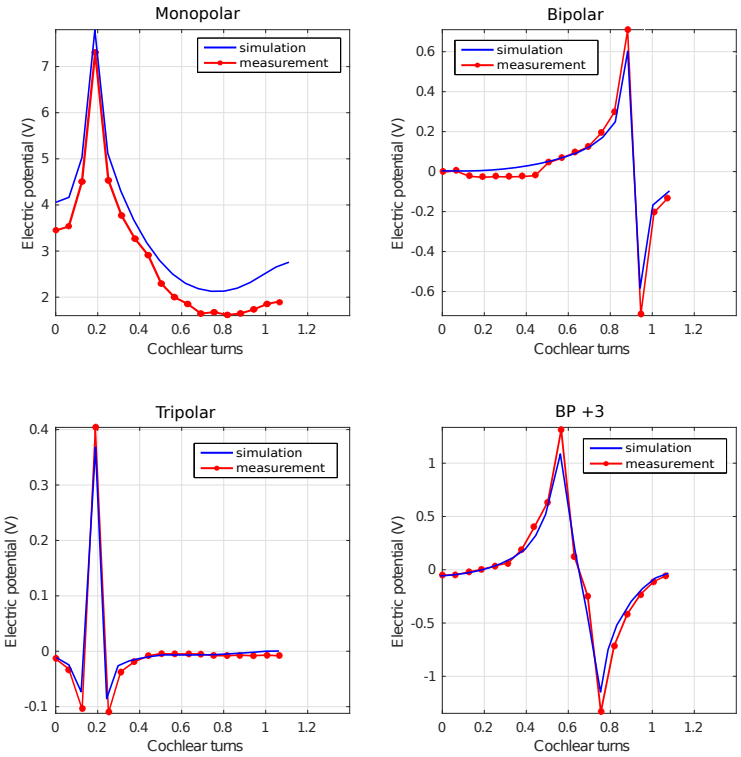

Figure 7.5: Comparison of the electric potential distribution between the simulation and the in situ measurements

between the grounding and the intracochlear electrodes while other stimulation modes generally did not, the coarse approximation of the temporal bone in the parametric cochlear model (a bounding sphere of the cochlea) could be the cause of the problem. In the other 3 plots, a good match was found between the simulation and the measurement.

To make quantitative estimations of the simulation error, the Relative Difference Measure (RDM) between the simulation and the measurement was computed according to equation 7.1:

$$RDM(V_s, V_m) = \left\| \frac{V_s}{\|V_s\|} - \frac{V_m}{\|V_m\|} \right\| \tag{7.1}$$

In equation 7.1, V_s is the simulation output while V_m is the measured potential. The results are given in table 7.1.

Table 7.1: RDM over different stimulation patterns

Stimulation mode	Monopolar	Bipolar	Tripolar	BP+3	Average
RDM	0.136	0.083	0.058	0.074	0.088

7.4 Current distribution measurements

The experimental setup for the in situ current distribution measurements of the MMG stimulation was the same as the in vitro measurement in chapter 6.

The stimulation pulse was biphasic with passive discharging. The amplitude and duration of the stimulation phase was 35 current units ($0.778mA$) and $60\mu s$. Hence the total amount of charge delivered by the stimulation phase was $46.67nC$. During the measurement, all the intracochlear electrodes have been selected for stimulation following the order of 1 to 20. For each stimulation electrode, the corresponding electric potential on the other 19 grounding intracochlear electrodes was recorded and converted to the current intensity on the electrode. The whole recording process was repeated 3 times to eliminate the random noise by averaging the recoded data.

Figure 7.6 gives a view of the experimental setup with 3 stitched photos taken during the measurements.

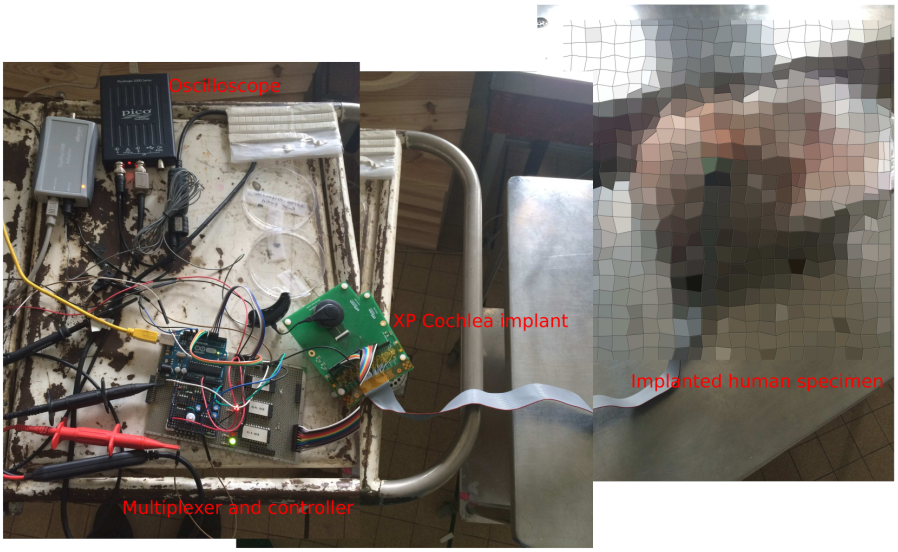

Figure 7.6: Photos of the experimental setup.

7.5 Results and discussions

The surgeon who performed the implantation process reported that the 4 basal electrodes could not be inserted into the scala tympani. Hence all the measurements were taken with this condition.

The raw voltage waveform recorded by the oscilloscope on a grounding intracochlear electrode is shown in figure 7.7. The waveform has the same shape as the one recorded from the in vitro measurement in chapter 6. Distribution of the stimulation current was computed based on the measured data, the result is plotted in figure 7.8.

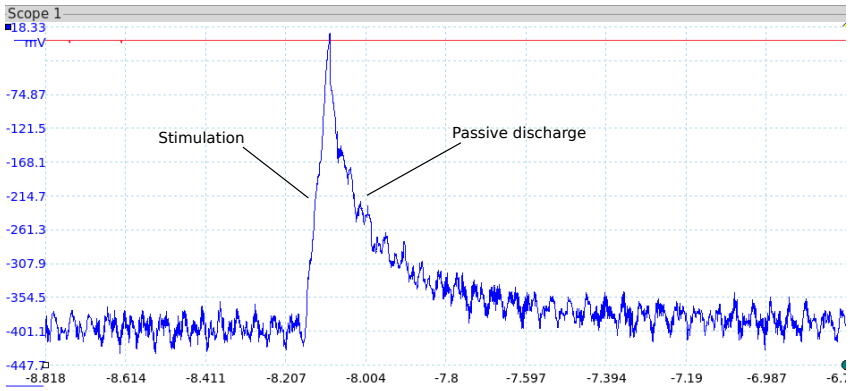

Figure 7.7: Raw voltage waveform recorded by the oscilloscope on a grounding intracochlear electrode

Excluding electrode 1 to 4 which were outside the cochlea when taking the measurements, the percentage of stimulation current that went through the reference electrode reduced from 20% to 15% as the stimulation site changed from electrode 5 (most basal) to 20 (most apical). Meanwhile, the maximum percentage of current that went through the intracochlear grounding electrodes was 9% and 16% the when the stimulation site was in the middle and apex of the array.

7.5.1 Validation of the simulated current distributions

Due to the low resolution of the CT scan, the available morphology information of the implanted cochlea used by the MMG measurements was limited. The parametric model was simply zoomed to the maximum radius R and height z of the cochlea measured from the CT scan. In order to simulate the partially inserted electrode array during the measurements, the electrode array in the model was pulled out

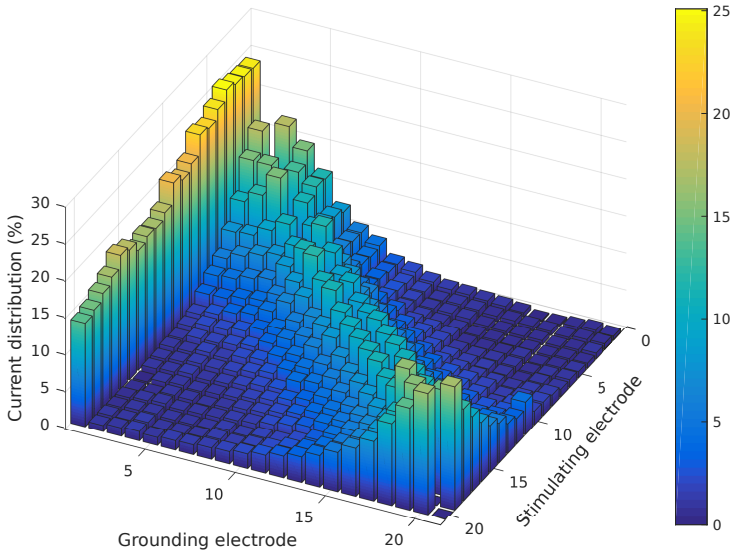

Figure 7.8: Distribution of the stimulation current with respect to the positions of the stimulating and grounding electrodes. Grounding electrode 0 refers to the reference electrode under the scalp. The stimulation mode was MMG. The values for the stimulating electrode on the diagonal of the plot were always 100%. These values were set to 0 in order to enlarge the rest parts of the plot.

of the original scala tympani mesh until the 4 basal electrodes are outside. Then a new scala tympani mesh was generated with an increased thickness of the most basal cross section. Therefore placement of the array was changed without causing mesh intersection.

A comparison of the measured and simulated current distributions was plotted in figure 7.9. The stimulating position was the 12th electrode. At $t = 0\mu s$, the simulated current distribution was more focused around the stimulating electrode. While at $t = 60\mu s$, which was the end of the active stimulation phase, the current distribution became more similar to the measured current distribution.

The contrast between the current distribution simulated at $t = 0\mu s$ and $t = 60\mu s$ indicates that the current distribution during the stimulation was changed by the blocking capacitors and the electrode-electrolyte interfaces. At the beginning of the stimulation, the voltages on these parts were almost zero, so most of the stimulation current return through the grounding electrodes closest to the stimulation site. As the stimulation continued, more and more charge was accumulated on the electrode

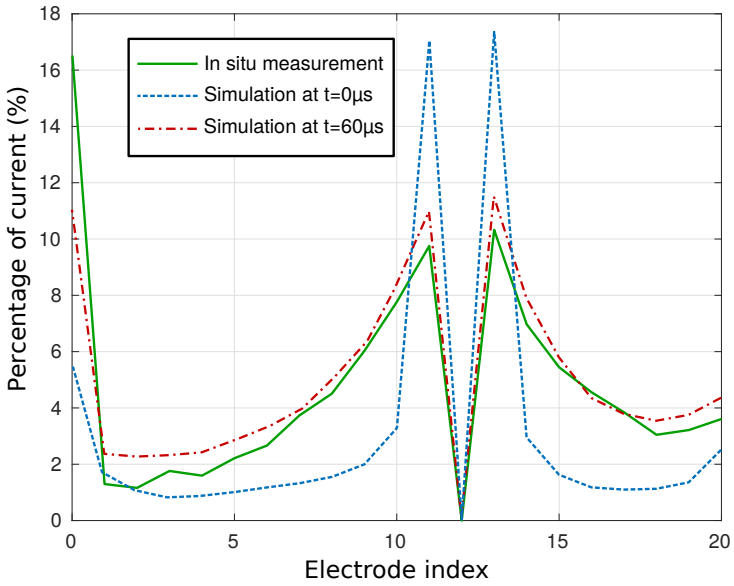

Figure 7.9: Measured and simulated current distributions on the grounding electrodes during the MMG stimulation. Electrode 12 was used for stimulation.

interfaces and blocking capacitors of the electrodes close to the stimulation site, which increased the impedances on theses electrodes. Therefore the current spread to farther grounding electrodes.

In the measurements, the current distribution was computed based on the maximum voltages recorded on the blocking capacitors, which appeared at the end of the stimulation phase. Therefore, it represented the average current distribution during the whole stimulation phase and was more close to the simulated current distribution at the $t = 60\mu s$.

As for the reference electrode, the simulated current intensity on it was much lower than the measured value. The cause of this issue was the same as the issue in the monopolar simulation result shown in figure 7.5: the roughly modeled temporal bone gave higher estimations of the impedances between the reference electrode and the intracochlear electrodes than the actual cases.

7.6 Conclusions

In this chapter, the simulation results of the parametric model was validated by the in situ measured data. The comparisons covered most of the commonly used

stimulation modes. The results showed that simulations made by the parametric cochlear model coupled with the electrode-electrolyte interface can give correct estimations of the potential and current distributions in the cochlea. However, the temporal bone surrounding the cochlea needs to be more carefully modeled to reduce the errors in monopolar and MMG simulations.

Chapter 8

Conclusion française

Contents

8.1 Sommaire

Dans cette thèse, une manière paramétrée de générer le modèle de maillage de surface cochléaire a été proposée. Les paramètres comprennent la forme générale de la cochlée, les détails morphologiques dans les sections transversales cochléaires, la trajectoire des fibres nerveuses auditives plus la disposition et le placement du réseau d'électrodes dans la cochlée. Le paramétrage a permis de partager l'information entre différentes sources d'informations morphologiques lors de la construction du modèle de la cochlée. Par exemple, lors de la modélisation d'une cochlée provenant de micro-tomodensitogrammes où seuls les scala tympani et scala vestibuli sont visibles, d'autres paramètres, tels que la trajectoire des fibres nerveuses, peuvent être rapidement empruntés à des données mesurées et moyennes afin d'avoir un modèle complet Pour le potentiel électrique et la simulation d'activation neurale. L'algorithme de simulation utilisé par le modèle paramétrique était le méthode d'éléments finis surfaciques symétrique symétrique implanté dans un logiciel de simulation appelé OpenMEEG. Le potentiel électrique simulé a été converti en motifs d'activation neurale à l'aide de la fonction d'activation.

Avec le modèle paramétrique, les mailles cochléaires réalisées à d'autres fins peuvent être transformées pour la simulation de potentiel électrique, ce qui a évité de créer des modèles complexes à partir de rien.

D'autres recherches sur la quantité d'informations nécessaires à l'adaptation de la géométrie montrent qu'un intervalle d'angle d'échantillonnage de 180◦ pourrait donner une bonne estimation de la position du pic de potentiel électrique dans la cochlée, tout en réduisant l'erreur dans la prédiction d'amplitude nécessite des données de plus de coupe transversale.

Les simulations des distributions de potentiel spatial utilisant le modèle paramétrique ont estimé la performance de la nouvelle matrice d'électrodes transmodiolaires lorsqu'elle a été utilisée soit pour la mise à la terre soit pour la stimulation. Les résultats de la simulation suggèrent que l'utilisation du réseau d'électrodes transmodiolaires comme sol de la stimulation monopolaire peut réduire efficacement la consommation d'énergie de stimulation, tandis que les excitations neurales indésirables à proximité du réseau d'électrodes transmodiolaires peuvent être réduites ou même éliminées en adoptant des électrodes à grande surface. Lors de l'utilisation de la matrice transmodiolaire pour la stimulation, des électrodes disposées en rotation ont été préférées et une insertion plus profonde dans le modiolus a

été recommandée pour éviter les fibres nerveuses obliques au sommet de la cochlée.

Les seuls modes de stimulation qui n'avaient pas encore été étudiés par les simulations cochléaires étaient le sol commun et la mise à la terre multi-mode. Pour simuler ces deux modes à l'aide du modèle paramétrique, on a proposé une méthode d'incorporation du modèle cochléaire résistif avec le modèle d'électrode électrolyte et les condensateurs de blocage de l'implant cochléaire. Après l'incorporation, le modèle a été capable de simuler des modes multi-mode de mise à la terre et de stimulation du sol commun et de donner des prédictions plus réalistes des formes d'onde du domaine temporel.

Pour valider les résultats de la simulation, des mesures in vitro et in situ de l'intensité du courant et de la distribution du potentiel électrique pendant les stimulations ont été effectuées à l'aide de dispositifs maison. Pour les mesures in vitro, il a été constaté que les distributions actuelles des modes de mise à la terre multi-mode et du sol commun étaient largement affectées par la forme du conteneur et que le conteneur en forme de tube pouvait mieux se rapprocher de la distribution actuelle dans la cochlée réelle . Pour effectuer des mesures de distribution de potentiel spatial, la matrice d'électrodes a été placée dans un conteneur en forme de tube imprimé en 3D. Des mesures ont été effectuées le long du réseau d'électrodes à l'aide d'une imprimante 3D programmée. Les mesures in situ ont couvert la plupart des modes de stimulation couramment utilisés. Les comparaisons entre les simulations et les mesures ont validé la distribution potentielle, la distribution actuelle et les formes d'onde du domaine temporel simulées par le modèle.

8.2 Suggestions de travaux futurs

Selon les résultats de la validation in situ, la première chose à améliorer dans le modèle cochléaire paramétrique est la manière de modéliser l'os temporel. Dans le modèle original, l'os temporel était simplement modélisé comme une sphère avec l'électrode de référence située sur sa limite extérieure. Les mailles cochléaires ont été placées au centre de la sphère. À l'avenir, la mise en œuvre d'un maillage de tête comme dans **?** ou Malherbe et al. (2015) et le placement de la cochlée dans la bonne position de l'os temporel pourrait réduire l'erreur de simulation sur les stimulations monopolaire et multi-mode.

Le couplage du modèle paramétrique avec l'interface électrode-électrolyte s'est révélé efficace par les données mesurées in vitro et in situ. Pour exploiter pleine-

ment la possibilité de simuler des formes d'ondes de potentiel électrique de domaine temporel, la façon actuelle d'estimer les activités neuronales à l'aide de la fonction d'activation devrait être remplacée par des modèles nerveux auditifs plus sophistiqués capables de gérer les changements potentiels dans le temps, comme celui utilisé par Kalkman et al. (2014) dans leurs modèles cochléaires. Les recherches effectuées par Ballestero et al. (2015) ont montré que la forme de pouls en rampe peut réduire la propagation de l'excitation. Avec le modèle nerveux amélioré, des simulations peuvent être faites sur les modèles d'activation neurale générés par différentes formes d'impulsions de stimulation.

La stimulation en phase par étapes vise à réduire le potentiel électrique sur les électrodes non stimulantes (van den Honert and Kelsall, 2007). Il atteint cette cible en tournant les intensités de courant sur les électrodes selon la matrice d'impédance intracochléaire. Cependant, à partir des simulations de domaine temporel réalisées par le modèle paramétrique, nous avons constaté que les impédances intracochléaires changent dynamiquement en raison des tensions variables sur les condensateurs de blocage et les interfaces électrolyte-électrolyte. Comment traiter l'impédance changeante est un autre sujet de recherche intéressant.

Chapter 9

Conclusion

Contents

9.1 Summary

In this thesis, a parameterized way of generating the cochlear surface mesh model has been proposed. The parameters covered the general shape of the cochlea, the morphological details in the cochlear cross-sections, the trajectory of the auditory nerve fibers plus the layout and placement of the electrode array in the cochlea. The parameterization allowed sharing information between different morphological information sources when building the cochlea model. For example, when modeling a cochlea from micro-CT scans where only the scala tympani and scala vestibuli are visible, other parameters, such as the nerve fiber trajectory, can be quickly borrowed from manually measured and averaged data in order to have a complete model for electric potential and neural activation simulation. The simulation algorithm used by the parametric model was the symmetric BEM implemented in a simulation software called OpenMEEG. The simulated electric potential was converted to neural activation patterns using the activation function.

With the parametric model, cochlear meshes made for other purposes can be transformed for electric potential simulation, which avoided making complex models from scratch.

Further investigations on the amount of information needed by the geometry adaptation shows that a 180° of sampling angle interval could give a good estimation on the position of the electric potential peak in the cochlea, while reducing the error in the amplitude prediction requires data from more cross-sections.

Simulations of the spatial potential distributions using the parametric model estimated the performance of the new transmodiolar electrode array when it was used either for grounding or stimulation. The simulation results suggests that using the transmodiolar electrode array as the ground of the monopolar stimulation can effectively reduce the stimulation energy consumption, meanwhile the unwanted neural excitations near the transmodiolar electrode array can be reduced or even removed by adopting electrodes with large surface areas. When using the transmodiolar array for stimulation, rotationally arranged electrodes were preferred and a deeper insertion into the modiolus was recommended to avoid the oblique nerve fibers at the apex of the cochlea.

The only stimulation modes that had not yet been studied by cochlear simulations were the common ground and multi-mode grounding. To simulate these two modes using the parametric model, a method of incorporating the resistive cochlear

model with the electrode-electrolyte interface model and the blocking capacitors of the cochlear implant has been proposed. After the incorporation, the model was able to simulate multi-mode grounding and common ground stimulation modes and give more realistic predictions of the time domain waveforms.

To validate the simulation results, in vitro and in situ measurements of current intensity and electric potential distribution during stimulations have been performed using homemade devices. For the in vitro measurements, it has been found that the current distributions of the multi-mode grounding and common ground modes were largely affected by the shape of the container, and that the tube shaped container could better approximate the current distribution in the actual cochlea. To make spatial potential distribution measurements, the electrode array was placed in a 3D printed tube shaped container. Measurements were taken along the electrode array using a programmed 3D printer. The in situ measurements covered most of the commonly used stimulation modes. The comparisons between simulations and measurements validated the potential distribution, current distribution and time domain waveforms simulated by the model.

9.2 Suggestions of future work

According to the results of in situ validation, the first thing needs to be improved in the parametric cochlear model is the way of modeling the temporal bone. In the original model, the temporal bone was simply modeled as a sphere with the reference electrode located on its outer boundary. The cochlear meshes were placed in the center of the sphere. In the future, implementing a head mesh as in Tran et al. (2015) or Malherbe et al. (2015) and placing the cochlea in the right position of the temporal bone could reduce the simulation error on the monopolar and multi-mode grounding stimulations.

The coupling of the parametric model with the electrode-electrolyte interface has been proved to be effective by the in vitro and in situ measured data. To fully exploit the ability of simulating time domain electrical potential waveforms, the current way of estimating neural activities using the activation function should be replaced by more sophisticated auditory nerve models that are able to handle the potential changes in time, such as the one used by Kalkman et al. (2014) in their cochlear models. Researches made by Ballestero et al. (2015) showed that the ramped pulse shape can reduce the spread of excitation. With the upgraded

nerve model, simulations can be made on the neural activation patterns generated by different stimulation pulse shapes.

The phased array stimulation is aimed at reducing the electric potential on the non-stimulating electrodes (van den Honert and Kelsall, 2007). It achieves this target by turning the current intensities on the electrodes according to the intracochlear impedance matrix. However, from the time domain simulations made by the parametric model, we found that the intracochlear impedances change dynamically due to the varying voltages on the blocking capacitors and electrode-electrolyte interfaces. How to handle the changing impedance is another interesting research topic.

Bibliography

Abbas, P. J., Brown, C. J., Shallop, J. K., Firszt, J. B., Hughes, M. L., Hong, S. H., and Staller, S. J. (1999). Summary of results using the nucleus ci24m implant to record the electrically evoked compound action potential. *Ear and Hearing*, 20(1):45–59.

Abbas, P. J., Hughes, M. L., Brown, C. J., Miller, C. A., and South, H. (2004). Channel interaction in cochlear implant users evaluated using the electrically evoked compound action potential. *Audiology and Neurotology*, 9(4):203–213.

Alliez, P., Jamin, C., Rineau, L., Tayeb, S., Tournois, J., and Yvinec, M. (2016). Cgal 4.9 - 3d mesh generation: User manual.

Ashmore, J. (1987). A fast motile response in guinea-pig outer hair cells: the cellular basis of the cochlear amplifier. *The Journal of Physiology*, 388:323.

Balkany, T. J., Eshraghi, A. A., and Yang, N. (2002). Modiolar proximity of three perimodiolar cochlear implant electrodes. *Acta oto-laryngologica*, 122(4):363–369.

Ballestero, J., Recugnat, M., Laudanski, J., Smith, K. E., Jagger, D. J., Gnansia, D., and McAlpine, D. (2015). Reducing current spread by use of a novel pulse shape for electrical stimulation of the auditory nerve. *Trends in hearing*, 19:23.

Bareket-Keren, L. and Hanein, Y. (2013). Carbon nanotube-based multi electrode arrays for neuronal interfacing: progress and prospects.

Bear, M. F., Connors, B. W., and Paradiso, M. A. (2007). *Neuroscience*, volume 2. Lippincott Williams & Wilkins.

Berenstein, C. K., Mens, L. H., Mulder, J. J., and Vanpoucke, F. J. (2008). Current steering and current focusing in cochlear implants: comparison of monopolar, tripolar, and virtual channel electrode configurations. *Ear and hearing*, 29(2):250–260.

Bierer, J. A. and Middlebrooks, J. C. (2002). Auditory cortical images of cochlear-implant stimuli: dependence on electrode configuration. *Journal of Neurophysiology*, 87(1):478–492.

Bisquert, J. (2000). Influence of the boundaries in the impedance of porous film electrodes. *Physical Chemistry Chemical Physics*, 2(18):4185–4192.

Bisquert, J., Belmonte, G. G., Santiago, F. F., Ferriols, N. S., Yamashita, M., and Pereira, E. C. (2000). Application of a distributed impedance model in the analysis of conducting polymer films. *Electrochemistry Communications*, 2(8):601–605.

Black, R., Clark, G. M., Tong, Y., and Patrick, J. (1983). Current distribution in cochlear stimulation. *Annals of the New York Academy of Sciences*, 405(1):137–145.

Blamey, P. J., Pyman, B. C., Clark, G. M., Dowell, R. C., Gordon, M., Brown, A. M., and Hollow, R. D. (1992). Factors predicting postoperative sentence scores in postlinguistically deaf adult cochlear implant patients. *Annals of Otology, Rhinology & Laryngology*, 101(4):342–348.

Bonham, B. H. and Litvak, L. M. (2008). Current focusing and steering: modeling, physiology, and psychophysics. *Hearing research*, 242(1):141–153.

Botros, A., van Dijk, B., and Killian, M. (2007). AutonrtTM: An automated system that measures ecap thresholds with the nucleus® freedomTM cochlear implant via machine intelligence. *Artificial Intelligence in Medicine*, 40(1):15–28.

Briaire, J. J. and Frijns, J. H. (2000). 3d mesh generation to solve the electrical volume conduction problem in the implanted inner ear. *Simulation Practice and Theory*, 8(1):57–73.

Briaire, J. J. and Frijns, J. H. (2005). Unraveling the electrically evoked compound action potential. *Hearing research*, 205(1):143–156.

Briaire, J. J. and Frijns, J. H. (2006). The consequences of neural degeneration regarding optimal cochlear implant position in scala tympani: a model approach. *Hearing research*, 214(1):17–27.

Brownell, W. E., Bader, C. R., Bertrand, D., and De Ribaupierre, Y. (1985). Evoked mechanical responses of isolated cochlear outer hair cells. *Science*, 227(4683):194–196.

Brug, G., Van Den Eeden, A., Sluyters-Rehbach, M., and Sluyters, J. (1984). The analysis of electrode impedances complicated by the presence of a constant phase element. *Journal of electroanalytical chemistry and interfacial electrochemistry*, 176(1-2):275–295.

Brummer, S. and Turner, M. (1977). Electrochemical considerations for safe electrical stimulation of the nervous system with platinum electrodes. *IEEE Transactions on Biomedical Engineering*, (1):59–63.

Brunton, E. K., Lowery, A. J., and Rajan, R. (2012). A comparison of microelectrodes for a visual cortical prosthesis using finite element analysis. *Frontiers in neuroengineering*, 5:23.

Busby, P., Whitford, L., Blamey, P. J., Richardson, L., and Clark, G. M. (1994). Pitch perception for different modes of stimulation using the cochlear multiple-electrode prosthesis. *The Journal of the Acoustical Society of America*, 95(5):2658–2669.

Cacciola, F. (2016). Cgal 4.9 - triangulated surface mesh simplification: User manual.

Calvetti, D., Morigi, S., Reichel, L., and Sgallari, F. (2000). Tikhonov regularization and the l-curve for large discrete ill-posed problems. *Journal of computational and applied mathematics*, 123(1):423–446.

Cantrell, D. R., Inayat, S., Taflove, A., Ruoff, R. S., and Troy, J. B. (2007). Incorporation of the electrode–electrolyte interface into finite-element models of metal microelectrodes. *Journal of neural engineering*, 5(1):54.

Chittka L, B. (2009). Perception space—the final frontier, a plos biology.

Choi, C. T. and Hsu, C.-H. (2009). Conditions for generating virtual channels in cochlear prosthesis systems. *Annals of biomedical engineering*, 37(3):614–624.

Choi, C. T., Lai, W.-D., and Chen, Y.-B. (2005). Comparison of the electrical stimulation performance of four cochlear implant electrodes. *IEEE transactions on magnetics*, 41(5):1920–1923.

Choi, C. T., Lai, W.-D., and Lee, S.-S. (2006). A novel approach to compute the impedance matrix of a cochlear implant system incorporating an electrode-tissue interface based on finite element method. *IEEE transactions on magnetics*, 42(4):1375–1378.

Choi, C. T. and Wang, S. P. (2014). Modeling ecap in cochlear implants using the fem and equivalent circuits. *IEEE Transactions on Magnetics*, 50(2):49–52.

Clark, J. R., Warren, F. M., and Abbott, J. J. (2011). A scalable model for human scala-tympani phantoms. *Journal of Medical Devices*, 5(1):014501.

Cohen, L. T., Richardson, L. M., Saunders, E., and Cowan, R. S. (2003). Spatial spread of neural excitation in cochlear implant recipients: comparison of improved ecap method and psychophysical forward masking. *Hearing research*, 179(1):72–87.

Cohen, L. T., Xu, J., Xu, S. A., and Clark, G. M. (1996). Improved and simplified methods for specifying positions of the electrode bands of a cochlear implant array. *The American Journal of Otology*, 17(6):859–865.

Colombo, J. and Parkins, C. W. (1987). A model of electrical excitation of the mammalian auditory-nerve neuron. *Hearing research*, 31(3):287–311.

Dallos, P. and Fay, R. R. (2012). *The cochlea*, volume 8. Springer Science & Business Media.

Dang, K., Clerc, M., Vandersteen, C., Guevara, N., and Gnansia, D. (2015). In situ validation of a parametric model of electrical field distribution in an implanted cochlea. In *Neural Engineering (NER), 2015 7th International IEEE/EMBS Conference on*, pages 667–670. IEEE.

De Fraissinette, A., Felix, H., Hoffmann, V., Johnsson, L.-G., and Gleeson, M. (1993). Human reissner's membrane in patients with age-related normal hearing and with sensorineural hearing loss. *ORL*, 55(2):68–72.

Demarcy, T., Vandersteen, C., Raffaelli, C., Gnansia, D., Guevara, N., Ayache, N., and Delingette, H. (2016). Uncertainty quantification of cochlear implant insertion from ct images. In *Workshop on Clinical Image-Based Procedures*, pages 27–35. Springer.

Dorman, M. F. and Wilson, B. S. (2004). The design and function of cochlear implants. *Am. Sci*, 92(5):436–445.

Duan, Y., Clark, G. M., and Cowan, R. (2004). A study of intra-cochlear electrodes and tissue interface by electrochemical impedance methods in vivo. *Biomaterials*, 25(17):3813–3828.

Duda, R. O. and Hart, P. E. (1972). Use of the hough transformation to detect lines and curves in pictures. *Communications of the ACM*, 15(1):11–15.

Dynes, S. B. and Delgutte, B. (1992). Phase-locking of auditory nerve discharges to sinusoidal electric stimulation of the cochlea. *Hearing research*, 58(1):79–90.

Engle, J. R., Tinling, S., and Recanzone, G. H. (2013). Age-related hearing loss in rhesus monkeys is correlated with cochlear histopathologies. *PLoS One*, 8(2):e55092.

Escudé, B., James, C., Deguine, O., Cochard, N., Eter, E., and Fraysse, B. (2006). The size of the cochlea and predictions of insertion depth angles for cochlear implant electrodes. *Audiology and Neurotology*, 11(Suppl. 1):27–33.

Everest, F. A. and Pohlmann, K. C. (2001). *The master handbook of acoustics*, volume 4. McGraw-Hill New York.

Fabri, A. and Pion, S. (2009). Cgal: The computational geometry algorithms library. In *Proceedings of the 17th ACM SIGSPATIAL international conference on advances in geographic information systems*, pages 538–539. ACM.

Finley, C. C. and Skinner, M. W. (2008). Role of electrode placement as a contributor to variability in cochlear implant outcomes. *Otology & neurotology: official publication of the American Otological Society, American Neurotology Society [and] European Academy of Otology and Neurotology*, 29(7):920.

Finley, C. C., Wilson, B. S., and White, M. W. (1990). Models of neural responsiveness to electrical stimulation. In *Cochlear implants*, pages 55–96. Springer.

Firszt, J. B., Koch, D. B., Downing, M., and Litvak, L. (2007). Current steering creates additional pitch percepts in adult cochlear implant recipients. *Otology & Neurotology*, 28(5):629–636.

Fishman, K. E., Shannon, R. V., and Slattery, W. H. (1997). Speech recognition as a function of the number of electrodes used in the speak cochlear implant speech processor. *Journal of Speech, Language, and Hearing Research*, 40(5):1201–1215.

Friesen, L. M., Shannon, R. V., Baskent, D., and Wang, X. (2001). Speech recognition in noise as a function of the number of spectral channels: comparison of acoustic hearing and cochlear implants. *The Journal of the Acoustical Society of America*, 110(2):1150–1163.

Frijns, J., De Snoo, S., and Schoonhoven, R. (1995). Potential distributions and neural excitation patterns in a rotationally symmetric model of the electrically stimulated cochlea. *Hearing research*, 87(1):170–186.

Frijns, J., De Snoo, S., and Ten Kate, J. (1996). Spatial selectivity in a rotationally symmetric model of the electrically stimulated cochlea. *Hearing Research*, 95(1):33–48.

Frijns, J. H., Dekker, D. M., and Briaire, J. J. (2011). Neural excitation patterns induced by phased-array stimulation in the implanted human cochlea. *Acta otolaryngologica*, 131(4):362–370.

Fu, Q.-J., Shannon, R. V., and Wang, X. (1998). Effects of noise and spectral resolution on vowel and consonant recognition: Acoustic and electric hearing. *The Journal of the Acoustical Society of America*, 104(6):3586–3596.

Geers, A. E. (2002). Factors affecting the development of speech, language, and literacy in children with early cochlear implantation. *Language, Speech, and Hearing Services in Schools*, 33(3):172–183.

Gfeller, K., Turner, C., Oleson, J., Zhang, X., Gantz, B., Froman, R., and Olszewski, C. (2007). Accuracy of cochlear implant recipients on pitch perception, melody recognition, and speech reception in noise. *Ear and hearing*, 28(3):412–423.

Gilroy, A. M., MacPherson, B. R., and Ross, L. M. (2008). *Atlas of anatomy*. New York: Thieme.

Gramfort, A., Papadopoulo, T., Olivi, E., and Clerc, M. (2010). Openmeeg: open-source software for quasistatic bioelectromagnetics. *Biomedical engineering online*, 9(1):45.

Gramfort, A., Papadopoulo, T., Olivi, E., and Clerc, M. (2011). Forward field computation with openmeeg. *Computational intelligence and neuroscience*, 2011.

Greenwood, D. D. (1961). Auditory masking and the critical band. *The journal of the acoustical society of America*, 33(4):484–502.

Greenwood, D. D. (1990). A cochlear frequency-position function for several species—29 years later. *The Journal of the Acoustical Society of America*, 87(6):2592–2605.

Hanekom, T. (2001). Three-dimensional spiraling finite element model of the electrically stimulated cochlea. *Ear and hearing*, 22(4):300–315.

Hanekom, T. (2005). Modelling encapsulation tissue around cochlear implant electrodes. *Medical and Biological Engineering and Computing*, 43(1):47–55.

Hansen, P. C. (1999). *The L-curve and its use in the numerical treatment of inverse problems*.

Hequembourg, S. and Liberman, M. C. (2001). Spiral ligament pathology: a major aspect of age-related cochlear degeneration in c57bl/6 mice. *Journal of the Association for Research in Otolaryngology*, 2(2):118–129.

Hochmair, I., Nopp, P., Jolly, C., Schmidt, M., Schößer, H., Garnham, C., and Anderson, I. (2006). Med-el cochlear implants: state of the art and a glimpse into the future. *Trends in amplification*, 10(4):201–219.

Inguva, C., Wong, P., Sue, A., McEwan, A., and Carter, P. (2015). Frequency-dependent simulation of volume conduction in a linear model of the implanted cochlea. In *Neural Engineering (NER), 2015 7th International IEEE/EMBS Conference on*, pages 426–429. IEEE.

Javel, E. and Shepherd, R. K. (2000). Electrical stimulation of the auditory nerve: Iii. response initiation sites and temporal fine structure. *Hearing research*, 140(1):45–76.

Johnson, D. H. (1980). The relationship between spike rate and synchrony in responses of auditory-nerve fibers to single tones. *The Journal of the Acoustical Society of America*, 68(4):1115–1122.

Jolly, C., Spelman, F., and Clopton, B. (1996). Quadrupolar stimulation for cochlear prostheses: modeling and experimental data. *IEEE transactions on biomedical engineering*, 43(8):857–865.

Kalkman, R. K., Briaire, J. J., Dekker, D. M., and Frijns, J. H. (2014). Place pitch versus electrode location in a realistic computational model of the implanted human cochlea. *Hearing research*, 315:10–24.

Kalkman, R. K., Briaire, J. J., and Frijns, J. H. (2015). Current focussing in cochlear implants: an analysis of neural recruitment in a computational model. *Hearing research*, 322:89–98.

Kalkman, R. K., Briaire, J. J., and Frijns, J. H. (2016). Stimulation strategies and electrode design in computational models of the electrically stimulated cochlea: an overview of existing literature. *Network: Computation in Neural Systems*, 27(2-3):107–134.

Koch, D. B., Downing, M., Osberger, M. J., and Litvak, L. (2007). Using current steering to increase spectral resolution in cii and hires 90k users. *Ear and hearing*, 28(2):38–41.

Kral, A., Hartmann, R., Mortazavi, D., and Klinke, R. (1998). Spatial resolution of cochlear implants: the electrical field and excitation of auditory afferents. *Hearing research*, 121(1):11–28.

Kybic, J., Clerc, M., Abboud, T., Faugeras, O., Keriven, R., and Papadopoulo, T. (2005). A common formalism for the integral formulations of the forward eeg problem. *IEEE transactions on medical imaging*, 24(1):12–28.

Lai, W.-D. and Choi, C. T. (2007). Incorporating the electrode-tissue interface to cochlear implant models. *IEEE Transactions on Magnetics*, 43(4):1721–1724.

Lai, W. K., Müller-Deile, J., Dillier, N., Almqvist, B., Stecker, M., Frohne, C., and Von Wallenberg, E. (2002). Measurement of the electrically evoked compound action potential via a neural response telemetry system. *Annals of Otology, Rhinology & Laryngology*, 111(5):407–414.

Landsberger, D. M., Padilla, M., and Srinivasan, A. G. (2012). Reducing current spread using current focusing in cochlear implant users. *Hearing research*, 284(1):16–24.

Lareida, A., Beckmann, F., SCHROTT-FISCHER, A., Glueckert, R., Freysinger, W., and Müller, B. (2009). High-resolution x-ray tomography of the human inner ear: synchrotron radiation-based study of nerve fibre bundles, membranes and ganglion cells. *Journal of microscopy*, 234(1):95–102.

Lim, H. H., McDermott, H. J., Tong, Y. C., and Wills, R. (1990). Approximation of intracochlear electrode impedance from telemetered measurements in a multi-electrode cochlear implant patient. In *Engineering in Medicine and Biology Society, 1990., Proceedings of the Twelfth Annual International Conference of the IEEE*, pages 2288–2289. IEEE.

Litvak, L. M., Spahr, A. J., and Emadi, G. (2007). Loudness growth observed under partially tripolar stimulation: model and data from cochlear implant listeners. *The Journal of the Acoustical Society of America*, 122(2):967–981.

Machado, J. T. et al. (2001). Discrete-time fractional-order controllers. *Fractional Calculus and Applied Analysis*, 4(1):47–66.

Malherbe, T., Hanekom, T., and Hanekom, J. (2015). Constructing a three-dimensional electrical model of a living cochlear implant user's cochlea. *International journal for numerical methods in biomedical engineering*, 32(7).

Manley, G. A. and Fay, R. R. (2007). *Active processes and otoacoustic emissions in hearing*, volume 30. Springer Science & Business Media.

McAdams, E., Lackermeier, A., McLaughlin, J., Macken, D., and Jossinet, J. (1995). The linear and non-linear electrical properties of the electrode-electrolyte interface. *Biosensors and Bioelectronics*, 10(1-2):67–74.

McCalla, W. J. (2012). *Fundamentals of computer-aided circuit simulation*, volume 37. Springer Science & Business Media.

McDermott, H. J. (2004). Music perception with cochlear implants: a review. *Trends in amplification*, 8(2):49–82.

McDermott, H. J. and McKay, C. M. (1994). Pitch ranking with nonsimultaneous dual-electrode electrical stimulation of the cochlea. *The Journal of the Acoustical Society of America*, 96(1):155–162.

McDermott, H. J., McKay, C. M., and Vandali, A. E. (1992). A new portable sound processor for the university of melbourne/nucleus limited multielectrode cochlear implant. *The Journal of the Acoustical Society of America*, 91(6):3367–3371.

Miller, C. A., Robinson, B. K., Rubinstein, J. T., Abbas, P. J., and Runge-Samuelson, C. L. (2001). Auditory nerve responses to monophasic and biphasic electric stimuli. *Hearing research*, 151(1):79–94.

Moore, B. C. and Alcántara, J. I. (2001). The use of psychophysical tuning curves to explore dead regions in the cochlea. *Ear and hearing*, 22(4):268–278.

Nadol, J. B., Young, Y.-S., and Glynn, R. J. (1989). Survival of spiral ganglion cells in profound sensorineural hearing loss: implications for cochlear implantation. *Annals of Otology, Rhinology & Laryngology*, 98(6):411–416.

Nelson, D. A., Donaldson, G. S., and Kreft, H. (2008). Forward-masked spatial tuning curves in cochlear implant users. *The Journal of the Acoustical Society of America*, 123(3):1522–1543.

Nichols, K., Kazmierski, T., Zwolinski, M., and Brown, A. (1994). Overview of spice-like circuit simulation algorithms. *IEE Proceedings-Circuits, Devices and Systems*, 141(4):242–250.

Nie, K., Barco, A., and Zeng, F.-G. (2006). Spectral and temporal cues in cochlear implant speech perception. *Ear and hearing*, 27(2):208–217.

O'Leary, M. J., House, W. F., Fayad, J., and Linthicum, F. H. (1991). Electrode insertion trauma in cochlear implantation. *Annals of Otology, Rhinology & Laryngology*, 100(9):695–699.

Olivi, E. (2011). *Coupling of numerical methods for the forward problem in Magneto- and Electro-EncephaloGraphy.* PhD thesis, Université Nice Sophia Antipolis.

Online-Encyclopaedia-Britannica (1997a). Basilar membrane: analysis of sound frequencies.

Online-Encyclopaedia-Britannica (1997b). Cochlea: cross section.

Online-Encyclopaedia-Britannica (1997c). Ear: organ of corti.

Palmer, J. M. (1984). *Anatomy for speech and hearing*. HarperCollins Publishers.

Patrick, J. F., Busby, P. A., and Gibson, P. J. (2006). The development of the nucleus® freedom™ cochlear implant system. *Trends in amplification*, 10(4):175–200.

Ramos-Miguel, A., Ramos-Macías, A., Artiles, J. V., and Zaballos, M. T. P. (2015). The effect of reference electrode position in cochlear implants. *J Int Adv Otol*, 11(3):222–8.

Rattay, F. (1986). Analysis of models for external stimulation of axons. *IEEE transactions on biomedical engineering*, (10):974–977.

Rattay, F., Leao, R. N., and Felix, H. (2001). A model of the electrically excited human cochlear neuron. ii. influence of the three-dimensional cochlear structure on neural excitability. *Hearing research*, 153(1):64–79.

Rebscher, S. J., Hetherington, A., Bonham, B., Wardrop, P., Whinney, D., and Leake, P. A. (2008). Considerations for the design of future cochlear implant electrode arrays: Electrode array stiffness, size and depth of insertion. *Journal of rehabilitation research and development*, 45(5):731.

Richardot, A. and McAdams, E. (2002). Harmonic analysis of low-frequency bioelectrode behavior. *IEEE transactions on medical imaging*, 21(6):604–612.

Robblee, L. S. and Rose, T. L. (1990). Electrochemical guidelines for selection of protocols and electrode materials for neural stimulation. *Neural prostheses: Fundamental studies*, pages 25–66.

Saba, R. (2012). *Cochlear implant modelling: stimulation and power consumption*. PhD thesis, University of Southampton.

Sadkowski, A. (1993). Time domain responses of constant phase electrodes. *Electrochimica acta*, 38(14):2051–2054.

Shannon, R. V., Fu, Q.-J., and Galvin Iii, J. (2004). The number of spectral channels required for speech recognition depends on the difficulty of the listening situation. *Acta Oto-Laryngologica*, 124(0):50–54.

Shannon, R. V., Zeng, F.-G., Kamath, V., Wygonski, J., and Ekelid, M. (1995). Speech recognition with primarily temporal cues. *Science*, 270(5234):303.

Shepherd, R., Murray, M., Hougiton, M., and Clark, G. M. (1985). Scanning electron microscopy of chronically stimulated platinum intracochlear electrodes. *Biomaterials*, 6(4):237–242.

Shepherd, R. K. (1999). Chronic electrical stimulation of the auditory nerve using non-charge-balanced stimuli. *Acta otolaryngologica*, 119(6):674–684.

Shepherd, R. K., Matsushima, J., Millard, R., and Clark, G. M. (1991). Cochlear pathology following chronic electrical stimulation using non charge balanced stimuli. *Acta otolaryngologica*, 111(5):848–860.

Shibata, T., Matsumoto, S., Agishi, T., and Nagano, T. (2009). Visualization of reissner membrane and the spiral ganglion in human fetal cochlea by microcomputed tomography. *American journal of otolaryngology*, 30(2):112–120.

Sit, J.-J. and Sarpeshkar, R. (2007). A low-power blocking-capacitor-free charge-balanced electrode-stimulator chip with less than 6 na dc error for 1-ma full-scale stimulation. *IEEE Transactions on Biomedical Circuits and Systems*, 1(3):172–183.

Smith, Z. M., Delgutte, B., and Oxenham, A. J. (2002). Chimaeric sounds reveal dichotomies in auditory perception. *Nature*, 416(6876):87–90.

Snyder, R. L., Bierer, J. A., and Middlebrooks, J. C. (2004). Topographic spread of inferior colliculus activation in response to acoustic and intracochlear electric stimulation. *Journal of the Association for Research in Otolaryngology*, 5(3):305–322.

Snyder, R. L., Middlebrooks, J. C., and Bonham, B. H. (2008). Cochlear implant electrode configuration effects on activation threshold and tonotopic selectivity. *Hearing research*, 235(1):23–38.

Spelman, F., Pfingst, B., Clopton, B., Jolly, C., and Rodenhiser, K. (1995). Effects of electrical current configuration on potential fields in the electrically stimulated cochlea: field models and measurements. *The Annals of otology, rhinology & laryngology. Supplement*, 166:131–136.

Stakhovskaya, O., Sridhar, D., Bonham, B. H., and Leake, P. A. (2007). Frequency map for the human cochlear spiral ganglion: implications for cochlear implants. *Journal for the Association for Research in Otolaryngology*, 8(2):220–233.

Strelioff, D. (1973). A computer simulation of the generation and distribution of cochlear potentials. *The Journal of the Acoustical Society of America*, 54(3):620–629.

Sue, A., Tran, P., Wong, P., Li, Q., and Carter, P. (2013). Time-domain finite element models of electrochemistry in intracochlear electrodes. In *Engineering in Medicine and Biology Society (EMBC), 2013 35th Annual International Conference of the IEEE*, pages 1554–1557. IEEE.

Sue, A., Wong, P., Tran, P., Li, Q., and Carter, P. (2015). Modeling the effects of electrode recessing on electrochemical safety in cochlear implant electrodes. In *Neural Engineering (NER), 2015 7th International IEEE/EMBS Conference on*, pages 490–493. IEEE.

Suesserman, M. and Spelman, F. (1993). Lumped-parameter model for in vivo cochlear stimulation. *IEEE Transactions on Biomedical Engineering*, 40(3):237–245.

Svirsky, M. A., Teoh, S.-W., and Neuburger, H. (2004). Development of language and speech perception in congenitally, profoundly deaf children as a function of age at cochlear implantation. *Audiology and Neurotology*, 9(4):224–233.

Thomopoulos, G. N., Spicer, S. S., Gratton, M. A., and Schulte, B. A. (1997). Age-related thickening of basement membrane in stria vascularis capillaries. *Hearing research*, 111(1):31–41.

Tognola, G., Pesatori, A., Norgia, M., Parazzini, M., Di Rienzo, L., Ravazzani, P., Burdo, S., Grandori, F., and Svelto, C. (2007). Numerical modeling and experimental measurements of the electric potential generated by cochlear implants in physiological tissues. *IEEE Transactions on Instrumentation and Measurement*, 56(1):187–193.

Tourrel, G. (2016). An electrode array for a transmodiolar implant and a manufacturing method. EP Patent App. EP20,140,192,294.

Toussaint, N., Souplet, J.-C., and Fillard, P. (2007). Medinria: Medical image navigation and research tool by inria. In *Proc. of MICCAI'07 Workshop on Interaction in medical image analysis and visualization*.

Tran, P., Sue, A., Wong, P., Li, Q., and Carter, P. (2015). Development of heather for cochlear implant stimulation using a new modeling workflow. *IEEE Transactions on Biomedical Engineering*, 62(2):728–735.

Tye-Murray, N., Spencer, L., and Woodworth, G. G. (1995). Acquisition of speech by children who have prolonged cochlear implant experience. *Journal of Speech, Language, and Hearing Research*, 38(2):327–337.

University-California-San-Francisco (2012). Cochlear implant.

Valsa, J., Friedl, M., and Dvorak, P. (2011). Network model of the cpe. *Radioengineering*.

van den Honert, C. and Kelsall, D. C. (2007). Focused intracochlear electric stimulation with phased array channelsa). *The Journal of the Acoustical Society of America*, 121(6):3703–3716.

van den Honert, C. and Mortimer, J. T. (1979). The response of the myelinated nerve fiber to short duration biphasic stimulating currents. *Annals of biomedical engineering*, 7(2):117–125.

Vanpoucke, F. J., Zarowski, A. J., and Peeters, S. A. (2004). Identification of the impedance model of an implanted cochlear prosthesis from intracochlear potential measurements. *IEEE Transactions on biomedical engineering*, 51(12):2174–2183.

Wardrop, P., Whinney, D., Rebscher, S. J., Luxford, W., and Leake, P. (2005a). A temporal bone study of insertion trauma and intracochlear position of cochlear implant electrodes. ii: Comparison of spiral clarion™ and hifocus ii™ electrodes. *Hearing research*, 203(1):68–79.

Wardrop, P., Whinney, D., Rebscher, S. J., Roland, J. T., Luxford, W., and Leake, P. A. (2005b). A temporal bone study of insertion trauma and intracochlear position of cochlear implant electrodes. i: Comparison of nucleus banded and nucleus contour™ electrodes. *Hearing research*, 203(1):54–67.

Wever, E. G. (1938). Ii the width of the basilar membrane in man. *Annals of Otology, Rhinology & Laryngology*, 47(1):37–47.

Wilson, B. S. and Dorman, M. F. (2008). Cochlear implants: a remarkable past and a brilliant future. *Hearing research*, 242(1):3–21.

Wilson, B. S., Finley, C. C., Lawson, D. T., Wolford, R. D., Eddington, D. K., and Rabinowitz, W. M. (1991). Better speech recognition with cochlear implants. *Nature*, 352(6332):236–238.

Wong, P., George, S., Tran, P., Sue, A., Carter, P., and Li, Q. (2016). Development and validation of a high-fidelity finite-element model of monopolar stimulation in the implanted guinea pig cochlea. *IEEE Transactions on Biomedical Engineering*, 63(1):188–198.

Wright, C. G., Roland, P. S., and Kuzma, J. (2005). Advanced bionics thin lateral and helix ii electrodes: a temporal bone study. *The Laryngoscope*, 115(11):2041–2045.

Wysocki, J. (1999). Dimensions of the human vestibular and tympanic scalae. *Hearing research*, 135(1-2):39.

Yoo, S. K., Wang, G., Rubinstein, J. T., Skinner, M. W., and Vannier, M. W. (2000). Three-dimensional modeling and visualization of the cochlea on the internet. *IEEE Transactions on Information Technology in biomedicine*, 4(2):144–151.

Zeng, F.-G., Grant, G., Niparko, J., Galvin, J., Shannon, R., Opie, J., and Segel, P. (2002). Speech dynamic range and its effect on cochlear implant performance. *The Journal of the Acoustical Society of America*, 111(1):377–386.

Zeng, F.-G., Rebscher, S., Harrison, W., Sun, X., and Feng, H. (2008). Cochlear implants: system design, integration, and evaluation. *IEEE reviews in biomedical engineering*, 1:115–142.

Zwolan, T. A., Kileny, P. R., Ashbaugh, C., and Telian, S. A. (1996). Patient performance with the cochlear corporation" 20+ 2" implant: bipolar versus monopolar activation. *Otology & Neurotology*, 17(5):717–723.